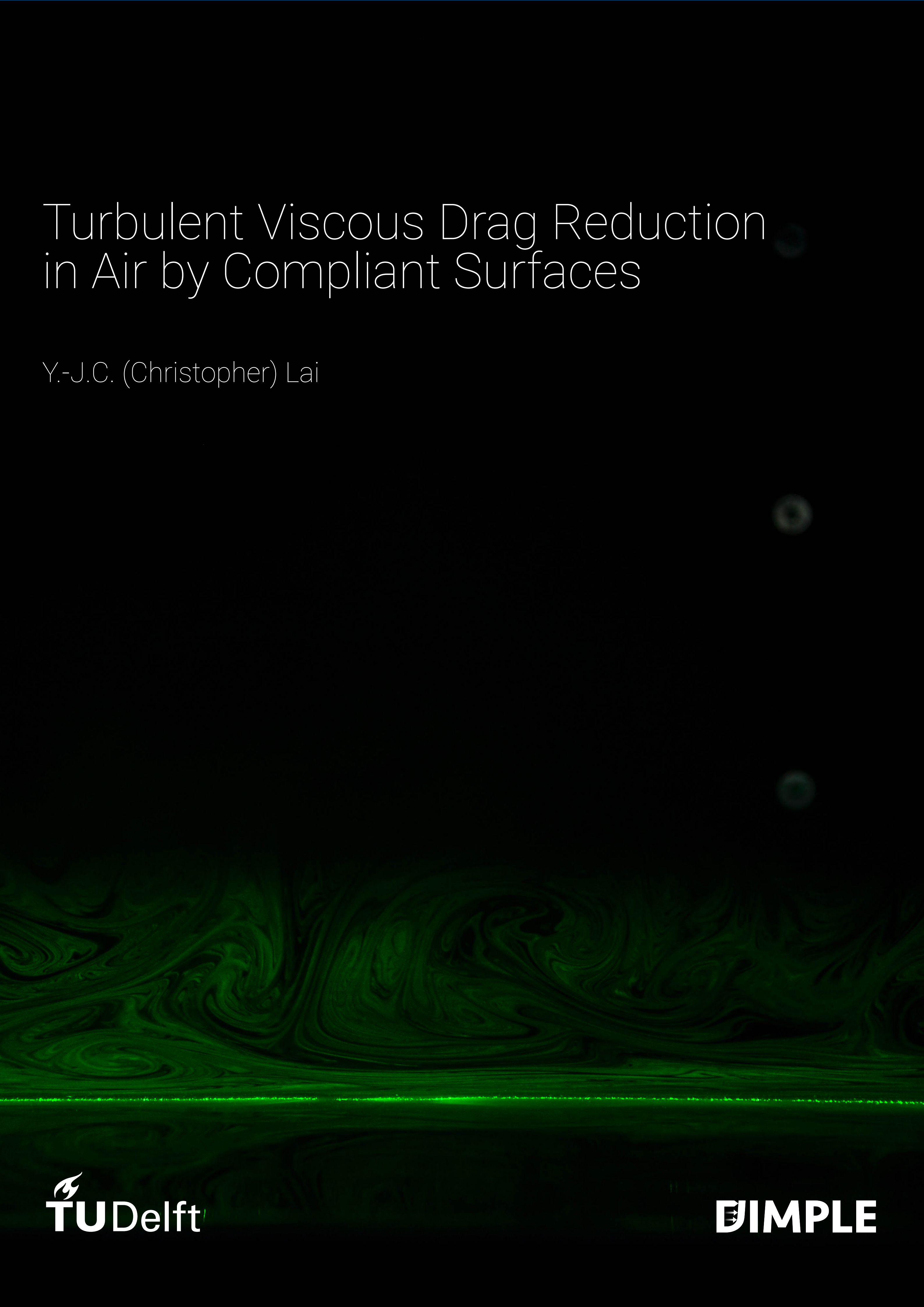

Turbulent Viscous Drag Reduction in Air by Compliant Surfaces

Y.-J.C. (Christopher) Lai

Turbulent Viscous Drag Reduction in Air by Compliant Surfaces

MSc Thesis

by

Y.-J.C. (Christopher) Lai

in fulfillment of the requirements for the degree of

Master of Science in Aerospace Engineering

at the Delft University of Technology.

Student number:	4788036		
Time and location of defense:	26th February, 2021 14:00, Delft		
Thesis duration:	2nd September, 2019 – 7th February, 2020 6th July, 2020 – 26th February, 2021		
Thesis committee:	Chair	Dr.ir. B.W. van Oudheusden	Delft University of Technology (LR)
	Supervisor	Dr.ir. F.F.J. Schrijer	Delft University of Technology (LR)
	Supervisor	Ir. M. van Nesselrooij	Dimple Aerospace B.V.
	Reader	Dr. R. Delfos	Delft University of Technology (3ME)
	Reader	Dr.ir. W.J. Baars	Delft University of Technology (LR)

This thesis is confidential and cannot be made public until 26th February, 2023
Op dit verslag is geheimhouding van toepassing tot en met 26 februari 2023

Acknowledgement

This thesis marks an end to what has been a fruitful yet tumultuous 2 years and 6 months of my master studies in aerodynamics at the Delft University of Technology. If I were to exemplify my experience here as a function, it would be a sine wave. While having its fair share of peaks and valleys, the overall experience on the cover was quite alright given by the geometric mean, but then the actual gain is quantified by the root-mean-square mean. My studies here in Delft have given me so much more then I could have imagined, and I owe this to the support from the people that I am surrounded with.

This project would not have been possible with the trust and support of Michiel van Nesselrooij and Olaf van Campenhout of Dimple Aerospace BV. Both of your bottomless enthusiasm and insightful guidance have been the cornerstone of this research. Most importantly, it has made this research fun and something to be excited about, which was what always kept me going during difficult times.

I would like to thank Dr. Bas van Oudheusden and Dr. Ferdinand Schrijer for their invaluable academic counsel throughout this research. I always looked forward to the feedback during every monthly meeting which led to a lot of priceless "why didn't I think of that" moments. I have learned so much from both of your aerodynamic intuition, research experience, and experimental aptitude, which laid the successful foundation of this research.

Thank you to Dr. Arnoud Greidanus and Dr. Henk Benschop for the initial guidance into the experimental and numerical aspects of compliant surface fluid-structure interaction. This research has benefited a great amount from both of your input.

I would also like to thank the staff that supported the wide range of experiments conducted in this research. At the High-Speed Laboratory Dennis Bruikman, Ir. Frits Donker Duyvis, Henk-Jan Siemer, Ir. Nando Timmer, Nico van Beek, and Peter Duyndam. At the Low-Speed Laboratory Dr. Marios Kotsonis, Emiel Langedijk, and Ir. Stefan Bernardy. At the Material Physics Lab of DASML Dr. Marlies Nijmeisland.

Although it was only for a brief four months before the pandemic started, I want to thank my fellow colleagues at the HSL basement. The lunch and coffee breaks with you guys were a much-needed oasis to briefly switch off.

And to my fellow Dimple experimentalists during the pandemic, Eric Claro Dietrich, Friso Hartog, Joost van der Voort Maarschalk; I really enjoyed the time we spent together at the HSL and also supporting each other's experiments. I will not miss the smell of the seal fur but I will definitely look back at the good times we had.

To my fellow Taiwanese friends in Delft, you guys made Delft like home far away from home with our weekly hot-pots at Friday nights. I want to especially thank my fellow Taiwanese Aerospace Engineering crew Jason Chuang and Yu-Yu Lin. I could not have imagined surviving the first year without you both; you guys really lifted me up to another level and kept me going through the hardships.

Finally to my loved ones. To my girlfriend, thank you for bearing with my selfishness of pursuing my dream. Although separated in distance, your unyielding support and counsel kept me moving forward throughout my time here in Delft. My family, whom provided the constant undiminished support from day one. Words cannot contain the gratitude I feel towards everything you have done for me. Thank you for never doubting me and letting me pursue my dream. Even at my lowest point, I knew that I could count on all of your support.

And to my past self who set foot in the Netherlands at 2018. You are going to be broken down, several times. A lot of things are still an unknown, but that is life. As long as you give your everything, everything will turn out to be fine.

Yu-Jui Christopher Lai
Delft, 17th January, 2021

Abstract

This research studies the fluid-structure interaction (FSI) of a compliant surface in air flows, with an objective of finding possible turbulent viscous drag reduction. A compliant surface is a thin layer of viscoelastic material drawing inspiration from dolphin epidermis, which was thought to have drag-reducing capabilities by Gray (1936). Research into the drag reduction capabilities of compliant surfaces has been long going for more than five decades starting with Kramer (1960), yet no firm conclusion has been reached. In addition, most of the experimental research has been focused on water flows, with air flows regarded as incapable of inertially forcing a compliant surface to deform. This thesis attempts to disprove this assumption by applying the proper inertial scaling to the FSI between the compliant surface and air flows.

This research proposes a two-step outer scaling of the FSI, first the Reynolds number then the Inertial ratio, alongside an inner scaling adapted from Benschop et al. (2019). Compliant surfaces are characterised by various properties, with the stiffness and thickness presumed to be of first-order influence to the FSI. The magnitude of complex shear modulus $|G^*|$ characterises the compliant surface stiffness. The mentioned scaling utilises the compliant surface stiffness to scale with the inertial potential of the surface to the flow.

A sweep of the compliant surface stiffness and thickness was conducted using direct drag measurements in the wind tunnel. Drag delta results confirm the possibility of turbulent viscous drag reduction by compliant surfaces, with a measured drag delta of -3.43%. This drag-reducing compliant surface is characterised by being the thickest (4.15 mm) and least stiff (2.18 kPa) of all the compliant surfaces tested. In addition, this compliant surface had noticeably high viscoelasticity, characterised by the loss tangent $\tan\delta_p$, with a value of 0.37. This drag reduction result is further supported by the reduction of 1D turbulence intensity at the trailing edge of the test plate from hot-wire measurements, and a smaller decay of the shape factor H from particle image velocimetry (PIV). Quadrant analysis of the PIV data found evidence of a reduction in combined Q2 and Q4 events, further supporting the drag delta observed.

Correlation between the compliant surface's viscoelastic properties and the drag delta found a negative correlation between the magnitude of complex shear modulus and a positive correlation between the loss tangent and drag reduction. No correlation was found between the thickness and drag delta. The unusually high loss tangent for the drag-reducing compliant surface and its subtle positive correlation with the drag reduction is an indication that the viscoelasticity might have a greater influence on the FSI than expected.

Table of Contents

List of Figures

List of Tables

Nomenclature

Acronyms and Abbreviations

A	Component A of PlatSil Gel OO
B	Component B of PlatSil Gel OO
CI	Confidence interval
CNC	Computer numerical control
CTA	Constant temperature anemometer
D	Deadener
DASML	Delft Aerospace Structures and Materials Laboratory
DE	Differential evolution
DIC	Digital image correlation
DNS	Direct numerical simulation
DOF	Degrees of freedom
DR	Drag reduction
FOV	Field of view
FSI	Fluid-structure interaction
H	Hardener, height
HSL	TU Delft High Speed Laboratory
HWA	Hot wire anemometry
KNMI	Royal Netherlands Meteorological Institute
LDV	Laser Doppler velocimetry
LE	Leading edge
LEBUs	Large-eddy breakup devices
LES	Large-eddy simulation
LSL	TU Delft Low Speed Laboratory
MDF	Medium-Density Fibreboard
MRO	Maintenance, repair, and operations
PCI	Pounds per cubic inch
PIV	Particle image velocimetry
PLA	Polylactide
PPI	Pores per inch
PTU	Programmable timing unit
PVC	Polyvinyl chloride
RMS	Root-mean-square
RMSE	Root-mean-square error
RTV	Room temperature vulcanised
SDGs	Sustainable Development Goals
SEBS	Triblock-copolymer polystyrene-b-(ethylene-co-butylene)-b-styrene
TE	Trailing edge
TRL	Technology Readiness Level
TSI	Tollmien-Schlichting instability
WT	Wind tunnel

English Symbols

Re	Reynolds number
C_D	Drag coefficient
C_f	Skin friction coefficient
c_s	Surface transverse wave velocity (Shear wave velocity)
D	Drag
E	Young’s (elastic) modulus
E’	Elastic storage modulus
E”	Elastic loss modulus
f	Lens focal length, frequency
f_0	Fundamental frequency of longitudinal vibration
$f_\#$	f-stop
F_a	Axial force
G	Shear modulus (Modulus of rigidity)
G’	Shear storage modulus
G”	Shear loss modulus
G^*	Complex shear modulus
H	Shape factor

I_r	Inertial ratio
M	Magnification factor
N	Ensemble sample size
R^2	Coefficient of determination
t	t-value
t_0^+	Non-dimensional period
$\mathrm{t}_{\mathrm{crit}}$	Critical t-value
u^+	Non-dimensional streamwise velocity
u_∞	Mean flow velocity
u_τ	Wall-friction velocity
u_r	Velocity ratio
y^+	Non-dimensional wall-normal distance

Greek Symbols

Δt	Laser pulse separation time
δ_b	Boundary layer thickness
δ_p	Phase lag between stress and strain
δ_s	Compliant surface or sample thickness
$\delta_{r\lambda}$	Ratio of surface thickness to wavelength of deformation
δ_{sub}	Viscous sublayer height
$\dot{\gamma}$	Shear strain rate
η	Complex viscosity
η'	Dynamic viscosity (Rheology)
η''	Storage viscosity
γ	Shear strain
γ_0	Shear strain amplitude
λ	Wavelength
μ	Dynamic viscosity (Fluid mechanics)
ν	Kinematic viscosity
ν_P	Poisson's ratio
ω	Angular velocity
ρ	Density
ρ_r	Density ratio
σ	Longitudinal stress
τ	Shear stress, characteristic time
τ^*	Complex shear stress
τ_w	Wall shear stress
ε	Strain, uncertainty

Subscript

e	Elastic
f	Flow
L	Test plate length
p	Particle
r	Ratio
s	Surface
v	Viscous

1

Introduction

Since the inception of the boundary layer concept by Prandtl, engineers have come a long way in understanding the viscous flow phenomenon. Although much-uncovered ground remains, scientists and engineers have looked into and partially succeeded in manipulating the flow by utilising flow control. While many flow control techniques exist, passive flow control is a preferred approach because there is no need for complex control mechanisms and energy expenditure for its operation. Viscous flow is can generate lift over a body but is also a source of drag. Several types of drag exist on an aeroplane with turbulent viscous drag as a significant contributor. A handful of passive flow control techniques have been proposed with some promising candidates, but much more careful evaluation is needed to assess each technique's capability. Of the surveyed longlist of passive flow control techniques, **compliant surfaces** for **turbulent viscous drag reduction** presents a large ground of unexplored potential.

Observations by Gray (1936) sparked the interest of research into drag reduction by compliant surfaces. Initially investigated by Kramer (1960) in search of boundary layer transition delay, later efforts followed looking for drag reduction in turbulent boundary layers. While constant experimental research output is present for water flows, initial ventures in the 1970s have deemed air flows impotent to deform compliant surfaces sufficiently to achieve drag reduction. However, there is no firm verdict on this, even for water flows. The lack of aerodynamic exploits for compliant surfaces and the ongoing debate regarding its capabilities to reduce turbulent viscous drag presents an opportunity to reopen this research field. This thesis aims to become an initial proof of concept for drag-reducing compliant surfaces in turbulent air flows and provide a basis for future endeavours into this field of research.

1.1. Turbulent viscous drag reduction

The drag an aeroplane sustains throughout flight is proportional to its fuel consumption. Therefore, drag reduction for aeroplanes will be not only economical for aircraft operators but also sustainable. With the Sustainable Development Goals (SDG) in mind, the world is on a collective mission to "achieve a better and more sustainable future for all" (United Nations General Assembly, 2015). Aviation accounts for 3% of the European Union's (EU) greenhouse gas emissions and a near 3% worldwide (Airbus, 2019). With an ever-increasing demand for air travel, the number of commercial aircraft in service is projected to double in the next 20 years. Limiting the impact of our demand for air travel has never been more critical.

Drag reduction can be divided into several categories: the prevention of laminar/turbulent separation, the prevention of transition, and the reduction of turbulent skin friction. Of which, the reduction of turbulent skin friction is crucial for an aircraft, as the majority of the impinged flow is turbulent due to the high Reynolds number and adverse pressure gradients. Due to the large velocity gradient of a turbulent boundary layer, viscous skin friction drag contributes to over half of the total drag generated on an aircraft, while overpowering the other component of viscous drag: pressure drag. This large portion of turbulent skin friction presents an opportunity to improve the sustainability of aviation further.

1.2. Flow Control

Flow control is a means to artificially modify flow characteristics from its natural development to meet performance benchmarks. Past efforts in flow control can be traced back to as early as 1904 by Prandtl

(Fischer and Ash, 1974). The later Second World War fuelled the development of flow control on military hardware such as aeroplanes and ships. Following the war, the development of flow control was stuck in hiatus with fairly low-priced petroleum. However, the Arab oil embargo in the 1970s incentivised the scientific community to develop beneficial flow control technology. The reader is referred to Fischer and Ash (1974); Wilkinson et al. (1988); Szodruch (1991); Choi (2000); Bushnell (2003); Spalart and McLean (2011) for further context into the historical development of flow control.

Flow control can be categorised into: passive, active, and reactive (Gad-el Hak, 2000). Passive flow control techniques require no energy expenditure, and are usually geometric or material modifications to the surface; riblet surfaces are of this kind. Active surfaces can be turned on and off, which require energy to operate. Reactive flow control is active flow control with a control loop added to smartly adapt to flow conditions, adding to the system's complexity. Of which, passive flow control offers the most elegant solution without requiring any energy expenditure or complex peripheries to operate them.

1.3. Compliant surfaces

Compliant surfaces are passive surfaces that are capable of deformation due to the mean flow. It was hypothesised that the compliant surface would induce meaningful fluid-structure interaction (FSI) that will reduce the drag of the flow. Figure 1.1 is a schematic of theoretical model of a compliant surface. The inception of this field of research was by Kramer (1960), where a tow-tank experiment produced a substantial drag reduction of 40 to 60%. Kramer hypothesised the drag reduction due to the delay of boundary layer transition, which he termed distributed flow damping. Later studies added to Kramer's results, where the drag reduction was assumed to be the reduction of turbulent viscous drag (Carpenter and Garrad, 1985). While the innovations in experimental and numerical machinery have aided in deepening the understanding of compliant surface FSI, a big question mark still hangs above their drag reduction capability. However, recent landmark experimental drag reduction results by Choi et al. (1997) and numerical results by Fukagata et al. (2008) have once more shed light on the unexplored potential of compliant surfaces for turbulent viscous drag reduction. However, there is a significant lack of experimental work for compliant surfaces in air, compared with what has been done in water. This research aims to fill in this research gap by investigating the turbulent drag reducing capabilities of compliant surfaces in air.

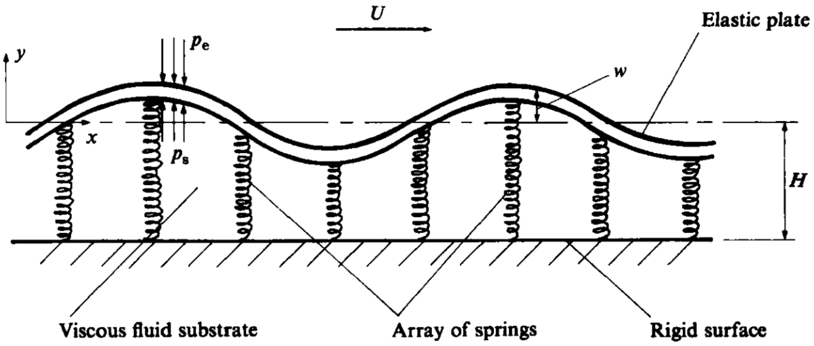

Figure 1.1. Schematic illustrating the theoretical model of a viscoelastic compliant surface (Carpenter and Garrad, 1985)

1.4. Scope

The scope of this research is presented here in the form of a research objective, research questions, and research hypotheses.

1.4.1. Research objective

The research objective has been formulated as the following:

> *To* ***unravel the unexplored potential*** *of compliant surfaces for turbulent viscous drag reduction in air flows, and* ***identify the parameter space*** *(thickness and stiffness) where this occurs. Furthermore, to identify* ***how the parameters mentioned above correlate with the amount of drag reduction****, and* ***visualise the flow field modulation and compliant surface deformation*** *due to the fluid-structure interaction (FSI) by particle image velocimetry (PIV) and digital image correlation (DIC).*

1.4.2. Research questions

With this research objective in mind, the research questions below are formulated in aim to achieve this objective:

1. **Will air flows be able to favourably deform a compliant surface to achieve turbulent viscous drag reduction, such as has been shown in water tunnels?**
2. **What is the optimal range of shear modulus and thickness for the compliant surface to achieve viscous drag reduction in turbulent air flows?**
3. **What characterises the surface deformation of a drag-reducing compliant surface from one that does not reduce turbulent viscous drag? What are the differences in the flow field as a result?**
4. **Can the reduction in the number of vortex bursts in the boundary layer as proposed by Bushnell et al. (1977) be observed for a drag-reducing compliant coating?**
   (a) **If drag reduction is not measured, is Bushnell et al.'s hypothesis still observed? If not, how does the compliant surface interact with the air flow?**

1.4.3. Research hypotheses

The hypotheses for the presented research questions are as follows:

H1 The inertial ratio properly scales the FSI between the compliant surface and the air flow. Based on this inertial ratio, raising the velocity of air can compensate for its low density, inducing favourable interaction between the compliant surface and air, leading to drag reduction.

H2 With precedence that moving wavy walls can reduce drag, the wavy deformation of a compliant surface is expected to have a similar effect on the flow. By varying the stiffness and thickness, the compliant surface's wavy deformation can be tuned to have a favourable interaction with the air flow to reduce turbulent viscous drag. Semenov (1991) has argued that the non-dimensional period of a drag-reducing compliant surface, a function of the shear modulus and surface thickness, lies between $50 < t_0^+ < 150$.

H3 For a compliant surface to have sufficient interaction with the flow, the compliant surface's normal deformation should approach but not exceed the viscous sublayer height. If the normal deformation exceeds the viscous sublayer height, the hydrodynamic roughness increases for the flow resulting in massive drag increase. Therefore, for a drag-reducing compliant surface, the normal deformation should be lower than the viscous sublayer height. Due to the decrease of skin friction drag, the boundary layer profile is expected to be leaner, as the velocity gradient at the wall is decreased.

H4 The periodic nature of a compliant surface's wavy deformation modifies the flow that reduces the turbulent kinetic energy production, which leads to skin friction reduction. Choi (1989) has shown that the period between the sweep events in turbulent boundary layers is $80 < t^+ < 100$, which coincides with the non-dimension period postulated by Semenov (1991) ($50 < t_0^+ < 150$). The inhibition of these sweep events alters the pulsating pressure field, reducing the number of bursts per unit time.

1.5. Structure of this thesis

With this chapter as the brief introduction to this thesis, the main matter of the thesis is structured in the following. Chapter 2 discusses the theoretical background behind turbulent flow, passive flow control, compliant surfaces, and the rheology of viscoelastic materials. Chapter 3 presents the experimental approach for this research. These include rheological, drag delta, and flow visualisation measurements. Chapter 4 presents and verifies the results from all of the experiments. Chapter 5 discusses the results, such as the correlation between the measured drag delta and viscoelastic properties of the compliant surface. Chapter 6 concludes the thesis with the main takeaways from this research. Finally, the recommendations for future research are given in Chapter 7.

2

Compliant surfaces for passive flow control of turbulent wall-bounded air flows

In this chapter, the theoretical background behind this research is given. Section 2.1 gives a brief overview of the aerodynamic background in this research. This research initially started as screening a list of passive flow control techniques. The goal was to choose a low Technology Readiness Level (TRL) technique with the most potential for turbulent viscous drag reduction to pursue further in this research. A brief overview of this process is given in Section 2.2. Out of the longlist of passive flow control techniques, compliant surfaces were determined to have the most unexplored potential. The historical and theoretical background regarding compliant surface research in drag reduction is given in Section 2.3. Finally, Section 2.4 gives a brief introduction to the rheology of viscoelastic materials.

2.1. Turbulent wall-bounded flows

This section briefly introduces the concept of incompressible turbulent boundary layers and relevant theories used to analyse the results. When a flow comes in contact with a wall boundary, a boundary layer is formed with the no-slip condition satisfied at the wall. The distinctive parabolic velocity profile is formed due to viscous shear stress between the layers of fluid retarding the flow. The streamwise velocity approaches the external flow velocity when moving away from the wall.

A boundary layer can be characterised by the Reynolds number (Re), a scaling parameter that is the ratio of the inertial and viscous characteristics of a flow:

$$\mathrm{Re} = \frac{\rho u_\infty L}{\mu} = \frac{u_\infty L}{\nu} \tag{2.1}$$

where ρ is the fluid density, u_∞ the free stream flow velocity, L the characteristic length, μ the dynamic viscosity, and ν the kinematic viscosity. The boundary layer is said to be laminar or turbulent depending on the Reynolds number. The critical Reynolds number is the deciding threshold where the transition from a laminar to turbulent boundary layer occurs. Due to the aeroplane's high cruising velocity, the boundary layer flow surrounding the aircraft is dominantly turbulent, exceeding the critical Reynolds number.

The fluid layers are mutually mixed for a turbulent boundary layer, resulting in a higher mass and momentum transfer. Turbulent boundary layers have higher energy content since it entrains energy from the mean flow due to the mixing. Furthermore, a fuller velocity profile is formed for the turbulent boundary layer to its laminar counterpart. A laminar boundary layer consists of distinctive layers where the streamwise velocity component dominates the movement of the fluid layers.

2.1.1. Viscous drag

Irrespective of the boundary layer's state, the total drag of a flow consists of induced, wave, and viscous drag. As this research's main focus is reducing the turbulent viscous drag, discussions will be limited to the viscous drag. Viscous drag is an outcome of flow viscosity, consisting of skin friction and pressure drag. Turbulent boundary layers have a large velocity gradient at the wall, distinguishing itself from its laminar counterpart. The skin friction is shown Equation (2.2).

$$\tau_w = \mu \left.\frac{\partial u}{\partial y}\right|_{y=0} \tag{2.2}$$

For a viscous flow, it must satisfy the no-slip condition at the wall. Therefore, a velocity gradient exists at the wall that contributes to skin friction. The other viscous drag component, the pressure drag is due to the separation of the flow from a surface and its resultant wake. Also known as profile or form drag, pressure drag is largely dependent on the object obstructing the flow. Separation occurs due to flow reversal caused by an adverse pressure gradient, and thus a recirculation zone is formed. This zone changes the effective shape seen by the flow, causing a pressure distribution that generates an excessive drag component, hence termed pressure drag. Separation does not occur in inviscid flows since there are no viscous losses that cause flow reversal. In turbulent flows, the lateral mixing due to the Reynolds stress fluctuations lowers and heightens pressure and skin friction drag, respectively. The mixing leads to higher energy content of the flow, making it resistant to flow separation; this makes the flow adhere to the surface with a higher velocity gradient. Therefore, the majority of turbulent viscous drag is contributed by the turbulent skin friction component.

2.1.2. Mean boundary layer properties

Several mean boundary layer properties are used in the later analysis of the development of the boundary layer. These properties will be briefly discussed.

Boundary layer thickness δ_b

The boundary layer thickness is defined as the height where the streamwise velocity is at 99% of the free-stream velocity. It is also denoted as $\delta_{99\%}$ in some literature. For a turbulent flow, the boundary layer thickness can be estimated with a power law expression of the streamwise location-based Reynolds number:

$$\frac{\delta_b}{x} \approx \frac{0.16}{\mathrm{Re}_x^{1/7}} \tag{2.3}$$

Displacement thickness δ^*

The displacement thickness δ^* signifies the displacement of the actual wall position felt by the particles in the free-stream. It is calculated by applying conservation of mass to the velocity deficit in boundary layer:

$$\delta^* = \int_0^\infty \left(1 - \frac{u}{u_\infty}\right) dy \tag{2.4}$$

Momentum thickness θ

The momentum thickness θ is a direct indication of the momentum flow rate within the boundary layer. It is the momentum deficit due to the formation of the viscous boundary layer, which is defined as:

$$\theta = \int_0^\infty \frac{u}{u_\infty}\left(1 - \frac{u}{u_\infty}\right) dy \tag{2.5}$$

which can be directly linked to the momentum loss due to the skin friction and thus the drag with the conservation of momentum in the x-direction: (White and Corfield (2006))

$$\theta = \frac{D}{\rho u^2} \tag{2.6}$$

This holds true for a incompressible turbulent flow above a flat plate. Kármán (1921) directly relates the momentum thickness to the drag ($C_D = D/\frac{1}{2}\rho u_\infty^2$)and friction ($C_f = \tau_w/\frac{1}{2}\rho u_\infty^2$) coefficient of the flat plate:

$$C_{f,\mathrm{plate}} = 2\frac{d\theta}{dx} \tag{2.7}$$

$$C_{D,\mathrm{plate}} = \frac{2\theta(L)}{L} \tag{2.8}$$

Shape factor H

The ratio of the displacement thickness δ^* and momentum thickness θ is defined as the shape factor H:

$$H = \frac{\delta^*}{\theta} \tag{2.9}$$

and is often used for stability analysis of the boundary layer. A high H indicates a more uplifted velocity profile towards the free-stream with a smaller velocity gradient and vice versa.

Turbulence intensity (T.I.)

The turbulence intensity (T.I) of a mean boundary layer profile can be calculated by the division of the velocity fluctuations with the velocity. It is defined as:

$$T.I. = \frac{\sqrt{\frac{1}{n}|\mathbf{u}'|^2}}{|\mathbf{u}|} \tag{2.10}$$

where $\mathbf{u}$ is the velocity vector, $\mathbf{u}'$ is the velocity fluctuation vector, and n signifies the dimensions considered for the velocity profile.

2.1.3. Coherent structures

Coherent structures in the form of hairpin vortices form within a near-wall turbulent flow. The formation process is illustrated in Figure 2.1.

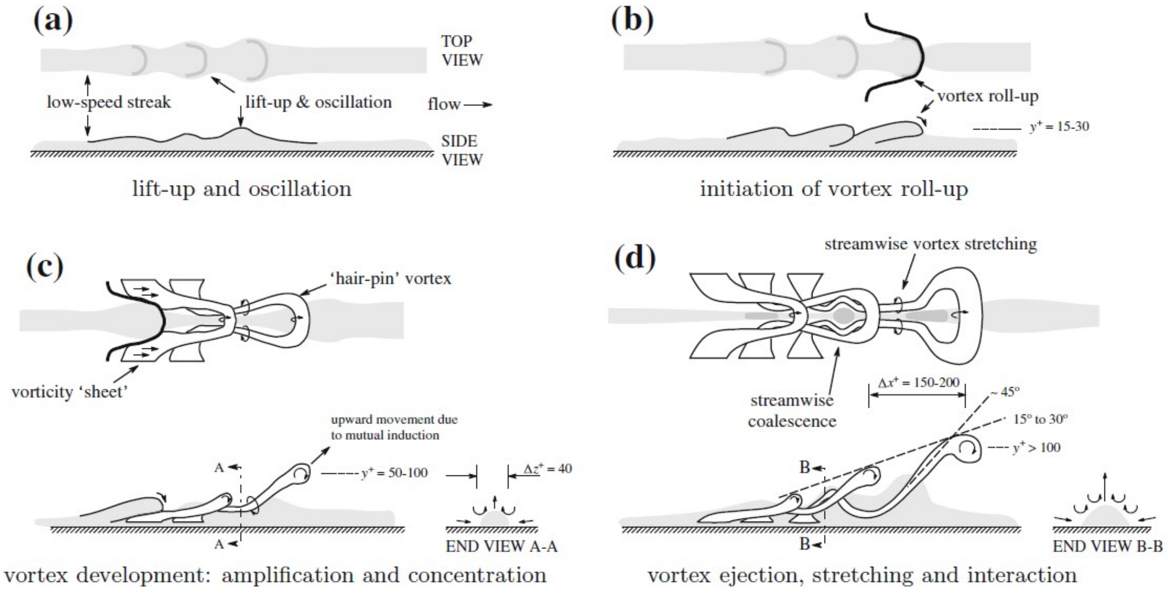

Figure 2.1. The formation process of hairpin vortices (Nieuwstadt et al., 2016)

The turbulent flow structures start as low-speed streaks in the near-wall region. These streaks are perturbed by Kelvin-Helmholtz instabilities which roll-up to form a vortex filament in the spanwise direction, connected with the near-wall streamwise streaks to form a hairpin vortex. The vortex is further lifted-up by a self-induced velocity field, which is stretched further towards the mean flow. During the vortex stretching process depicted in Figure 2.1 (d), the strength of the hairpin vortex reaches a certain amount that renders it unstable. The hairpin vortices then "bursts" into smaller flow structures. The bursting phenomenon of a turbulent flow is a source of Reynolds stress and turbulent kinetic energy (Nieuwstadt et al., 2016). Therefore, this "ejection" event of the flow from the near-wall region to the mean flow is a great source of turbulent kinetic energy production. The ejection event is further coupled with "sweep" events, where the high-speed mean flow replaces the ejected low-speed streaks. Both of these ejection and sweep events contribute to the Reynolds stress and the production of turbulent kinetic energy.

2.1.4. Quadrant analysis

The coherent structures of a turbulent flow may be categorised into quadrants according to the sign of the velocity fluctuations. The velocity of the flow can be decomposed into a mean term and fluctuation term by employing Reynolds decomposition:

$$\mathbf{u} = \bar{\mathbf{u}} + \mathbf{u}' \tag{2.11}$$

where $\bar{\mathbf{u}}$ is the mean term, and $\mathbf{u}'$ is the fluctuating term. The Reynolds stress tensor, the main culprit behind the production of turbulent kinetic energy, consists of the product of the fluctuation terms:

$$S_{ij} = -\rho \overline{\mathbf{u'_i u'_j}} \tag{2.12}$$

where for a 2D flow, the cross-term $u'v'$ dominates the Reynolds stress term. A negative velocity fluctuation product $-u'v'$ would lead to the increase of the Reynolds stress. Wallace et al. (1972) devised a method that categorises this cross-term into four quadrants according to the sign of each fluctuation term; this is visualised in Figure 2.2. The Q2 and Q4 events correspond to the ejection and sweep, respectively, which are present in the coherent structures of a turbulent flow and responsible for the production of Reynolds stress. The event occurrence probability can be calculated by counting the number of points in each quadrant and dividing it by the total number of data points. Figure 2.3 shows an example of a scatter plot of the quadrant event occurrences of a turbulent flow.

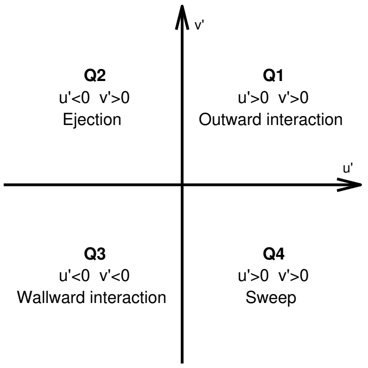

Figure 2.2. The division of velocity fluctuations into four quadrants, with the corresponding flow structure (Wallace et al., 1972)

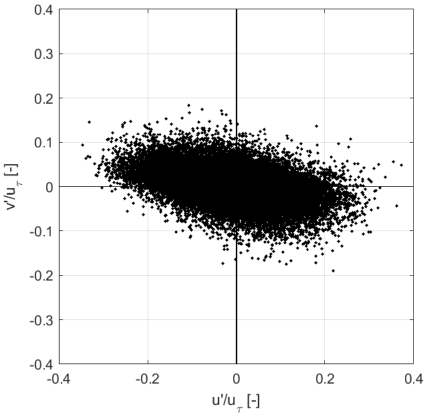

Figure 2.3. Scatter plot of event occurrences (DNS data of Lin (2021))

The occurrence of each quadrant event can be further visualised by the joint probability density function (JPDF). The JPDF of an event occurrence plot can be calculated by discretising the plot domain into a mesh, with a schematic shown in Figure 2.4. The number of occurrences for each mesh box is calculated then plotted as a contour plot; an example is shown in Figure 2.5a. On the other hand, a weighted JPDF multiplies the number of occurrences of each mesh box with the local magnitude of velocity fluctuations; an example is shown in Figure 2.5b. For the JPDF, it only considers the statistical occurrence of the quadrant events. In contrast, the weighted-JPDF further considers the magnitude of the velocity fluctuations, where the direct contribution of each event occurrence to the total Reynolds stress can be visualised. Thus, the Reynolds shear stress of a 2D turbulent boundary layer flow can be related to the weighted JPDF by:

$$\overline{u'v'} = \int_{+\infty}^{-\infty} u'v' \ \mathrm{JPDF}(u', v') \ du'dv'. \tag{2.13}$$

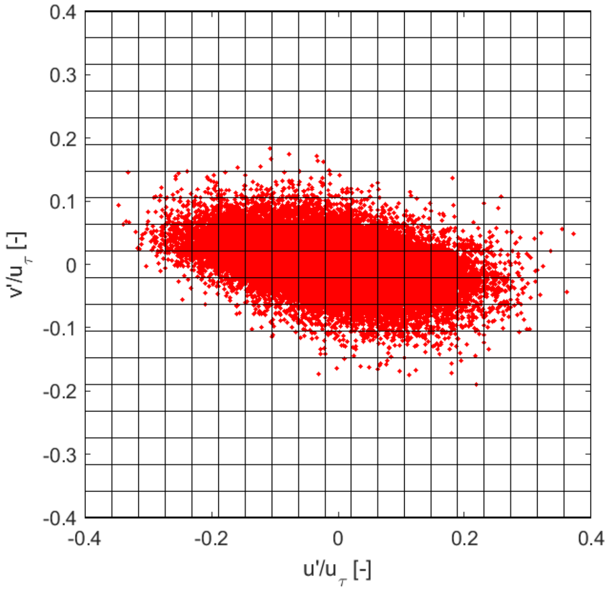

Figure 2.4. Schematic of discretisation grid for JPDF
(DNS data of Lin (2021))

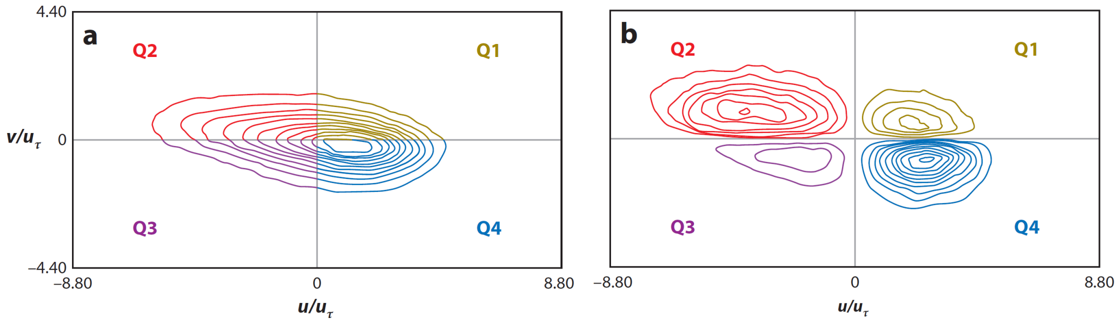

(a) JPDF

(b) Weighted JPDF

Figure 2.5. An example of a JPDF and weighted JPDF contour plot (Wallace, 2016)

2.1.5. Law of the wall

A turbulent boundary layer can be scaled into viscous units at different heights in the flow. The streamwise velocity and wall-normal distance are non-dimensionalised with u_τ and ν:

$$\begin{cases} u^+ = \dfrac{u}{u_\tau} & (2.14a) \\ y^+ = \dfrac{y u_\tau}{\nu} & (2.14b) \end{cases}$$

where u_τ is the wall-friction velocity defined by the shear stress at the wall:

$$u_\tau = \sqrt{\frac{\tau_w}{\rho_f}} \tag{2.15}$$

In addition, ν / u_τ is commonly known as the viscous length scale of a turbulent boundary layer.

The scaling of the turbulent boundary layer profile can be split in to several regions according to the non-dimensionalised wall-normal distance y^+:

$$\begin{cases} 0 \leqslant y^+ \leqslant 5: \text{ Viscous sublayer} & (2.16a) \\ 5 \leqslant y^+ \leqslant 30: \text{ Buffer layer} & (2.16b) \\ 30 \leqslant y^+ \leqslant 100: \text{ Logarithmic layer} & (2.16c) \\ 100 \leqslant y^+: \text{ Core wake region} & (2.16d) \end{cases}$$

A general agreement is reached for the scaling at the viscous sublayer and the log layer:

$$\begin{cases} \text{Viscous sublayer: } u^+ = y^+ & (2.17a) \\ \text{Logarithmic layer: } u^+ = \frac{1}{\kappa} \ln y^+ + B & (2.17b) \end{cases}$$

where κ is the von Kármán constant with a value of $\kappa \cong 0.4$ and B with a value of $B = 4$. Spalding (1961) gives a single composite formula for the scaling of a turbulent boundary layer:

$$y^+ = u^+ + e^{-\kappa B}\left[e^{\kappa u^+} - 1 - \kappa u^+ - \frac{(\kappa u^+)^2}{2} - \frac{(\kappa u^+)^3}{6}\right] \tag{2.18}$$

which was found to have good agreement with experimental data nearly throughout the wall-influenced flow; this is shown in Figure 2.6. A slight deviation is observed in the core wake region of the turbulent flow.

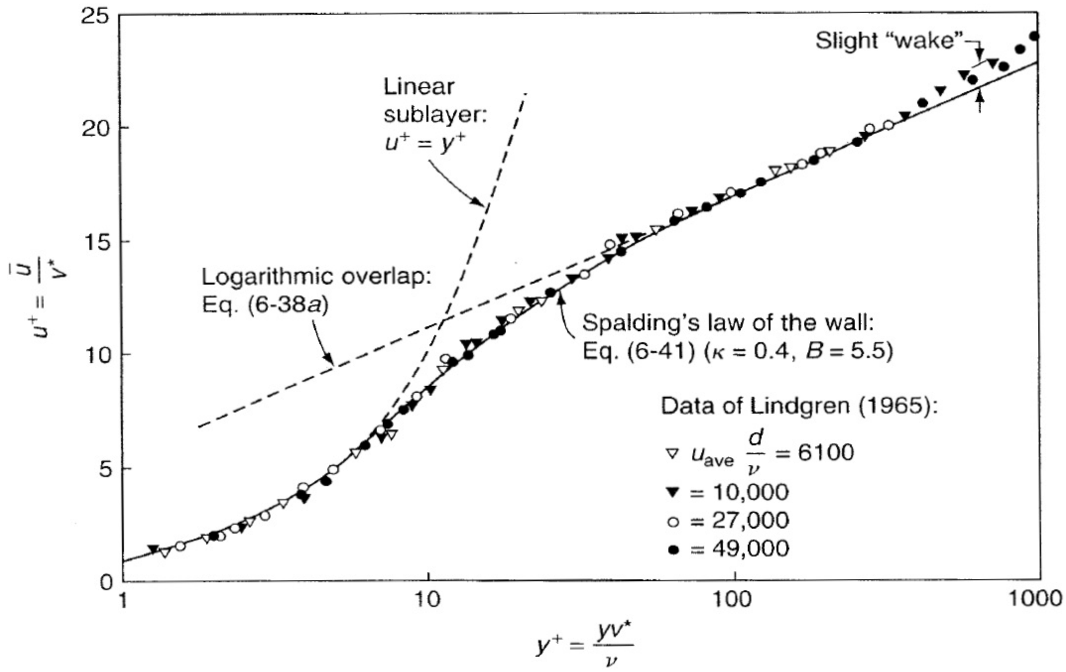

Figure 2.6. Overlap of Spalding (1961) to experimental data of Lindgren (1965)

2.2. Passive flow control for turbulent viscous drag reduction

Since the 1970s, an abundance of research has looked into passive flow control techniques that have the potential to reduce turbulent viscous drag. This section gives an overview of the literature review of existing passive flow control techniques surveyed in the initial stages of this research. Each of the flow control techniques mentioned was evaluated to the following criteria: cost, drag reduction, implementation, maintenance, and unexplored potential in turbulent viscous drag reduction. Of which, compliant surfaces were chosen to further pursue in this research. For a more detailed overview of the literature, the reader is referred to the literature review by Lai (2020).

2.2.1. Dimpled surface

Dimples are shallow indentations on a surface that closely resemble the dimpled surface on a golf ball shown in Figure 2.7. While on a golf ball it forces transition aiming to reduce laminar pressure drag, it also has the potential to reduce turbulent viscous drag. They are relatively easy to apply since they are macroscopic geometric modifications to the surface. The dimples can be applied to surfaces by milling out the material, or possibly by plastic deformation using machines that are standard in maintenance, repair, and operations (MRO) companies.

Drag reduction via dimpled surfaces was accidentally found by a group of Soviet scientists at the Kurchatov Nuclear Energy Institute in the USSR in 1977; their motivation was to enhance heat transfer characteristics of the surface. Kiknadze et al. (1984) attributed this phenomenon to a tornado-like flow topology. In recent years, a group at the Delft University of Technology is actively looking into dimpled surfaces for turbulent viscous drag reduction. van Nesselrooij et al. (2016) found a 4% drag reduction with respect to flat surfaces. van Campenhout et al. (2018) later found the turbulent drag reduction characteristics of a dimpled surface was sensitive to the presence of pressure gradients. van Nesselrooij et al. (2016) and van Campenhout et al. (2018) have hypothesised the working mechanism of turbulent drag reduction to the oscillation of the flow, rather than the tornado-like hypothesis raised by Kiknadze et al. (1984).

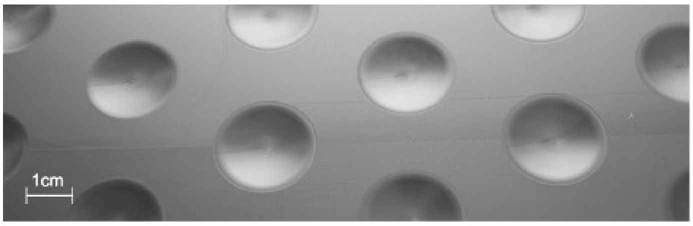

Figure 2.7. Dimpled surface (van Nesselrooij et al., 2016)

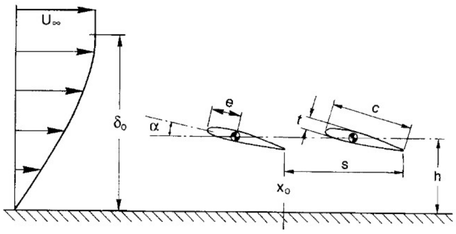

Figure 2.8. Configuration of LEBUs (Lynn et al., 1995)

2.2.2. Large-eddy breakup devices (LEBUs)

Large-eddy breakup devices (LEBUs) are physical obstructions placed in the outer regions of the boundary layer, shown in Figure 2.8. They reduce the turbulent skin friction drag by the destruction or "breaking up" of the large scale turbulent structures in the outer part of a turbulent boundary layer (Chin et al. (2017b)). Savill and Mumford (1988) indicated that LEBUs induce a downwash component affecting the near-wall region of the flow downstream of the device. LEBUs have been demonstrated in literature to decrease skin friction, but not net viscous drag reduction. This is due to the LEBU "device drag" (pressure drag) overpowering the skin friction reduction. This was concluded in a comprehensive experimental study by Lynn et al. (1995). Although the magnitude of skin friction reduction is proportional to the LEBU device's size, the pressure drag proportionality is even higher. Recent large-eddy simulations (LES) by Chin et al. (2017a,b) further upheld the verdict on the LEBUs' diminished potential for turbulent viscous drag reduction.

2.2.3. Riblets

Riblets are ribbed surfaces with microscopic grooves in the streamwise direction, which are considered a type of surface with an anisotropic roughness (García-Mayoral and Jiménez, 2011). A schematic of a longitudinal riblet with is shown in Figure 2.9a, with a spanwise cross-section of a riblet with a scale in Figure 2.9b. The inspiration of riblets is drawn from the shark skin, where 3D riblet structures in the streamwise direction are exhibited (Dean and Bhushan, 2010). Walsh and Weinstein (1978) led the initial endeavour into turbulent viscous drag reduction by riblets; 5% ~ 8% net drag reduction was achieved testing with various riblet geometries. The drag reduction was dependent on its surface finish; sharper peaks had more drag reduction, while notched peaks increased the range of spanwise wall units where turbulent viscous drag reduction was possible. Other groups over the years, including Enyutin et al. (1987) and Takahashi et al. (2018) also achieved consistent magnitudes of net drag reduction. Flight tests by McLean et al. (1987) and Szodruch (1991) have also been conducted and resulted in a net drag reduction of about 6% and 2%, respectively. Many hypotheses have been raised regarding the working mechanism behind the turbulent drag reduction (Viswanath (2002)), and the discussion is still ongoing today. The restriction of spanwise oscillation for the longitudinal vortices has been most frequently postulated as the underlying mechanism. Research on the effect of riblets on turbulent flow has had a stable output for the past two decades; with this concept being validated at both laboratory and flight tests, the development of riblets are at a relatively high TRL.

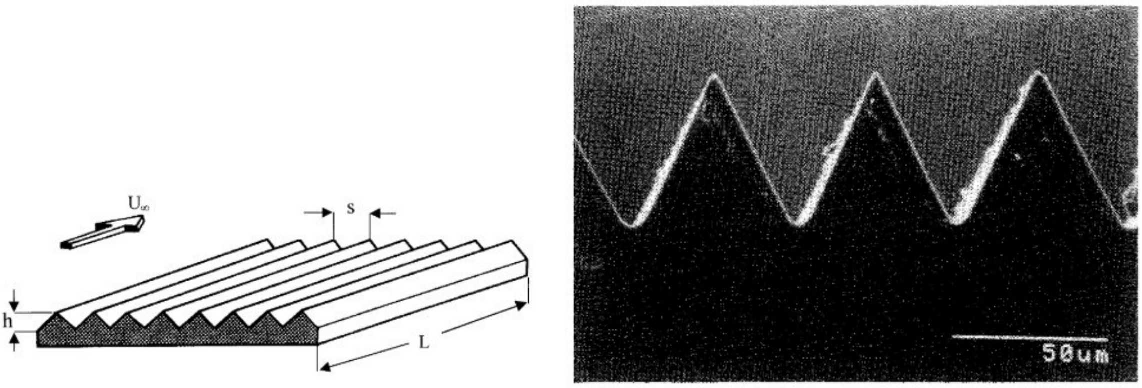

(a) Longitudinal riblet surface (Robert, 1992)

(b) Spanwise cross-section snapshot of a riblet surface. (Walsh, 1990)

Figure 2.9. Riblet surfaces

2.2.4. Hydrophobic and hydrophilic surfaces

Observation of living organisms in nature and imitating them, so-called biomimetics, has played a significant role in deriving engineering solutions to our every-day problems. Hydrophobic and hydrophilic surfaces are one of the most discussed derivatives of this nature. Bhushan and Jung (2011) and Barthlott et al. (2017) give a good overview of the observations regarding these types of surfaces. The turbulent viscous drag reduction of hydrophobic and hydrophilic surfaces is dependent on the slip boundary condition imposed on the surface by a three-phase contact. The three-phase contact is made possible by micro or nanoscale surface roughness (fig. 2.10a) that trap air or fluid packets within for hydrophobic and hydrophilic surfaces, respectively (Daniello et al., 2009). This creates a slip boundary condition such that a water droplet is suspended by the surface instead of wetting it (fig. 2.10b). As a result, the intensity of the turbulence and near-wall streamwise vortices are weakened, and the turbulent skin friction drag is decreased (Min and Kim, 2004). Both numerical (Min and Kim, 2004; Fukagata et al., 2006) and experimental (Daniello et al., 2009; Gose et al., 2018) research have indicated a reduction of turbulent skin friction drag for a hydrophobic surface in water.

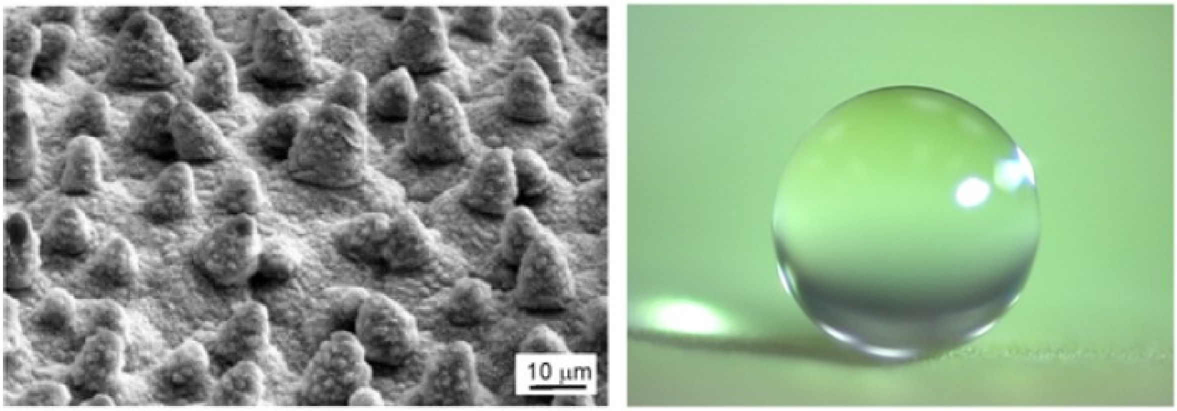

(a) Scanning electron microscopy micrographs of a lotus surface

(b) A water droplet of the surface of a lotus leaf

Figure 2.10. The hydrophobic surface of a lotus (*Melumbo nucifera*) leaf (Bhushan and Jung, 2011)

However, the working principle is dependent on the three-phase interface. A hydrophobic surface traps air within the surface roughness, and the surface would inherently be a riblet if the mean flow were air. Hydrophilic surfaces, which impregnate the surface with water instead of air, may have the potential for drag reduction on land and air. However, the drainage of water in high-Re flows necessitates another water-feeding system to refill the hydrophilic surface, making it an active system rather than passive. Drag reduction results have been widely-varying and inconsistent in the order of $\mathcal{O}(10\%)$ and not well-characterised.

2.2.5. Super-smooth surface

The super-smooth surface is a conceptual design intended to minimise, even eliminate the velocity gradient at the wall, and thus the skin friction. The first approach is that of a molecularly smooth surface. The atoms that form the surface are perfectly aligned on the same plane without any peaks and valleys. Another approach would be a specularly smooth surface (Garcia, 2019). When a light beam is exposed upon a specular surface, the light's entirety goes through specular reflection, meaning that all the light rays have an identical incidence and reflective angle with respect to the mean surface normal.

However, Bhushan et al. (1995) argues that with a perfectly smooth surface, the wetted area of the mean flow increases due to the absence of roughness. This increase means that the number of contact points needing to satisfy the no-slip condition increases, effectively increasing skin friction. This corroborates with skin friction reduction by surface roughness such as riblets. In addition, maintaining a perfectly smooth surface would be immensely difficult in a non-vacuum environment. Abrasion due to foreign objects such as dust would roughen such surfaces. Constant maintenance would be needed to retain smoothness, and the maintenance has to be conducted by equipment with molecular precision.

2.2.6. Permeable surface

Turbulent flows over permeable surfaces may be found in various cases; such as flows in pipelines and river beds. They are also used in engineering applications due to their capability to enhance mass and heat transfer with its increased contact area. Permeable surfaces are surfaces which contain isotropic or anisotropic permeability. A permeable surface can be characterised by its porosity and permeability (Suga et al., 2010). Porosity is the ratio of the space taken by the material over the total space; permeability is the ease of fluid flowing through a permeable medium, which can be quantified in the surface-normal, streamwise, and spanwise direction. Surfaces with varying anisotropic permeability are shown in Figure 2.11. The flow within a permeable surface can be described by an empirical relation derived by Darcy (1856). The surface's permeability allows a slip boundary condition to be applied at the surface, hence decreasing the turbulent skin friction drag.

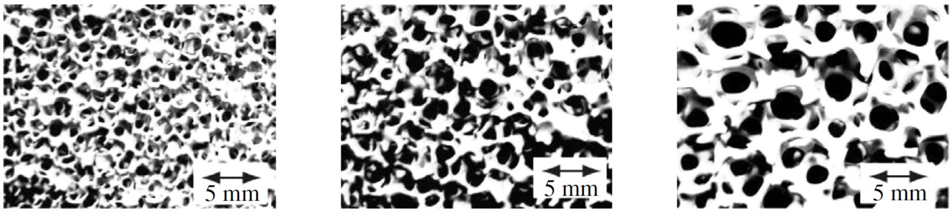

Figure 2.11. Surfaces with different anisotropic permeabilities. Permeability increases from the left to right figures. (Suga et al., 2017)

However, not all types of permeable surfaces are capable of turbulent skin friction drag reduction. Isotropic permeable surfaces increase the skin friction drag due to the enhancement of large spanwise coherent structures, which promote momentum transfer and thus increase the Reynolds stress (Hahn et al., 2002; Breugem et al., 2006; Suga et al., 2010). On the other hand, anisotropic permeable surfaces with a preferred permeability in the streamwise direction can reduce the turbulent skin friction (Gómez-De-Segura et al., 2018). Rosti et al. (2018) simulated a turbulent channel flow with varying streamwise-to-surface-normal permeability ratios, indicating a net drag reduction ranging $-20\% \sim 20\%$ when the ratio was larger than 1. This result comes into agreement with drag-reducing surfaces that have streamwise-preferred geometry such as riblets (Luchini et al., 1991). An excess of surface-normal permeability is deleterious for turbulent drag reduction since it triggers the growth of Kelvin-Helmholtz rollers (Kuwata and Suga, 2016; Gómez-De-Segura et al., 2018).

2.2.7. Rigid wavy surface

Rigid wavy surfaces are smooth surfaces with sinusoidal undulations in the streamwise direction. The geometry of the wave can be tuned by changing the amplitude or wavelength. Although the most general shape is a sine wave, different waves, such as a skewed wave, have also been investigated. Some of the types of rigid wavy surfaces used in an experimental study by Lin et al. (1984) are shown in Figure 2.12.

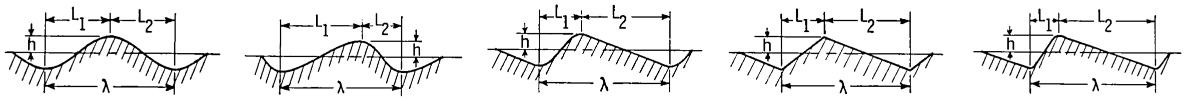

(**a**) Sine Wave (**b**) Splined Sine Wave (**c**) Sine Wave with Straight Ramp (**d**) Transverse V-Grooves (**e**) Circular Arc with Straight Ramp

Figure 2.12. Compilation of rigid wavy surfaces tested by Lin et al. (1984)

Past efforts in resolving the flow structure over a rigid wavy surface have been consistent regardless of a numerical or experimental approach. Fundamental turbulence studies have indicated the separation of the flow, forming a shear layer between the mean flow and the recirculation zone (Buckles et al., 1984). The shear layer coincides with the streamwise loci of the maximum Reynolds shear stress, which means that the turbulent skin friction is reduced (Hudson et al., 1996; Cherukat et al., 1998). Turbulent statistics have also indicated that the turbulent kinetic energy production shifted away from the wall (Maaß and Schumann, 1996; De Angelis et al., 1997), which is also an indication for turbulent skin friction reduction (Fukagata et al., 2002). However, the pressure drag due to the separation consistently annuls the skin friction reduction, rendering no net turbulent viscous drag reduction. Experimental campaigns by Lin et al. (1984); Hudson et al. (1996); Mamori et al. (2018) comes into agreement with the numerical results and turbulent statistics, with a clear indication of no net drag reduction over a range of wave amplitudes, wavelengths, and Reynolds numbers. However, it must be noted that the error margin of the experiments coincided with the drag reduction measured. This warrants further investigation with a higher fidelity measurement setup.

2.2.8. Benchmarking and verdict

As a conclusion of this evaluation, each passive flow control technique was benchmarked, and compliant surfaces were chosen as the best candidate to proceed with respect to the postulated criteria. Table 2.1 is a longlist of the evaluated passive control techniques with brief descriptions of its advantages and disadvantages. Table 2.2 is a scorecard with the score calculated by the weighted total of each criterion; the list is ordered from highest to lowest weighted total.

Dimples were not considered since research is ongoing within the Aerodynamics Group of the Delft University of Technology. LEBUs and rigid wavy walls were rejected since overwhelming evidence suggests that these techniques are drag-increasing. Riblets have been proved to be drag-reducing both in wind tunnels and flight tests, making it a high-TRL technique and out of scope. The working mechanism for hydrophobic and hydrophilic surfaces are dependent on the three-phase contact, which make them unsuitable for passive application. Lastly, the super-smooth surfaces are highly conceptual with weak literature support basis.

Table 2.1. The advantages and disadvantages passive flow control techniques

Technique	Advantages	Disadvantages	TRL
Dimpled surface	Simple implementation; not prone to clogging	Drag reduction sensitive to flow direction	4
LEBUs	Simple application; significant skin friction reduction	Device drag overpowers and nullifies skin friction reduction	6
Riblets	Simple geometry; net drag reduction observed both in wind tunnel and flight tests; stable research output	Drag reduction dependent on surface finish; difficult maintenance; marginal drag reduction on flight tests	7
Hydrophobic/philic surfaces	Surface roughness treatment; stable research output in hydrodynamic uses	Drag reduction dependent on three-phase contact; high variability in drag reduction; difficulty of maintenance	4
Super-smooth surface	(Unexplored)	Prone to abrasion and difficult maintenance of smoothness	1
Permeable surface	Consistent drag reduction with streamwise-preferred permeability	Foreseeable clogging problems and difficult maintenance	3
Rigid Wavy surface	Geometric modifications to the surface; reduces turbulent skin friction	Pressure drag due to separation overpowers skin friction reduction	3
Compliant surface	Deformation of surface identical to moving waves	Ageing of elastic material and exposure to varying climate	4

Table 2.2. Ranked weighted total scorecard evaluation of passive flow control techniques (Scale of 1 ~ 5)
Criteria: **C**: Cost; **DR**: Drag reduction; **I**: Implementation; **M**: Maintenance; **UP**: Unexplored potential

Technique \ Criteria (Weight)	TRL	DR [%]	C (3)	DR (2)	I (1)	M (2)	UP (3)	Total
Dimpled surface	4	4	3	3	3	4	4	38
Compliant surface	4	5	2	3	2	2	4	31
Rigid Wavy surface	3	1	3	1	4	4	3	30
Riblets	7	7	2	4	2	1	3	29
LEBUs	6	-1	4	1	5	4	1	27
Permeable surface	3	15	2	4	2	1	2	26
Super-smooth surface	1	-	1	1	1	1	5	23
Hydrophobic/philic surfaces	4	Varying	2	2	1	1	2	19

2.3. Compliant surfaces

The concept of compliant surfaces came about with some inspiration from the epidermis of dolphins. Gray (1936) attempted to estimate the drag of a dolphin by using a towing tank. He found that it would only be possible to overcome this drag if the muscles could generate seven-times the energy than other mammal species. This result led to the Gray's induction that the dolphin skin must have some drag reduction or thrust augmentation effect. This induction was called the Gray's Paradox, and it became the preface of compliant surface research for drag reduction. Compliant surfaces have been hypothesised and partially confirmed to induce a favourable FSI capable of delaying transition, reducing turbulent skin friction drag, reduction of flow-induced noise, or the enhancement of mixing and heat transfer (Kim and Choi, 2014).

2.3.1. Historical overview

Kramer (1960, 1961, 1962) was the pioneer of modelling the dolphin epidermis, conducting towing tank experiments at Long Beach Harbour in California. A substantial drag reduction of 40 ~ 60% was achieved. Kramer hypothesised that by tuning a compliant surface's natural frequency to that of the most unstable Tollmien-Schlichting instabilities (TSI), the surface would dissipate the instability waves partially to delay transition; this phenomenon was termed as distributed flow damping.

However, later attempts to replicate Kramer's results were a failure (Puryear, 1962; Nisewanger, 1964; Ritter and Messum, 1964; Ritter and Porteous, 1965). These results argued that Kramer might not have had sufficient knowledge regarding the structure of dolphin epidermis. It is also argued that the test environment of Kramer's experiments were less than ideal being an open and uncontrolled environment. Johnson (1980) concluded that Kramer's setup did not meet scientific standards. However, Carpenter and Garrad (1985) mentioned that the attempts to replicate Kramer's experiment were also inconclusive in the sense that they were not proper duplicates of Kramer's setup; therefore, Kramer's findings should not be disregarded.

Kramer's efforts were not in vain as it sparked the interest of the scientific world. A series of theoretical work concerning the delay of transition by Landahl (1962) and Benjamin (1960, 1963) categorised the various compliant surface instabilities that derive from the FSI that could lead to possible transition delay. Carpenter (1988) had the same conclusion, but noted the drag reduction might source from turbulent skin friction reduction. Benjamin (1964) hypothesised that compliant surfaces could modify the flow's turbulent structures of the flow, leading to skin friction reduction. A group at the University of Oklahoma conducted a series of wind tunnel experiments searching for turbulent viscous drag reduction (Fisher and Blick, 1966; Looney and Blick, 1966; Blick and Walters, 1968; Blick et al., 1969; Chu and Blick, 1969; Walters, 1969; Chu, 1971), measuring skin friction reductions up to 38%.

Sharing the same fate as Kramer, later analysis similarly rebuked the results from the University of Oklahoma. Lissaman and Harris (1969) found only 10% reduction of skin friction. McAlister and Wynn (1974) and McMichael et al. (1980) tested with the same type of compliant surfaces resulting in either identical or increased drag, with the latter measuring a decrease in Reynolds stress. Ffowcs-Williams (1963) implicated the decrease of Reynolds stress is only possible within a small range of surface and flow parameters. Although research followed in the 1980s, no net drag reduction was observed (Riley et al., 1988).

Since the 1990s, promising results emerged from water tunnel experiments. Lee et al. (1993) observed an upward shift of the logarithmic layer of the boundary layer, which has been viewed as an indication of drag reduction (Lumley, 1973). Kulik et al. (1991) acquired a net turbulent drag reduction of 20% with a towing tank in a lake. Choi et al. (1997) obtained a net drag reduction of 7% in a water tunnel. The skin friction and the Reynolds stresses also showed a reduction in intensities just aft of the compliant surface; 7% and 19%, respectively. This reduction was attributed to a smaller magnitude in the skin friction fluctuation energy spectrum. Latter replications by Choi (2003) also acquired turbulent drag reduction albeit at a smaller magnitude. This performance change was attributed to the different flow conditions and also the ageing of the compliant surfaces. An international effort by the US, UK, and Russia by Bandyopadhyay et al. (2005) looked into how the ageing of the silicone surfaces affected the amount of drag reduction. More recent hydrodynamic measurements did not yield ideal results. Ivanov et al. (2017) measured a drag increase of 6.5%, which aligned with a prediction by the Clauser chart method. Greidanus et al. (2017) measured a downshift of the logarithmic layer, attributing it to the surface roughness introduced by the normal surface deformation. Delfos et al. (2017) acquired similar conclusions with no drag reduction measured.

Numerical simulations of the compliant surface FSI have become possible in recent years with the increasing capacity of computing power. Modelling the compliant surface with a spring-mass-damper system, Endo and Himeno (2002) predicted a 2.7% net turbulent drag reduction. Xu et al. (2003) acquired no drag reduction and rebutted the results of Endo and Himeno. Fukagata et al. (2008) performed a numerical optimisation scheme modelling an anisotropic compliant surface. With a much longer integration time than Endo ($0 \leqslant t^+ \leqslant 1000$) and Xu ($0 \leqslant t^+ \leqslant 3000$), Fukagata acquired a maximum drag reduction of 8%. The spanwise vortical structures are found to be increased, which was consistent with a previous study in Fukagata et al. (2005). In addition, the equilibrium state of the drag-reducing anisotropic surface indicated a dependence of the wall deformation on wall-shear stress. However, a drag increase due to large wall-normal velocity fluctuations was measured when the streamwise domain doubled in length. This was due to the over-development of the downstream travelling deformation, which induced excessively large wall-normal velocities, demonstrating the sensitivity of such modelling to the domain size. Drag reduction was measured in a recent DNS study by Józsa et al. (2019) demonstrating a 3.7% drag reduction. However, the drag reduction mechanism was stated as an in-plane streamwise rather than a wall-normal deformation; the magnitude of deformation needed was also unrealistic for a compliant surface.

A compilation of the turbulent drag delta measured in past research is shown in Table 2.3. This table exhibits the mixed and inconclusive nature of research into drag reduction by compliant surfaces. While this table indicates the amount of drag reduction achieved, the wide range of testing parameters, regardless of a numerical or experimental approach, indicates how large the optimisation space is for turbulent drag reduction by compliant surfaces. In the following sections, the properties that constitute a compliant surface will be discussed.

Table 2.3. Compilation of drag reduction results over time; "-" in the method and DR column indicates only direct drag measurements and no drag reduction, respectively. Negative drag reduction (DR) indicates drag increase. If several setups were tested by author, the maximum indicated drag reduction is mentioned.

Author(s)	Setting	Approach	Method	DR [%]
Kramer (1961)	Water	Experimental	-	60.0
Blick and Walters (1968)	Air	Experimental	-	38.0
Lissaman and Harris (1969)	Air	Experimental	-	10.0
McMichael et al. (1980)	Air	Experimental	HWA	-
Choi et al. (1997)	Water	Experimental	HWA	7.0
Choi et al. (1999, 2001)	Water	Experimental	HWA	5.0
Endo and Himeno (2002)	-	Numerical	DNS	2.7
Xu et al. (2003)	-	Numerical	DNS	-
Semenov et al. (2007)	Water	Experimental	-	2.7
Fukagata et al. (2008)	-	Numerical	DNS	8.0
Lee et al. (2009)	Air	Experimental	HWA	5.0
Delfos et al. (2017)	Water	Experimental	PIV	-
Ivanov et al. (2017)	Water	Experimental	LDV	-6.5
Kulik et al. (2017)	Water	Experimental	-	33.0
Józsa et al. (2019)	-	Numerical	DNS	3.7

2.3.2. Surface types

In this section, the various types of compliant surfaces that have been modelled in numerical calculations and manufactured in experimental campaigns are discussed. The various types of compliant surfaces are compiled in Figure 2.13.

Numerical Approach

Numerical attempts in simulating the behaviour of a compliant surface in a turbulent flow have modelled the surface as a mass-spring-damper model, as shown in Figure 2.13 (b) and (d). The inputs for the simulations are the spring, damper, and mass constants. Surface (b) is a type of isotropic mass-spring surface that only allows deformations in the wall-normal direction due to pressure fluctuations. Surface type (d) allows an additional deformation in the streamwise direction, which originates from the shear forcing of the flow; these are anisotropic surfaces. Fukagata et al. (2008) tested with the surfaces in (d) where the equilibrium angle of the swivel arm (indicated by θ) was at 60°. This indicates the significant shear forcing of the surface, which may be coupled with the observed drag reduction.

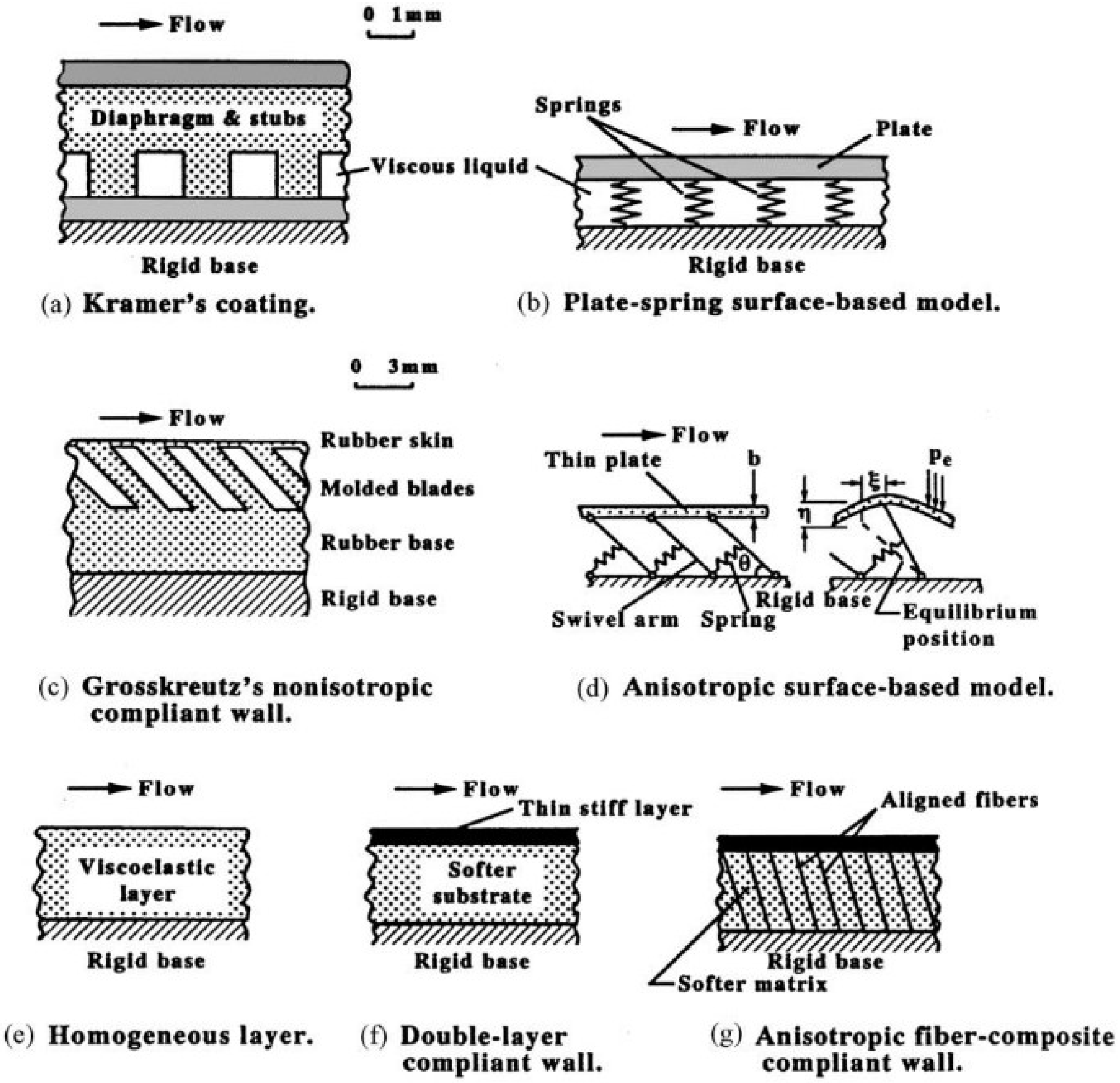

(a) **Kramer's coating.** (b) **Plate-spring surface-based model.** (c) **Grosskreutz's nonisotropic compliant wall.** (d) **Anisotropic surface-based model.** (e) **Homogeneous layer.** (f) **Double-layer compliant wall.** (g) **Anisotropic fiber-composite compliant wall.**

Figure 2.13. The various types of compliant surfaces designed over time (Gad-El-Hak (2002), adapted from Carpenter (1990))

Experimental Approach

Various types of compliant surfaces have been realised in past experimental research. A select few have been reviewed as possible candidates for the experimentation of this research and is be discussed in the following paragraphs.

Kramer type surface Kramer's rendition of dolphin epidermis is shown in Figure 2.13 (a), which consists of rubber stubs and a diaphragm. The void between the diaphragm and rubber stubs could be filled with damping fluid such as motor oil. The stiffness of the surface was quantified in pounds per cubic inch (PCI). Proper sealing of the damping fluid within the void and cleaning must be done after exchanging different damping fluids to attain proper results. It has been speculated that the seepage of the viscous damping fluid might have acted as drag-reducing polymers in Kramer's measurements (Gad-El-Hak, 2002). This type of surface has been later used by Puryear (1962), Nisewanger (1964), Ritter and Messum (1964), and Ritter and Porteous (1965) in attempts to replicate Kramer's experiments, but became extinct in the subsequent years.

Two-layer surface The two-layer compliant surface consists of a membrane or thin stiff layer (usually polyvinyl chloride (PVC)) with a polyurethane foam substrate underneath, shown in Figure 2.13 (f). The foam substrate could be saturated with water and damping fluid such as polyox-water solutions, similar to that of a Kramer type surface. The pores per inch (PPI) of the foam and the amount of water saturation may be varied to test different damping characteristics of the surface. A group at the University of Oklahoma led by Blick, and some later experiments by Lissaman and Harris (1969), McAlister and Wynn (1974), and McMichael et al. (1980) used this type of surface. The tension that sustains the membrane plays a critical role in the deformation of the surface, as the amount of tension affects the stiffness of the surface (McMichael et al., 1980). A stronger tension means a stiffer surface, vice-versa.

Homogeneous surface Latter experiments since the 1990s tested with homogeneous-single-layer viscoelastic compliant surfaces shown in Figure 2.13 (e). This surface type is more simplistic than the two-layer since the surface can be characterised more properly with material properties such as the shear modulus. Since the shear modulus is a measure of the resistance of a material to forcing, the FSI between the mean flow and the compliant surface can be scaled. A brief overview of the materials that used in previous literature is compiled in Table 2.4. Most of the surfaces contain elastomers that have viscoelastic properties. Homogeneous surfaces offer the flexibility in varying the material parameters, mainly the shear modulus and the density.

Table 2.4. A compilation of materials used in past research for homogeneous sheet of compliant surface

Author	**Material** (*Manufacturer*)
Hansen and Hunston (1974)	PVC & resin & di-2-ethyhexyl phthalate (plasticiser) & dibutylin maleate (stabiliser)
Gad-el Hak (1986b)	PVC & dioctyl-phtalate (plasticiser) & dibutyl tin maleate (stabiliser)
Lee et al. (1993)	Elastomer Sylgard 184 (*Dow Corning*) & Silicone Oil 200-series (*Dow Corning*)
Choi et al. (1997)	Silicone rubber (*Not specified*)
Lee et al. (2009)	Room temperature vulcanised (RTV) Silicone rubber Silastic S-2 (*Dow Corning*)
Zhang et al. (2015)	Elastomer Sylgard 184 (*Dow Corning*)
Greidanus et al. (2017)	Triblock-copolymer (SEBS) & mid-block paraffin oil
Ivanov et al. (2017)	Silicone rubber Mold Max 10 (*Smooth-On*)
Kulik et al. (2017)	RTV 3133 BASE (*Xiameter*)
Huynh and McKeon (2020)	Gelatine

In conclusion, the homogeneous surface provides flexibility in varying the properties of the surface. This type is easily characterised by material properties that can be used in scaling the FSI. Compared with the other experimental surfaces, the end product is much less complex. Therefore, the homogeneous surface is chosen to proceed with for experimentation.

2.3.3. Properties of a compliant surface

In this section, the defining parameters characterising a homogeneous compliant surface is elaborated. Five aspects of the surface have been considered: stiffness, thickness, density, viscoelasticity, and compressibility (Benschop et al., 2019). Each of them is quantified in different parameters, as shown in Table 2.5.

Table 2.5. Properties of the compliant surface that are taken into account

Property	**Parameter**	**Units**	
Stiffness	G	[Pa]	(Shear modulus)
Thickness	δ_s	[mm]	
Density	ρ_s	[kg/m^3]	
Viscoelasticity	$\tan(\delta_p)$	[-]	(Loss tangent)
Compressibility	ν_P	[-]	(Poisson's ratio)

The shear modulus and thickness of a compliant surface have a 1st-order effect on the deformation; while the density, viscoelasticity, and compressibility has a 2nd-order effect (Benschop, 2019). Furthermore, the modification of the stiffness and thickness is easier than the other parameters (Greidanus, 2019).

The density of a homogeneous compliant surface, while varying the composition, varies only slightly, as observed by Choi et al. (1997) and Greidanus et al. (2017). Furthermore, the density of the base elastomer materials of a compliant surface varies only slightly from 1000 kg/m^3. Therefore, the density of the compliant surface is overlooked for now.

Benschop et al. (2019) has also categorised viscoelasticity as a 2nd order parameter, yet it has been speculated several times in past literature that it plays a crucial role; specifically, the working mechanism hypothesised by Bushnell et al. (1977). Viscoelasticity introduces a phase lag between the stress and strain applied upon the compliant surface, which will be later discussed in Section 2.4. While varying the viscoelastic properties is challenging (Greidanus, 2019), its influence should still be kept in mind during the analysis.

The Poisson's ratio ν_p is the negative ratio of transverse strain to axial strain. It is assumed that the compliant surface is incompressible and capable of elastic deformation; thus, a fixed value of $\nu_P = 0.5$ is prescribed. This assumption has been frequently made by past literature (Greidanus et al., 2017; Zhang et al., 2017). The subscript "P" is used to differentiate between the kinematic viscosity of a fluid ν. The Poisson's ratio has been mentioned to be of minor importance to the deformation of the compliant surface (Benschop, 2019; Benschop et al., 2019; Greidanus, 2019).

Therefore, the stiffness, thickness, and viscoelasticity of a compliant surface have been considered as critical properties in its drag reduction capabilities.

Stiffness

The stiffness of the compliant surface can be approached from a material or FSI perspective. From a materials perspective, a commonly used measure of stiffness is the shear modulus:

$$G\ [\mathrm{Pa}] = \frac{\tau}{\gamma} \tag{2.19}$$

which is defined by the ratio of shear stress and strain.

The Young's modulus, or the modulus of elasticity, is defined as the ratio of longitudinal stress and strain:

$$E\ [\mathrm{Pa}] = \frac{\sigma}{\epsilon} \tag{2.20}$$

There has not been a definite rule in which modulus (Young's or shear) to define the stiffness of the compliant surface. It was shown by Rosti and Brandt (2017) that the skin friction increased monotonically with the Young's modulus. On the other hand, Benschop (2019) mentioned that the shear modulus is a 1st-order parameter of a compliant surface that plays a crucial role in its deformation. Fortunately, the Young's and shear modulus is related by:

$$G = \frac{E}{2(1+\nu_P)} \tag{2.21}$$

where ν_P is the Poisson's ratio. Assuming a fixed Poisson's ratio, the relation between the Young's and shear modulus is a constant multiple of 3.

The shear modulus will be used for the stiffness of the compliant surface, as it is involved in the scaling of the FSI, and could be converted to the Young's modulus assuming a constant Poisson's ratio. From the shear modulus of the compliant surface, the shear wave velocity is derived, which is the convective velocity in the transverse direction of a solid, and the lowest propagation velocity of transverse shear waves in a surface (Gad-El-Hak et al., 1984; Gad-el Hak, 1986b):

$$c_s = \sqrt{\frac{G}{\rho_s}} \tag{2.22}$$

c_s, inherently a material property, should not be confused with the shear velocity (or wall-friction velocity) u_τ of the boundary layer, a fluidic property for normalising turbulent boundary layer properties into viscous units.

Another approach to define surface stiffness is to compare the inertial potency of the mean flow and the compliant surface. Initially, the velocity ratio of the mean flow and surface shear velocity was used to link the properties of the flow and surface:

$$u_r = \frac{u_\infty}{c_s} \tag{2.23}$$

Hydrodynamic experiments used Equation (2.23) as a threshold for the onset of instabilities; soft materials are more prone to prompt the formation of static-divergence waves (Hansen and Hunston, 1983). A surface may be considered soft if $u_r > 1$ and stiff if $u_r < 1$. Other ratios have been proposed in past research to link the properties of the mean flow and surface; namely, the density ratio:

$$\rho_r = \frac{\rho_f}{\rho_s} \tag{2.24}$$

and the inertia ratio:

$$I_r = \frac{\rho_f u_\infty^2}{\rho_s c_s^2} \tag{2.25}$$

These ratios in Equation (2.23), (2.24), (2.25) have all been used in past literature to scale the FSI between the compliant surface and mean flow. The validity of these ratios will be commented on later in Section 2.3.4.

Thickness

The allowed deformation of a compliant surface is confined within its thickness, making it a crucial parameter. Kulik et al. (2017) conducted a thickness sweep ranging from 4 ~ 12 mm in which drag reduction was achieved, shown in Figure 2.14. Compliant surface thickness in literature have fallen around the order of magnitude of $\delta_s \sim \mathcal{O}(1\ \text{mm})$. Zhang et al. (2017) found that the compliant surface response to the flow can be tuned by varying the thickness.

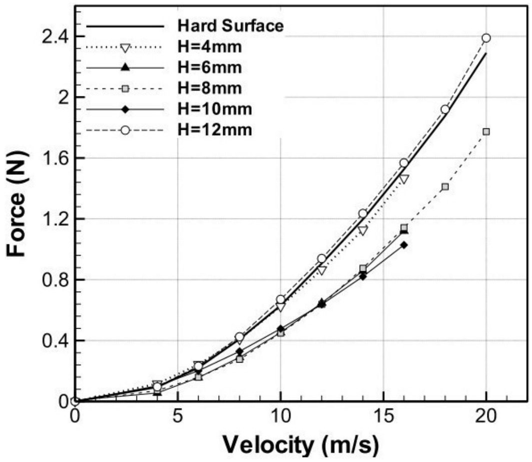

Figure 2.14. Drag reduction with respect to different compliant surface thickness (Kulik et al., 2017)

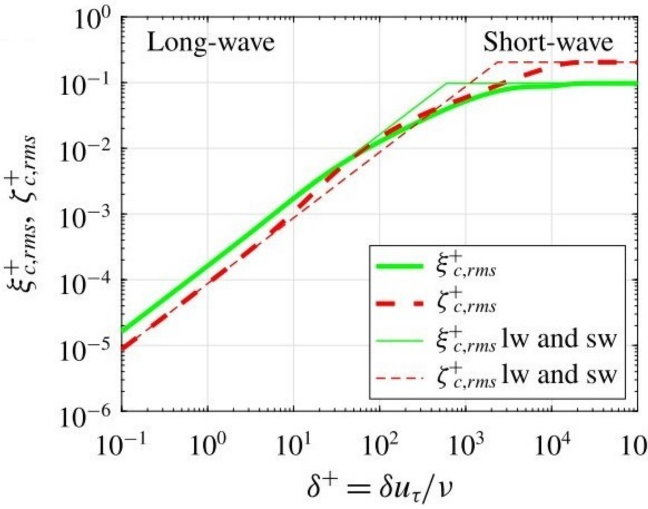

Figure 2.15. Normalised surface-normal (ζ) and streamwise (ξ) deformation of the compliant surface with respect to the normalised thickness. The uncoupling of the deformation can be seen if the thickness is increased to a certain point. (Benschop et al., 2019)

Ash et al. (1975) and Orszag (1977) have indicated that the wave response of a compliant surface is limited to low frequency and large wavelength motions. However, recent findings by Benschop et al. (2019) show that the response consists of a broad spectrum of stress waves. Depending on the surface thickness, the deformation could be either a long-wave or short-wave dominant response. Long-wave and short-wave limits can be defined for the thickness-dependent wall-normal deformation (Kulik, 2012; Vedeneev, 2016; Benschop et al., 2019). A long-wave limit indicates that the wavelength of the wavy deformation is much larger than the surface thickness; vice-versa for a short-wave limit. The threshold between these two categories is defined by the ratio of the thickness δ_s to the wavelength λ of the wavy deformation $\delta_{r\lambda} = \delta_s/\lambda$. Before hitting the short-wave limit, the surface-normal deformation is linearly proportional to the compliant surface thickness; after the short-wave limit, the surface-normal deformation approaches a constant value becoming independent of the surface thickness, as shown in Figure 2.15 (Benschop et al., 2019). This approach provides a good reference in selecting the range of compliant surface thicknesses to be tested.

2.3.4. Deformation of a compliant surface

In this section, the deformation of the compliant surface due to the FSI is discussed. The wavy response of compliant surfaces has been observed over the years, both in numerical and experimental cases. While the response holds the key to turbulent viscous drag reduction, it could also increase the drag. The deformation of compliant surfaces introduces a hydrodynamic surface roughness that can induce instabilities in the flow.

Therefore, the design of a compliant surface must be taken with care if the aim for turbulent drag reduction is to be achieved.

Wave response

The wavy response of a compliant surface in a fluid flow is the most consistent outcome of compliant surface research. This has been observed by Kramer (1960) to modern numerical (Kim and Choi, 2014; Rosti and Brandt, 2017) and experimental (Zhang et al., 2015; Delfos et al., 2017) research. It has also been observed that the wavy deformation comes in the form of a downstream travelling wave (Endo and Himeno, 2002; Fukagata et al., 2008). The propagation speed of these surface waves was observed by Kim and Choi (2014) to be proportional to compliant surface's stiffness. Figure 2.16 is a DNS simulation of a compliant surface by Rosti and Brandt (2017). The wavy deformation becomes quite pronounced when the compliant surface becomes softer; the same could be said for the pressure distribution.

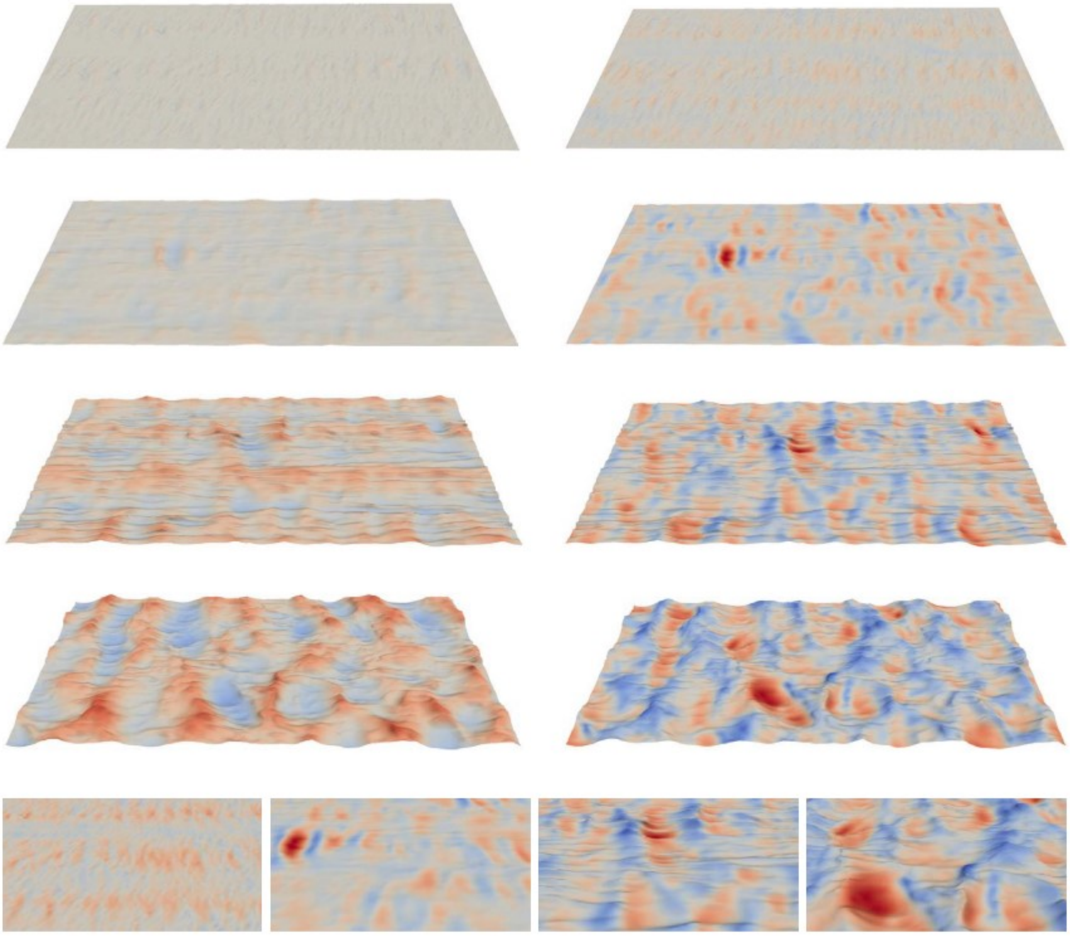

Figure 2.16. Instantaneous surface deformation (Left column) and pressure distribution (Right column) of flow from left to right over simulated hyperelastic wall. Red colouring means positive deformation and flow pressure, whereas blue indicates negative deformation and flow pressure. Bottom row is a magnified version of the right column. (Rosti and Brandt, 2017)

An active flow control technique in the form of travelling wave boundaries has achieved drag reduction by the suppression of separation and turbulence reduction (Shen et al., 2003). This result was made possible by relaminarising and reattaching the flow by introducing a vertical velocity component; which can be seen in Figure 2.17. The outcome of this is that it eliminates the pressure drag due to separation, which was the main culprit in the increase of drag for rigid wavy surfaces in Section 2.2.7 being incapable of reducing net turbulent drag. The relation between the downstream travelling wavy deformation of a compliant surface and the drag reducing capability of a downstream travelling wavy boundary sheds some drag reduction potential on compliant surfaces.

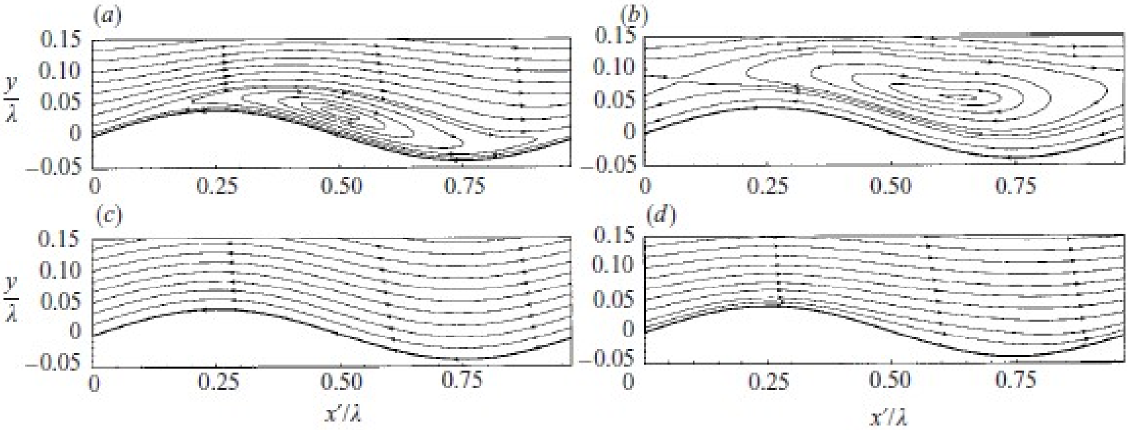

Figure 2.17. Streamline pattern of the mean flow in a frame moving in a phase velocity *c* (a) c/U = 0.4 (b) c/U = 0.8 (c) c/U = 1.2 (d) c/U = -0.4. The streamline shape for when *c* = 0 is analogous to that of c/U = 0.4. (Shen et al., 2003)

Instabilities

The surface and flow instabilities caused by the FSI play a vital role in a drag-reducing compliant surface. The presence of surface instabilities causes drag by introducing a hydrodynamic roughness protruding the viscous sublayer. However, this type of two-way coupling is necessary for the surface to affect the flow to reduce drag. If only one-way coupling were present, the flow affects the surface but not vice versa. While suppressing a single instability may be reasonably simple, other instabilities may also proliferate, making it fairly challenging (Gad-El-Hak, 2002).

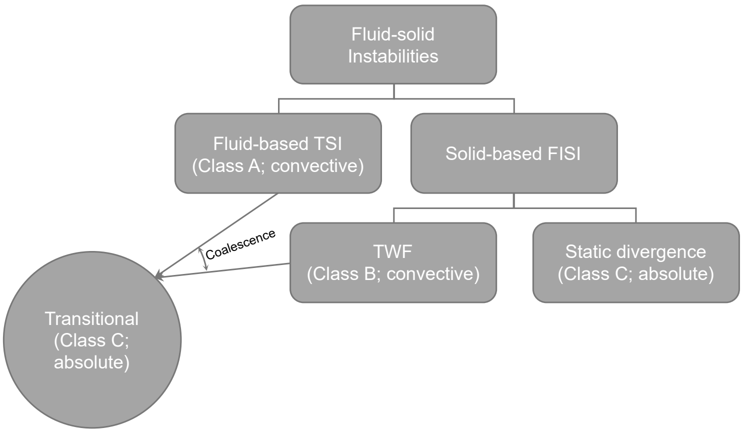

Figure 2.18. Classification of the instabilities originating from FSI raised by Landahl (1962); Benjamin (1960, 1963) (Adapted from Gad-El-Hak (2002))

Types of instabilities Landahl (1962); Benjamin (1960, 1963) were able to differentiate the instabilities into several categories shown in Figure 2.18. Class A waves are TSI of the flow which the surface compliance can modify. Class B waves are wall-based instabilities that consist of free-surface waves that can be modified by the flow. These two classes are convective instabilities that involve energy exchanges between the surface and flow. Lastly, Class C waves are similar to that of Kelvin-Helmholtz instabilities; this type of static-divergence surface waves occur when the pressure forcing of the fluid overpowers the surface stiffness, causing a one-way transfer of energy from the fluid to the solid. Carpenter and Garrad (1985, 1986) characterises class A instabilities as fluid-based, and class B and C instabilities as solid-based.

Since TSI (Class A) are the main culprit behind boundary layer transition, the instabilities that concern turbulent flows are the solid-based instabilities (Class B and C). If a surface is too compliant to the flow, they are susceptible to elastic instabilities such as travelling wave flutter (TWF), a dynamic instability, and static-divergence waves. The formation and growth of travelling wave flutter come from an irreversible transfer of energy from the flow to the surface (Lucey and Carpenter, 1995), which comes in the form of a downstream travelling wave as observed by Gad-el Hak (1986a) in Figure 2.19. Static-divergence waves occur when the static forcing of the fluid overpowers a compliant surface's stiffness. The hydrodynamic roughness of a surface will be elaborated further in a later section. These instabilities have been observed when the fluid flow exceeds a certain inertial threshold, which will be discussed in the following section.

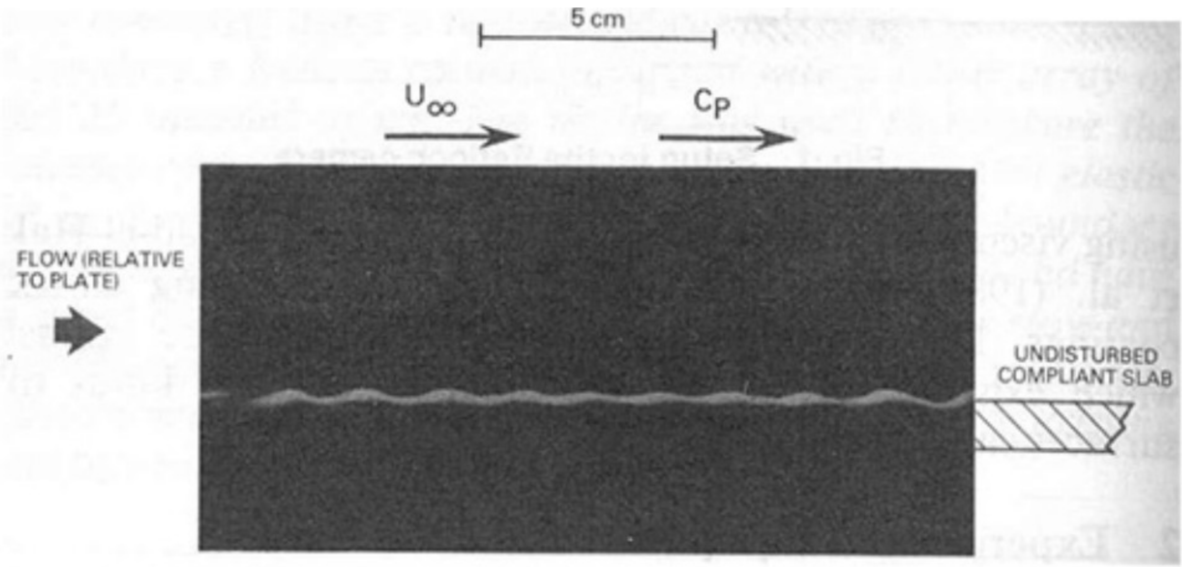

Figure 2.19. Visualisation of travelling wave flutter on a elastic compliant surface ($u_\infty = 0.7$ m/s, $u_r = 1.8$, $thickness = 1.05$ cm) (Gad-el Hak, 1986a)

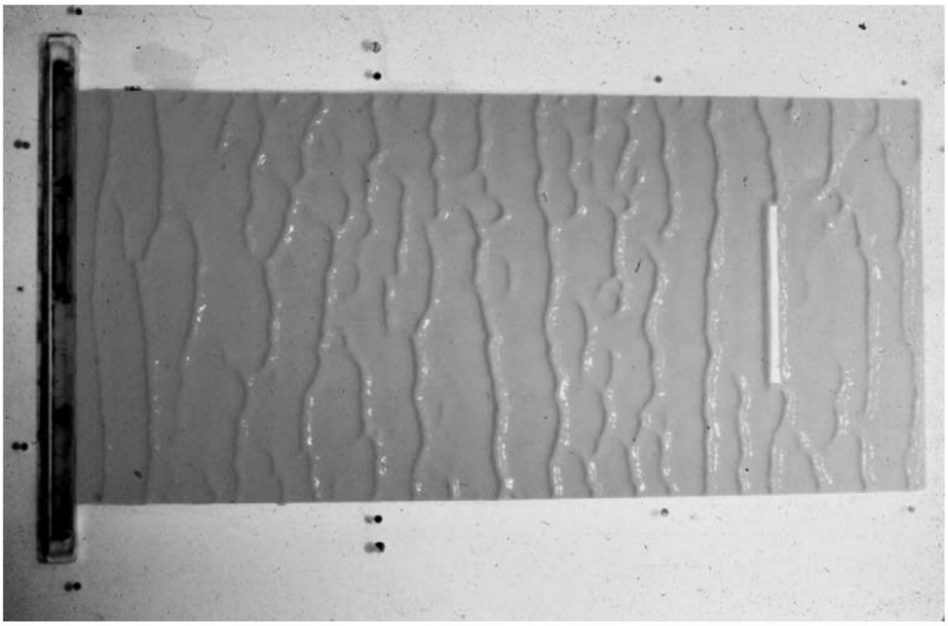

Figure 2.20. Static-divergence waves are observed after the mean flow velocity exceeds a certain threshold (Gad-El-Hak et al., 1984)

Inertial scaling Inertial scaling parameters signify the inertial threshold for the onset of instabilities; they link the compliant surface's inertial properties to the flow. The ratios that were briefly mentioned in the discussion of the surface stiffness in Section 2.3.3 are revisited: the velocity ratio, the density ratio, and the inertia ratio:

$$u_r = \frac{u_\infty}{c_s} \tag{2.23}$$

$$\rho_r = \frac{\rho_f}{\rho_s} \tag{2.24}$$

$$I_r = \frac{\rho_f u_\infty^2}{\rho_s c_s^2} \tag{2.25}$$

which can be related by:

$$I_r = \rho_r u_r^2 \tag{2.26}$$

These parameters scale the inertial potency of the flow to deform the compliant surface and the compliant surface's capability to resist deformation.

- **Velocity ratio u_r**
  Equation (2.23) is the ratio of the flow velocity and shear velocity of the compliant surface. A surface may be considered soft if $u_r > 1$ and stiff if $u_r < 1$. Soft surfaces prompt the formation of static-divergence waves travelling downstream (Hansen and Hunston, 1983). The wave amplitude is inversely proportional to the stiffness of the compliant surface. Hansen et al. (1980) found that large-amplitude static-divergence waves develop when the ratio exceeds a critical value of 3. Gad-El-Hak et al. (1984) also observed static-divergence waves when the mean flow velocity exceeded the surface shear velocity, shown in Figure 2.20. Depending on the thickness of the compliant surface, the onset threshold of static-divergence waves ranged between $4 \leqslant u_r \leqslant 12$, where the thickness was inversely proportional to the threshold of the velocity ratio. A later analytical study by Duncan et al. (1985) found that the onset threshold instabilities for a turbulent flow was $u_r \approx 2.86$. Travelling wave flutter was not so much observed in these attempts; Carpenter and Garrad (1985) argued that the viscoelastic damping of the surface inhibits the travelling wave flutter but fails to diminish the static-divergence waves effectively.

- **Density ratio ρ_r**
  Equation (2.24) is the density ratio of the fluid to the compliant surface. After Blick in the 1960s, there were not many attempts in aerodynamic experimentation of compliant surfaces. This lack of experiments has been largely due to the belief that air is impotent to deform the compliant surface owing to a low density ratio (Benschop, 2019). For water the density ratio is approximately $\rho_{H_2O}/\rho_s \approx 1$ while for air $\rho_{air}/\rho_s \approx 0.001$, assuming a surface density of $\rho_s = 10^3$ kg/m^3. It was later concluded by McMichael et al. (1980) that aerodynamic turbulent drag reduction for compliant surfaces is not going to be as successful as it is for hydrodynamic turbulent drag reduction.

- **Inertia ratio I_r**
  The inertia ratio in Equation (2.25) relates the inertial potency of a flow and surface. This approach is more logical as inertia is a team effort by the mass (hence density) and velocity. Duncan et al. (1985) pitched that the criteria for the onset of instabilities should be characterised by:

  $$\frac{u_\infty}{c_s} = \sqrt{I_r/\rho_r} \tag{2.27}$$

  for a certain inertia ratio I_r

  $$I_r = \frac{\rho_f u_\infty^2}{\rho_s c_s^2} \tag{2.25}$$

  Since the denominator of the inertia ratio is equivalent to the shear modulus of the compliant surface, Equation (2.25) can be rewritten as:

  $$I_r = \frac{\rho_f u_\infty^2}{\rho_s c_s^2} = \frac{\rho_f u_\infty^2}{G} \tag{2.28}$$

A later analysis by Duncan (1986) concluded that the onset of instability when $\sqrt{\rho_r}u_\infty/|c_s| \geqslant 2$. Rewriting it with Equation (2.28):

$$\frac{\rho_f u_\infty^2}{G} \geqslant 4 \tag{2.29}$$

While it has been hypothesised that air flows have insufficient inertial potency to deform the flow, the air flow velocity can be increased to compensate the low density, per the inertia ratio in Equation (2.28). The author believes that the inertia ratio more properly scales the FSI since it includes both the density and velocity, which are core components to the flow's inertial potency.

The proposed inertia ratio is a scaling parameter that can define the threshold for the onset of instabilities and the stiffness of the surface (from an FSI perspective). This ratio is also not limited to the type of surface and mean flow that is being tested. This inertial scaling will be used later in defining the range of compliant surface stiffness to be tested in experimentation.

In addition to the inertial scaling, Semenov (1991) proposed that compliant surfaces are capable of drag reduction if the non-dimensional period falls within $50 < t_0^+ < 150$. The non-dimensional period is defined as:

$$t_0^+ = \frac{u_\tau}{f_0 \nu} \tag{2.30}$$

with the fundamental frequency f_0 (Rossing and Fletcher, 1995):

$$f_0 = \frac{\sqrt{3G/\rho_s}}{4\delta_s} \tag{2.31}$$

This range compliments the scaling of the inertia ratio by also considering the thickness of the compliant surface.

Hydrodynamic roughness

The deformation of a compliant surface introduces a certain hydrodynamic roughness to the flow. Clauser (1954) quantified the surface roughness as a mean velocity profile shift in the logarithmic layer (Rosti and Brandt, 2017). The onset of instabilities mentioned in Section 2.3.4 makes the surface hydrodynamically rough (fig. 2.20) that disrupts the flow and generates excess drag (Gad-El-Hak et al., 1984; Lee et al., 1993). An analogous observation was made by Fukagata et al. (2008) where the modelled surface's excessive wall-normal velocities led to a drag-increase. The threshold between a hydrodynamically smooth and rough surface is the viscous sublayer height δ_{sub} (Semenov, 1991; Choi et al., 1997; Delfos et al., 2017; Greidanus, 2019). Similar conclusions have been reached for Hansen et al. (1980) and McMichael et al. (1980).

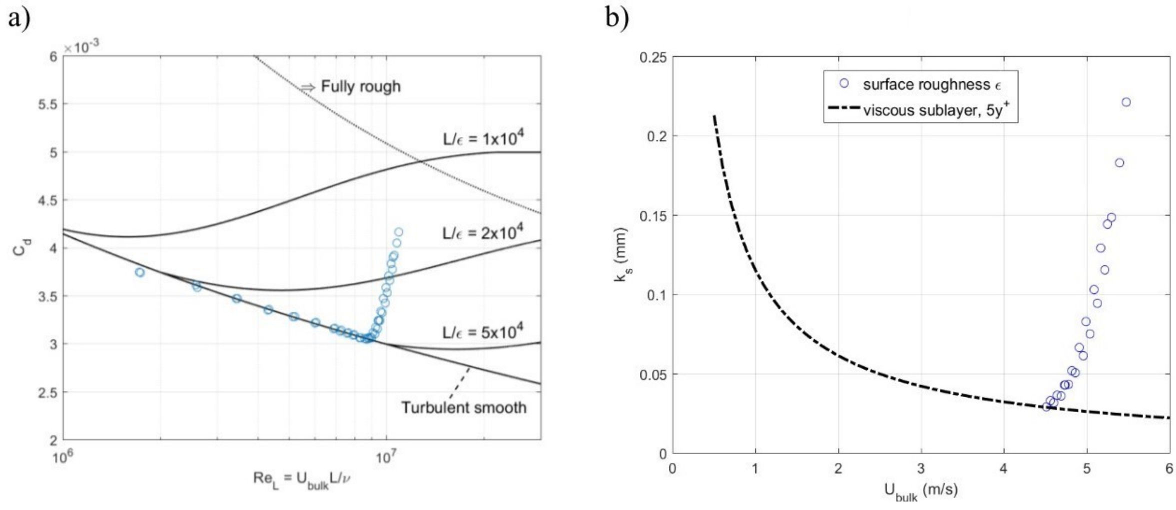

Figure 2.21. Experimentation results of compliant surfaces in a water tunnel by Delfos et al. (2017). The circles indicate the measurement results of coating 1.
(a) Drag coefficient to bulk Reynolds number (b) Surface roughness to bulk velocity

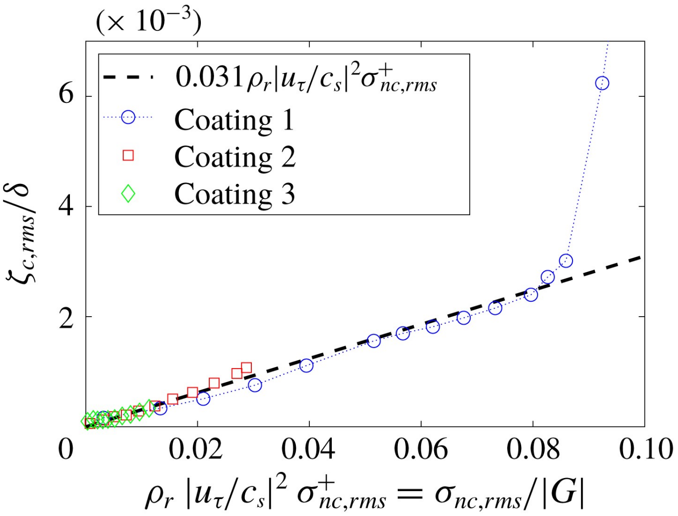

Figure 2.22. The measured vertical surface displacement as a function of normalised stress (Benschop et al., 2019)

Delfos et al. (2017) plotted the measured drag onto a flat-plate equivalent of a pipe-flow Moody diagram, and also the measured surface roughness with respect to the viscous sublayer height in Figure 2.21. When the compliant surface's roughness exceeds the viscous sublayer height at higher bulk velocities, it is coupled with a drag increase that quickly approaches that of a fully rough surface. The wall-normal deformation of the same coating is plotted with an analytical model by Benschop et al. (2019) as a function of the ratio of normalised wall pressure and shear modulus in Figure 2.22. At a ratio of $\sigma_{rms}/|G| \approx 0.08$, the onset of two-way coupling causes a sudden increase of wall-normal deformation, corresponding with Figure 2.21. This ratio will be used to fine-tune the compliant surface parameter space for the experiments.

2.3.5. Flow structure above a compliant surface

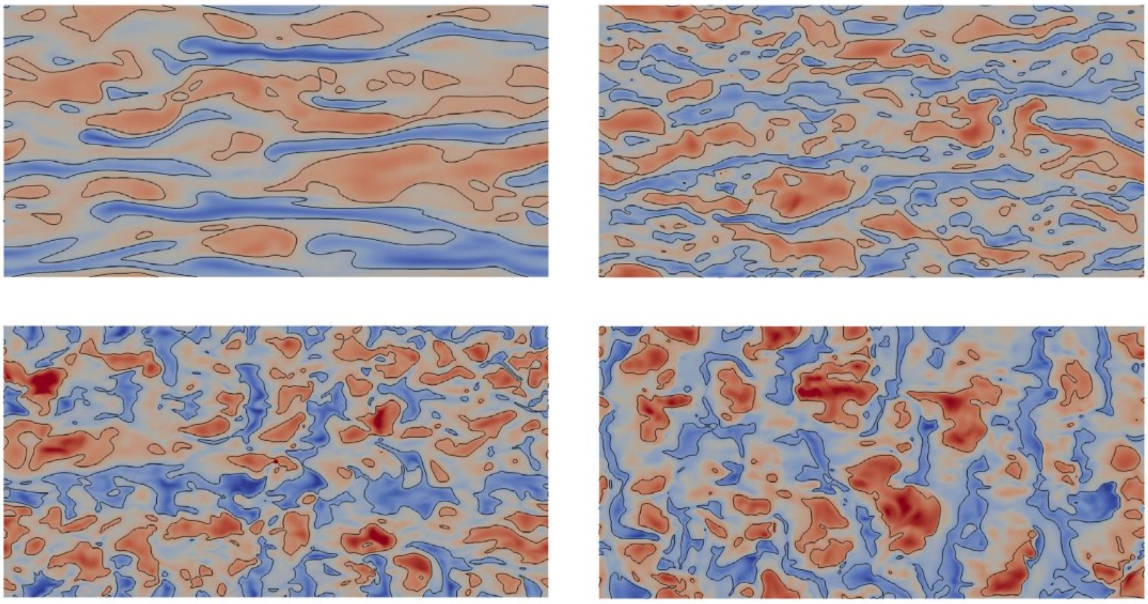

Figure 2.23. Contour map of streamwise velocity fluctuations in a wall-parallel plane 0.15 channel height above. Surface stiffness from top-left to bottom-right is from high to low. (Rosti and Brandt, 2017)

Low-speed streaks near the wall are typical flow structures present in wall-bounded turbulent flow (fig. 2.23 (top left)). Numerical simulations of a hyperelastic surface by Rosti and Brandt (2017) saw the modifications of the flow structure by the deformation of the compliant surface in Figure 2.23. Due to the compliant surface's wavy deformation, the prevalent low-speed-streaks in turbulent flows disintegrate into small pieces. As the compliant surface stiffness decreases, the wavy deformation becomes more pronounced with higher wave amplitudes, leading to the disruption of coherent spanwise flow structure.

Per the discussion in Section 2.3.4, the deformation of a compliant surface introduces a hydrodynamic surface roughness to the flow. One-way coupling will dominate if the deformation is considered to be hydrodynamically smooth. Once the inertia ratio exceeds the onset threshold of instabilities, two-way coupling makes the surface hydrodynamically rough, leading to large-amplitude quasi-2D downstream travelling waves. This subsequently leads to an increase of pressure drag and produces large amounts of near-wall vortical structures with increased intensities (Kim and Choi, 2014). Finding the surface that gives an optimum FSI for a given flow regime is the key challenge in finding a drag-reducing compliant surface.

2.3.6. Mechanism for turbulent drag reduction

In this section, some of the hypothesised turbulent drag reduction mechanisms of compliant surfaces are discussed. No firm agreement exists on the working mechanism of the turbulent viscous drag reduction of compliant surfaces. Below is a list of the hypothesised mechanisms that have been frequently mentioned in literature.

1. **Inhibition of turbulent bursting feedback loop**
   Bushnell et al. (1977) hypothesised a feedback loop where older bursts in the outer part of the boundary layer induce a pulsating pressure field that prompts the formation of new bursts near the flow. He further proposed that a compliant surface, if tuned accordingly, could provide a short wave response that alters the pressure fluctuations to inhibit the feedback loop of turbulence bursting. As a result, a reduction in the number of bursts per unit time would lead to skin friction reduction.

2. **Upshift of the logarithmic layer**
   The inner layer of the boundary consists of the viscous sublayer and the logarithmic layer (with an overlapping buffer layer sandwiched in between). A strong shear layer exists on top of the viscous sublayer next to the logarithmic layer (Nieuwstadt et al., 2016), which is a significant source of Reynolds stress and turbulence production. As the skin friction is a distance (from the wall) weighted integral of the Reynolds stress (Fukagata et al., 2008), an upshift of the logarithmic layer means the lowering of the skin friction, hence drag reduction. Choi et al. (1997) argues that this is possible when the compliant surface's natural frequency coincides with the period between the sweeping events of the flow, associated with the ejection of low-momentum flow near the wall. As a result, the compliant surface's periodic deformation weakens the strength of upwash events of turbulent coherent structures.

   This shift of the logarithmic layer can also be seen as a redistribution of the turbulent energy production and viscous dissipation (Choi et al., 1997). The thickening of the viscous sublayer highlights this redistribution, which is due to the size increase of the smallest turbulent eddies within the sublayer (Lumley, 1973). As the core area of the turbulent energy production is shifted away from the surface, this is an indication of turbulent skin friction reduction. This shift has also been observed in other drag reduction techniques: polymer additives to the flow (Virk, 1975) and riblets (Choi, 1989).

2.4. Rheology of viscoelastic material

The knowledge of rheology is required to characterise the forcing and deformation of viscoelastic material. The study of rheology concerns fluid and solid-like behaviour of materials; namely the viscoelasticity of materials. For a perfectly elastic material, the stress-strain response is immediate; the material deforms without delay with the application of stress. However, for perfectly viscous material, there exists a phase lag of $\delta_p = \pi/2$ between stress and strain. A viscoelastic material has both viscous and elastic behaviour simultaneously, meaning that the phase lag is in between $0 \leqslant \delta_p \leqslant \pi/2$. This is shown in Equation (2.32).

$$\begin{cases} \delta_p = 0: \text{ Elastic} & \text{(2.32a)} \\ 0 < \delta_p < \pi/2: \text{ Viscoelastic} & \text{(2.32b)} \\ \delta_p = \pi/2: \text{ Viscous} & \text{(2.32c)} \end{cases}$$

This leads to the characterisation of both the elastic and viscous component of a viscoelastic material. The elasticity of a material can be characterised by the shear modulus G, where the viscous component is by the dynamic viscosity η. This η is identical to the dynamic viscosity μ seen in fluid mechanics. For a perfectly elastic and viscous material, the resultant shear stress of applying a sinusoidal shear strain $\gamma(t) = \gamma_0 \sin(\omega t)$ would be:

$$\tau_e = G\gamma = G\gamma_0 \sin(\omega t) \tag{2.33}$$

$$\tau_v = \eta\dot{\gamma} = \eta\omega\gamma_0 \sin(\omega t + \pi/2) \tag{2.34}$$

where the elastic shear stress is dependent on the shear strain, and the viscous shear stress is dependent on the shear strain rate. With trigonometric manipulation of the strain rate, the formerly cosine term becomes a sine term with a phase lag of $\delta_p = \pi/2$.

While there are various linear viscoelastic models such as the Kelvin-Voigt model (which will not be elaborated further), the general conclusion is that a viscoelastic material has phase lag in between the stress and strain, with the value ranging in $0 < \delta_p < \pi/2$. This means that with a sinusoidal strain applied to a viscoelastic material, there is a combined elastic and viscous stress response of:

$$\begin{aligned} \tau &= \tau_0 \sin(\omega t + \delta_p) \\ &= \tau_0[\sin(\omega t)\cos(\delta_p) + \cos(\omega t)\sin(\delta_p)] \end{aligned} \tag{2.35}$$

To isolate the elastic and viscous contribution of the shear stress, the shear strain rate and shear strain are set to zero, respectively (eq. (2.33),(2.34)). Thus acquiring

$$\begin{cases} \tau_0' = \tau_0 \sin(\delta_p) & \text{(2.36a)} \\ \tau_0'' = \tau_0 \cos(\delta_p) & \text{(2.36b)} \end{cases}$$

where the prime and double-prime indicates the elastic and viscous component, respectively. Equation (2.36) can be further written in complex form:

$$\tau^* = \tau_0' \cos(\omega t) + i\tau_0'' \sin(\omega t) \tag{2.37}$$

arriving at the complex shear stress τ^*, where $i = \sqrt{-1}$. This is an indication that the viscoelasticity of the material makes the stress-strain relation dependent on the forcing period or frequency. Three viscoelastic properties can be extracted from this derivation, which are the storage shear modulus, the loss shear modulus, and the loss tangent:

$$\begin{aligned} G' &= \frac{\tau_0'}{\gamma_0} = \frac{\tau_0}{\gamma_0}\cos(\delta_p) \\ G'' &= \frac{\tau_0''}{\gamma_0} = \frac{\tau_0}{\gamma_0}\sin(\delta_p) \\ \tan(\delta_p) &= \frac{\tau_0''}{\tau_0'} = \frac{G''}{G'} \end{aligned} \tag{2.38}$$

The storage modulus indicates the material's capability store elastic energy that can be recovered, whereas the loss modulus is an indication of the amount of viscous losses due to stress. These two form the complex shear modulus, which is a defining viscoelastic property in this research:

$$G^* = G' + iG''. \tag{2.39}$$

from which its magnitude is a defines the stiffness of the compliant surface:

$$\left|G^*\right| = \sqrt{(G')^2 + (G'')^2} \tag{2.40}$$

The commonly known shear modulus in material mechanics is a special case of the formulation in Equation (2.40). If a material is considered entirely elastic, the loss shear modulus is zero. This leads to the retardation of the complex shear modulus to only contain the storage shear modulus, which is indeed the shear modulus for a completely elastic material. The loss tangent also becomes zero, indicating zero viscoelasticity. Since this is a more general form of stiffness that encompasses the viscoelasticity of compliant surface material, the stiffness of a compliant surface is referred to as the magnitude of the complex shear modulus $|G^*|$ in later text.

The viscosity η can also be represented in complex form η^*, an indication of the material's resistance to sinusoidal stress, in a similar manner:

$$\begin{cases} \eta' = \dfrac{G''}{\omega} = \dfrac{\tau_0}{\gamma_0\omega}\sin(\delta_p) & \text{(2.41a)} \\ \eta'' = \dfrac{G'}{\omega} = \dfrac{\tau_0}{\gamma_0\omega}\cos(\delta_p) & \text{(2.41b)} \end{cases}$$

The loss tangent directly relates the elastic and viscous properties of a material. A lower loss tangent signifies a more solid-like behaviour while a higher value indicates a more fluid-like material behaviour. The above derivation also works for axial stress and strain and applied sinusoidal stress instead of strain.

The viscoelasticity of a compliant surface plays a vital role in this review, since the phase lag between the forcing of the flow and the deformation of the surface may play a role in the modulation of flow characteristics, hence drag reduction. Choi et al. (1997) reasoned that the loss tangent of a compliant surface must be chosen such that its natural frequency makes the surface capable of interacting with the flow. One of the drag reduction mechanism hypothesised by Bushnell et al. (1977) involves the inhibition of the feedback mechanism of turbulence bursts, in which a near-wall burst increases the near-wall turbulence. While it has been argued by Benschop (2019) that the loss tangent is of second-order importance in the overall deformation of the compliant surface, the role that it plays during the resonance should not be diminished (Greidanus, 2019), as it may affect the drag reduction.

3

Experimental methodology

In this chapter, the experimental methodology and motivation behind the approach chosen is discussed. This discussion largely divided into 2 categories:

1. **Outside of wind-tunnel**
   a. Definition of compliant surface parameter space and material (Section 3.1)
   b. Evaluation of material viscoelastic properties with a rheometer (Section 3.2)
   c. Compliant surface test plate design and manufacture (Section 3.3)
2. **Inside of wind-tunnel**
   a. Description of the M-Tunnel (Section 3.4)
   b. Drag measurements with the Hill system (Section 3.5)
   c. Flow visualisation with particle image velocimetry (PIV) (Section 3.6)
   d. Compliant surface test matrix and wind tunnel measurement plan (Section 3.7)
   e. Stastistical analysis techniques for data validation (Section 3.8)

First, the parameter space of the compliant surface is defined in Section 3.1 by scaling experiments from past literature to the M-tunnel, the wind tunnel used in this research. A material survey is then conducted in Section 3.2 to find a suitable material that falls within the defined parameter space. The formula of the mixture is defined to vary the stiffness and thickness of the compliant surface. Section 3.3 elaborates on the design of the compliant surface test plate and manufacture setup.

Section 3.4 gives a description of the wind tunnel, the M-Tunnel, used in this research. Section 3.5 describes "the Hill" setup, the integrated drag and hot-wire measurement apparatus used for this research. Section 3.6 gives an overview of the PIV setup and configuration for visualisation of the flow. Section 3.7 presents the compliant surface test matrix and the wind tunnel measurement plan for the Holl and PIV. Finally, Section 3.8 gives an overview of the statistical measures used to validate with raw results from the wind tunnel measurements.

3.1. Compliant surface parameter space and material

This section elaborates on the definition of the parameter space and material of the compliant surfaces manufactured in this research. In the previous chapter, various types of compliant surfaces seen in past literature were discussed. Of which, the single-layer homogeneous compliant surface approach was chosen for its straightforward characterisation of its material properties. The parameter space is defined by scaling the flow properties and compliant surface stiffness of several successful turbulent drag reduction cases to the M-Tunnel. Most of these successful experiments were hydrodynamic experiments. A material that corresponds to the defined parameter space is then chosen.

3.1.1. Parameter space

The stiffness $|G^*|$ and thickness δ_s of the compliant surface constitutes the parameter space for experimentation in this research. Due to the limitations of the Hill setup, discussed later in Section 3.3 and 3.5, the thickness has a fixed range of:

$$1 \leqslant \delta_s \text{ [mm]} \leqslant 4 \tag{3.1}$$

For the stiffness, an outer and inner FSI scaling was applied to successful compliant surface turbulent drag reduction cases to pinpoint the parameter space. For both of these scaling schemes, the inertial capability of the mean flow and surface are scaled to the wind tunnel setup to be used. These approaches were considered simultaneously to broadly encompass the possible range where turbulent drag reduction is probable.

Outer scaling

An outer scaling is proposed to scale the mean boundary layer and surface properties in two steps. First, the Reynolds number is scaled to achieve flow similarity and acquire the equivalent air speed. Then, the inertial scaling of the FSI by the inertia ratio is applied to calculate the scaled stiffness of the compliant surface. The Reynolds number and the recalled inertia ratio are shown below.

$$\text{Re} = \frac{u_\infty \delta_b}{\nu} \tag{3.2}$$

$$I_r = \frac{\rho_f u_\infty}{|G^*|} \tag{3.3}$$

The shear modulus in Equation (3.3) has been changed to the magnitude of the complex shear modulus (compare eq. (2.28)). This makes sense since for a purely elastic material, the complex shear modulus would retard to the shear storage modulus, which is the shear modulus as seen in material mechanics. For a viscoelastic material, the viscous contribution must be taken into consideration. The magnitude of the complex shear modulus will be referred to as the stiffness hereafter.

This two-step outer scaling is applied to several drag reduction cases in literature presented in Table 3.1. A scatter plot of the outer-scaled surface stiffness of the cases and the drag reduction is shown in Figure 3.1. Most of these cases were hydrodynamic measurements and provided sufficient information to be properly scaled to air flows. An asymptotic trend is seen where with the surface stiffness is inversely proportional to the drag reduction measured. Cases where drag reduction was measured largely falls within the stiffness range of:

$$1 < |G^*|\text{[kPa]} < 100 \tag{3.4}$$

which is considered as the initial stiffness range of the compliant surface.

Table 3.1. Turbulent drag reduction cases for outer scaling

			Original		**Scaled**	
	Case	**DR [%]**	$\lvert G^*\rvert$[kPa]	u_∞[m/s]	$\lvert G^*\rvert$[kPa]	u_∞[m/s]
Water	Choi et al. (1997)	7	940	2	63.23	15
		1.5	568	2.5	38.25	18.75
	Semenov et al. (2007)	17	200	5.5	1.96	15.57
		16	430	5.25	4.22	14.96
	Kulik et al. (2017)	31.6	140	16	71.1	329.15
Air	Lee et al. (2009)	0	383.33	14	-	-
		0	200	14	-	-
		4	100	26	-	-

Inner scaling

The inner scaling scales the FSI near the wall; it utilises the ratio of the pressure fluctuation at the wall and the magnitude of complex shear modulus. This ratio was seen in x-axis of Figure 2.22 from Benschop et al. (2019), which at a value of

$$\frac{\sigma_{rms}}{|G^*|} = 0.08 \tag{3.5}$$

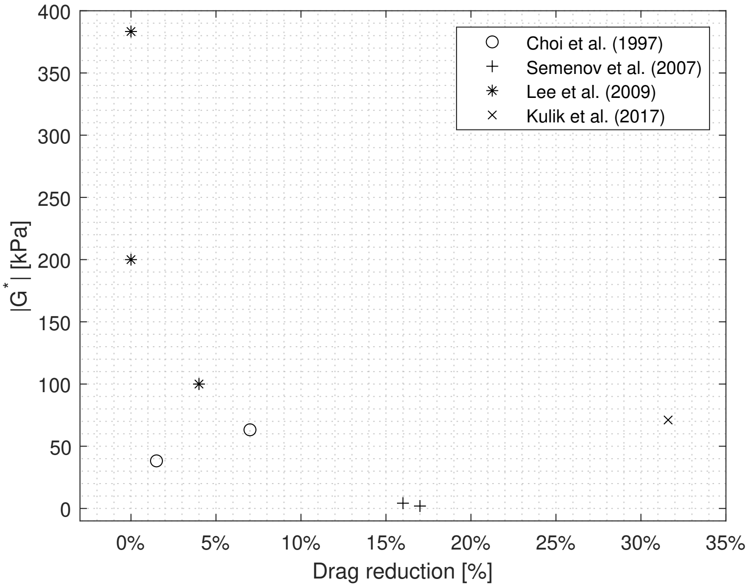

Figure 3.1. Resultant magnitude of complex shear modulus with outer scaling applied to drag reduction cases in Table 3.1

the normal deformation is seen to have a dramatic increase, coupled with increase of drag seen in Figure 2.21. This is seen as the onset of two-way coupling which provides a threshold for the inner scaling of the FSI, as it is assumed that two-set coupling is necessary for turbulent drag reduction.

The pressure fluctuation at the wall can be calculated by the empirical spectral model by Goody (2004), based on modelling experimental surface pressure spectra across a large range of Reynolds numbers. The mean-square pressure can be acquired by integrating the spectral power density of the pressure fluctuations across all frequencies:

$$\sigma_{ms} = \int_0^\infty \Phi(\omega)\mathrm{d}\omega \tag{3.6}$$

where σ_{rms} is simply equal to $\sqrt{\sigma_{\mathrm{ms}}}$. The spectral power density $\Phi(\omega)$ is defined as:

$$\Phi(\omega) = \frac{\tau_{\mathrm{w}}^2\delta_b}{u_\infty}\frac{3.0\,(\omega\delta_b/u_\infty)^2}{\left[(\omega\delta_b/u_\infty)^{0.75}+0.5\right]^{3.7}+\left[\left(1.1R_T^{-0.57}\right)(\omega\delta_b/u_\infty)\right]^7} \tag{3.7}$$

and the ratio of outer and inner timescales of the boundary layer R_T is:

$$R_T = 0.11\left(\frac{u_\infty\theta}{\nu}\right)^{0.75} \tag{3.8}$$

Based on this method, the pressure fluctuations in the M-Tunnel was calculated to be:

$$\sigma_{\mathrm{rms,M-Tunnel}} = 2.1740 \text{ Pa} \tag{3.9}$$

Table 3.2. M-Tunnel flow parameters used for the inner scaling (van Nesselrooij et al., 2016)

u_τ [m/s]	τ_w [Pa]	ν [m^2/s]	u_∞ [m/s]	δ_b [mm]	θ [mm]
0.6721	0.5421	$1.5*10^{-5}$	35	19	4.3

This calculation is based on the boundary layer parameters of a flow above a flat plate acquired by van Nesselrooij et al. (2016) at the M-tunnel, shown in Table 3.2. Applying Equation (3.9) to the ratio in Equation (3.5), a stiffness for the compliant surface is acquired for the onset of two-way coupling:

$$|G^*|_{\mathrm{M-Tunnel}} = 27.175 \text{ Pa} = 0.0027 \text{ kPa} \tag{3.10}$$

which expands the range from the outcome of the outer scaling in Equation (3.4) into:

$$0.01 < |G^*|[\mathrm{kPa}] < 100 \tag{3.11}$$

3.1.2. Surface material

With the parameter space defined in Equation (3.11), a survey of suitable viscoelastic materials was conducted. Only one material will be chosen for wind tunnel experimentation to reduce the complexity of handling the materials when manufacturing the compliant surface test plates. Figure 3.2 shows the stiffness range of several mainstream materials used in past literature (table 2.4) alongside the target stiffness range defined for this research.

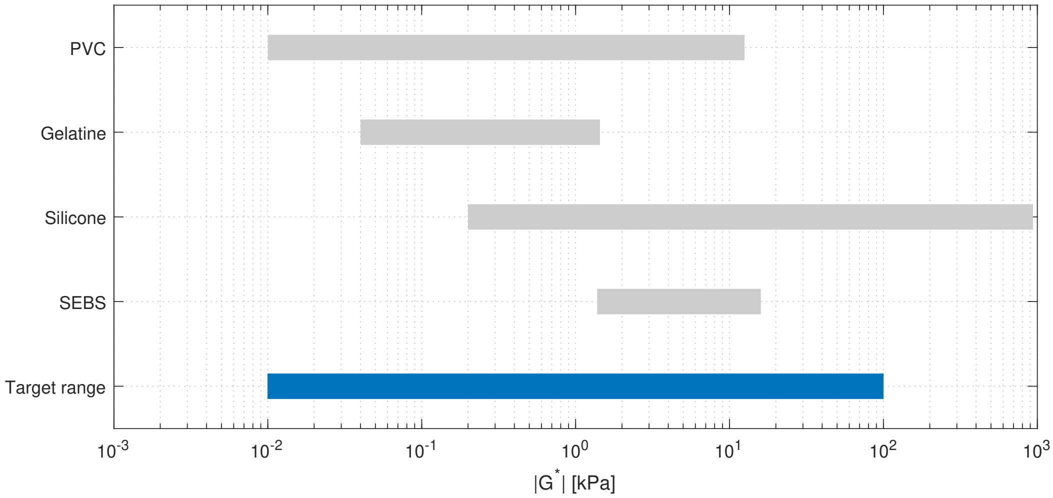

Figure 3.2. Stiffness range of materials from past literature with stiffness range for this research

Of these four groups, silicone presented the most suitable choice for this research. The rationale behind this decision involves the ease and safety of material handling and the manufacturing process. Also, the materials science aspect of the compliant surface is not the main focus of this research. While PVC gives a good overlap with the target range, the raw materials are highly carcinogenic with a complicated manufacture process. Gelatine is easily accessible and safe, but the pre-cured mixture is too viscous and not compatible with the manufacturing process and test plate design, which will be discussed in Section 3.3. SEBS has been mentioned by Greidanus (2020) to be resistant to ageing and falls well within the target range. However, the manufacturing process required materials science expertise and therefore regarded as too tedious.

PlatSil Gel OO, a two-component room-temperature-vulcanised (RTV) silicone from Polytek Development Corp. was chosen to make the compliant surface test plates. This was due to the ease of access and handling, and the capability of vulcanising (curing) under room temperature at a relatively short time. PlatSil Gel OO best fit the target stiffness range among several other RTV silcones that were also tested. Details of these other silicones are included in Appendix A. This was the conclusion of rheometer measurements and also based on the technical data sheet included in the Appendix B. The industry standard for the stiffness of silicones is given in Shore hardness instead of shear modulus. A conversion from various Shore hardness to the elastic modulus by Mix and Giacomin (2011) gives a range of elastic modulus for PlatSil Gel OO of $9.07 \leqslant |E^{*}|$ [kPa] $\leqslant 2163.8$, which gives a shear modulus range of $3.02 \leqslant |G^{*}|$ [kPa] $\leqslant 721.27$ assuming a Poisson ration of $\nu_{p} = 0.5$. The conversion plot is included in Appendix C.

PlatSil Gel OO comes off the shelf in A and B components, which are subsequently mixed in identical weight to trigger the curing process. Additives can be added to the main mixture (A and B) to modify the cured product's material properties. These additives include the deadener and hardener, which softens and stiffens the cured product, respectively. Retarder was also added to increase the working time before curing starts. This was necessary due to the large area of the test plate and minimal working time of the PlatSil mixture. The manufacture of the compliant surfaces will be discussed with more depth in Section 3.3.

3.2. Evaluation of viscoelastic properties: Rheometer

The evaluation of the viscoelastic properties of the PlatSil Gel OO is conducted by a rheometer. These properties, mainly the complex shear modulus and loss tangent, can be modified by adding deadener or hardener. It is aimed to acquire the spread and gradient of these properties with respect to the addition of deadener or hardener.

3.2.1. Rheometer

The Thermo Fisher Haake Mars III rheometer at the Delft Aerospace Structures and Materials Laboratory (DASML) was used for this research, shown in Figure 3.3. The rheometer applies a sinusoidal shear strain and measures the resultant shear stress; this is done throughout a range of frequencies thus acquiring the viscoelastic properties as a function of frequency. All of the rheometer measurements were conducted at a controlled indoor environment with a room temperature of approximately 23°C.

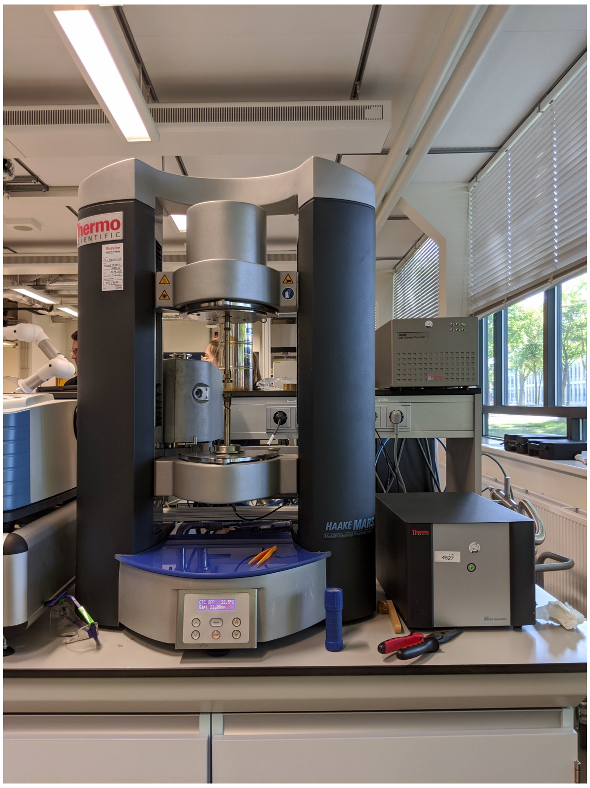

Figure 3.3. Thermo Fisher HAAKE MARS III rheometer

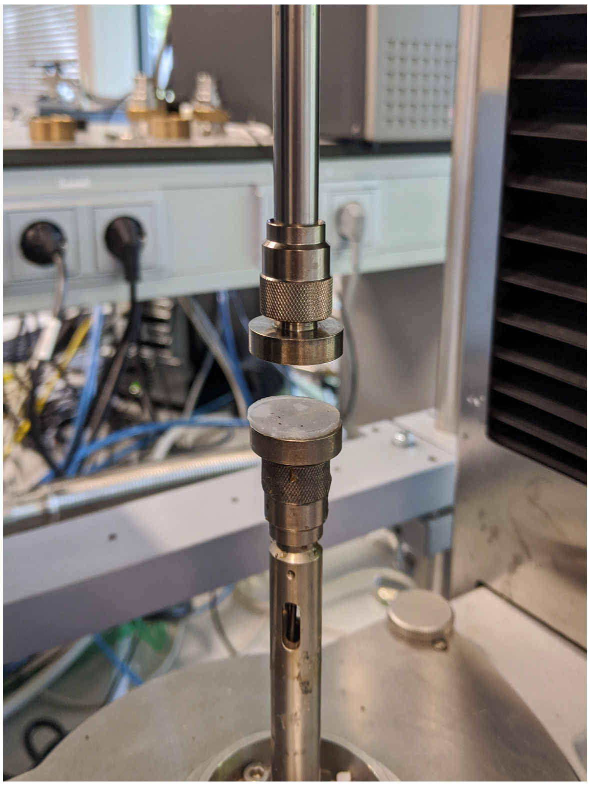

Figure 3.4. Rheometer parallel plate configuration for the sample

A parallel plate configuration is used for the rheometer measurements, where the rheometer sample is placed on the bottom plate, shown in Figure 3.4; the plate has a diameter of 20 mm. Rheometer samples were made by using a mixing cup as a mould that had a base diameter of ~ 13cm. For the compliant surface test plates, samples were made from the same mixture to test in the rheometer. After the silicone was cured in a flat patty shape, a rheometer sample was made using a hammer and circular punch shown in Figure 3.5.

Once the sample is placed within the parallel plates, the upper bar is lowered to clamp the sample in place by applying axial force; an axial force 0.1 N was applied for this research. The shear strain is applied from the upper bar connected to a servomotor and air bearing. Before the frequency sweep, an amplitude (shear strain) sweep must be conducted to determine a suitable amplitude for the frequency sweep within the material plastic range. A shear strain amplitude of 0.5 % was determined and applied for each sample. The range of measurement frequencies was defined as $0.1 \leqslant f\,[\text{Hz}] \leqslant 100$.

The post-processing of the rheometer data was done in a self-written MATLAB code. This code plotted the frequency-dependent viscoelastic properties and calculated the averaged properties with a specified cut-off frequency for every sample.

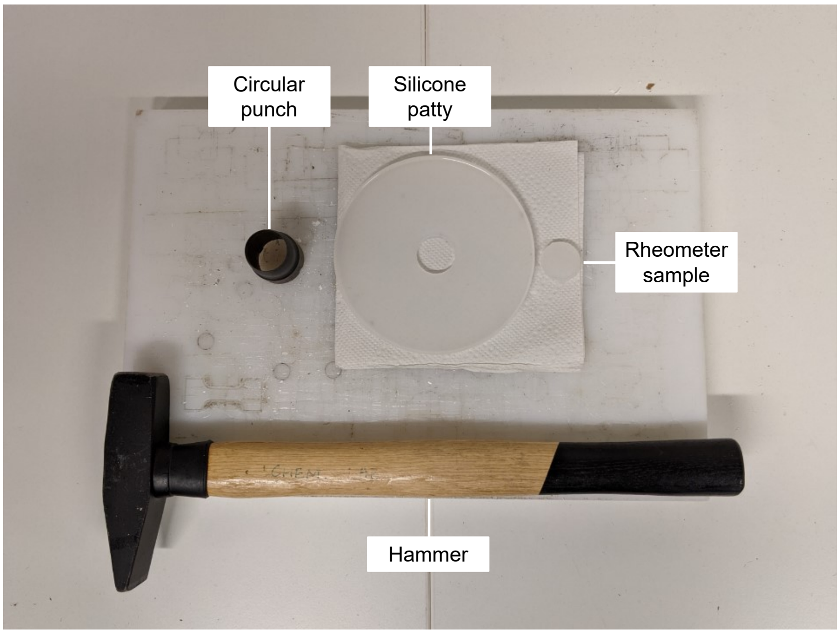

Figure 3.5. The hammer and circular punch used for punching the rheometer sample out of the patty

3.2.2. Spread and additive gradient of PlatSil Gel OO

Initial rheometer measurements of the PlatSil Gel OO mixture were conducted to map out its stiffness spread and gradient of additives; this is shown in Figure 3.6. D and H signify the deadener and hardener additive, respectively. This PlatSil mixture gives a good overlap with the prescribed target range according to the scaling. However, it was found that the lowest stiffness possible for the PlatSil was around the order of magnitude of $\mathcal{O}(|G^*|)\,[\text{kPa}] \sim 1$. Since the type of mixture material will be limited to the PlatSil Gel OO mixture, the stiffness range is modified in the target parameter space to become:

$$\begin{cases} 1 \leqslant \delta_s\ [\text{mm}] \leqslant 4 \\ 1 < |G^*|\ [\text{kPa}] < 100 \end{cases} \tag{3.12}$$

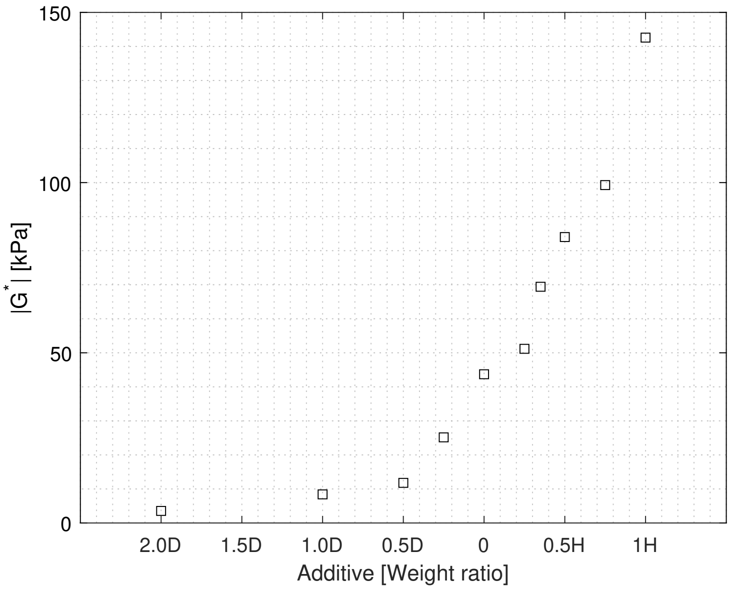

Figure 3.6. $|G^*|$ spread of PlatSil Gel OO mixture with additives

3.3. Compliant surface mould and test plate design

In this section, the design and manufacture of the compliant surface test plates are discussed.

3.3.1. Mould design

A mould assembly with a two-piece mould and an aluminium profile support structure were designed, shown in Figure 3.7 alongside with the schematic in Figure 3.8.

Figure 3.7. The compliant surface mould assembly

The two-piece mould consists of a laser-cut aluminium base and rim. The mould base has holes of d = 100 mm drilled for demoulding the compliant surface. The two-piece mould is then screwed to the t-slots of the aluminium profile support structure around the perimeter and two additional cross-beams evenly distributed in the streamwise direction (not visible in fig. 3.7 and 3.8). Screwing in the two-piece mould also mitigated the slight skewness each piece had. These profiles coming in direct contact with the mould were assembled on a perfectly level table to ensure levelness. The support structure has three feet profiles with adjustable rubber feet attached at the bottom for good levelling capabilities.

3.3.2. Test plate design

The compliant surface test plate design is shown in Figure 3.9. The geometric dimensions is largely driven by the allowed test plate size in the Hill, the drag and hot-wire measurement system to be used. The allowed test plate dimensions are 881.3 × 366.3 × 5 mm^3 (L×W×H), which are also the dimensions of the compliant surface test plate. The test plate is a two-layer structure with the compliant surface resting on a 1 mm aluminium base plate. This allowed easy test plate swapping in the measurement setup and prevents internal stress build-up within the compliant surface. It also ensured the longevity of preserving the compliant surface since it minimises the possibility of coming in contact with foreign objects. This thus defines the thickness range of the compliant surfaces mentioned in Equation (3.12). Space for 4 corner pieces were cut out from the compliant surface to fit the corner pieces, shown in Figure 3.9b. They acted as a fixing mechanism of the

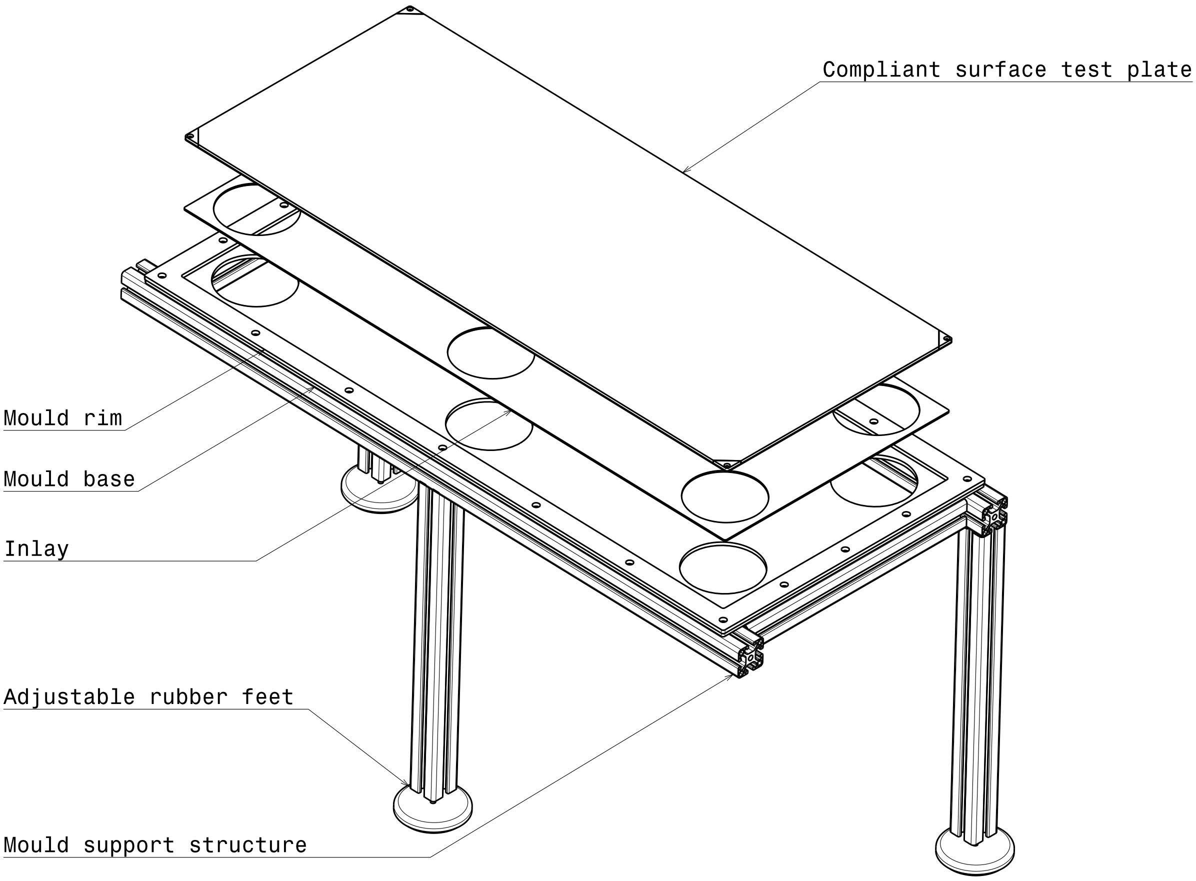

Figure 3.8. Design schematic of the compliant surface mould assembly

test plate to prevent its detachment from the experimental setup.

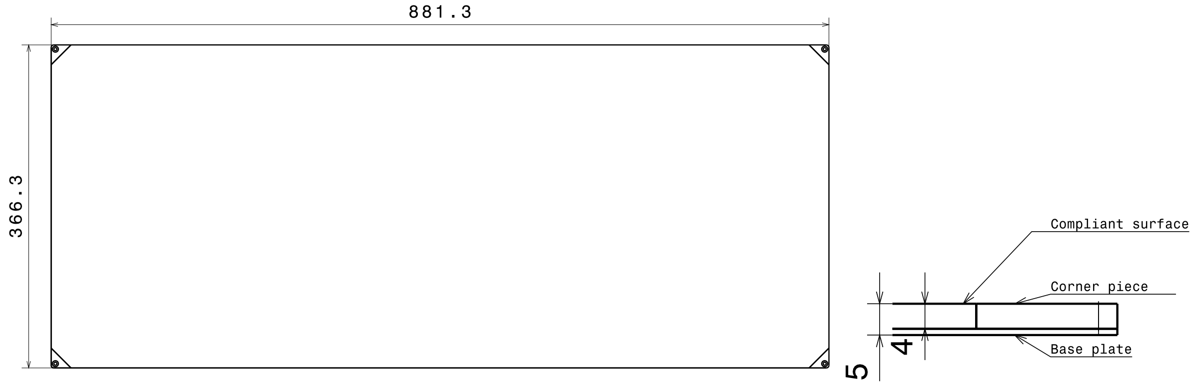

(a) Top view with dimensions

(b) Side view of a 4 mm compliant surface test plate corner

Figure 3.9. Design schematic of the compliant surface test plate. Dimensions all in mm

3.3.3. Manufacture process

The manufacture of the compliant surface test plates can be divided into 5 steps, which are briefly introduced here. A detailed overview of every step in the manufacture process is included in Appendix D.1.

1. **Priming the mould**
   The mould cavity is wiped clean by cloth applied with some ethanol. A Vaseline release agent is applied

to the mould for easier demoulding. Then the base plate where the compliant surface rests on is placed within the cavity. For thinner surfaces, an extra inlay is placed to adjust the thickness.

2. **Mixing**
   The PlatSil Gel OO mixture is mixed together according to the formula for the specific thickness and stiffness of the compliant surface to be made. All the additives are mixed with component A before adding component B, which triggers the start of the curing process. The mixture is thoroughly degassed to ensure no air packets form within the compliant surface when cured.

3. **Pouring**
   The mixture is poured within the mould cavity. The mixture is very viscous and does not spread quick enough within the pouring time. Therefore, pouring evenly across the cavity is necessary to ensure the flatness of the cured compliant surface. The mixture is manually spread out with a mixing stick if necessary. While the mould has been levelled, overflow might still occur due to uneven pouring or local gradients. This requires constant wiping of overflowing edges to ensure good edge finish.

4. **Demoulding**
   Each compliant surface takes approximately 8 hours to cure. When cured, the compliant surface is demoulded by pushing through the holes in the mould base. While the rim has been tightened as much as possible to the base, seeping might still occur in between which makes demoulding slightly harder, since the seeping silicone has also cured. After the compliant surface has been demoulded, plastic foil is applied on top for preservation and ensures that it is quarantined from foreign objects.

5. **Post-processing**
   The compliant surface adheres to the aluminium base plate quite well when cured. This being said, further enhancements were made to ensure that the compliant surface stays in place. Silicone glue was applied around the perimeter for better adherence of the compliant surface to the base plate. Corners of the compliant surface was cut off to place 3D-printed corner pieces for screwing in the test plate to the measurement setup. Spacers were applied at the bottom of the test plate near the edges to compensate for steps due to the surface finish of the test plate. Figure 3.10, 3.11, and 3.12 shows the compliant surface edge finish, the corner piece in place, and a cured compliant surface, respectively.

Figure 3.10. Compliant surface test plate edge

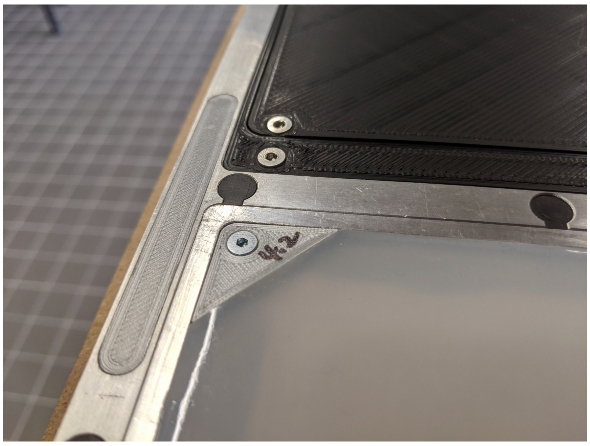

Figure 3.11. Compliant surface test plate corner piece

Figure 3.12. A cured compliant surface test plate

3.4. Wind tunnel

The M-tunnel at the Low-speed Wind Tunnel Laboratory (LSL) of the Delft University of Technology was used for the wind tunnel experiments, shown in Figure 3.13. The tunnel can be used in a closed or open-loop configuration, which the latter was used for this research. Although the closed-loop configuration can be run with flow speeds up to 50 m/s, which gives a more extensive velocity range, the flow temperature heats up rapidly under such configuration. With the closed-loop configuration, flow speeds up to 35 m/s can be reached. The wind tunnel turbine has a maximum operating RPM of 2,900. A LabView program controls the wind tunnel; it is integrated with the Hill control program during drag and hot-wire measurements, whereas it is controlled in a separate program from the PIV control program.

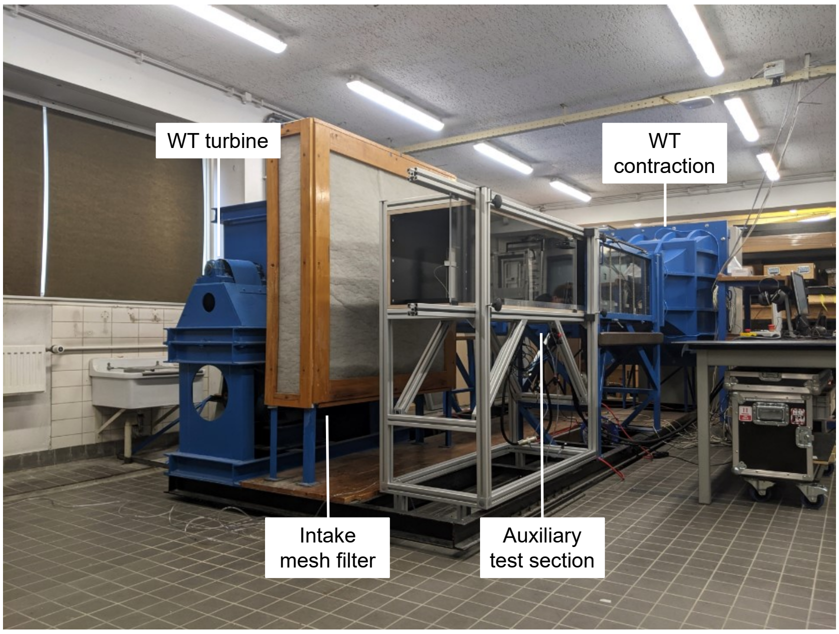

Figure 3.13. The M-Tunnel at the Low Speed Wind Tunnel Laboratory of Delft University of Technology

An auxiliary test section was built and attached downstream of the original test section of the M-tunnel. This ensured ease of access to the measurement apparatus and changing the test plates, which was much more flexible than the M-Tunnel's original test section. Different test sections shown in Figure 3.14 were used for the drag measurements and the flow visualisation. There was no particular reason behind using two different test sections, except that the Medium-Density Fibreboard (MDF) test section was a transitional setup before the aluminium profile test section was assembled. The verification of these two test sections using the Hill's drag measurements is discussed later in Section 4.2.1. Both test sections have a cross-section of $400 \times 400\ \mathrm{mm}^2$ (W × H) when empty, $400 \times 370\ \mathrm{mm}^2$ (W × H) with the Hill or PHill placed (after the top ramp of the MDF test section).

The MDF test section was used throughout the majority of measurements by the Hill system. It consists of MDF panels resting on the M-Tunnel's support structure downstream of the original test section. The front panel of the test section can be opened with hinges attached to the top panel. A 3D-printed transitional ramp was placed at the top leading edge of the test section to eliminate the step that was present. This step was due to the design of this test section, which was originally for the W-Tunnel at the High Speed Laboratory (HSL) of Delft university of Technology.

The aluminium profile test section was used for part of the Hill measurements and all PIV measurements. It consists of an aluminium profile beam structure with computer numerical control (CNC)-milled wooden betonplex plates forming the test section. A Plexiglas door was used as the front panel, which can slide downstream for access to the test section; the Plexiglas also allows for optical access to the test section when conducting PIV measurements. The door is fixed in place with four hand-tight screws at the corners.

Figure 3.15 is a schematic illustrating the overall setup of the wind tunnel measurements, and the coordinate system defined for this research. The x,y, and z coordinates represent the streamwise, wall-normal, and spanwise direction, respectively. The zero location of the streamwise, wall-normal, and spanwise coordinates is defined at the leading edge, the surface, and the mid-span of the test plate, respectively.

(a) MDF auxiliary test section used for drag measurements

(b) Aluminium profile assembly auxiliary test section used for flow visualisation

Figure 3.14. Wind tunnel auxiliary test sections used in this research

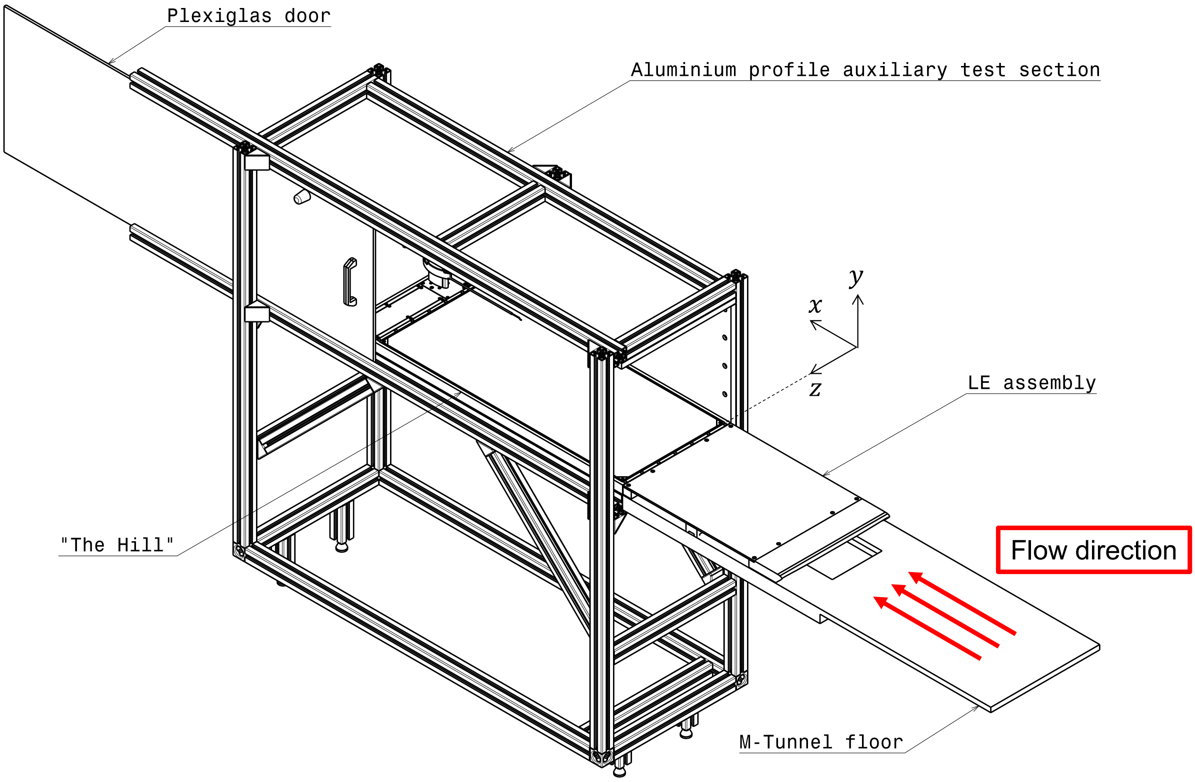

Figure 3.15. Schematic of M-Tunnel setup with the aluminium profile auxiliary test section and coordinate system used in this research

3.5. Drag delta and hot-wire measurements: The Hill

Drag delta and hot-wire measurements were performed with the dedicated flat plate drag measurement system 'The Hill' provided by Dimple Aerospace BV, shown in Figure 3.16. The patent-pending system employs calibrated direct force measurements for velocities up to Mach 1 that are corrected for the (minimised) pressure forces acting on the streamwise-facing surfaces of the suspended part of the system. The measurement repeatability is within 0.5%. The Hill also incorporates a hot-wire capable of conducting a boundary layer profile scan.

(a) Overview with the reference plate fitted in

(b) With a compliant surface test plate fitted in

Figure 3.16. The Hill drag delta and hot-wire measurement system

An overview schematic of the Hill with is shown in Figure 3.17 with a detailed view of the components in Figure 3.18. The Hill mainly consists of 4 groups: the base which houses the electronics including the force sensor, the Periscope near the trailing edge that is mounted with a hot-wire and pitot-static tube, the connector tray that is the interface between the test plate and the force sensor, and the control box that houses the control system of the Hill and a compact data acquisition (cDAQ) system from National Instruments. A LabView program on a computer controls the Hill and the data acquisition. The drag and hot-wire measurements are fully automated based on several user-specified acquisition parameters. An overview of the entire system's data acquisition channels is shown in Table 3.3. Data acquisition channels and sensors at the wind-tunnel side (the Periscope and the base) are connected to the control box, then connected to the computer.

Table 3.3. Data acquisition channels of the Hill system

Group	Data
Base	Test plate perimeter pressures Drag force
Periscope	Total pressure Static pressure Wind tunnel temperature Humidity Hot-wire probe voltage
Control box	Ambient temperature Ambient pressure

The Hill's base has dimensions of $1,020 \times 395 \times 5\ \text{mm}^3$ (L×W×H) which fits within the auxiliary test sections. Tapered extensions can be fitted for tests at larger wind tunnels forming a thin hill on the floor, hence the namesake. The Hill is made to take up as less space as possible when mounted inside a test section, minimising the setup's disturbance to the flow. With a height of 30 mm, excluding the Periscope, the Hill is relatively compact and flexible compared to typical measurement systems that need to be mounted to the ground. This flexibility makes for faster development of new test plate designs.

The connector tray is made with an aluminium frame with a carbon fibre base to minimise deformation under the test plate's weight. It is mounted into the cavity of the base and suspended by 0.3 mm titanium

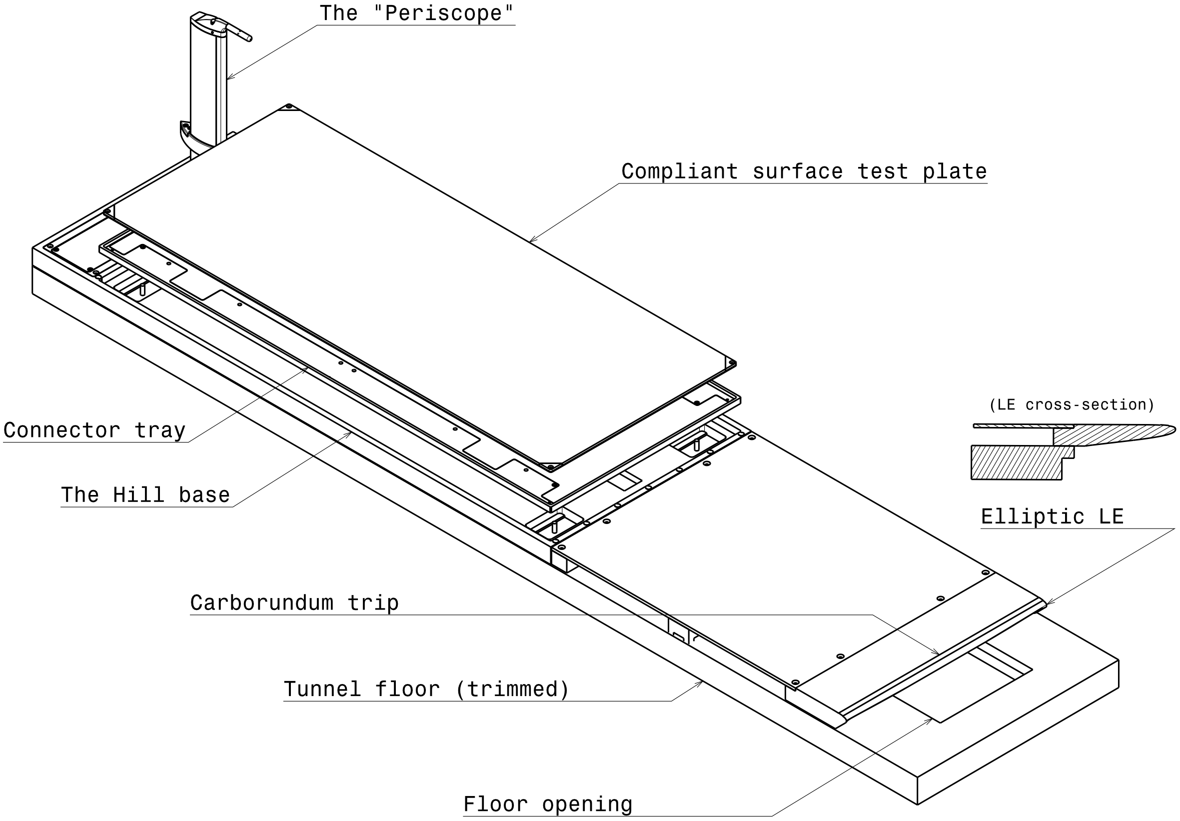

Figure 3.17. Overall schematic of the Hill system with a cross-section view of the elliptic leading edge

flexures placed in the four corners of the base. The test plate is placed in the connector tray for measurements, allowing for a test plate size of $881.3 \times 366.3 \times 5$ mm^3 (L×W×H). These are also the dimensions for the compliant surface test plates investigated in this research. While it was possible to configure the Hill to be compatible with thicker test plates, this was not possible for this thesis' monetary scope and time-planning. Three miniature air pistons in the base can be pneumatically activated to lift the test plate out of the connector tray; holes are made in the connector tray to allow these pistons to penetrate through and push out the test plate. Sorbothane feet are installed at the bottom of the base to damp out the vibrations of the wind tunnel turbine and the test section.

In front of the Hill, a leading edge assembly with a carborundum trip was placed to start a new turbulent boundary layer. The assembly has an elliptic leading edge that divides the incoming upstream flow into two. The bottom portion, which is the boundary layer coming from the upstream, is deflected and ejected from an opening in the wind tunnel floor. The undisturbed mean flow in the upper portion is then tripped by the carborundum strip and starts a new turbulent boundary layer. This was to ensure that the boundary layer was turbulent above the test plate and acquire a clear indication of the turbulent boundary layer's origin.

3.5.1. Drag force measurements

Drag is measured with a force sensor placed in the centre of the base and aligned in the streamwise direction. A sweep of 10 velocities from low to high was conducted with zero measurements before and after the 10 points. This whole process was automated with user-defined inputs shown in Table 3.4. The force sensor is a KD40s S-type force sensor by ME-Meßsysteme GmbH, which can measure forces up to 2 N with an accuracy of 0.1%. When the force sensor is active, the sensor pin rests on the connector tray holding the test plate, thus measuring the test plate's accrued drag. The cavity is slightly larger than the connector tray to allow the forcing of the force sensor pin. The connector tray would oscillate on the titanium flexures if the test plate is appropriately mounted.

Two corrections are applied to the measured force from the force sensor; a typical composition of the raw and corrected drag is shown in Figure 3.19. The raw force is first corrected by the null-force shift, which accounts overshoot of force measured due to the internal stress buildup within the force sensor. This correction

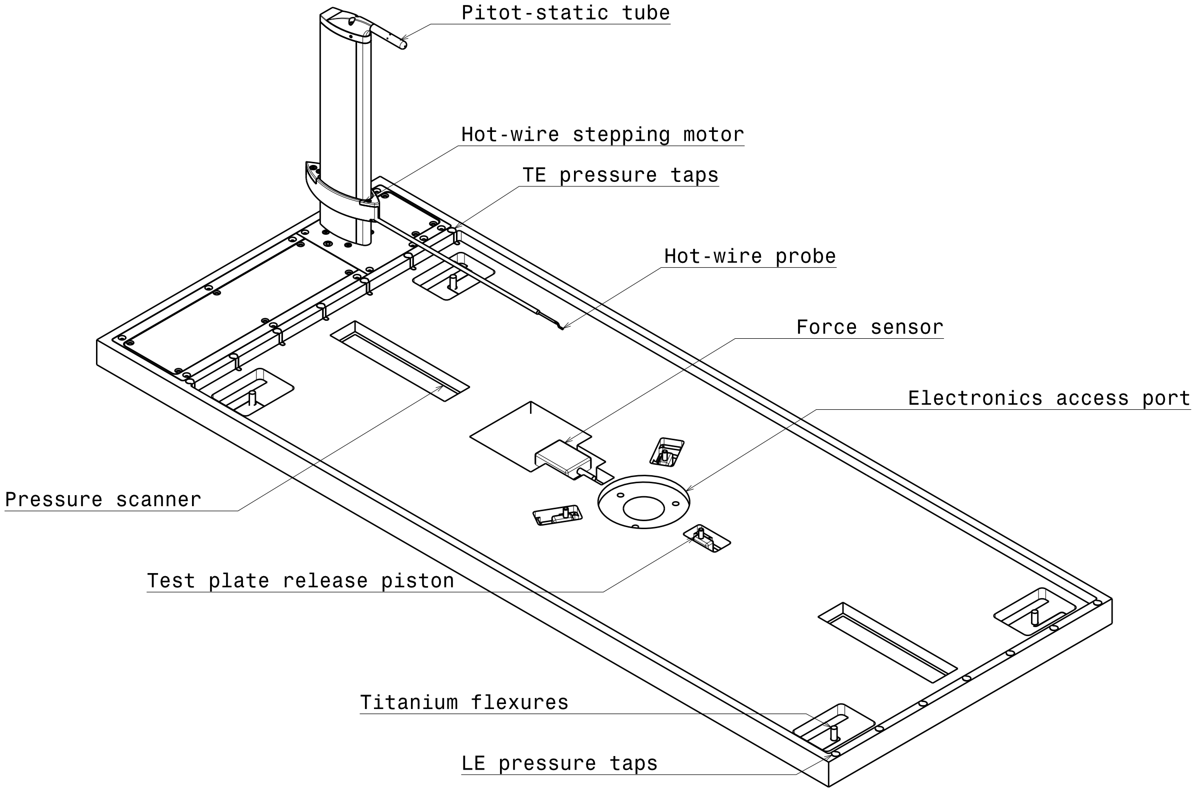

Figure 3.18. Detailed schematic of the Hill system

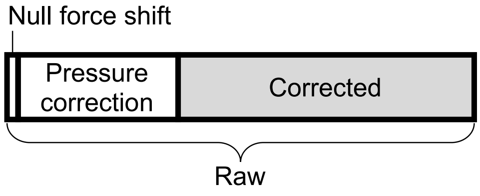

Figure 3.19. Schematic illustrating the decomposition of the total drag and corrections

is linearly interpolated to each velocity point from the zero-force measurements before and after the velocity sweep. The null-force corrected drag is defined as the raw drag force that is measured. This raw force is then corrected with the streamwise pressure drag calculated from pressure taps lined in the base adjacent to the leading and trailing edge of the connector tray. There are 7 and 8 pressure taps lined at the leading and trailing edge, respectively. At the leading edge, the pressure taps are evenly distributed at a depth of 5 mm from the test plate's surface. At the trailing edge, the pressure taps are placed at identical locations as the leading edge, with the exception of the mid-span location with two pressure taps placed at depths of 2.5 and 7.5 mm. The measured pressure is integrated throughout streamwise-facing surfaces at the leading and trailing edge to acquire the streamwise pressure drag. The pressure taps are connected to a custom printed circuit board (PCB) that incorporate Honeywell RSC pressure sensors with a measurement range of ±250 Pa.

The drag reduction of a test plate is calculated with respect to the drag of a reference test plate. Therefore, the measurement plan consists of 'sandwiches' of the compliant surface and reference test plate illustrated in Figure 3.20. A sandwich consists of compliant surface test plates measured in-between reference test plate measurements. The drag reduction of the compliant surfaces is calculated with respect to the neighbouring reference measurements' average drag curve. For this research, three measurement sandwiches are done per compliant surface batch to validate the repeatability of the measurements. As part of the output, the RMSE spread of the drag reduction for each compliant surface is calculated. For this research, three surfaces formed a triple sandwich to accommodate the large number of compliant surface configurations within schedule. This measurement plan was validated in previous experiments and therefore assumed to be the same for this research. Once all the compliant surfaces were measured, surfaces that demonstrated interesting results were

Table 3.4. The Hill drag measurement setup parameters

Measurement break [s]	20
Measurement duration [s]	10
Force sensor acquisition frequency [kHz]	25
Pressure scanner acquisition frequency [Hz]	28
Creep recovery period [min]	5
Number of measurements [-]	10
Lowest operating point [%]	25
Highest operating point [%]	100

remeasured as a single sandwich for better fidelity.

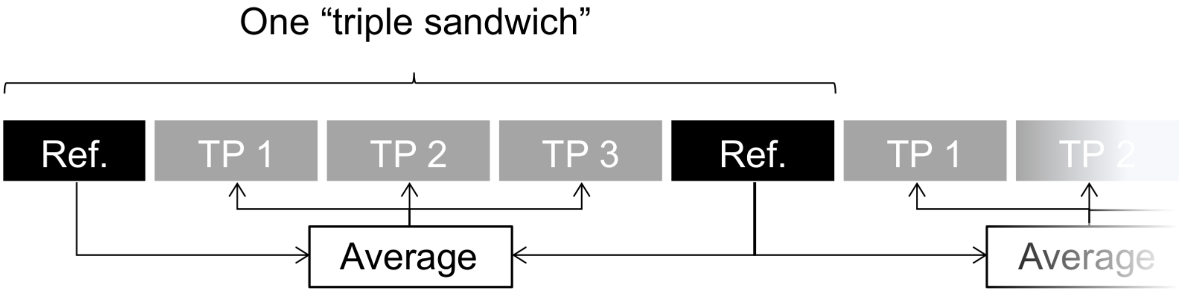

Figure 3.20. Schematic illustrating the ‘sandwiched’ measurement plan for the drag measurements

3.5.2. Hot-wire anemometry (HWA) and Periscope

The hot-wire is placed on the "Periscope" with a height of approximately 250 mm. The spanwise location of the Periscope was offset due to the wiring of the hot-wire probe. The hot-wire probe is a Dantec Dynamics 55P15 constant temperature anemometer (CTA) placed on a lead screw traversed along the height of the Periscope by a stepping motor housed below the Periscope. The stepping motor is capable of traversing the hot-wire with a minimum traverse accuracy of 5 μm. The hot wire axial direction is aligned in the spanwise direction. The zero location (at the wall) of the hot-wire probe is determined by the naked eye by traversing the probe close to the wall. On top of the Periscope is a pitot-static tube connected to a Honeywell RSC pressure sensor with a measurement range of $\pm 1,250$ Pa. This data channel is also used as a reference port for all the other pressure sensors in the Hill. The pitot-static tube is printed by the FormLabs Form 3 stereolithography (SLA) 3D printer.

The hot-wire measurement is automated within the LabView program based on several user-defined inputs shown in Table 3.5. It first does a velocity sweep placed in the mean flow to acquire the hot-wire calibration curve, where 25 calibration points were used. The hot-wire boundary layer sweep is divided into three stages: 25 evenly spaced measurement points on the top 50% of the boundary layer, 25 points for 50 ~ 75%, and 50 points for the lower 25%; this is illustrated in Figure 3.21. A measurement time of 5 s is done for each measurement point. The wind tunnel is operated at 95% capacity to prevent the test section and wind tunnel motor from overheating due to the longer measurement times.

Table 3.5. The Hill HWA measurement setup parameters

Traversing height [mm]	40
Acquisition frequency [kHz]	10
Measurement time [s]	5
Tunnel operation point [%]	95

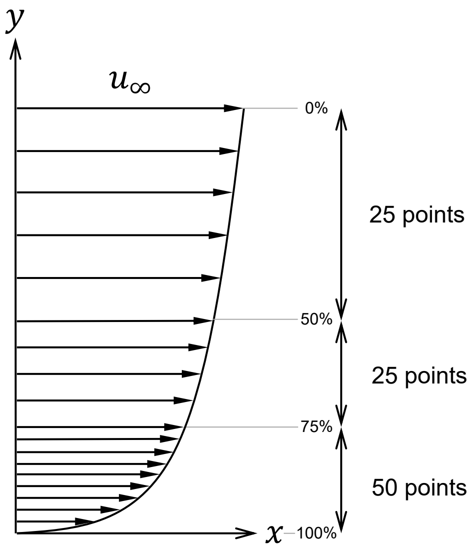

Figure 3.21. Distribution of hot-wire boundary layer sweep measurement points

3.5.3. Post-processing

Post-processing of the drag delta and hot-wire data is conducted in MATLAB. For the drag measurements, the null-shift and the pressure drag correction are applied. The Reynolds number is calculated from the pitot-static tube pressures and the local humidity and temperature. The RMSE spread of the drag is calculated from the repeatability measurement sandwiches.

For the hot-wire measurement, a calibration curve is computed using a 4th order polynomial fit based on convection theory. The hot-wire voltage is corrected with respect to the local temperature (Bruun, 1996). Then, the hot-wire voltage from the boundary layer sweep is translated into velocity. The velocity is then decomposed to the mean $\overline{u}$ and perturbation u' component to the acquire the velocity and turbulence intensity profile, respectively. The mean boundary layer properties are then extracted through a characterisation scheme by Rodríguez-López et al. (2015) implemented with a differential evolution (DE) algorithm. This characterisation scheme aims to extract the mean shear stress at the wall and find the hot-wire's accurate relative position to the wall, with the zero location previously set according to the naked eye. The DE algorithm improves the characterisation by iteratively trying out new candidates with respect to a given population. The lowest data point's wall-normal position is set to zero, then shifted upwards with the determined wall location from the characterisation. With the extracted mean boundary layer properties and the wall location, a curve fit of the non-dimensionalised velocity profile is acquired.

3.6. Flow visualisation: Particle image velocimetry (PIV)

Planar (2D-2C) particle image velocimetry (PIV) is conducted to visualise the flow above a drag-reducing compliant surface, and comparing it with flow above a reference flat plate and a drag-increasing compliant surface. The setup is shown in Figure 3.22. The control of the experiments and the post-processing of the data both utilise DaVis 10 of LaVision GmbH.

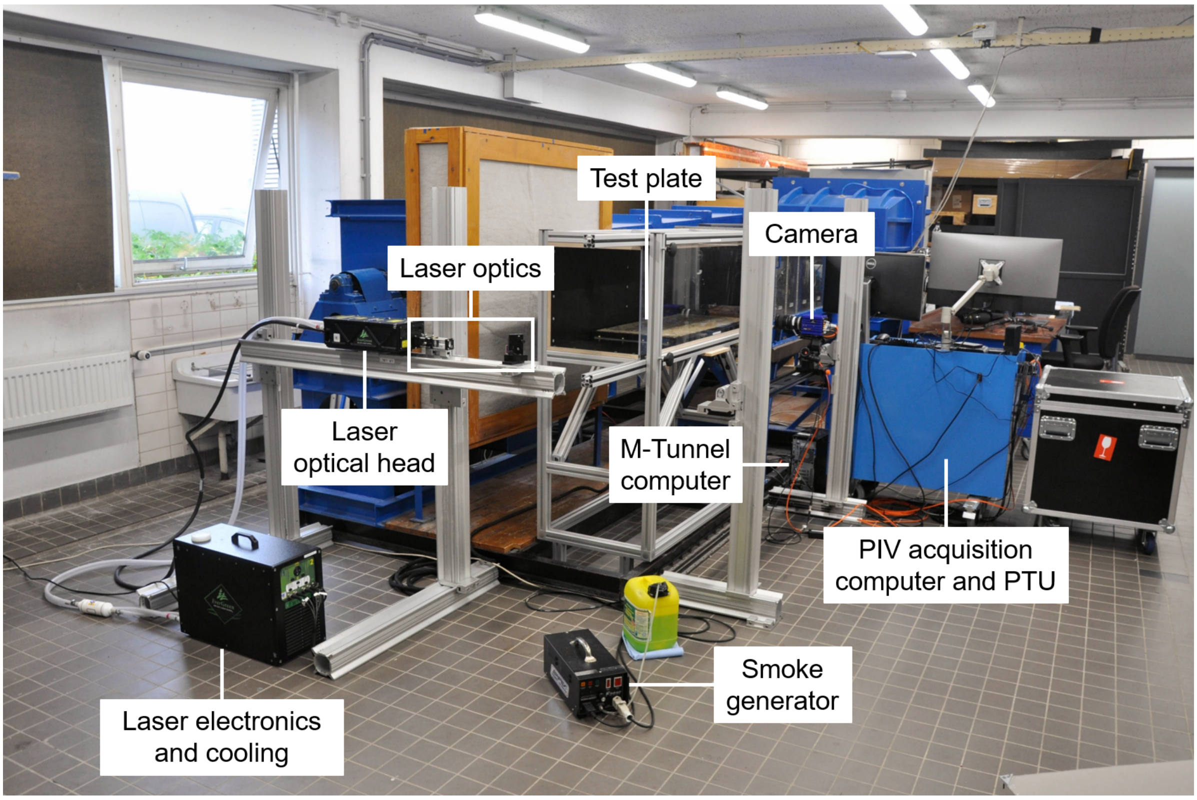

Figure 3.22. Setup for PIV experiment

3.6.1. Hardware

The PHill

A test plate mount is designed to replicate the placement of the Hill system. Named the PHill (PIV Hill), it is a three-piece construction printed by the Creality CR-10 Max 3D printer using black polylactide (PLA) filament. The assembly schematic is shown in Figure 3.23. The three pieces are joined together by nuts and screws placed inside the printed cavities. Cross-beams are printed to increase structural integrity and support for the test plate. A wooden inlay is placed first into the cavity before placing the test plate; the inlay doubles as a structural element for the PHill and support for the test plate. Thread inserts are placed in the four corners and two mid-streamwise points for fixing the inlay and test plate. The test plates are also fixed with the same corner pieces used in the drag measurements. The thickness of the PHill is identical to the Hill, and therefore could be directly integrated with the leading edge assembly used in the drag measurements. Two strips of 0.2 mm spacers were placed on the leading edge surface of the PHill to eliminate steps caused by the shrinkage of the PLA.

Camera

A single Imager sCMOS CLHS camera from LaVision GmbH is used for this research. The camera has a pixel size of 6.5 μm with a sensor size of 2560×2160 px^2, with the longer side of the sensor aligned in the streamwise direction. The camera is set to double frame mode with an exposure time of 15 μs. The camera is screwed to a 3-axis mount placed on an X-beam structure allowing for traversing to different streamwise positions, shown in Figure 3.24a. The traversing beam is mounted at a height where reflections from the compliant surface are at a minimum. This meant adjusting the camera lens height to be completely level

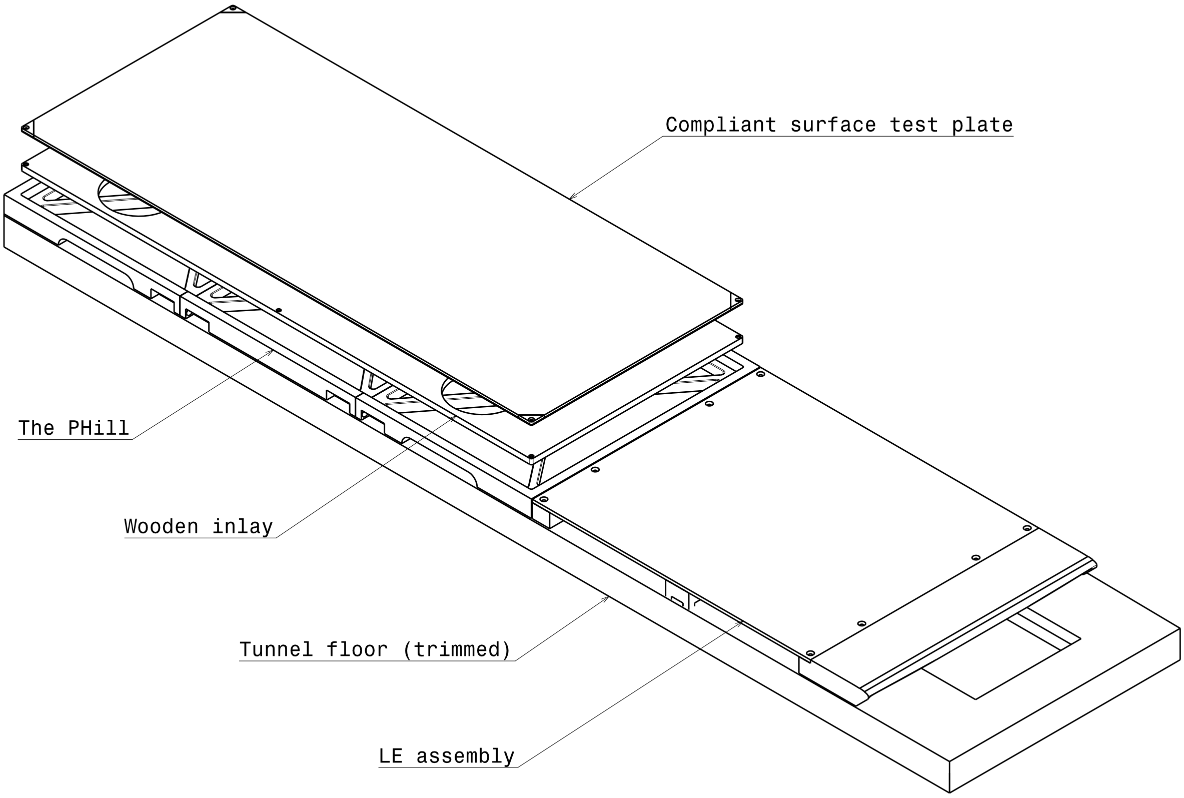

Figure 3.23. Schematic of the PHill with the leading edge assembly and wind tunnel floor

with the surface, leading to the camera sensor not fully employed to the capture flow field in the wall-normal direction. Nevertheless, previous hot-wire measurements by the Hill has indicated that the field of view (FOV) due to the camera placement is sufficient to encompass the boundary layer.

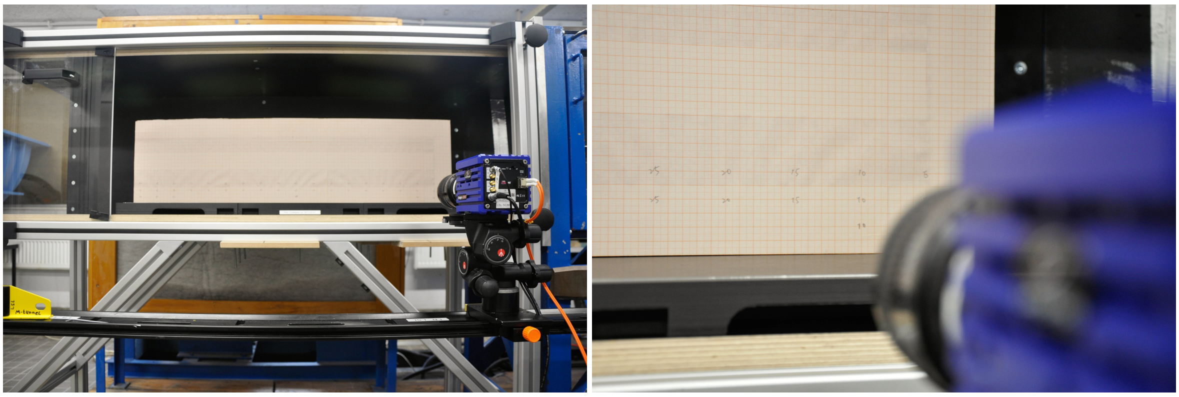
(a) Camera streamwise traversing setup **(b)** Camera and millimetric paper calibration plate

Figure 3.24. Planar PIV camera setup and calibration

The camera is calibrated by placing a millimetric paper calibration board at the mid-span streamwise plane, shown in Figure 3.24b. The camera is refocused to the calibration plate every time the location of the camera is changed. The f# is set to the lowest value of 2.8 for a small depth-of-field when focusing the lens. Once in focus, a calibration photo is taken, and the magnification factor (M) is calculated. With the M acquired, the f# for the optimal particle image size of 3 px is calculated and adjusted on the lens accordingly.

Two camera lenses with different focal lengths were used: the Micro-Nikkor f/2.8 60 mm and 105 mm. The FOV of each lens is shown in Figure 3.25. The 60 mm lens is used to capture a panoramic view of the flow across the test plate's entire streamwise length, consisting of several FOVs. For the 105 mm lens, it is aimed to zoom into the boundary layer. The FOV of the 105 mm is roughly over a quarter of the 60 mm lens FOV, both shown in Figure 3.25. An overview of the PIV configuration for these two acquisition categories are shown in Table 3.6 and 3.7.

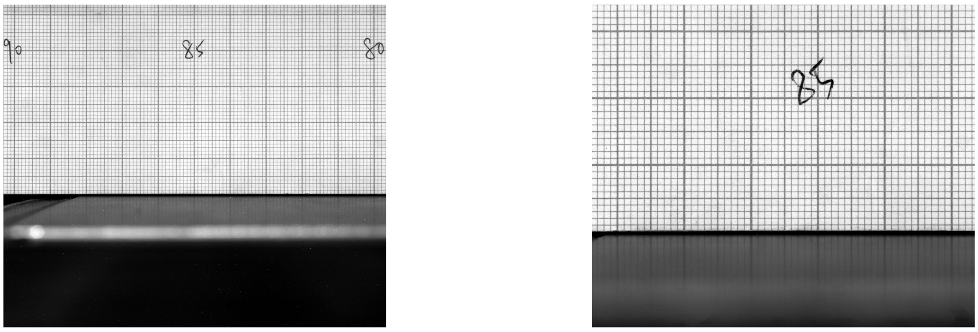

(a) f = 60 mm **(b)** f = 105 mm

Figure 3.25. PIV FOVs for the f=60 and f=105 mm lens

Table 3.6. PIV Camera configuration for panorama and zoomed-in setup

	Lens f [mm]	**FOV** [cm^2]	**M** [-]	**px/mm**	**f#** [-]
Panorama	60	11 × 5.5	0.15	23.3	11
Zoomed-in	105	5.8 × 3.4	0.29	44.4	11

Table 3.7. PIV laser separation time $\Delta t [\mu s]$ and wind tunnel RPM for each flow velocity and PIV configuration

WT RPM	925	1,795	2,900
u_∞ [m/s]	**10**	**20**	**35**
Panorama	55	27	16
Zoomed-in	26	14	8

Laser sheet formation

The Evergreen 200 by Quantel Laser is used to illuminate the tracer particles. It is a double-pulsed ND:Yag laser with a wavelength of 532 nm, triggered at a maximum rate of 15 Hz. Each pulse has a width of 7 ns at an energy of 180 mJ. The laser is set to full power for both oscillators on the control panel of the laser electronics and cooling box. In DaVis, the laser pulse intensity is both set to 50%. The laser beam is shaped into a sheet with a series of cylindrical and spherical lenses, then reflected by a mirror and shot into the test section from downstream. Figure 3.26a gives an overview of the laser sheet formation. The placement of the laser optic lenses is shown in Figure 3.26b. The resultant laser sheet is shown in Figure 3.26c. The laser sheet is aligned with mid-span markers on the PHill. A consistent laser sheet thickness of 3 mm was generated throughout the test plate, measured by a spanwise millimetric paper calibration board similar to the one in Figure 3.24b. The timing and triggering of the laser and camera are coordinated by a programmable timing unit (PTU) from LaVision GmbH.

Tracer particles

The tracer particles are generated by the SAFEX Fog 2010+ smoke generator. The tracer particles have a mean diameter of approximately 1 μm. The smoke generator is placed on the floor with a feed tube connected to a smoke fluid canister. The entire tunnel hall is smoked with tracer particles when conducting experiments, thus being sucked into the wind tunnel by the wind tunnel turbine. The Stokes number of the particles is below 1, indicating good tracing capabilities.

Flow properties

The Tempest module equipped in the M-Tunnel is also used to acquire flow characteristics in addition to the PIV setup. This data is used as an extra reference to accompany the PIV data, as it also measures the flow speed and the temperature.

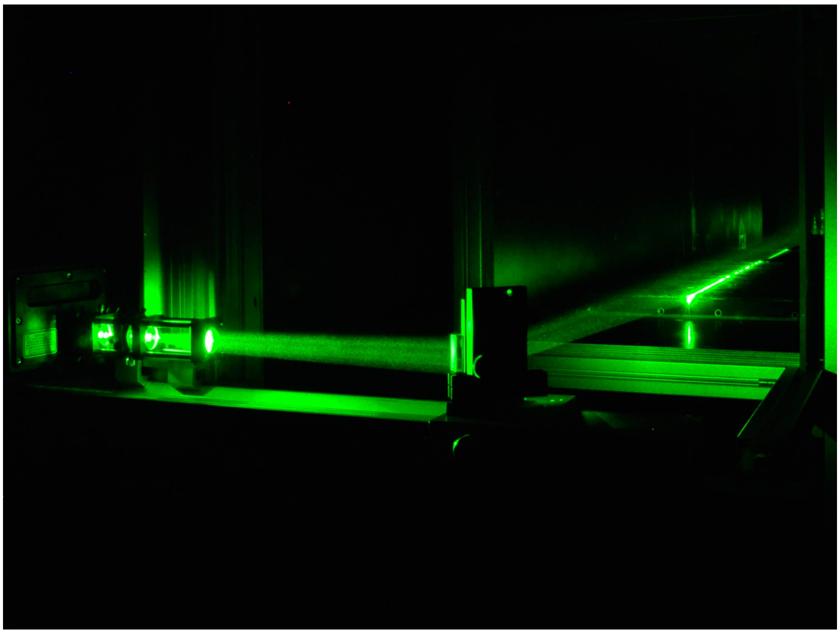

(a) Overview

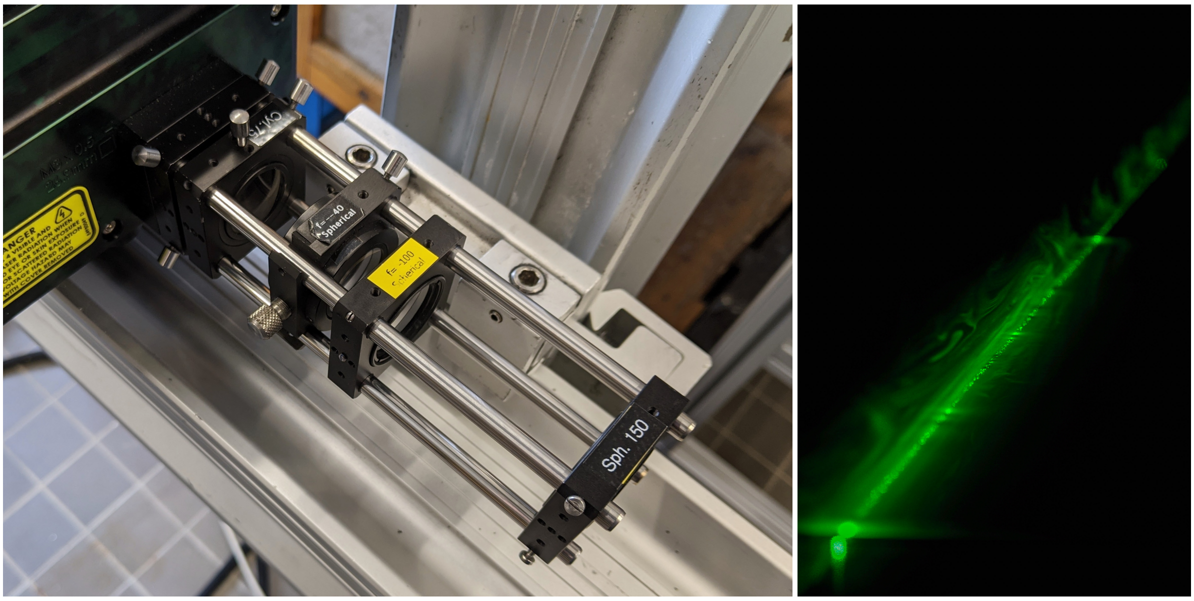

(b) Optical lens setup **(c)** Laser sheet above the test plate

Figure 3.26. Planar PIV Laser sheet formation

3.6.2. Data processing

Data processing of the raw flow field images are done in DaVis 10. The images are pre-processed before conducting the cross-correlation analysis. The result of this analysis is the 2D vector field of the FOV from which the scalar values can be further extracted. These scalar values are further analysed in MATLAB.

1. **Calibration** The images are scaled to the physical location and length of the FOV. This is done by using calibration pictures (fig. 3.24b) of the millimetric calibration board taken prior to the measurement after moving and refocusing the camera. Each FOV is calibrated individually to account for local discrepancies in the setup.

2. **Apply mask** The bottom portion of the FOV is masked out since it is not the flow. Masking this region out eliminates the errors in cross-correlation at interrogation windows near the wall. It also lightens the load on the computer, as less interrogation windows need to be cross-correlated.

3. **Subtract minimum intensity** The minimum intensity of each data set is subtracted for every image pair of that data set. This is to reduce the background noise of the images.

4. **Append data sets** The two of the pre-processed data sets with 300 image pairs are appended together to form the 600 image pairs to conduct cross-correlation analysis.

5. **Cross-correlation** With the pre-processed data prepared, cross-correlation analysis is conducted. An initial pass with an interrogation window size of 256×256 px^2 and overlap of 50% is done, then with 4 final passes with an interrogation window 16×16 and overlap of 75%.

6. **Vector post-processing** The mean boundary layer profile is taken from 600 image pairs for each FOV. Vector outliers outside three times the standard deviation from the mean are removed. The output data from the vector post-processing is then analysed using MATLAB, which will be further discussed in Chapter 5.

3.7. Compliant surface test matrix and wind tunnel measurement plan

This section presents the compliant surface test matrix and measurement plans for the wind tunnel measurements. The test matrix consists of 11 compliant surface test plates; the measurement results of these compliant surfaces are compared to a reference flat plate TP0000, a 5 mm thick aluminium plate with a matte car foil applied on top. Two measurement campaigns were conducted: first, the drag delta and hot-wire measurements by the Hill, and second, the flow visualisation by PIV.

3.7.1. Compliant surface test matrix

With the spread and gradient acquired from the rheometer measurements in Section 3.2.2, the compliant surface test matrix for the wind tunnel measurements can be defined. The defined "M-shaped" test matrix is shown in Table 3.8. A denser distribution of compliant surfaces was prescribed at the largest thickness smallest stiffness ranges since it is assumed these regions are more probable to have two-way coupling. Three different compliant surface thickness were prescribed with more points on the thinner limit of the thickness. This is to see how thin compliant surfaces can be to have a favourable FSI, as application on aircraft skin would prefer thinner compliant surfaces. Based on the spread and gradient acquired from the initial rheometer measurements, Table 3.9 shows the additives needed for each of the target stiffness for the test matrix. The discrepancy between the minimum stiffness mentioned here and Equation (3.12) is due to the initial target range based on the order of magnitude. The minimum target stiffness mentioned here is more realistic as it is closer to the actual value. An overview of all the compliant surfaces made during this research is included in Appendix A.2.

Table 3.8. The compliant surface test matrix with the corresponding surface ID

		$\lvert G^* \rvert$ [kPa]				
		5	**20**	**40**	**60**	**100**
δ_s [mm]	**4**	CC207	CC204	CC203	CC205	CC214
	2	CC210	-	CC208	-	CC213
	1	CC211	-	CC209	-	CC212

Table 3.9. The amount of additive needed for the target stiffness in the test matrix

Target stiffness [kPa]	**Additive** [weight ratio]
5	2D
20	0.25D
40	-
60	0.35H
100	0.75H

3.7.2. Drag measurements

Each surface is measured in normal (Norm.) and reversed (Rev.) streamwise orientations to see if there are any dependencies on the compliant surface mould. This precaution isolates the effects of possible leading and trailing edge steps where the resultant negative pressure drag correction may correct a drag increase to drag reduction. With 11 compliant surface test plates, this results in 22 test plate-orientation pairings. After every measurement, a Shore durometer is used to measure the Shore hardness and keep track of the stiffness to see if there are any changes over time.

The initial measurement for all surfaces was conducted in units of three triple sandwiches. After each measurement unit, the data was immediately processed to see verify the data. Each measurement unit plus processing time took about 4 hours 30 minutes, allowing for two measurement units per day. Table 3.10 shows the planned measurement schedule for the drag measurements. With a 2-week wind tunnel time slot, the amount of samples fits well within the given time, leaving an abundance of buffer time for unexpected schedule changes. The buffer time was used to remeasure compliant surface test plates for repeatability of results and redo measurements where errors were present.

Table 3.10. Planned measurement schedule for drag measurements (Week 1)

(2020)	24/8	25/8	26/8	27/8	28/8
Morning	CC214 Norm. CC205 Norm. CC203 Norm.	CC204 Norm. CC207 Norm. CC213 Norm.	CC208 Norm. CC210 Norm. CC212 Norm.	CC209 Norm. CC211 Norm.	(Buffer)
Afternoon	CC214 Rev. CC205 Rev. CC203 Rev.	CC204 Rev. CC207 Rev. CC213 Rev.	CC208 Rev. CC210 Rev. CC212 Rev.	CC209 Rev. CC211 Rev.	(Buffer)

3.7.3. Flow visualisation

The PIV experiments aim to visualise the flow structure above drag-reducing and drag-increasing compliant surfaces and compare with the reference test plate TP0000. From the drag delta measurements, the drag-reducing compliant surface was chosen to be the CC207 Rev., and the drag-increasing compliant surface the CC204 Norm. Two categories of data acquisition were conducted: the panoramic and zoomed-in view of the flow. All three test plates are measured at three different flow velocities for both the panoramic and zoomed-in configuration: 10 m/s, 20m/s, and 35 m/s. 35 m/s is at which the M-Tunnel operates at full capacity.

For both categories, each FOV has nine acquisition points shown in Table 3.11, with the number indicating the order of acquisition. Two sets of 300 image pairs were taken for each acquisition point, totalling to 600 image pairs. The split of image pairs into two sets ensures sufficient seeding in the wind tunnel, as a long acquisition time may lead to insufficient particles in the latter image pairs. This acquisition procedure is further illustrated in Figure 3.27. The procedure first prioritises the velocity sweep, followed by the different test plates, and then the camera's location; the prioritisation reflects the flexibility of each change. The flow velocity can be easily changed with the different wind tunnel RPM inputs. Changing the test plate requires removing and fastening the corner pieces and test plates while changing the camera location requires the refocusing and readjusting the camera's attitude. Due to the compliant surfaces' tacky nature, placement of the streamwise millimetric calibration board on the compliant surface with every camera location change would be infeasible as it damages the surface finish. Furthermore, an identical FOV for each test plate at the same location would be ideal for comparison of results.

Table 3.11. Order of PIV acquisition with respect to test plate and flow velocity for every FOV

For each FOV		u_∞ [m/s]		
		10	**20**	**35**
Test plate	**TP0000**	1	2	3
	CC207 Rev.	4	5	6
	CC204 Norm.	7	8	9

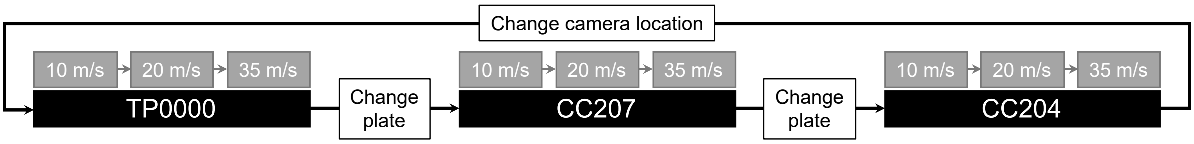

Figure 3.27. Flowchart of PIV acquisition procedure

Panoramic view

For the panoramic view, the entire streamwise length of the test plate can be covered with 11 FOVs with 15% overlap using the f = 60 camera lens. This coverage is shown in Figure 3.28. The streamwise location of each panoramic FOV is shown in Table 3.12. The zero location in the streamwise direction is located at the leading edge of the test plate. The camera is aligned to these locations via the streamwise millimetric calibration board.

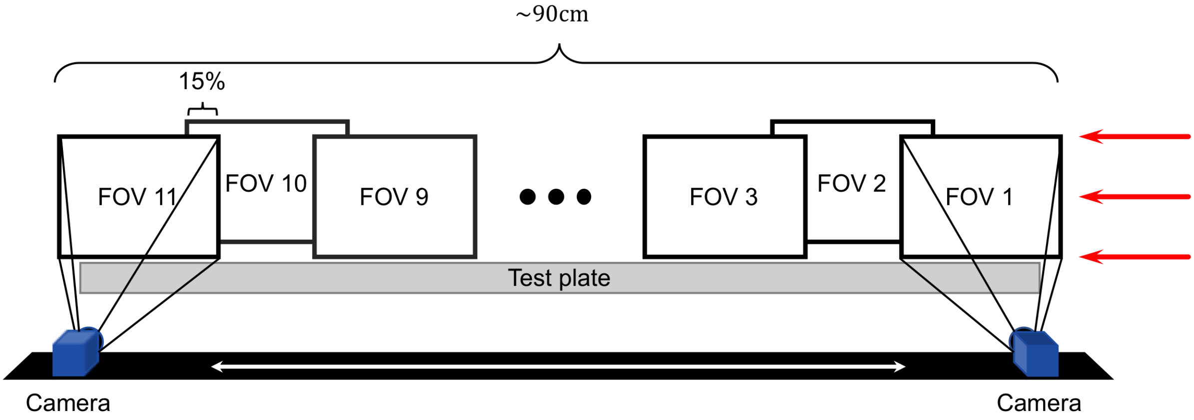

Figure 3.28. Schematic of PIV panoramic FOVs in the streamwise direction

Table 3.12. Streamwise locations of the PIV panoramic FOVs

ID	**Downstream** [mm]	**Upstream** [mm]
1 (LE)	28.63	-81.24
2	122.02	12.15
3	215.41	105.54
4	308.80	198.93
5	402.20	292.32
6 (Mid)	495.59	385.71
7	588.98	479.10
8	682.37	572.50
9	775.76	665.89
10	869.15	759.28
11 (TE)	962.54	852.67

Zoomed-in view

Acquisition of the zoomed-in views were conducted at the leading and trailing edge of the test plate. These FOVs are shown in Figure 3.29, with the streamwise locations shown in Table 3.13 .

Table 3.13. Streamwise locations of the PIV zoomed-in FOVs

	Downstream [mm]	**Upstream** [mm]
LE	53	-3.5
TE	884	826.7

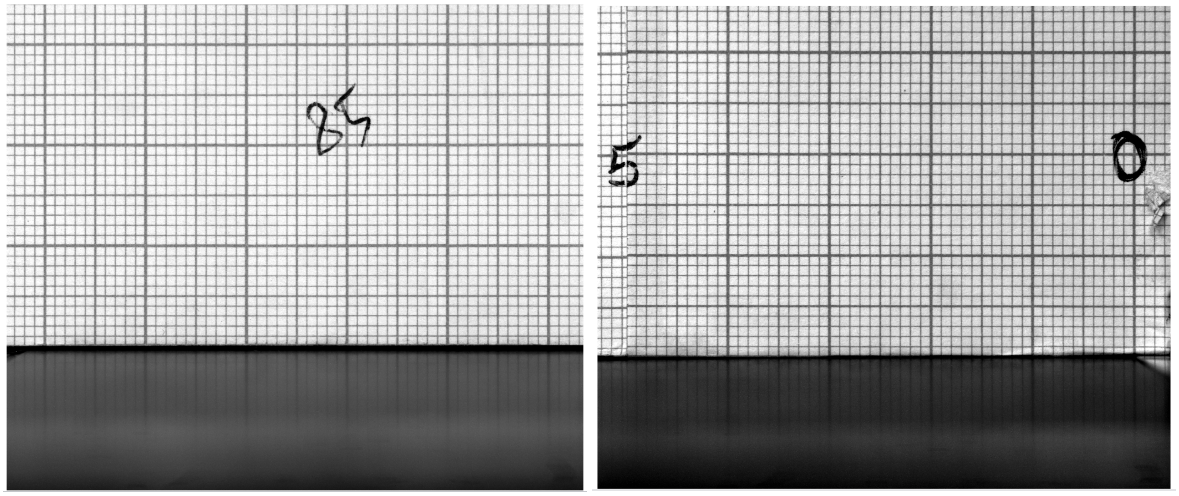

(a) Trailing edge

(b) Leading edge

Figure 3.29. FOVs of the PIV zoomed-in view

3.8. Statistical analysis

In this section, statistical methods and measures used in the validation of experiment results are briefly discussed.

Root mean squared error (RMSE)

The root-mean-square error (RMSE) is used for verifying the spread of measurement results. For a variable x, the RMSE is calculated by:

$$\mathrm{RMSE} = \sqrt{\frac{\sum_{i=1}^{N}(x_i - x_{\mathrm{mean}})^2}{\mathrm{N}}} \tag{3.13}$$

where N signifies the sample size.

$\mathbf{R}^2$

The R^2 (pronounced "R-squared") value, or the coefficient of determination, is used to determine the quality of curve regression with respect to a given data set. It is defined as 1 subtracted by the ratio of the total sum of squares to the residual sum of squares:

$$\mathrm{R}^2 = 1 - \frac{\Sigma_i (y_i - f_i)^2}{\Sigma_i (y_i - \overline{y})^2} \tag{3.14}$$

where y is the data set in question, and f the values of the curve regression of the y data set.

Welch's t-test

Welch's t-test is used to ensure that the discrepancy between each test plate result is not a causal effect of noise. It is used to analyse the statistical independence of measurement signals of different plates. Proposed by Welch (1938), Welch's t-test evaluates the t-value, which indicates the closeness of two data sets' mean value. This test assumes that the two samples have unequal variances and/or sample sizes. The t-value is given by

$$t = \frac{\bar{X}_1 - \bar{X}_2}{\sqrt{\frac{\sigma_1^2}{N_1} + \frac{\sigma_2^2}{N_2}}} \tag{3.15}$$

where the subscript numbers indicate the two samples, $\bar{X}$ the mean, σ the variance, and N the sample size. If the t-value of two data sets exceeds a critical value t_{crit}, the results can be described as statistically significant. t_{crit} is determined by the statistical degree of freedom (DOF) and the prescribed confidence interval

(CI). The DOF of two data sets can be calculated by the Welch–Satterthwaite equation for two data sets:

$$DOF \approx \frac{\left(\frac{\sigma_1^2}{N_1} + \frac{\sigma_2^2}{N_2}\right)^2}{\frac{1}{N_1-1}\left(\frac{\sigma_1^2}{N_1}\right)^2 + \frac{1}{N_2-1}\left(\frac{\sigma_2^2}{N_2}\right)^2} \tag{3.16}$$

t_{crit} is proportional to the confidence interval and inversely proportional to the sample size. Sample sizes beyond 30 are considered fairly large, where the critical t-value approaches that of a normal distribution. The critical t-values for a normal distribution is shown in Table 3.14.

Table 3.14. t_{crit} for a normal distribution at a given CI

CI	80%	90%	95%	98%	99%	99.9%
t_{crit}	1.281552	1.644854	1.95996	2.32635	2.57583	4.2905

4

Results from experiments

In this chapter, the outcome of the various experiments mentioned in Chapter 3 is presented and verified. First, the outcome of manufacturing of compliant surfaces and its viscoelastic properties are discussed in Section 4.1. The drag delta measurements of the entire M-shaped test matrix is presented in Section 4.2. Hot-wire measurements of the drag-reducing compliant surface CC207 Rev. compared with the reference plate TP0000 is presented in Section 4.3. Finally, the flow visualisation results for the drag-reducing compliant surface CC207 Rev., drag-increasing compliant surface CC204 Norm., and the reference plate TP0000 is presented in Section 4.4.

4.1. Compliant surfaces

In this section, the resultant product of the manufacture of compliant surface, and its viscoelastic properties is presented. The results from the rheometer is also verified.

4.1.1. Surface texture

Figure 4.1 shows a photo of the surface texture of the CC204 compliant surface. Shallow troughs are present on the cured compliant surface. The formation of these troughs are due to two reasons: the forcing of the mixture when the curing process has started, and inhomogeneous curing due to inner temperature gradients. An oily layer of silicone oil is formed on top of the surfaces after it is cured. While silicone is known for its non-stick capabilities, the surface tackiness increases with the addition of the deadener, vice versa for the hardener. This observation is consistent with the technical data sheet of the PlatSil Gel OO (appendix B). Therefore, to prevent dust from adhering to the compliant surface, plastic foil was applied on the surfaces and stored in a flight case in the absence of direct sunlight. However, the application of plastic foil displaced the oily layer into obvious patterns on the surface. Though the potential effect of this displacement to the flow is unknown, it is assumed that the added texture is relatively minor, and the prevention of dust by applying plastic foil made it an acceptable trade-off, as the dust had a more pronounced effect on the flow. Also, the application of the silicone adhesive in the surrounding edges slightly lifted the compliant surface. However, this lift-up was compensated with a drooping top surface due to the mixture's capillary effect at the mould rim edges.

The edges of the compliant surface proved to be the most tricky part of getting a good finish. This finish mainly depended on the pouring of the mixture in the mould, and the amount of mixture that was poured in. The compensate the steps present at the edges, strips of 0.2 mm thickness spacers were applied at the bottom of the test plate around the perimeter, mainly for the backwards-facing steps at the leading edge. Figure 4.2 shows the spacers applied to the CC207 plate; the left side of the test plate is the leading edge. These spacers were applied throughout the drag and flow visualisation measurements.

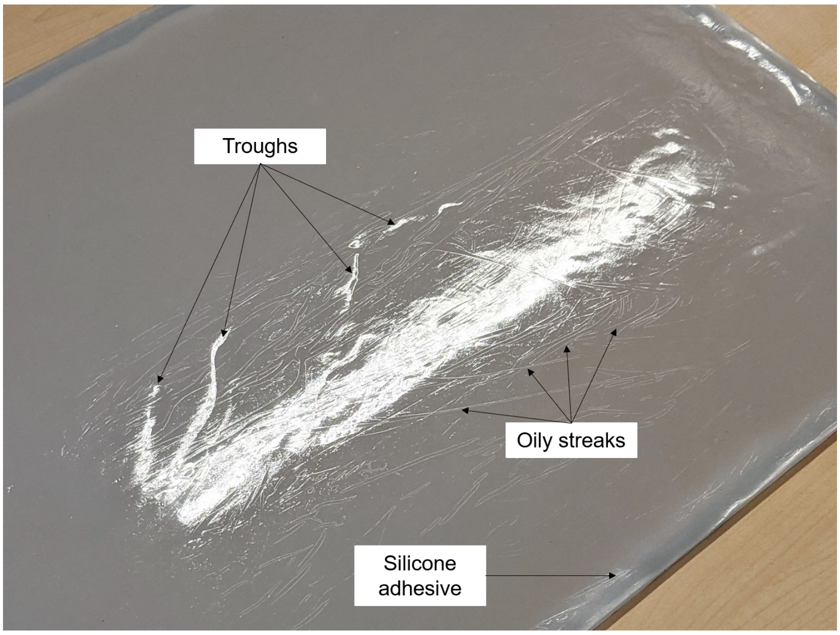

Figure 4.1. Textures on the compliant surfaces (CC204)

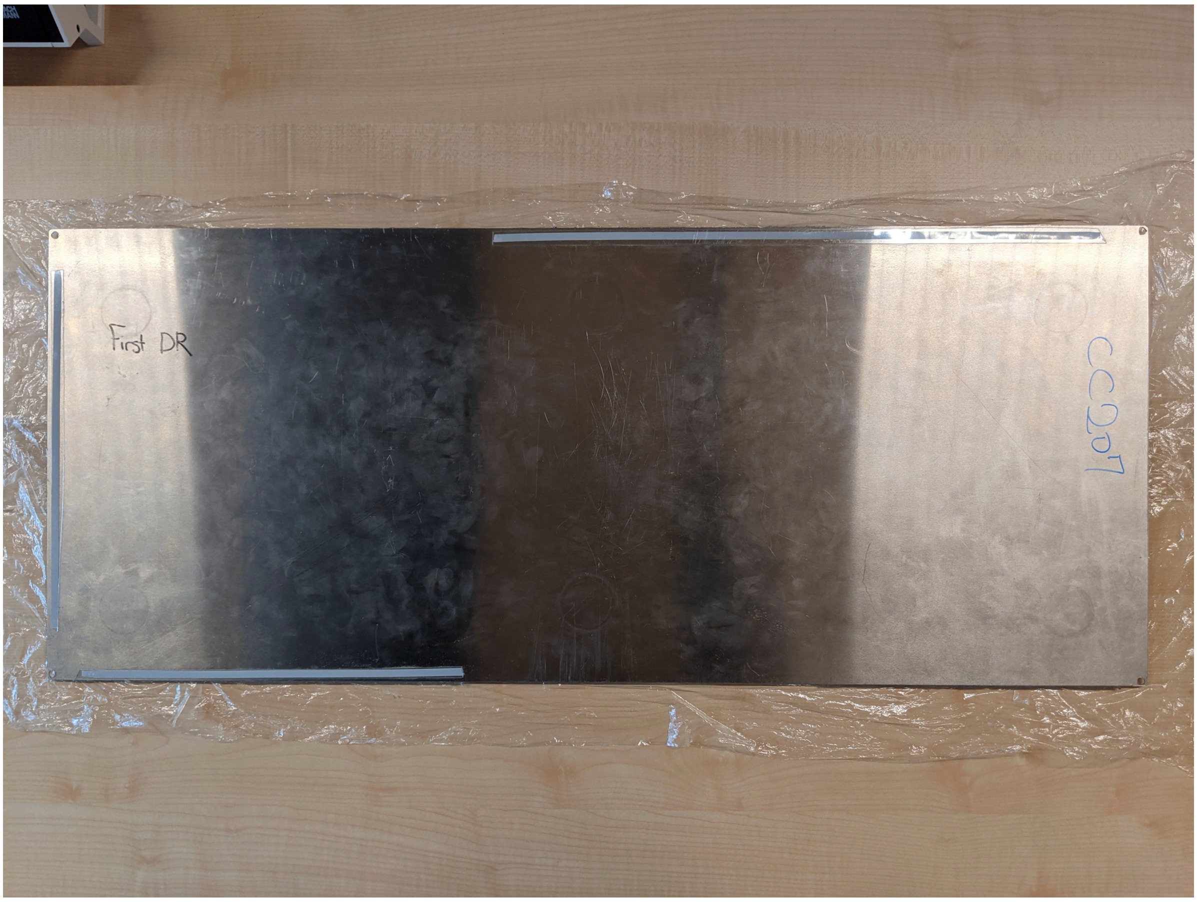

Figure 4.2. Application of spacers at the bottom of the CC207 test plate

4.1.2. Viscoelastic properties

The viscoelastic properties of the Platsil Gel OO mixture defined by the rheometer are elaborated in this section. Namely, the magnitude of complex shear modulus $|G^*|$, the shear storage modulus G', the shear loss modulus G'', and the loss tangent $\tan(\delta_p)$. The repeatability and the RMSE spread of the rheometer measurements are also discussed in this section. The frequency-averaged magnitude of complex shear modulus was calculated with a cut-off frequency of 1 Hz, where the effect of the cut-off frequency will also be discussed in this section.

Resultant test matrix

Figure 4.3 shows the actual test matrix overlapped with the target test matrix. The viscoelastic properties of the compliant surface were evaluated with a rheometer sample made from the same mixture as the compliant surface test plate. The discrepancy between the actual and target stiffness is assumed to be due to two reasons. The test plates were manufactured during the summer heatwave at the beginning of August 2020. The meteorological data from the Royal Netherlands Meteorological Institute (KNMI) is included in the appendix (fig. A.1). The curing of the PlatSil silicone is highly sensitive to the ambient temperature, therefore affecting the material properties of the cured product. It is worth noting the mixtures with the same stiffness has a close magnitude of shift, as seen in the stiffest target mixture of 100 kPa. The other possible reason is the rheometer samples' sliding between the parallel plates of the rheometer leading to an underestimation of the viscoelastic properties.

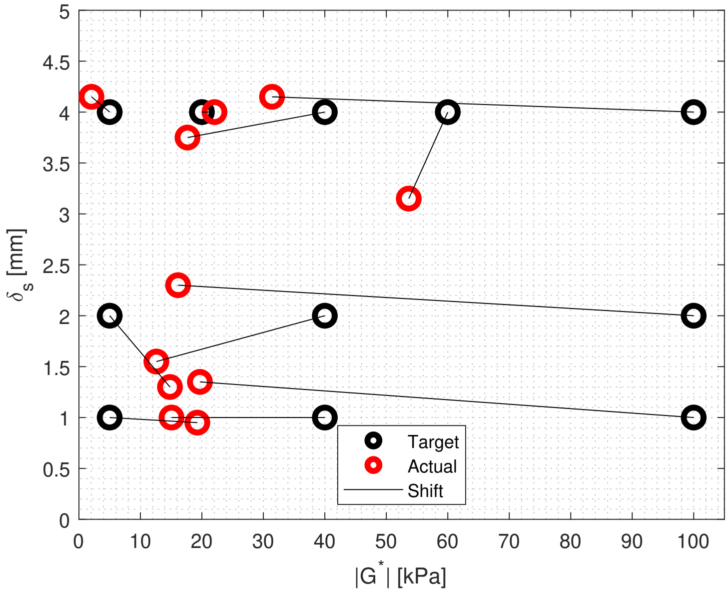

Figure 4.3. Actual and target compliant surface test matrix

The thickness of the surface was evaluated by averaging the thickness of the four corner pieces. While the variability between the target and actual thickness is smaller than the stiffness, most thinner surfaces had varying thickness throughout the plate. This variability can be traced back to the premature curing due to the higher ambient temperature allowing less pouring time. With thinner surfaces, the normal temperature gradient was larger, leading to premature curing, reducing the pouring time. As a result, the 1 and 2 mm surfaces shows explicit inhomogeneity in the surface finish throughout the plate, leading to uneven thickness. As for the 4 mm surfaces, the surface finish was acceptable with the thickness largely maintained throughout the plate. This surface finish can be distinguished by the light and image reflection on the surface as seen in Figure 3.16b.

Repeatability of rheometer measurements

Before discussing the PlatSil Gel OO's viscoelastic properties, the repeatability of the rheometer measurements is discussed. The repeatability was quantified by the RMSE spread of $|G^*|$ and $\tan(\delta_p)$ from the rheometer, characterised for four categories: axial force, rheometer repeatability, manufacture repeatability, and sample thickness. These are shown in Table 4.1, with all measurements conducted on a 1A:1B mixture sample without any additives. For the axial force category, six measurements where conducted in the range of $0.1 \leqslant F_a$ [N] $\leqslant 50$. For the rheometer repeatability, three frequency sweeps on the same sample were conducted in consecutive manner with the same parallel-plate separation and axial force. For the manufacture repeatability, three different silicone patties were made according to the same mixture ratio. For the sample thickness, three silicone patties with different thickness were made from the same mixture. The largest variability is seen in both the axial forceand sample thickness category, where an RMSE of approximately 10 kPa for the magnitude of complex shear modulus, and approximately 0.02 for the loss tangent is observed.

Table 4.1. RMSE spread of rheometer measurements with respect to axial force applied, repeatability of rheometer, repeatability of manufacture, and sample thickness

	Axial force	**Rheometer repeatability**	**Manufacture repeatability**	**Sample thickness**
$\lvert G^*\rvert$ [kPa]	10.7889	6.9690	1.0945	10.3703
$\tan(\delta_p)$ [−]	0.0189	0.0014	0.0006	0.0201

Effects of adding deadener and hardener

The magnitude of complex shear modulus $|G^*|$, s, the loss tangent $\tan(\delta_p)$, the shear storage G' and loss G'' shear modulus with respect to the amount of deadener and hardener in the mixture is shown in Figure 4.4. These were measurements of the rheometer samples used for investigation of the PlatSil Gel OO mixture. The magnitude of the complex modulus and loss tangent are plotted in the same figure for direct comparison.

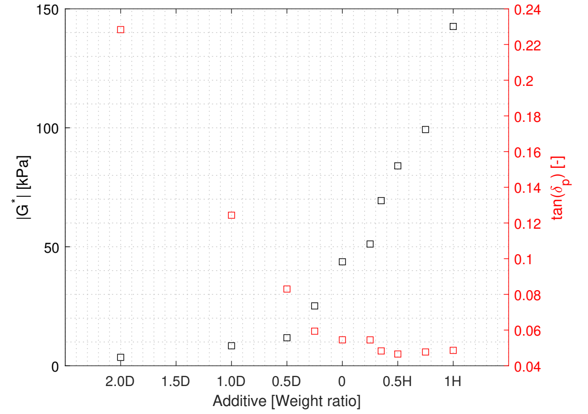

(a) $|G^*|$ and $\tan(\delta_p)$

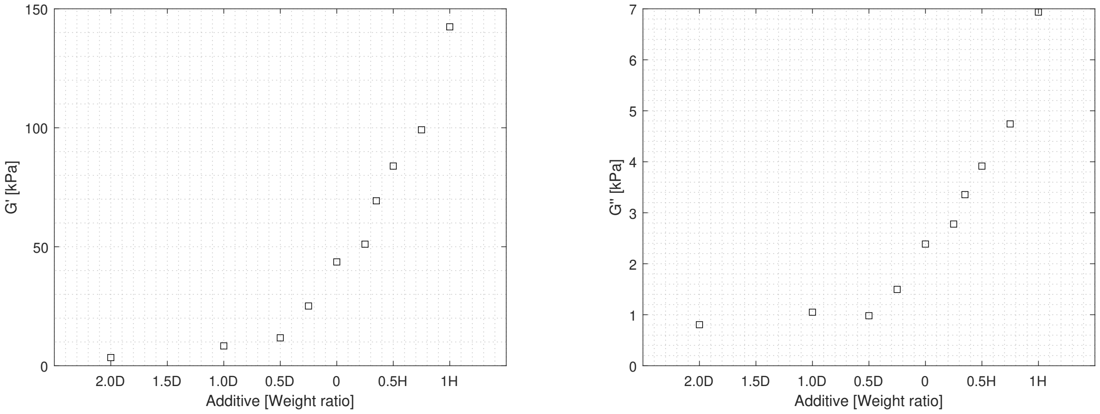

(b) G' **(c)** G''

Figure 4.4. Viscoelastic property variation of PlatSil Gel OO with respect to the deadener and hardener additives

The storage and loss shear modulus follows the trend of the magnitude of the complex shear modulus in different scales. The loss tangent, a combined characterisation of the storage and loss shear modulus, shows an inversely proportional trend compared to the magnitude of complex shear modulus. This is seen as the effect of the deadener added, as the addition of the hardener only varies the loss tangent slightly compared with no additives added. Adding the deadener, a low-viscosity fluid, to the main mixture essentially increases the viscous component of the viscoelasticity, therefore increasing the loss tangent.

The measurements of samples with the hardener additive were observed to have high variability in the complex shear modulus. Measurements were frequently seen to underestimate the actual complex shear modulus. This is assumed to be the sample not properly clamped by the parallel plates, resulting in sliding when the sinusoidal strain is applied. The addition of the hardener makes the sample surface texture less tacky than the baseline and deadener-added samples. More axial force may be applied to keep the sample in place, but the RMSE spread due to different axial forces must be considered. Another typical method used to keep the samples in place is adding grains of roughness elements between the parallel plates and the sample. However, this method was not considered in this research.

Property dependence on cut-off frequency

The compliant surface's viscoelastic properties are frequency-dependent, as a sweep of sinusoidal strain with different frequencies is conducted. A cut-off frequency is specified to calculate a mean value for these properties. Figure 4.5 shows the plot of the frequency-dependent viscoelastic properties of magnitude of complex shear modulus $|G^*|$, the loss tangent $\tan(\delta_p)$, the shear storage G' and loss G'' modulus. Values for all properties gradually increase with the frequency of the applied sinusoidal strain. The properties of the 2 Deadener sample increase the most with respect to the frequency, comparing with the other samples. At frequencies around 30 Hz, the properties of all samples experience a dip, and an exponential increase subsequently. This is because, at higher frequencies, the silicone does not have sufficient time to react to the sinusoidal strain, therefore resulting in artificially high moduli.

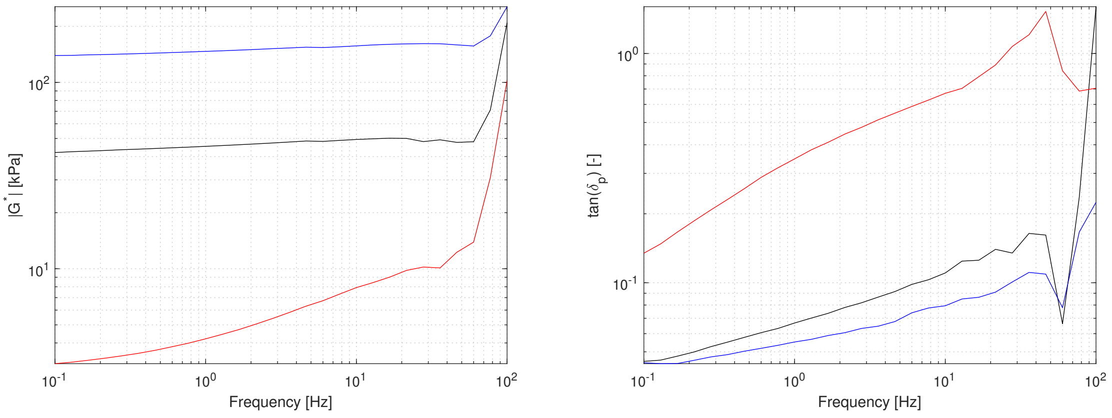

(a) $|G^*|$ **(b)** $\tan(\delta_p)$

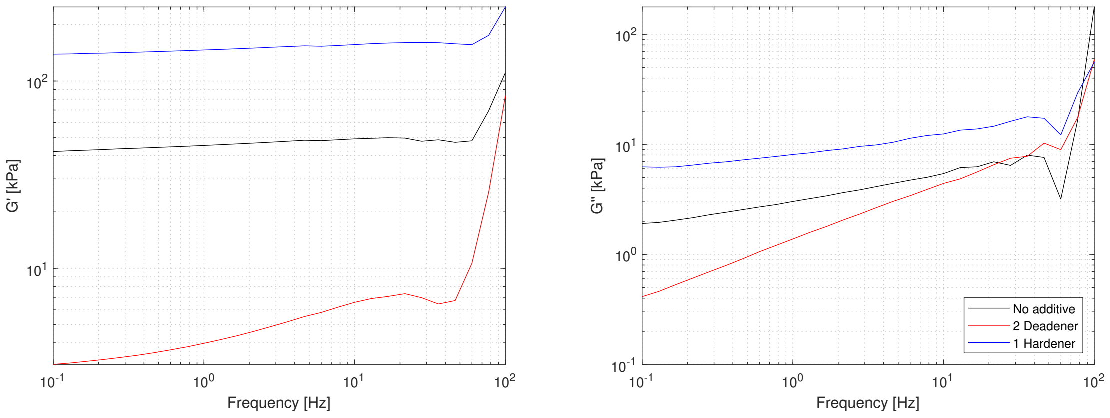

(c) G' **(d)** G''

Figure 4.5. Viscoelastic property variation of PlatSil Gel OO with respect to additives

The mean of these viscoelastic properties is calculated by taking the geometric mean of the data points up to the specified cut-off frequency. Figure 4.6 shows the viscoelastic properties' dependency on three different cut-off frequencies: 1, 10, and 100 Hz. The solid lines represent the absolute values, where the dashed lines are deltas zeroed with respect to the mean properties at 1 Hz. The mean viscoelastic properties are proportional to the cut-off frequency. The increase of each property is proportional to its initial value at the lower frequencies. This increase is the same for cut-off frequencies of 10 and 100 Hz, with the 100 Hz having a large delta due to incorporating the peak values at the higher frequencies. Disregarding these peaks, $|G^*|$ and G have an approximate 4 kPa spread with respect to the different cut-off frequencies. For the loss tangent, the increase for the 2 Deadener sample is significant comparing with the other two samples. This delta is assumed to be due to the increased phase lag, on top of the sample not reacting to the sinusoidal strain properly, resulting in the loss tangent's higher delta value. After discussion with the technical staff of the DASML Material Physics lab, a suitable cut-off frequency of 1 Hz was chosen for the analysis of results (Nijemeisland, 2020).

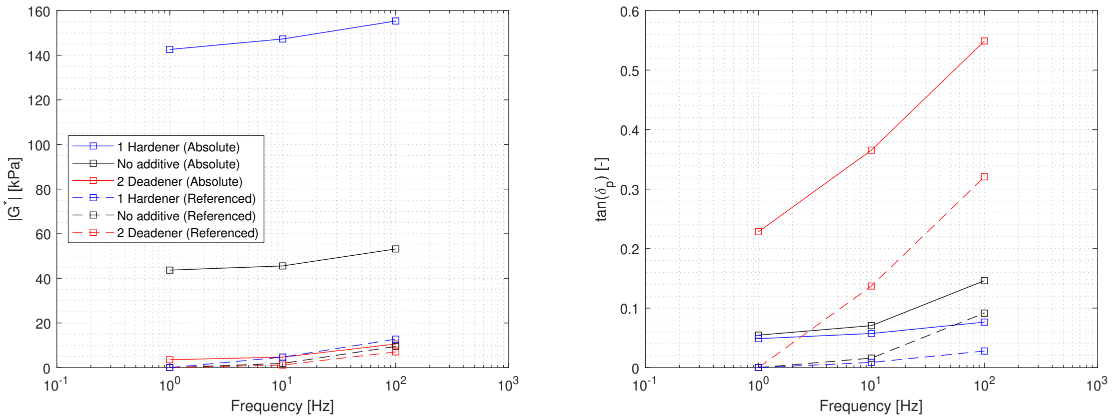

(a) $|G^*|$ **(b)** $\tan(\delta_p)$

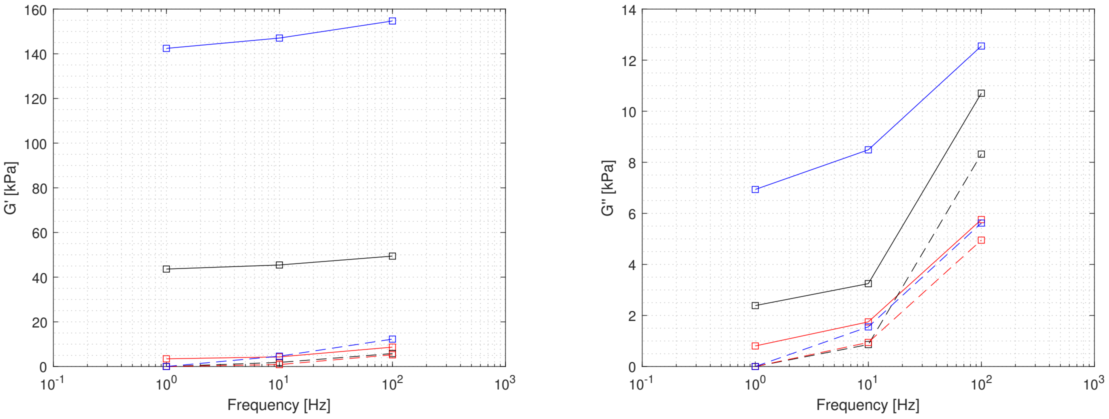

(c) G' **(d)** G''

Figure 4.6. Viscoelastic property variation of PlatSil Gel OO with respect to the cut-off frequency. Three cut-off frequencies are compared: 1, 10, and 100 Hz. Solid lines indicate the absolute value of the measured viscoelastic properties. The dashed lines are deltas referenced the averaged viscoelastic property with a cut-off frequency of 1 Hz.

Ageing of material

Silicones are known to age over time where changes in its viscoelastic properties occur (Bandyopadhyay et al., 2005). The ageing of the PlatSil Gel OO mixture was investigated with three measurements over time, where the evolution of the magnitude of complex shear modulus $|G^*|$, the loss tangent $\tan(\delta_p)$, the shear storage G' and loss G'' modulus are shown in Figure 4.7. The measurements were conducted at 08/06/2020, 08/07/2020, and 03/12/2020.

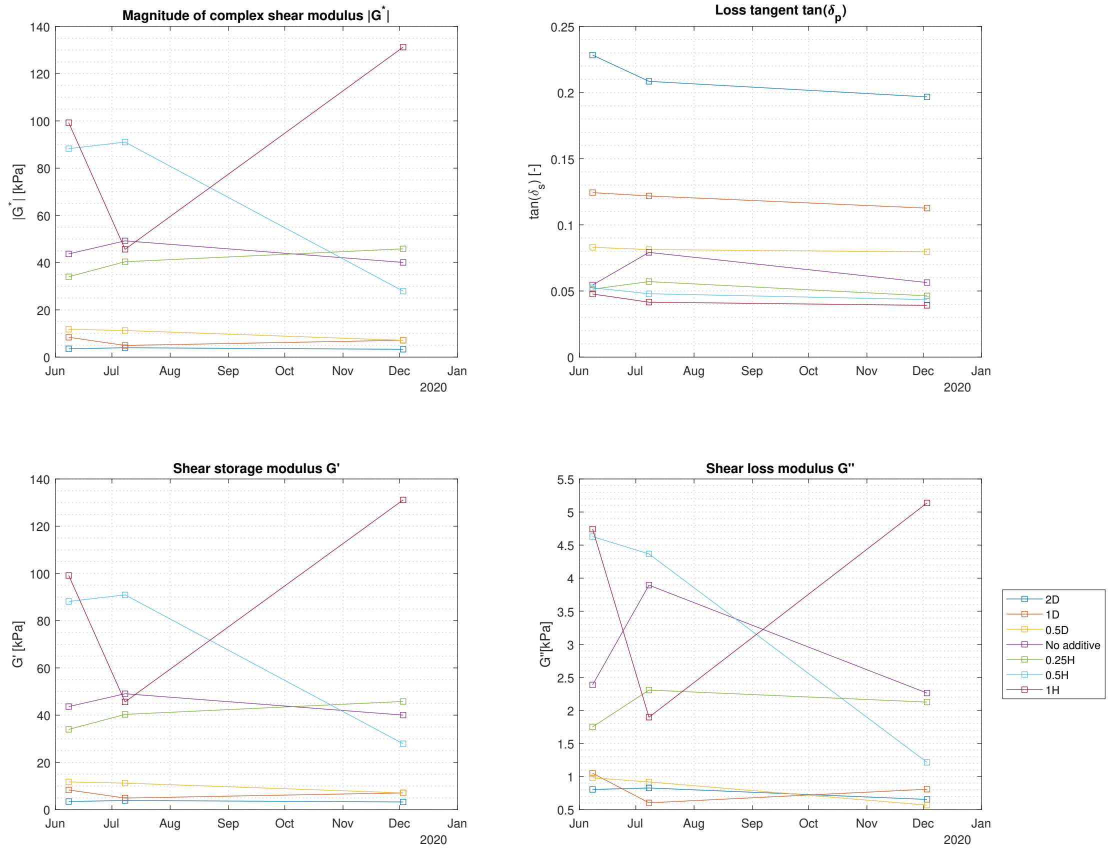
Magnitude of complex shear modulus |G*|

Loss tangent tan(δ_p)

Shear storage modulus G'

Shear loss modulus G''

Figure 4.7. Ageing effects on the viscoelastic properties of PlatSil Gel OO. The ageing rheometer measurements were conducted three times over sixth months. The samples tested cover the full range of stiffness with the maximum amount of additives according to the technical data sheet in Appendix B. D and H indicate the deadener and hardener, respectively.

Stable development of viscoelastic properties is observed over time; other than the significant variations present for the 0.5H, 1H, and partially the sample without additives. For the samples with deadener, G' and $|G^*|$ varies around a 5 kPa range, and G'' a 1 kPa range over time. Also, the loss tangent is decreasing over time for these deadener additive samples, with the amount of decrease proportional to the amount of deadener added. Looking at the loss tangent, it is an indication that the change of material properties is confined to a certain minimal range with no significant change. The same can be said for the other stable properties of some samples. These results coincide with the Shore durometer measurements conducted on the compliant surfaces after every drag measurement.

High variability for some of the hardener additive samples is seen in the $|G^*|$, G', and G''. This variability is assumed to be due to local measurement errors affecting the absolute values of these properties. The degree of fluctuations for these properties also coincides with each other in a relative sense. This can be deduced from $\tan(\delta_p)$, where the variability is relatively calmer than other properties, even with the fluctuations. As the loss tangent can be seen as a normalising property for the storage and loss shear modulus, its stable development throughout time coupled with the coinciding fluctuations of the various properties leads to deducing that these fluctuations are due to local measurement errors.

4.2. Drag delta measurements

The results of the drag delta measurements of the compliant surface test plates according to the M-shaped test matrix are shown in Figure 4.10. The drag delta shown here is from the measurement at the highest Reynolds number for each compliant surface. Negative values of ΔC_D indicate a drag reduction, while positive values indicate a drag increase. Each compliant surface was tested in the normal (Norm.) and reversed (Rev.) streamwise orientation based on mould. The resultant drag delta is shown in the blue bar, which is the sum of the raw drag reduction in the left bar corrected by the pressure drag shown in the middle bar. The value of drag delta for each test plate and its orientation are shown on top of each bar group, alongside the RMSE of the measurement.

4.2.1. Verification

Before conclusions are drawn from Figure 4.10, the drag delta measurements need to be verified in certain aspects. First is the statistical analysis of the sensor signals coming from the drag force sensor and the pressure scanners. Then the null-force and pressure drag corrections are observed for every case and different thickness groups. The RMSE spread of the drag delta is inspected for gaining confidence in the results. This is coupled with the repeatability of the results.

Welch's t-test

Welch's t-test is applied to the drag signal from the force sensor, and the pressure signal from a pressure scanner at the Hill's leading edge. The two data sets are from measurements of the TP0000 and CC207 Rev. test plates.

Force signal The raw force sensor signal and the result of the t-test are shown in Figure 4.8 and 4.9, respectively. The force sensor has an acquisition frequency of 25 kHz with a measurement time of 10 s for each velocity point. The t-value of the force sensor signal is statistically significant way beyond the critical t-value of 99.9% CI. This outcome gives confidence in interpreting the drag delta results.

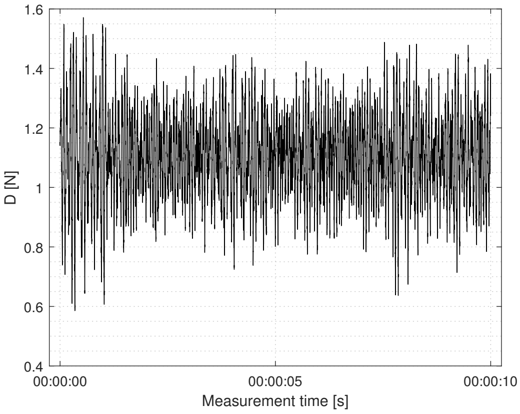

Figure 4.8. Raw drag force sensor signal

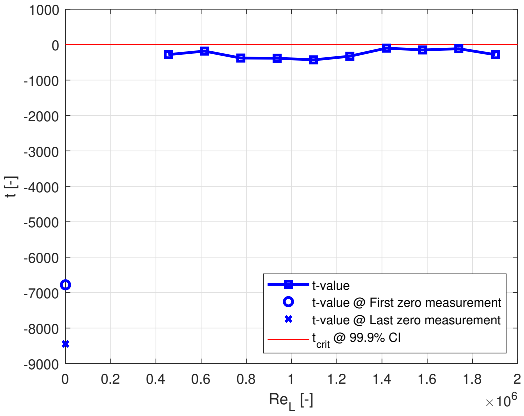

Figure 4.9. t-value of drag force sensor signal for TP0000 and CC207 Rev. test plates

Pressure signal The raw pressure scanner signal and the result of the t-test are shown in Figure 4.11 and 4.12, respectively. The pressure scanner has an acquisition frequency of 28 Hz with a measurement time of 10 s for each velocity point. The t-value of the pressure scanner signal around the mid-range Reynolds numbers only show 90% CI t-values, even below 80% CI for one of the velocities. This result gives partial confidence in interpreting significant pressure corrections near the mid-Reynolds number range and should be kept in mind in latter analysis. This being said, the observed drag reduction shown in Figure 4.10 is always taken from the measurement at the highest Reynolds number, at which the pressure corrections applied are statistically significant at a 99% CI.

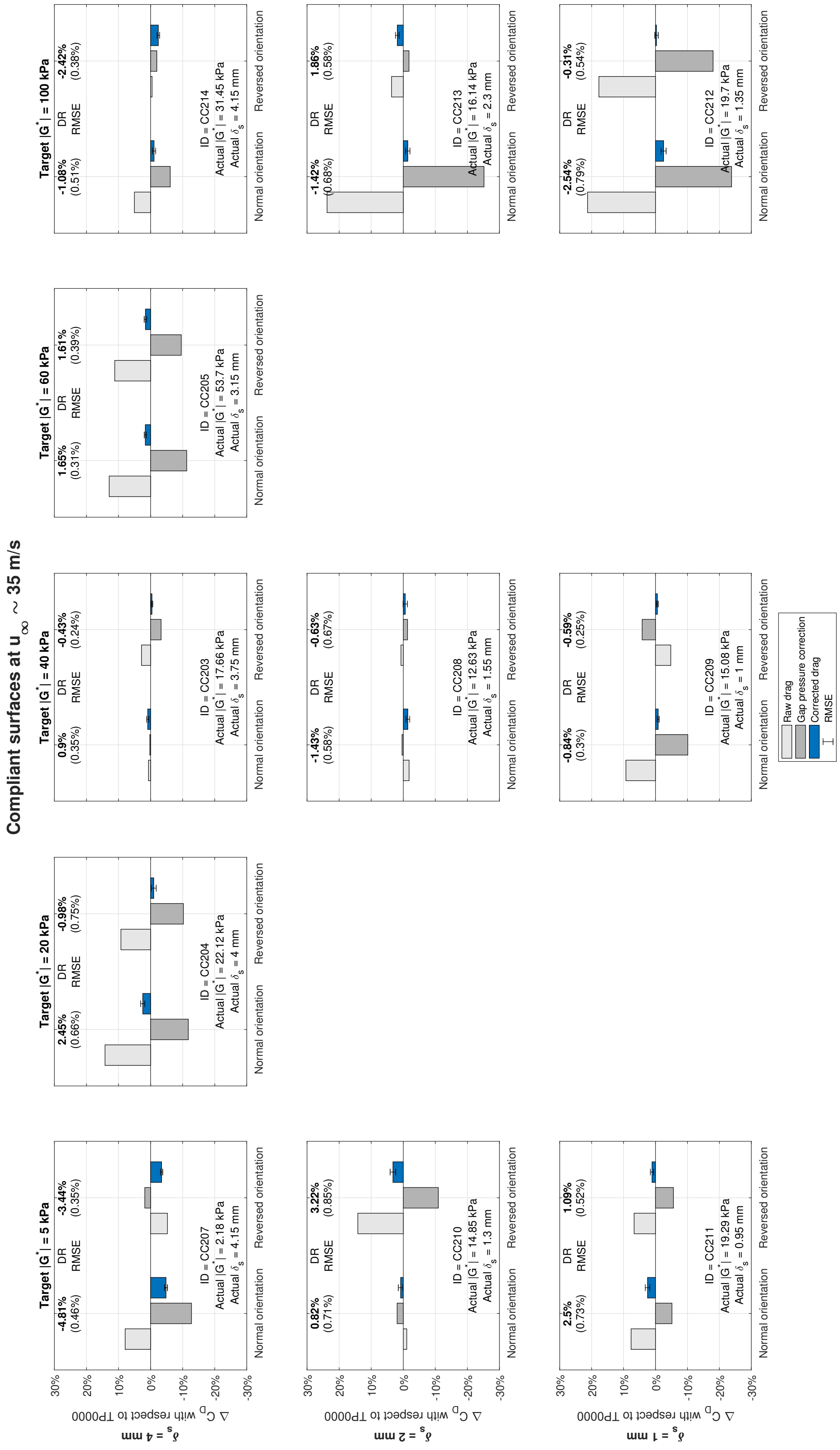

Figure 4.10. Drag delta measurement results of the compliant surface test plates by the Hill. Figure may also be accompanied with Table 3.8 for better association of surfaces

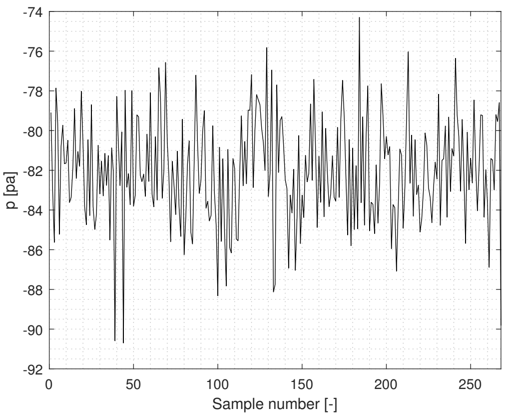

Figure 4.11. Raw pressure scanner signal at the leading edge

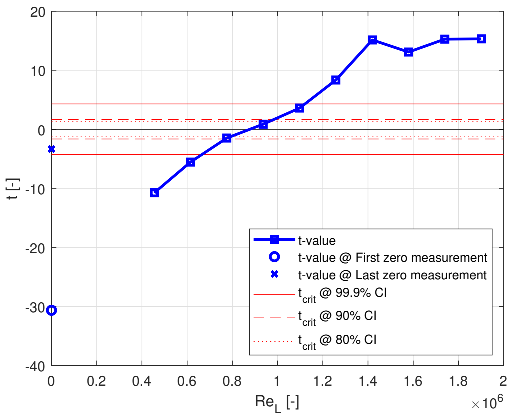

Figure 4.12. t-value of pressure scanner signal for TP0000 and CC207 Rev. test plates

Force corrections

Null-shift force correction Figure 4.13 shows the RMSE spread of the null-shift force corrections applied for all the test plates at different Reynolds numbers. The spread for each compliant surface thickness group is also presented. The thick black line is the geometric mean of all the measurements, indicated with a dotted line. The null-force correction is quite consistent throughout all plates at different Reynolds numbers. Corrections for different thickness groups are also consistent. The compliant surface test plate's weight varies with the surface thickness since aluminium inlays are put in for thinner surfaces, leading to a higher test plate weight. This consistency indicates that the force sensor pin was properly rested on the connector tray without measuring any irregular forces other than the drag.

Pressure drag correction Pressure drag correction is applied according to the measured gap pressure at the leading and trailing edge. These gap pressures are mainly due to the steps generated by the surface finish of the compliant surface test plate. Spacers and silicone adhesive were applied to the bottom of the test plate and between the compliant surface and base plate, respectively, to eliminate these steps. However, gap pressures were still present in many of the test plates. Therefore, the magnitude of pressure correction can also be an indication of the compliant surface quality.

While some surfaces indicate a net drag reduction, a few of them achieved drag reduction with the help of the pressure correction, such as CC212 and CC213 at the right leg of the M. The dependency of the drag reduction on the pressure correction warrants further investigation into the pressure field above the compliant surface. These results should be treated with care without drawing conclusions too quickly.

Therefore, good quality results must have minimal pressure drag correction to the raw drag, and also minimal dependence on the pressure drag correction for the drag reduction. Drag reduction cases such as the CC207 Rev. and the CC208 Norm. fit such criteria. On the other hand, drag increase results with the same criteria should also be considered to the drag reduction parameter space. These results include the CC204 Norm. and the CC205 in both orientations.

RMSE spread of drag delta

The RMSE spread of the drag measurements for all compliant surface test plates, and also for each surface thickness group is shown in Figure 4.14. The thick black line is the geometric mean of all the measurements indicated with a dotted line. The averaged RMSE values for each surface thickness group are shown in Table 4.2.

Table 4.2. Average RMSE values for the all compliant surface test plates and each thickness group

	All	**4 mm**	**2 mm**	**1 mm**
Average RMSE [%]	0.45	0.39	0.59	0.41

Looking at Figure 4.14a, peaks are present surrounding the lowest Reynolds number and at Re $\approx 1.6 * 10^6$. These peaks are thought to be the resonance between the wind tunnel turbine and the MDF test section

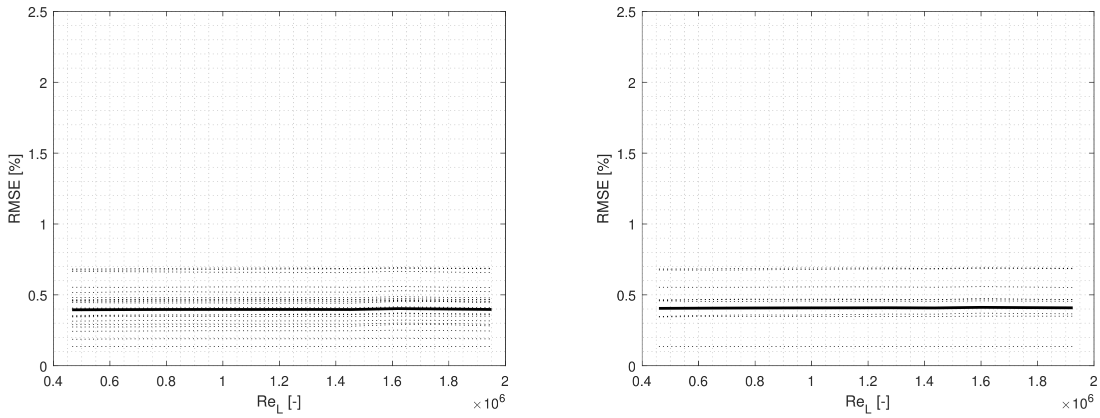

(a) For all test plates

(b) δ_s = 4 mm

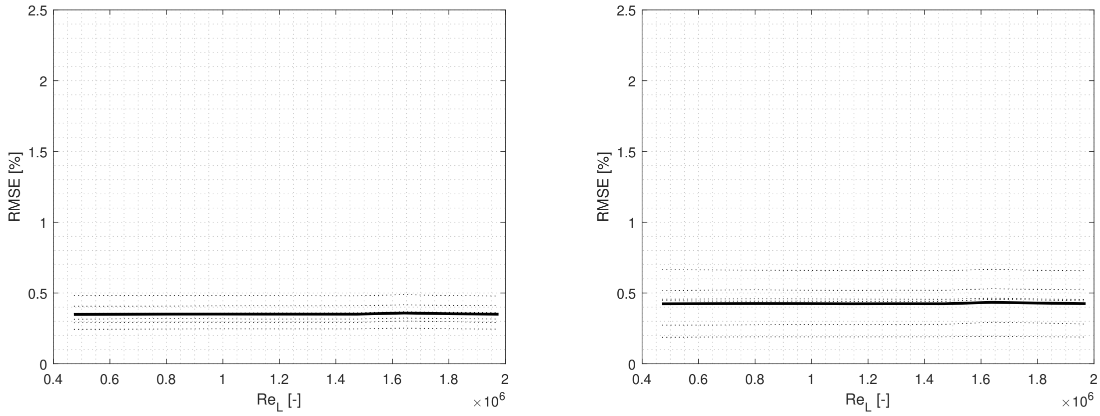

(c) δ_s = 2 mm

(d) δ_s = 1 mm

Figure 4.13. RMSE spread of null-force correction of the drag force sensor in the Hill

affecting the measurement by the drag force sensor. Acoustic resonance of the wind tunnel was overheard during the experiments. The latter peak becomes more prominent as the compliant surface becomes thinner. It is presumed that vibrations occur due to the placement of the aluminium inlay, making the test plate a two-piece assembly instead of the one-piece assembly like the 4 mm compliant surface test plates. The larger RMSE spread of the thinner plates could also be linked to the quality of the compliant surfaces, as mentioned in the Section 4.1. The leading edge of the thinner compliant surface test plates was prone to be lifted from the aluminium base by incoming air flow. While silicone adhesive was applied, some of the compliant surface edgeswere not properly glued to the base plate, thus leading to the lift-up of the compliant surface and relatively higher RMSE.

Of all the thickness groups, the 4 mm compliant surface test plates demonstrate the best overall RMSE spread of the three thickness groups. It is worth noting that the two outlying RMSE curves in Figure 4.14b raise the overall mean RMSE; without these outliers, the average RMSE lowers to 0.32 %. The RMSE magnitude must be compared with the measured drag delta when interpreting the results; the drag delta must be larger than the RMSE for the data to be considered trustworthy.

Repeatability of measurements

The repeatability of the drag measurements will be inspected for the three single sandwiches of a test plate, alongside a repeated measurement of the same test plate at a later time. The drag reduction results of CC207 Rev. at two different measurements and its RMSE spread of the drag reduction are shown in Figure 4.15. An averaged drag reduction of -3.16% was observed at the highest Reynolds number. Both of these measurements were conducted with the MDF test section.

Other than at the resonance peaks mentioned in the previous section, the drag reduction of the two measurements coincides with each other quite well in Figure 4.15a. Even after the discrepancy in the drag reduc-

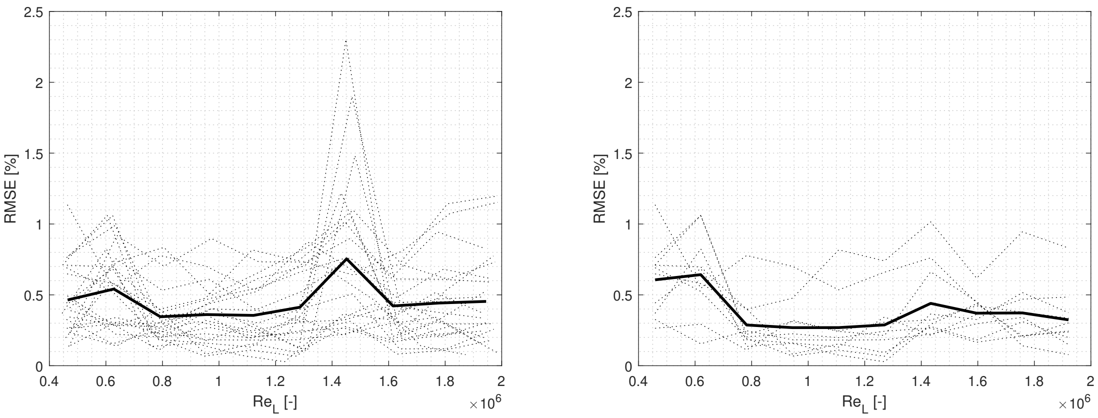

(a) For all test plates **(b)** $\delta_s = 4$ mm

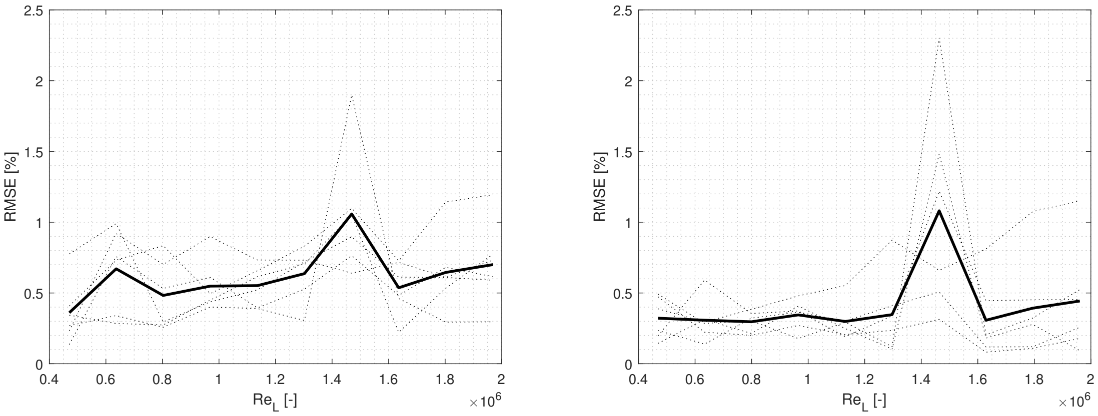

(c) $\delta_s = 2$ mm **(d)** $\delta_s = 1$ mm

Figure 4.14. RMSE spread of drag delta measured with the Hill

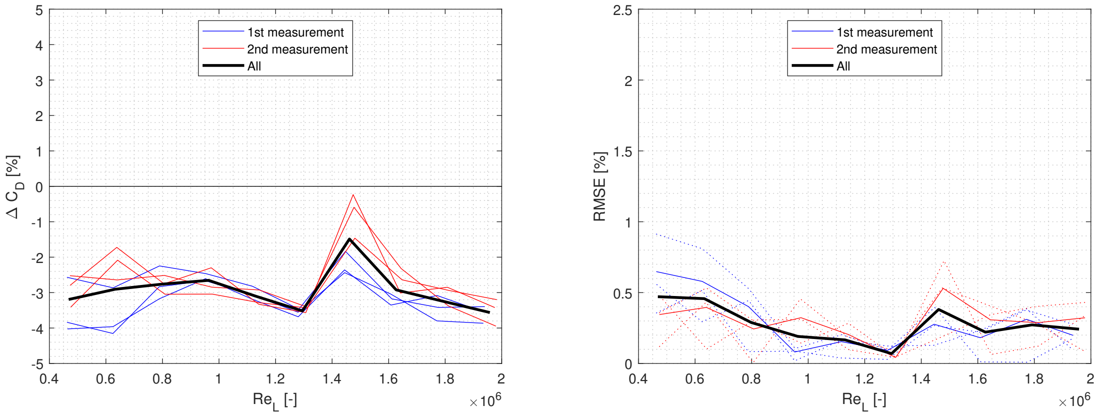

(a) Drag delta of the CC207 Rev. test plate at two different measurements **(b)** RMSE spread of the drag delta for the two measurements

Figure 4.15. The drag delta and RMSE spread of the CC207 Rev. test plate at two different measurements

tion of the latter peak, the magnitude of drag reduction converges for the two measurements approaching higher Reynolds numbers. This discrepancy is highlighted with drag delta RMSE for all measurements in Figure 4.15b. The dotted lines signify the drag delta deviation from the mean for each measurement. While significant peaks are observed for the RMSE of all measurements, a good RMSE spread for each measurement is observed where it is generally below 0.5 % for all Reynolds numbers.

Verification of test sections

The Hill's high repeatability of drag delta measurements is used to verify the two different auxiliary test sections. Since the drag delta and PIV measurements are conducted in different test sections, the flow conditions due to the different test sections must be similar. An aluminium flat plate with riblet foil on top was used as the benchmark; this is the same riblet foil used by Airbus ((Szodruch, 1991)) which is proven to exert drag reduction. Figure 4.16 shows the drag delta (4.16a) and RMSE spread (4.16b) of the riblet foil plate for the two test sections.

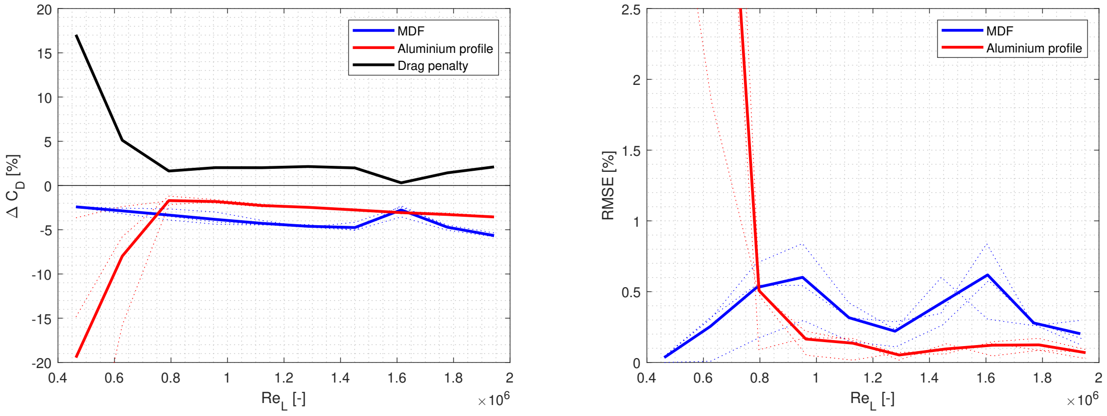

(a) Drag delta **(b)** RMSE spread

Figure 4.16. The drag delta and RMSE spread of the riblet foil plate in the MDF and aluminium profile test section

The aluminium profile test section exhibits a significant RMSE spike at lower Reynolds numbers. The average RMSE is 2.14 %, lowering to 0.16 % if the peak points were disregarded. The MDF test section has an average RMSE of 0.35 %. However, the overall RMSE spread for the aluminium profile test section is better than the MDF test section, which exhibits two RMSE peaks. A maximum drag reduction of 5.66 % and 3.55 % is observed for the MDF and aluminium profile test section, respectively. A drag penalty is present between the two test sections, represented by the black line in Figure 4.16a. Excluding the outlier points due to the RMSE peaks, an average drag penalty of 1.91 % is observed. While the aluminium profile test section offers a good RMSE spread of the drag reduction, the drag penalty must also be considered when interpreting the results from each test section. One explanation may be the ramp in the MDF test section causing a positive pressure gradient along the streamwise direction.

4.2.2. Quality of the delta drag results

The quality of drag delta results for each test plate-orientation pairing are evaluated according to a set of criteria:

1. Is the corrected drag largely independent of the pressure drag correction (**PD**)
2. Is the RMSE smaller than the half of the corrected drag delta(**RMSE**)

The result of this evaluation is shown in Table 4.3. The test plate-orientation pairings that satisfy every criterion are highlighted in green. While over half of the test plate-orientation pairings achieved drag reduction, a majority of those results had pressure drag corrections close to that of the raw drag. Most of the pairings had a satisfactory RMSE spread according to criteria (2). Only four pairings out of the 22 had a result with satisfactory quality. Within these four, two pairings observed a drag reduction; namely the CC207 Rev. and CC208 Norm. compliant surfaces, with the CC207 Rev. having a drag reduction of 3.44%. Also, the surface texture of these two compliant surfaces were of good quality, with only the oily patterns present on the surface. Furthermore, the CC207 Rev. compliant surface was tacky enough to properly adhere to the aluminium test plate, diminishing the need to apply silicone adhesive at the edges, meaning that the compliant surface edges are in better shape compared to the other compliant surfaces. This compliant surface was also the thickest and softest out of all the 11 compliant surfaces.

Table 4.3. Quality evaluation of drag delta measurements from the Hill. Green-coloured cells with a V means passing of criterion

Test plate	Orientation	PD	RMSE
CC203	Norm.	V	V
	Rev.		
CC204	Norm.		V
	Rev.		
CC205	Norm.		V
	Rev.		V
CC207	Norm.		V
	Rev.	V	V
CC208	Norm.	V	V
	Rev.	V	
CC209	Norm.		V
	Rev.		V
CC210	Norm.		
	Rev.		V
CC211	Norm.		V
	Rev.		V
CC212	Norm.		V
	Rev.		
CC213	Norm.		V
	Rev.	V	V
CC214	Norm.		V
	Rev.		V

4.3. Hot-wire Anemometry (HWA)

In this section, the 1D velocity profile measured by the hot-wire anemometry of the Hill is presented and verified.

4.3.1. Boundary layer profile

HWA was conducted for the reference test plate TP0000 and the drag-reducing compliant surface test plate CC207 Rev. near the trailing edge. Figure 4.17 shows the consolidated normalised mean streamwise velocity profile (4.17a) and 1D turbulence intensity (4.17b). The mean streamwise velocity boundary layer profiles for the two plates were plugged into the boundary layer characterisation scheme based on Rodríguez-López et al. (2015) embedded with a DE algorithm; the results are shown in Figure 4.18. With the blue and red scatter plots indicating the TP0000 and CC207 Rev. test plates, the corresponding black curves are the respective curve fits of the data points. The curve regression has a R^2 value of 0.9997 and 0.9827 for the TP0000 and CC207 Rev. test plates, respectively; this indicates a regression with good quality.

The mean streamwise velocity profile in Figure 4.17a for CC207 Rev. is seen to be slightly lifted upwards in comparison with TP0000. This uplift is coupled with the reduced 1D turbulence intensity in Figure 4.17b. These observations coincide well with the drag reduction that was observed for the CC207 Rev. compliant surface. However, a downshift of the logarithmic layer is observed, which is the opposite of the results of Choi et al. (1997).

4.3.2. Verification by Welch's t-test

Welch's t-test was conducted on the hot-wire voltage signal for the hot-wire measurements of TP0000 ,and CC207 Rev. The raw voltage signal from the hot-wire probe and the Welch's t-test on the signal is presented in Figure 4.19 and 4.20, respectively. For wall-normal locations near and far from the wall, the t-values extend well beyond the critical t-value of 99.9% CI. However, t-values of the signals at the middle portion of the boundary layer approach the zero t-value line.

Figure 4.21 provides a zoomed-in view of the region in question. The cut-off portions of the boundary layer exceed the 99.9% CI critical t-value. More points gather around the zero t-value line at the lower portion more than at the higher portion of this range. At the lower half, points at $10 < y$ [mm] < 15 congregate together

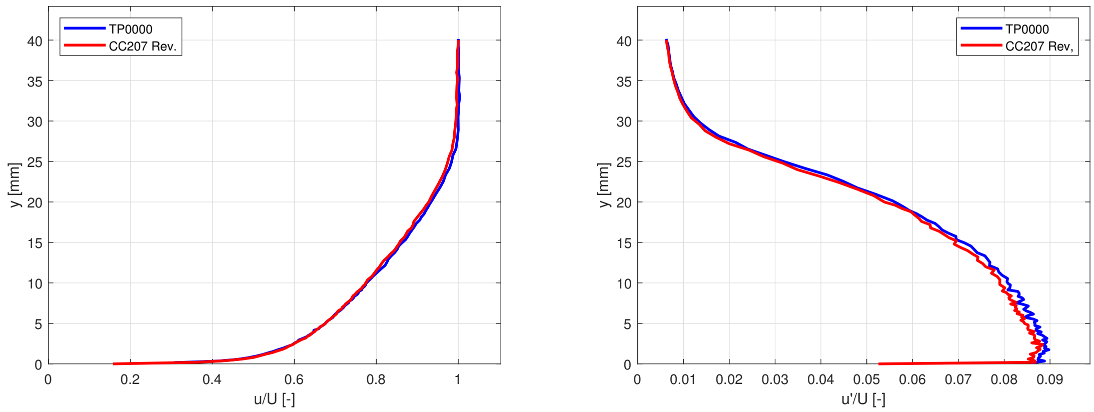

(a) Mean streamwise velocity

(b) 1D turbulence intensity

Figure 4.17. The consolidated normalised boundary layer profiles of TP0000 and CC207 Rev. from the hot-wire of the Hill

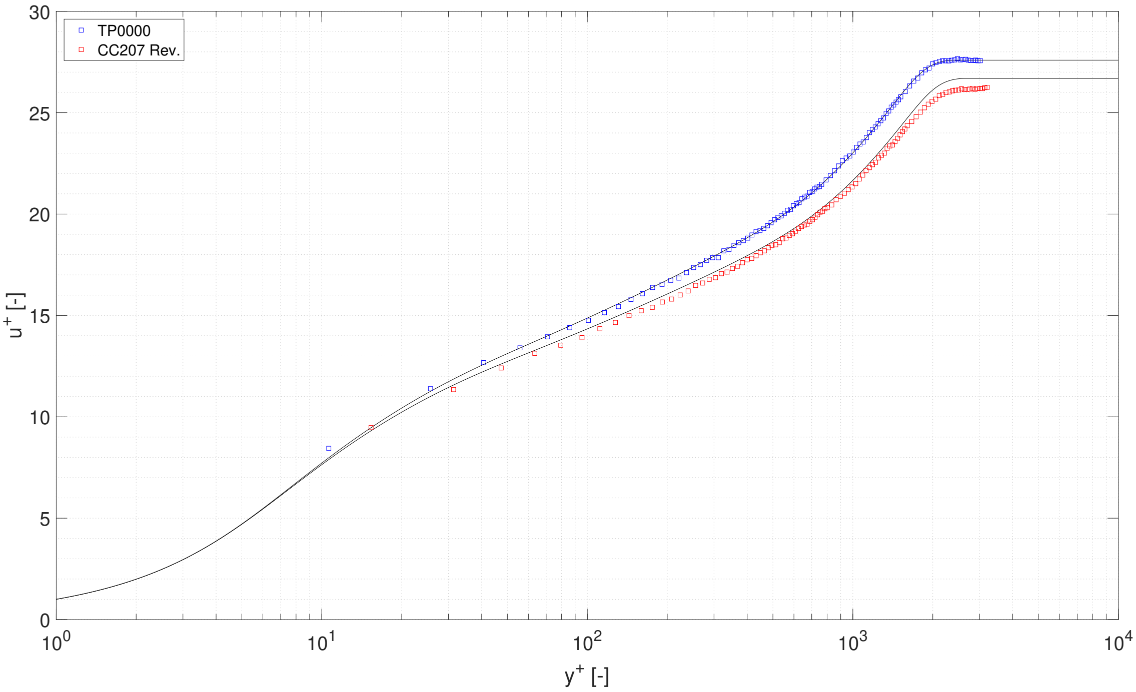

Figure 4.18. Results of boundary layer characterisation of TP0000 and CC207 Rev. boundary layer profiles based on method by Rodríguez-López et al. (2015)

near the zero-value, which coincides with the gap in 1D turbulence intensity seen in Figure 4.17b. However, the t-values then fall beyond the 99.9 CI critical t-value when moving towards the wall, where the most significant discrepancy in the turbulence intensity is observed. This outcome gives confidence in the reduction of turbulence intensity by CC207 Rev., further supporting the existence of drag reduction.

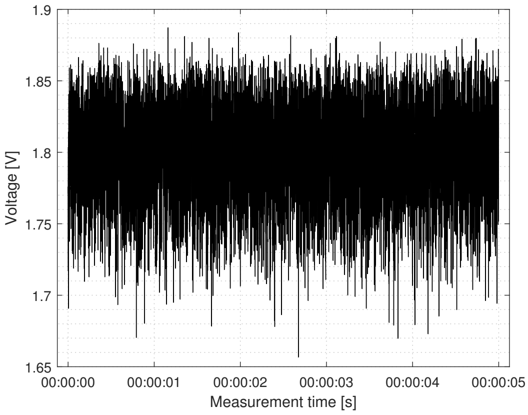

Figure 4.19. The raw voltage signal from the hot-wire probe of one velocity point

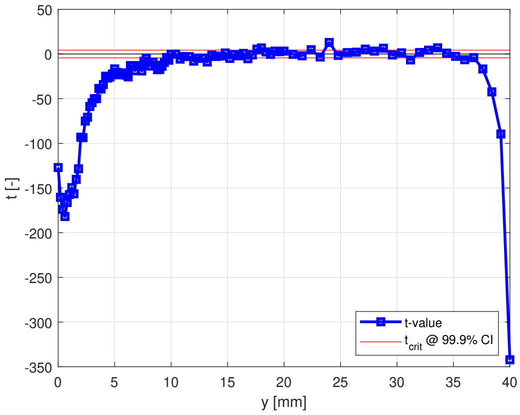

Figure 4.20. t-values of HWA voltage signal for TP0000 and CC207 Rev.

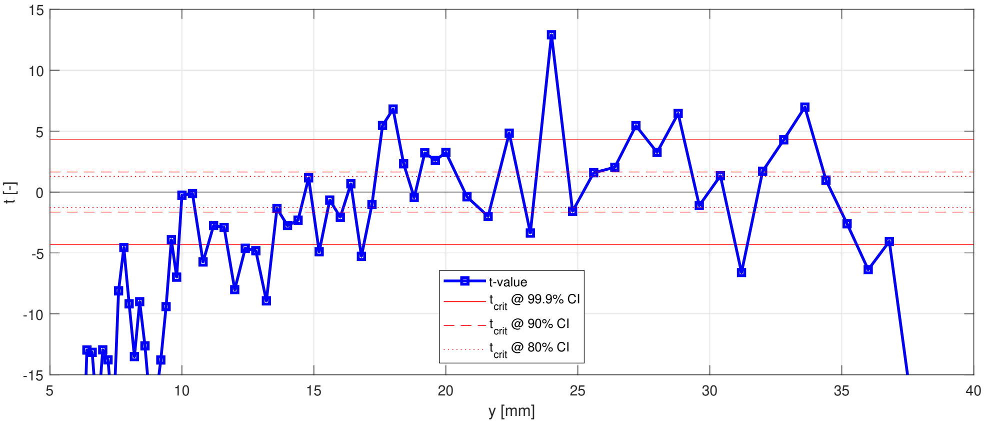

Figure 4.21. Zoomed-in view of Figure 4.20

4.4. Flow visualisation

In this section, the results of the flow visualisation by PIV are presented and verified. Due to the large amount of data acquired and the time frame of this research, only the raw images acquired from the highest velocity ($u_\infty = 35$ m/s) were processed. The FSI is expected to be the most prominent at this highest velocity.

4.4.1. Selection of compliant surfaces for flow visualisation

Out of all the test plate-orientation pairings, the CC207 Rev. observed the most drag reduction and simultaneously had quality results. The results were also repeatable for a second time ten days after the first measurement (fig. 4.15a). Furthermore, the drag reduction was more significant than the other good-quality drag-reducing test plate- orientation pairing: CC208 Norm. In addition, the boundary layer profile of the 1D turbulence intensity was reduced in comparison with the reference flat plate TP0000 (fig. 4.17b). Therefore, the drag-reducing CC207 Rev. compliant surface was chosen for flow visualisation experiments by PIV. Alongside CC207 Rev., the drag-increasing compliant surface CC204 Norm. was chosen for comparison; this selection was due to the obvious drag increase even after a large pressure correction, and also good surface texture qualities.

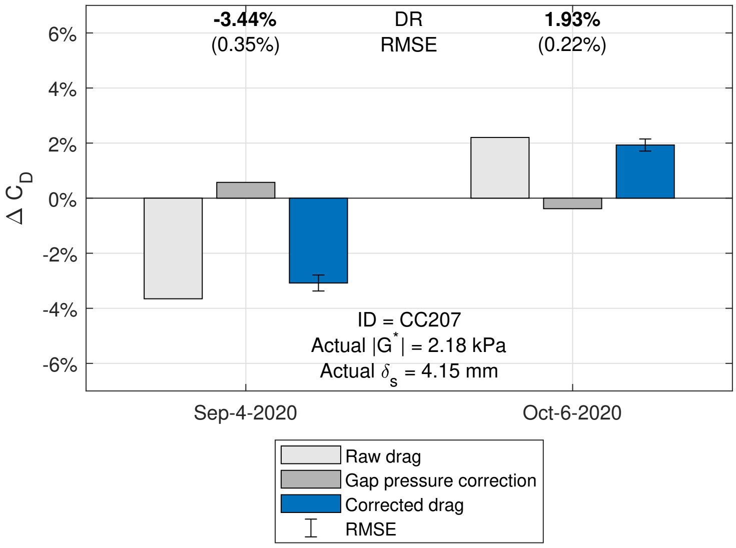

Figure 4.22. The discrepancy between drag delta for CC207 Rev. measured at two separate times.

While the first and second measurement of the CC207 Rev. compliant surface exhibited drag reduction, a third drag delta measurement conducted right before the PIV measurements indicated a drag increase. The results of the second (Sep-4-2020) and third (Oct-6-2020) measurement are shown in Figure 4.22. The drag delta was taken at the second-highest velocity for both measurements, since high RMSE was present at the third measurement's highest velocity. Notably, the pressure drag correction and the RMSE spread for both the second and third measurement is of good quality. A drag delta difference of 5.37% is observed between the measurements. The possible reason for this change may be two-fold. For the second and third measurement, the MDF and aluminium profile test section were used, respectively. The drag penalty (fig. 4.16a) measured on the riblet foil plates may be present on the compliant surface test plates. However, the drag penalty for the riblet foil plates does not sufficiently explain the drag penalty for the compliant surface.

The other difference was the change of properties in the compliant surface. Slight shrinkage of the surface was observed when placed within the Hill; this coupled with a changed weight distribution of the surface, where the connector tray did not properly oscillate. This was thought to be due to the ageing of the material. The compliant surface test plate had to be slightly bent to spread out the test plate's weight distribution on the titanium flexures. However, the Shore durometer measurements of the compliant surface at the third drag delta measurement was consistent with the Shore durometer measurements during the first and second drag delta measurements. This is supported by the ageing study for PlatSil Gel OO in Section 4.1.2. Given the consistent stiffness, which is assumed to be of first order influence to the FSI, the CC207 Rev. is still of interest for flow visualisation by PIV.

4.4.2. Raw images

Figure 4.23 shows the raw images of the sixth panoramic view FOV at $u_\infty = 35$ m/s. The flow is moving from the right to the left side of the images, coinciding with the camera setup and its positioning relative to the air flow. All raw and pre-processed images follow this sign convention. For all of the test plates, the moving particles in the flow have been sufficiently captured by the camera. The laser sheet reflections on the surface, indicated by the white band near the wall, are more prominent on the compliant surfaces. This reflection region for the compliant surface test plates and the reference test plate are approximately 1 mm and 0.25 mm thick. This is even after adjusting the camera's vertical position to reduce the reflection being captured. The reflections from the compliant surfaces are also non-uniform throughout the streamwise direction, in contrast with the reference plate TP0000. Light speckles are also present on the compliant surfaces, which are the reflection of laser sheet on the dust particles adhering to the compliant surface. While it was possible to wipe off the dust for TP0000 with precision wipes, further contact with the compliant surfaces deteriorated the surface finish quality. While the dust speckles did provoke a loss of data points near the wall, it was not prevalent throughout the streamwise direction, as can be seen in Figure 4.23b.

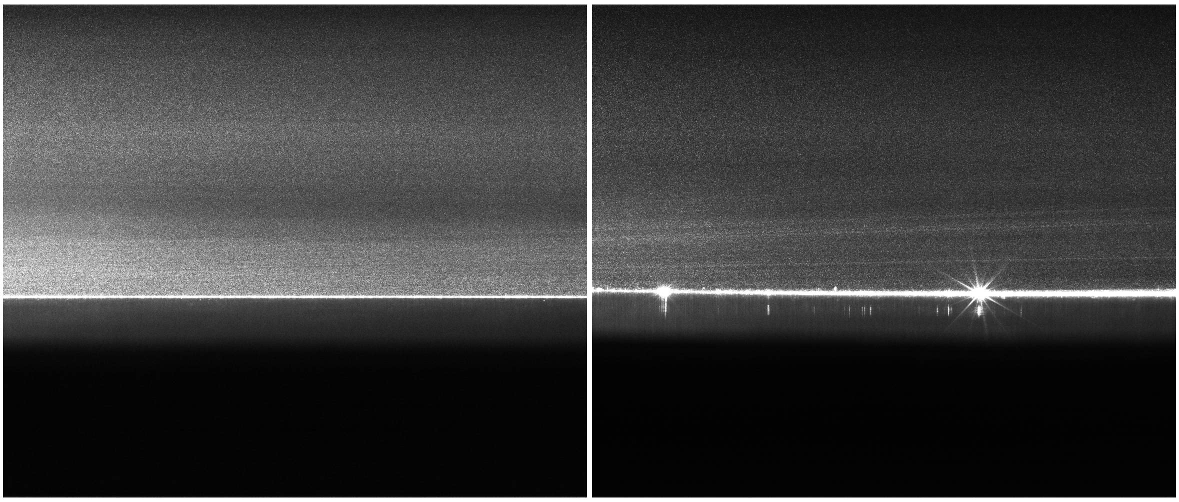

(a) TP0000 **(b)** CC207 Rev.

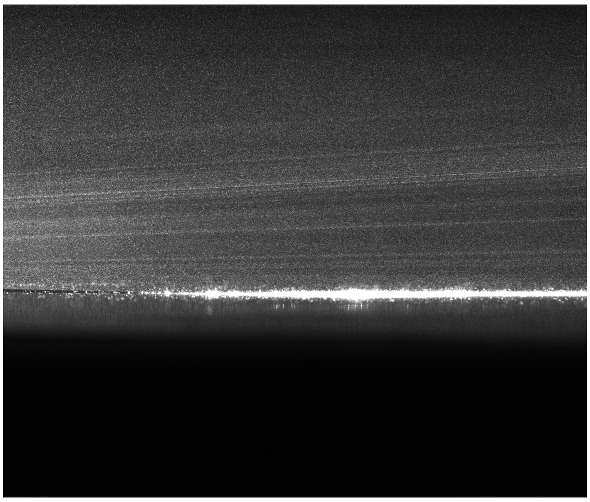

(c) CC204 Norm.

Figure 4.23. Raw images of the 6th panoramic view FOV at $u_\infty = 30$ m/s

Laser light rays are observed on top of the compliant surfaces in Figure 4.23b and 4.23c. This is assumed to be the effect of the surface textures mentioned in Section 4.1.1, and the slight bending of the test plates due to the spacers at the bottom of the test plate. The light rays did not have an observed effect on the cross-correlation of the images. The changing flow velocity also contributed to the test plate's bending; this bending can be seen in Figure 4.24, which is a stacked image of the FOV of CC207 Rev. compliant near the trailing edge at u_∞ =10 and 35 m/s. The moving white band at the wall indicates the flexing of the compliant surface test plate, which the bottom and top white band is at u_∞ = 10 and 35 m/s, respectively. The vertical displacement is approximately 1.3 mm, which was more prominent at FOVs approaching the trailing edge. The same flexing was also present for the CC204 Norm. compliant surface. Therefore, due to the different positions of the wall for each plate, different masking settings were also applied for each test plate at each FOV.

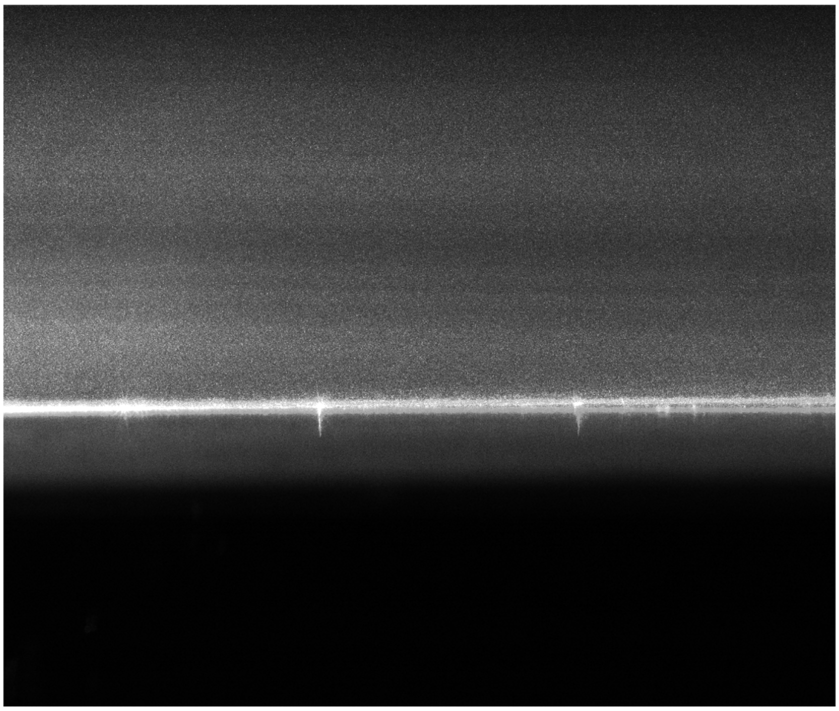

Figure 4.24. Stacked image of FOV near the trailing edge of the CC207 Rev. test plate at u_∞ =10 and 35 m/s

4.4.3. Preprocessing

The raw images taken were pre-processed before conducting the cross-correlation to acquire the 2D velocity vector field. First, the two 300 image-pair data sets are masked with the same masking settings. Then, each data sets minimum intensity is subtracted from each data set to reduce local background noise. The two data sets are then appended together to form the 600 image-pair data set for the cross-correlation analysis. The before and after the subtraction of the minimum intensity for every test plate is shown in Figure 4.25, 4.26, and 4.27. This is the sixth FOV of the panorama view at u_∞ = 35 m/s; the air flows from the right to the left of the image. The contrast of intensity between the background and particles for every test plate is properly enhanced by the subtraction of the minimum intensity.

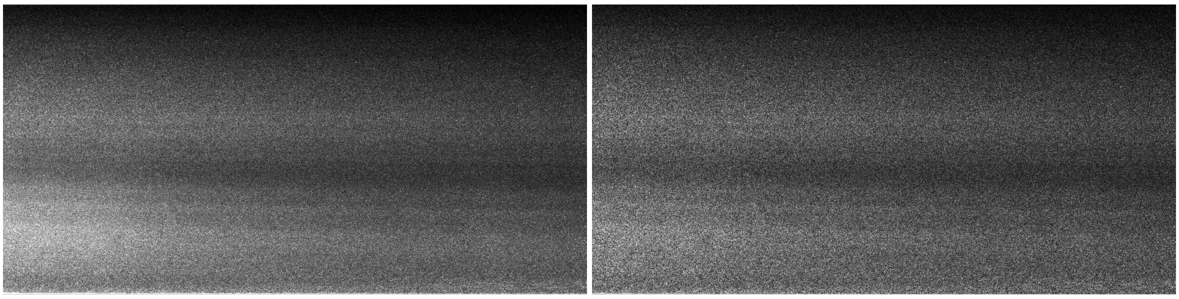

(a) Before (b) After

Figure 4.25. The subtraction of minimum intensity for masked FOVs of TP0000

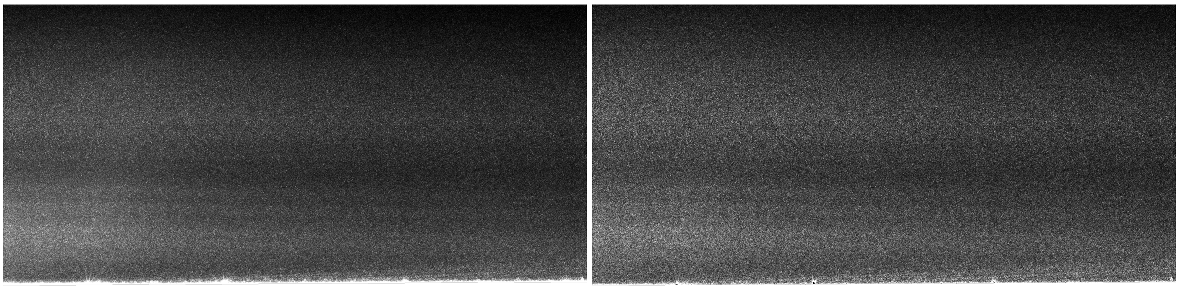

(a) Before (b) After

Figure 4.26. The subtraction of minimum intensity for masked FOVs of CC207 Rev.

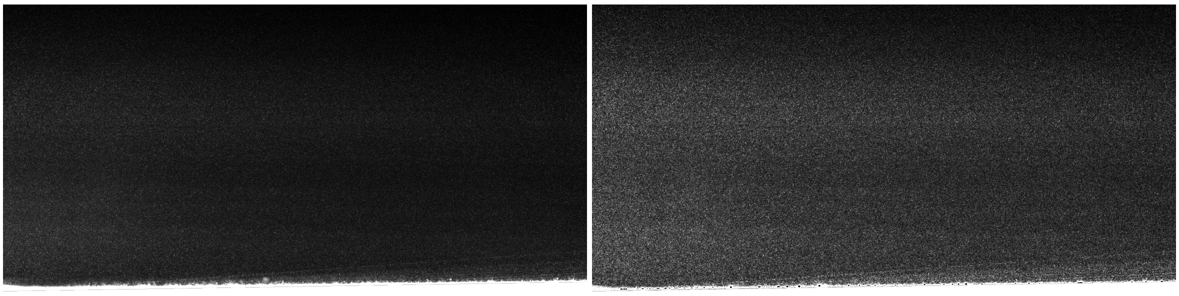

(a) Before (b) After

Figure 4.27. The subtraction of minimum intensity for masked FOVs of CC204 Norm.

4.4.4. 2D velocity field

The 2D velocity field resulting from the cross-correlation of image pairs for the panorama and zoomed-in view are shown in Figure 4.28, 4.29, and 4.30 at $u_\infty = 35$ m/s; the instantaneous streamwise velocity component is shown here in the contour plots. The flow direction is aligned to the x axis, flowing from left to right of the figure. All processed data follow this sign convention. For the panorama view, the sixth FOV is shown; for the zoomed-in view, the trailing edge FOV is shown. For both views, the scale of the axes were set to the same. The x and y locations are based on the scaling settings within DaVis. The different sizes of the FOV are due to different masking settings applied for each test plate and FOV

The outcome of the cross-correlation of the pre-processed image pairs properly visualises the flow. The flow structure within the turbulent boundary layer are slightly visible with the cloud like contours. Also, the streamwise velocity contours exhibit an approximately 15° line with the wall at several locations in the FOV. The effect of the dust reflection is present in the cross-correlation (the blue blot), comparing Figure 4.29a with Figure 4.26. However, pixelated regions are present within the FOV, which is thought to be an artefact of the small interrogation windows used in the final passes of cross-correlation.

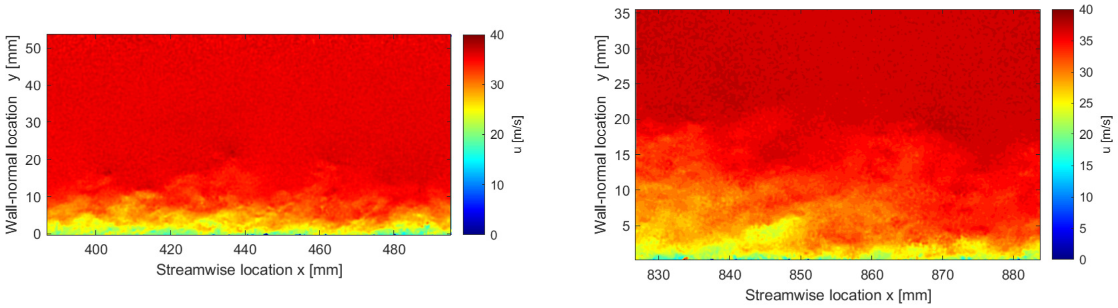

(a) Panorama **(b)** Zoomed-in

Figure 4.28. Instantaneous streamwise velocity field for TP0000

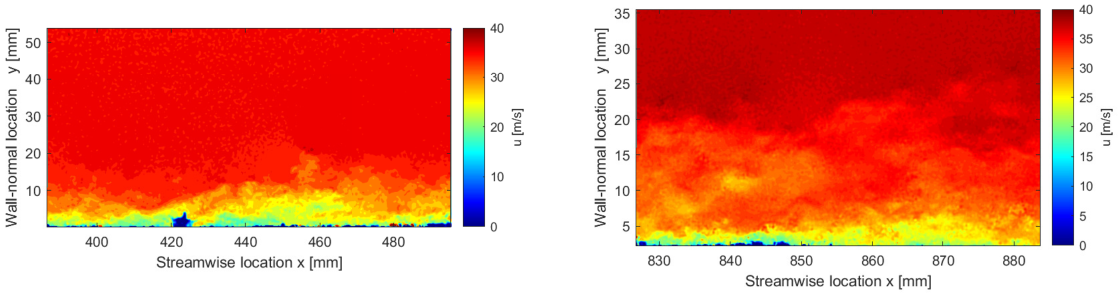

(a) Panorama **(b)** Zoomed-in

Figure 4.29. Instantaneous streamwise velocity field for CC207 Rev.

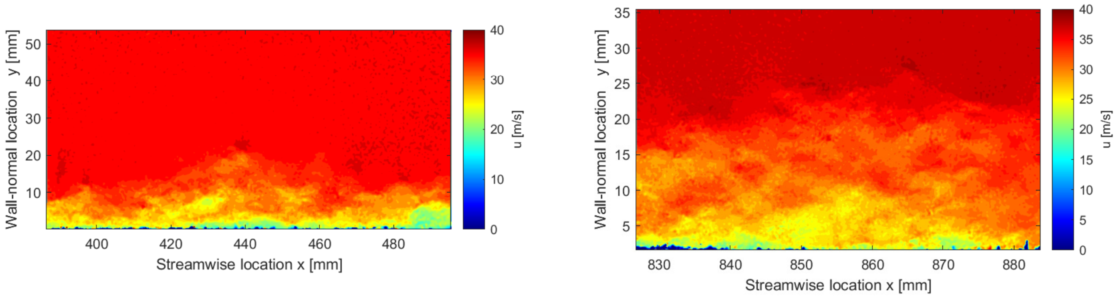

(a) Panorama **(b)** Zoomed-in

Figure 4.30. Instantaneous streamwise velocity field for CC204 Norm.

4.4.5. Uncertainty quantification

The uncertainty of the mean and perturbation component of the velocity resolved from PIV is quantified. A method by Benedict and Gould (1996) defines the uncertainty of the mean and perturbation component of the velocity with:

$$\varepsilon_{\bar{\mathbf{u}}_i} = \frac{\mathbf{u}'_i}{\sqrt{N}} \tag{4.1}$$

$$\varepsilon_{\mathbf{u}'_i} = \frac{\mathbf{u}'_i}{\sqrt{2N}} \tag{4.2}$$

where N signifies the ensemble sample size, which is 600 in this research. The uncertainty for the PIV experiments at $u_\infty = 35$ m/s for each test plate and view is shown in Figure 4.31, as a percentage of the free-stream velocity u_∞. The mean value of all the FOVs for each test plate and view is shown in Table 4.4. For the trailing edge zoomed-in view of the CC204 Rev. test plate, only 300 image pairs were acquired due to local measurement errors. The uncertainty for this specific case is shown in Table 4.5. While slight variations in uncertainty can be seen between the different test plates, the uncertainty significantly small compared to a free-stream velocity of $u_\infty = 35$ m/s. Therefore, it is deemed that the uncertainty is inconsequential.

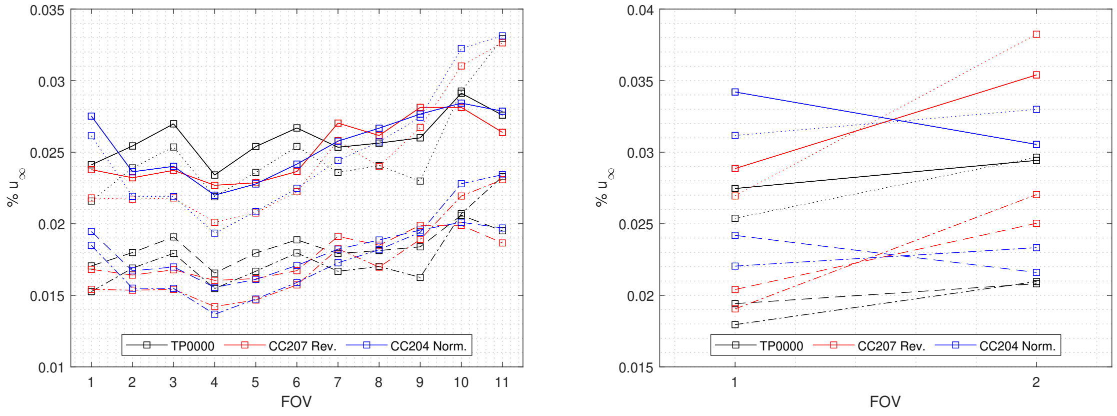

(a) Panorama view

(b) Zoomed-in view

Figure 4.31. Uncertainty quantification of the flow velocities from the PIV data at $u_\infty = 35$ m/s and $N = 600$ as % u_∞. The solid, dashed, dotted, dot-dash lines are the uncertainty for the mean streamwise velocity, streamwise velocity fluctuation, mean wall-normal velocity, and wall-normal velocity fluctuation.

Table 4.4. Mean uncertainty of the flow velocities from the PIV data for all test plates and views at $u_\infty = 35$ m/s and $N = 600$ as % u_∞

(a) Panorama

Panorama	$\varepsilon_{\bar{u}}$	$\varepsilon_{u'}$	ε_{v}	$\varepsilon_{v'}$
TP0000	0.026	0.018	0.025	0.018
CC207 Rev.	0.025	0.019	0.024	0.017
CC204 Norm.	0.026	0.018	0.025	0.018

(b) Zoomed-in

Zoomed-in	$\varepsilon_{\bar{u}}$	$\varepsilon_{u'}$	ε_{v}	$\varepsilon_{v'}$
TP0000	0.028	0.020	0.028	0.020
CC207 Rev.	0.032	0.023	0.033	0.023
CC204 Norm.	0.032	0.023	0.032	0.023

Table 4.5. Uncertainty quantification of the flow velocities for the trailing edge FOV of the CC204 Norm. at $u_\infty = 35$ m/s and $N = 300$ as % u_∞

$\varepsilon_{\bar{u}}$	$\varepsilon_{u'}$	ε_{v}	$\varepsilon_{v'}$
0.043	0.031	0.047	0.033

The propagation of error for the product of the velocity fluctuations must also be verified, since it signifies the magnitude of the Reynolds stresses. For a product of multiplication or division of multiple variables:

$$Q = \frac{ab\cdots c}{xy\cdots z} \tag{4.3}$$

The uncertainty of each variable propagates according to:

$$\varepsilon_Q = |Q|\sqrt{\left(\frac{\varepsilon_a}{a}\right)^2 + \left(\frac{\varepsilon_b}{b}\right)^2 + \cdots + \left(\frac{\varepsilon_c}{c}\right)^2 + \left(\frac{\varepsilon_x}{x}\right)^2 + \left(\frac{\varepsilon_y}{y}\right)^2 + \cdots + \left(\frac{\varepsilon_z}{z}\right)^2} \tag{4.4}$$

Identical plots and tables are made for the propagation of uncertainty in the Reynolds stresses, and these are shown in Figure 4.32, Table 4.6 and 4.7. The same can be said for the uncertainty propagation in the Reynolds stresses; its magnitude is fairly small compared with the free-stream velocity of $u_\infty = 35 m/s$, and therefore deemed inconsequential.

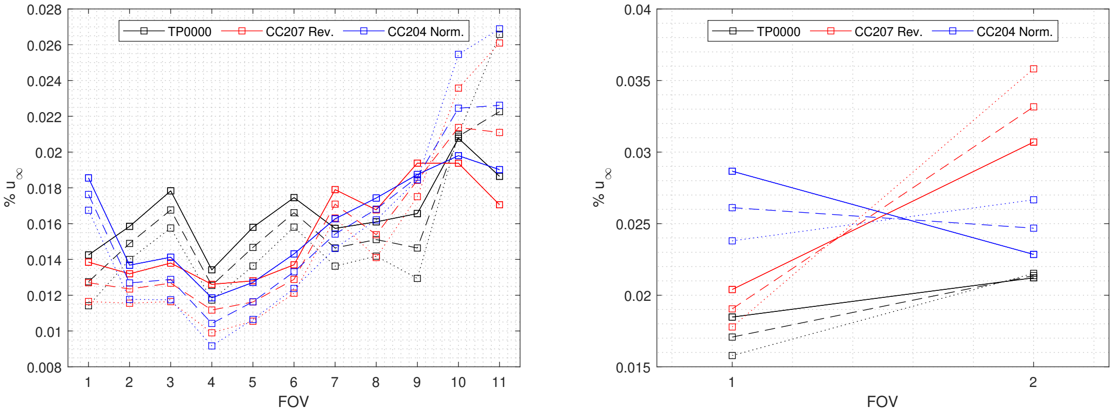

(a) Panorama view

(b) Zoomed-in view

Figure 4.32. Uncertainty quantification of the Reynolds stresses from the PIV data at $u_\infty = 35$ m/s and $N = 600$ as % u_∞. The solid, dashed, dotted lines are the uncertainty for the $u'u'$, $u'v'$, and $v'v'$ components of the Reynolds stress tensor.

Table 4.6. Mean uncertainty of the Reynolds stresses from the PIV data for all test plates and views at $u_\infty = 35$ m/s and $N = 600$ as % u_∞

(a) Panorama

Panorama	$\varepsilon_{u'u'}$	$\varepsilon_{u'v'}$	$\varepsilon_{v'v'}$
TP0000	0.017	0.016	0.016
CC207 Rev.	0.016	0.015	0.016
CC204 Norm.	0.016	0.016	0.016

(b) Zoomed-in

Zoomed-in	$\varepsilon_{u'u'}$	$\varepsilon_{u'v'}$	$\varepsilon_{v'v'}$
TP0000	0.020	0.019	0.019
CC207 Rev.	0.026	0.026	0.027
CC204 Norm.	0.026	0.025	0.025

Table 4.7. Uncertainty quantification trailing edge FOV of the CC204 Norm. at $u_\infty = 35$ m/s and $N = 300$ as % u_∞

$\varepsilon_{u'u'}$	$\varepsilon_{u'v'}$	$\varepsilon_{v'v'}$
0.032	0.035	0.038

5

Discussion of results

The correlation between all experimental results is discussed in this chapter. From material measurements in the rheometer to the flow experiments in the wind tunnel using the Hill and PIV, it is aimed to pinpoint the parameter space of turbulent drag reduction, and see what effect the FSI has on the flow. Section 5.1 discusses the correlation between the drag delta and the viscoelastic properties of the compliant surface. Section 5.2 investigates the streamwise evolution of the mean boundary layer properties by characterising the boundary layer data from the panorama view of the PIV. Finally, Section 5.3 examines the Reynolds stress production of the flow by conducting quadrant analysis on the zoomed-in view of the PIV.

5.1. Correlation between drag delta and viscoelastic properties

Figure 5.1 shows the interpolated and extrapolated drag reduction contour plot with respect to the magnitude of complex shear modulus and thickness of the compliant surface. The compliant surface test plates measured in the Hill are marked with black circles; the filled-in circles are the quality data points considered in Table 4.3, and are used for the interpolation and extrapolation of the shown contour. Natural neighbour interpolation and linear extrapolation were used. Red and green contours indicate a negative and positive drag delta, respectively. The drag delta considered was measured at the highest Reynolds number. For each compliant surface, the streamwise orientation with the lower RMSE is selected. The CC203 compliant surface's stiffness was converted from a Shore durometer measurement of the surface using a method by Mix and Giacomin (2011). The conversion chart is included in Appendix C. This was due to underestimating the mixture amount during the manufacture, rendering it impossible to make a rheometer sample.

A general trend of decreasing drag is observed when moving towards the thicker and softer parameter space. A dividing white line is observed in the contour plot which indicates zero drag delta, with the isocontour lines largely orthogonal to the direction towards the upper-left corner of the contour plot. This trend is the outcome of the CC207 Rev. compliant surface, which is the top-left circle in the contour plot. CC207 Rev. measured a drag reduction of 3.44% with $\delta_s = 4.15$ mm and $|G^*| = 2.18$ kPa. The RMSE of this measurement was 0.35%. This measurement fits the criteria where the RMSE and the pressure drag correction are low, and the drag reduction does not have a dependence on the pressure drag correction.

The outer scaling ratios for this drag-reducing compliant surface, CC207 Rev., is compared with the outer scaling reference cases (from table 3.1) in Figure 5.2. For this research, the mean of density and velocity of the air flow was taken at the highest measurement velocity for the first and second drag-reduction measurement. The compliant surface density was directly taken from the technical data sheet of the PlatSil Gel OO, which gives the density of the cured product (table B.1). For the reference cases, the flow and material properties are the values mentioned in Table 3.1, with the density of air and water taken at a fixed value of 1.2 kg/m^3 and 997 kg/m^3, respectively. Experiments in air are colour-coded in red, with water experiments in blue.

For the density ratio, a clear distinction is made between the air and water experiments. This distinction is because the RTV silicone was used for all of these cases. Therefore the flow density has a more significant effect on the density ratio than the flow density. For the velocity ratio, this research's compliant surface has a relatively high value compared to the reference cases considered. This is due to the coupling of a high flow velocity and low magnitude of complex shear modulus. As for the inertia ratio, the spread for all the cases converges well within a certain range, compared to the density and velocity ratio. This gives rise to the

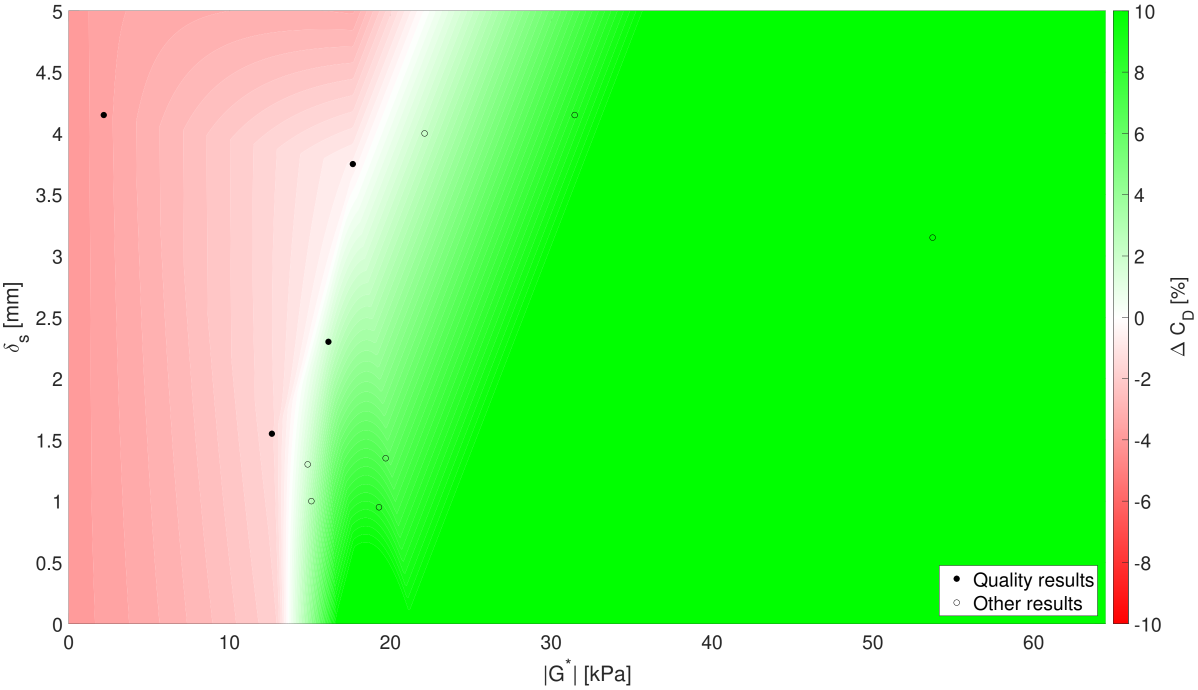

Figure 5.1. Drag reduction contour plot with respect to compliant surface thickness and stiffness

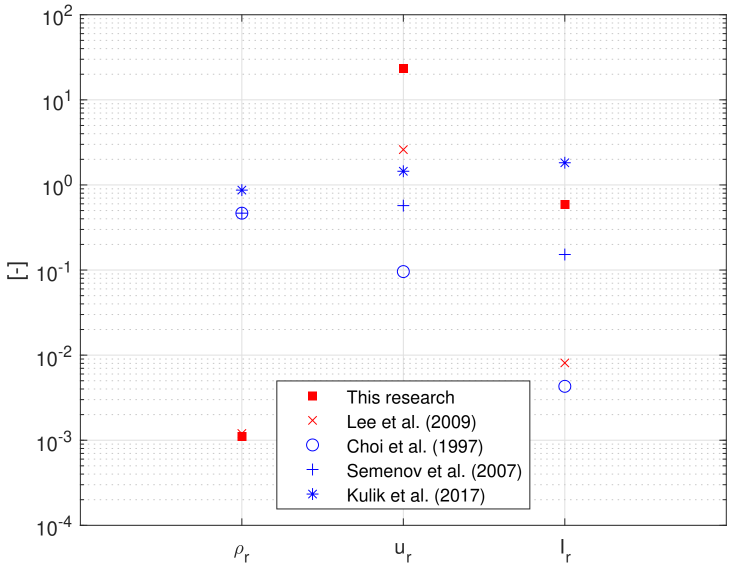

Figure 5.2. The density, velocity, and inertial ratio of CC207 Rev. at the highest measurement velocity, compared with the outer scaling cases. Water and air experiments are colour-coded in blue and red, respectively

possibility that the inertia ratio should fall within a certain range for a drag-reducing compliant surface. The magnitude of the inertia ratio acquired from both the air and water experiments congregates, contrary to the density and velocity ratio. This outcome gives confidence towards the inertia ratio as a better outer scaling parameter when considering the drag reduction of compliant surfaces in various flows.

Plugging in the surface and flow properties to the inertia ratio of instability onset proposed by Duncan (1986) in Equation (2.29), this gives a value of 0.59, which is below the instability onset threshold of 4. Most of the outer scaling cases also fall below this threshold. However, the CC207 Rev. compliant surface does not fall within the drag-reducing range proposed by Semenov (1991) ($50 < t_0^+ < 150$), having a non-dimensional period of $t_0^+ = 557.03$. The drag reduction measured by Choi et al. (1997) also did not fit within this range, where they acquired a non-dimensional period range of $5 < t_0^+ < 44$ (Choi, 2003). These two results shed doubt on the validity of this drag-reducing range proposed by Semenov (1991).

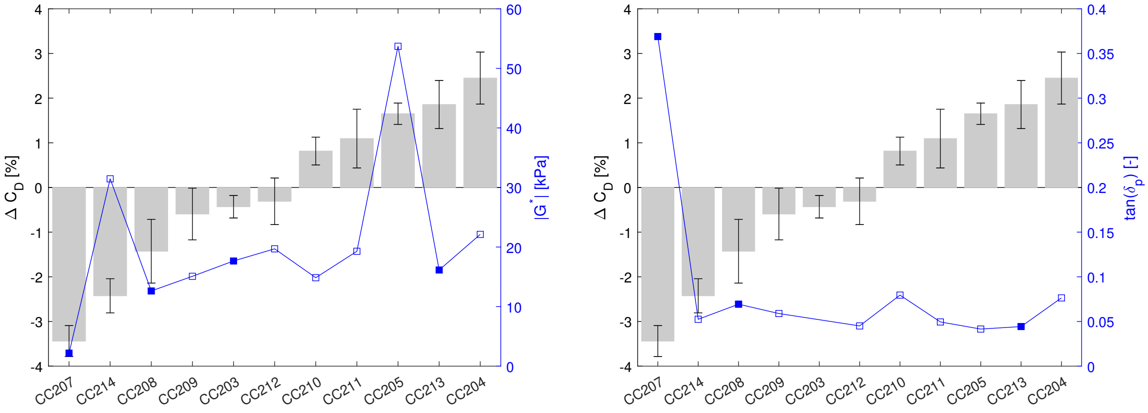

(a) $|G^*|$ **(b)** $\tan(\delta_p)$

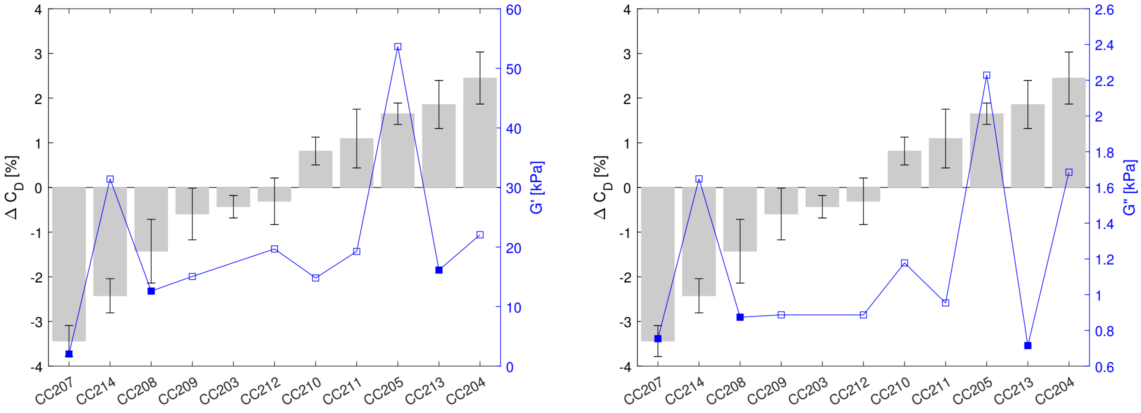

(c) G' **(d)** G''

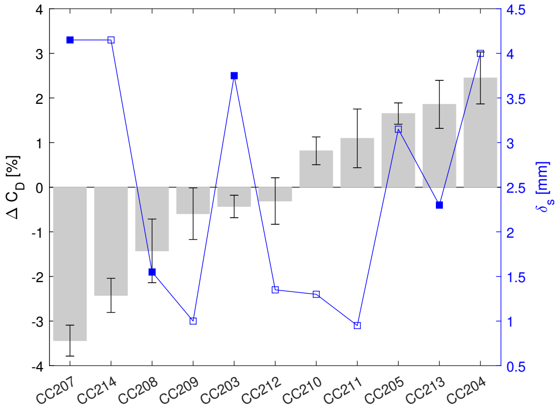

(e) δ_s

Figure 5.3. Correlation between the measured drag delta and various compliant surface viscoelastic properties. The grey bars indicate the drag delta measured for each compliant surface test plate indicated in the x-axis. The error bars indicate the RMSE of each measurement. The blue lines indicate the viscoelastic property of each test plate, the filled in markers indicate quality data from the evaluation in Table 4.3.

The relation between the drag delta and the magnitude of complex shear modulus $|G^*|$, loss tangent $\tan(\delta_p)$, shear storage modulus G', shear loss modulus G'', and the thickness δ_s of the compliant surfaces are plotted in Figure 5.3. The bar chart for all the plots is the same, which is ordered in the magnitude of drag delta from negative (left) to positive (right). The streamwise orientation with a lower RMSE was chosen for each compliant surface. The error bar for each drag delta bar is the RMSE of this measurement. The corresponding material property for each surface is plotted with the blue line, with its axis on the right-hand side of the figure. The filled blue squares correspond to the quality results from the evaluation in Table 4.3. Surface properties other than the magnitude of complex shear modulus is excluded for the CC203 compliant surface since no rheometer sample was manufactured. The magnitude of complex shear modulus for this surface is calculated by the conversion of Shore OO hardness by the method of Mix and Giacomin (2011) (appendix C).

An observable trend is present for the magnitude of complex shear modulus and shear storage modulus, as their magnitude is close due to the small shear loss modulus. An overall decrease of the magnitude of complex shear modulus corresponds with a decrease in drag delta. The same trend can be said for the quality results indicated by the filled marker. The two outlying surfaces, CC214 and CC205, have significantly higher $|G^*|$, G', and G'' comparing with neighbouring drag delta surfaces. These outliers are thought to be local rheometer measurement errors leading to high absolute values. Furthermore, the loss tangent values for the CC214 and CC205 compliant surfaces its values properly follow the same trend in Figure 4.4a with respect to the amount of additive added. In addition, the drag reduction measured for the CC214 is largely dependent on the pressure drag correction. Therefore, these results are disregarded for now.

While the loss tangent levels are quite close for almost all compliant surfaces, the drag-reducing compliant surface has an unusually high loss tangent of 0.37; this is due to the large amount of deadener contained within the mixture. There seems to be a positive correlation between the loss tangent and the drag reduction for the drag-reducing compliant surfaces. While the surfaces with relatively high loss tangent, CC210 and CC204, do not fall in line with this trend, they have relatively high pressure corrections and RMSE for the drag delta measurements. An identical trend can also be observed for the quality results. This trend puts the loss tangent in play for its potential influence on the FSI, joining the likes of the magnitude of complex shear modulus.

No conclusive relation can be drawn from the varying surface thickness with respect to the drag delta. Also, the effect of surface thickness with respect to the same stiffness can not be properly correlated due to the varying stiffness of the original M-shaped test matrix. The compliant surface thickness should also be taken with care due to the inconsistent thickness for the 1 and 2 mm compliant surfaces. Also, the current method of characterising the surface thickness does not take into account the varying surface textures. The characterisation can be improved by using a 3D scan of the surface, or improve the quality of the manufacture for thickness to be consistent throughout the entire compliant surface.

5.2. Boundary layer characterisation of panorama PIV data

The panorama view of the PIV data was used to study the development of mean boundary properties across the test plate. Along the 11 FOVs, 55 evenly spaced streamwise positions from 3 cm in front of the test plate leading edge to its trailing edge are considered for this analysis. Streamwise positions in the overlap zones of the FOVs are taken at both FOVs; the mean boundary layer properties at these locations are taken as the average of the two overlapping points. A further three points are taken on top of the trailing edge of the PHill since the compliant surface reflections are not present. This selection totals up to 58 points per test plate throughout the streamwise direction.

These boundary layer profiles extracted from the PIV data were preprocessed to filter unnatural data points near the wall using the flow velocity's streamwise component. These filtered points mainly source from the laser sheet reflections on the compliant surface, including negative velocities, positive velocity gradients, and linear velocity profiles. The number of data points in the boundary layer profile for every streamwise location after this filtering is shown in Figure 5.4. The reason behind the lower amount of data points for the compliant surfaces are two-fold. First is the loss of data points near the wall due to the laser sheet reflections on the test plate surface. The other reason is the slight flexing of the compliant surface test plates due to the placement of spacers and the air flow. A significant drop is seen around the streamwise position of 500 mm. This drop is due to the upwards shift of the compliant surface due to the spacers placed at the trailing edge. Around ten fewer data points are available for the compliant surfaces than the reference test plate up to a streamwise location of 500 mm. After this location till the test plate trailing edge, the compliant surfaces have around 20 fewer data points. The data points for all test plates converge around the same amount aft of the test plate trailing edge, as the points taken there are above the trailing edge of the PHill where less laser sheet reflections are present.

The filtered profiles were then plugged into the DE boundary characterisation method previously used in the Hill's hot-wire measurements. The output from the characterisation is further filtered by the coefficient of determination R^2 with a value of 0.999. The streamwise points preserved after the R^2 filtering are shown in Figure 5.5, with the number of points shown in Table 5.1. Only the streamwise points preserved by the $R^2 = 0.999$ filter are considered in the upcoming analysis.

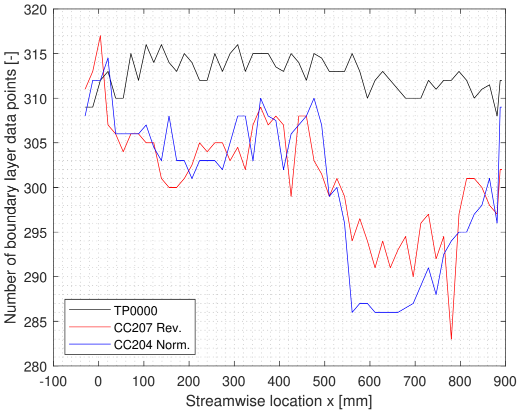

Figure 5.4. The number of wall-normal data points preserved for the boundary layer after filtering out the unnatural data points for each test plate at each streamwise station

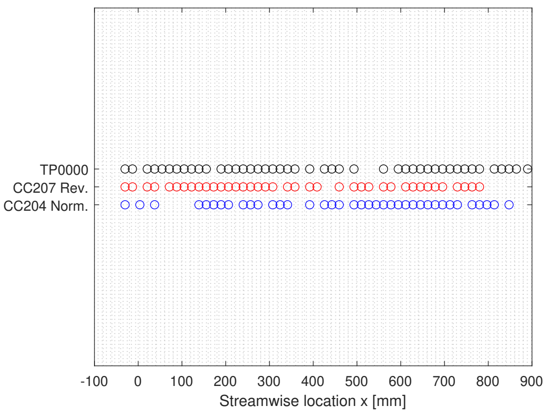

Figure 5.5. The streamwise data points preserved for each test plate at each streamwise location after applying the R^2 filter

Table 5.1. The number of streamwise data points preserved after the R^2 filter

	TP0000	CC207 Rev.	CC204 Norm.
Data points preserved	45	39	38

5.2.1. Resolved depth of the boundary layer

The resolved boundary layer depth of the panorama PIV, namely how close to the wall flow data can be acquired, can be determined from the results of the boundary layer characterisation. The limited into the boundary layer is an artefact of the laser sheet reflections on the compliant surface. The minimum value of the resolved non-dimensionalized wall distance y^+_{min} for each streamwise data point is shown in Figure 5.6. The geometric mean of y^+_{min} for each test plate is shown in Table 5.2.

Table 5.2. The mean y^+_{min} for each test plate

	TP0000	CC207 Rev.	CC204 Norm.
Mean y^+_{min} [-]	61.37	81.66	106.41

The reference test plate has the most depth in data, with several points hitting near $y^+ \sim 30$. As for the compliant surfaces, CC207 Rev. has better data depth out of the two. The depth of the mean y^+_{min} can be correlated with the number of data points kept after unnatural near-wall data point filtering in Figure 5.4 and the R^2 filtering in Figure 5.5. All of these are indications of the severity of reflection for each test plate. TP0000 had the least reflections due to the matte black surface, with CC207 Rev. having fewer reflections than CC204 Norm. This leads to loss of valuable boundary layer information at the lower side of the logarithmic layer, or even below that. Possible solutions to overcome these reflections include mixing matte black pigment into the compliant surface mixture for the test plates to make it opaque. Also, placing a knife-edge just downstream of the test plate could possibly help by only allowing laser just above the test plate to enter the test section, avoiding any reflections on the compliant surface.

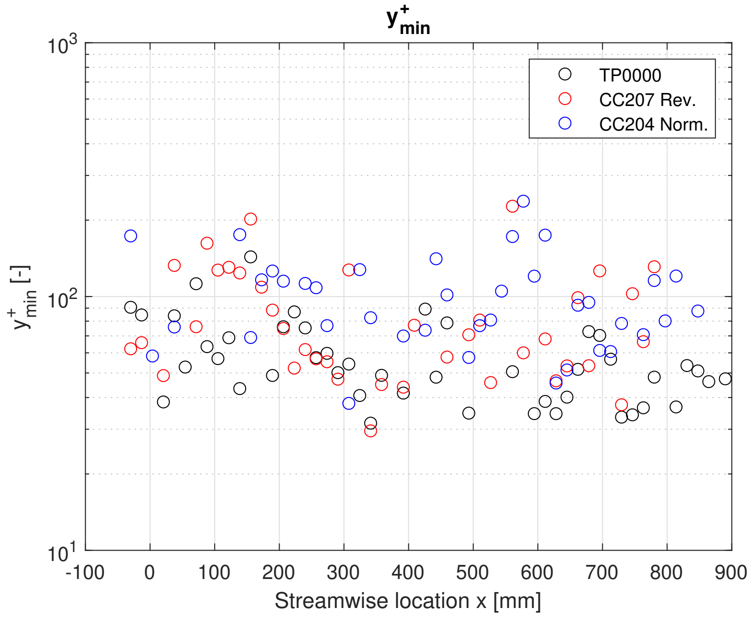

Figure 5.6. The resolved depth of the boundary layer determined from characterisation of PIV data

5.2.2. Streamwise development of mean boundary layer properties

The development of the boundary layer thickness δ_b and the wall-friction velocity u_τ, momentum thickness θ, and displacement thickness δ^* are shown in Figure 5.7. The scatter plot is the data points, with the dashed lines a sliding-average with the neighbouring 2 points. The boundary layer's streamwise development is properly captured by the increasing boundary layer thickness across the test plate. The characterised u_τ, on the other hand, has a large spread even with the R^2 filtered data points. This large spread is due to the sensitivity of the characterisation scheme to the initial conditions near the wall. Since the acquired data from PIV suffers from laser sheet reflections, the near-wall region was not sufficiently resolved to acquire a good grasp of the u_τ. Nevertheless, the outer regions of the boundary layer are well-captured with PIV, with the mean boundary layer properties such as δ_b showing a good trend moving downstream the test plates.

The referenced streamwise development of the momentum thickness θ and the shape factor H are shown in Figure 5.8 and 5.9, both referenced to the initial values for the sliding-average for each test plate. The scattered points are the data points with the dashed line a sliding-average with the neighbouring 2 points, which is the same method as in Figure 5.7. For a flat plate, the momentum thickness' magnitude is a direct indication of the accrued drag. With respect to the drag delta results from the Hill, the momentum thickness delta for the drag-increasing and drag-reducing compliant surfaces should be above and below the reference flat plate, respectively. However, this is not the case in Figure 5.8, as the momentum thickness delta is both smaller than the reference plate for the two compliant surfaces. This discrepancy is an artefact of the less wall-normal data points in the boundary layer for the compliant surfaces. The relative positions of the mean boundary layer property sliding-average curves for each test plate are somewhat consistent with the number of wall-normal data points in the boundary layer along the streamwise direction seen in Figure 5.4.

This result points out the suitability of plugging in the current PIV data to the boundary layer characterisation method by Rodríguez-López et al. (2015). This method is fairly robust with errors of less than 1% as long as at least one data point at $y^+ \leqslant 10$, which is not the case for the current PIV data sets as shown in Table 5.2. A noticeable increase in error is present in the outcome of the characterisation scheme when the available data point closest to the wall moves beyond $y^+ = 10$ (Rodríguez-López et al., 2015). Looking closely and comparing the sliding-average momentum thickness and number of wall-normal data points for the two compliant surfaces, the streamwise location at which the crossover of curves happen is quite consistent. This makes it difficult to draw any conclusions from the characterised mean boundary layer properties shown in Figure 5.7 and 5.8 with confidence.

However, the shape factor's H streamwise development shown in Figure 5.9 possibly sheds some light on the evolution of the flow. For the drag-reducing CC207 Rev. compliant surface, the shape factor has a developing trend with a smaller decrease compared to the reference test plate and the drag-increasing CC204

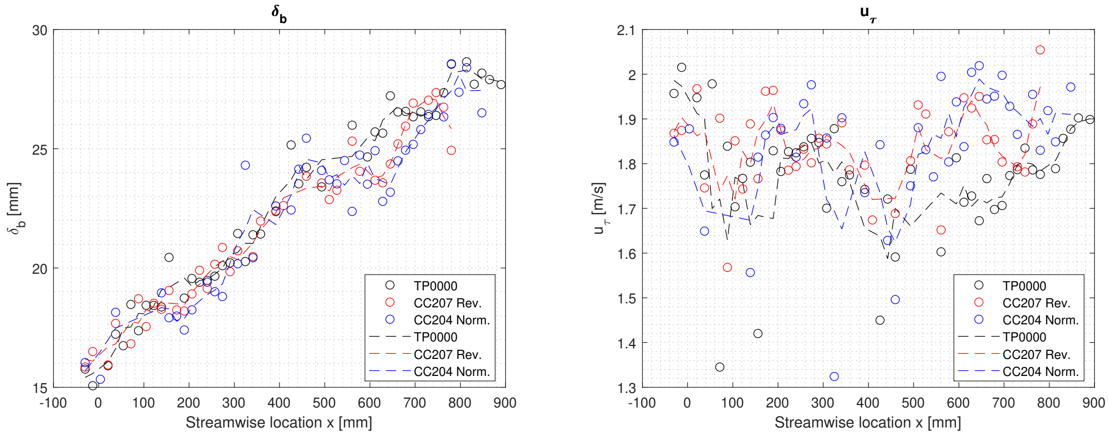

(a) Boundary layer thickness δ_b **(b)** Wall-friction velocity u_τ

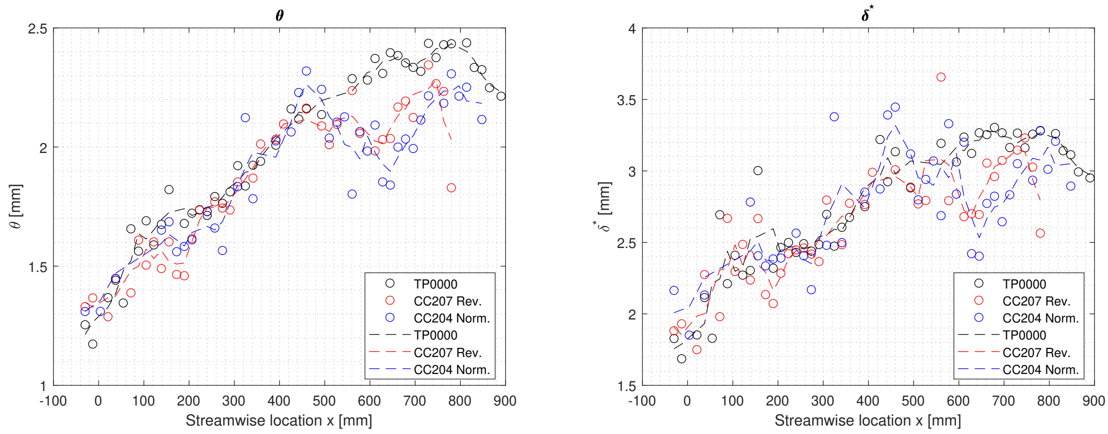

(c) Momentum thickness θ **(d)** Displacement thickness δ^*

Figure 5.7. Streamwise development of the boundary layer thickness δ_b and wall-friction velocity u_τ over the test plates. The circles indicate the data points considered with the dashed lines the sliding average of these data points with the neighbouring two points.

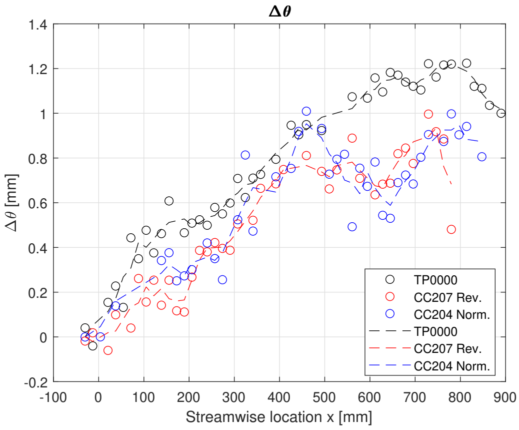

Figure 5.8. Streamwise development of the momentum thickness $\Delta\theta$ referenced to the initial value of the sliding-average curve

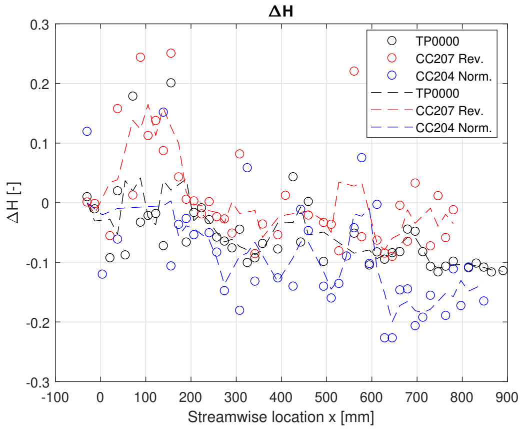

Figure 5.9. Streamwise development of the shape factor ΔH referenced to the initial value of the sliding-average curve

Norm. compliant surface. Furthermore, the drag-increasing compliant surface also shows a larger decrease in the shape factor than the reference plate. A higher shape factor means a leaner boundary layer velocity profile, contrasting with a fuller boundary velocity profile for a lower shape factor. This means that with a lower shape factor, the velocity gradient at the wall is smaller, leading to a smaller magnitude of skin friction. Therefore, the streamwise development of the shape factor in Figure 5.9 gives an indication consistent with the observations made in the drag measurements with the Hill.

The streamwise development of the shape factor shows an evident independence from the artefacts of Figure 5.4 in comparison with the other mean boundary layer properties shown in Figure 5.7 and 5.8. The shape factor is thought to damp out the artefacts by normalisation through the division of the displacement thickness by the momentum thickness. As seen in the momentum thickness, the streamwise development of the displacement thickness in Figure 5.7d also has the same artefacts from the lack of data points near the wall. While some of these artefacts are vaguely present in some locations, the normalising nature of the shape factor gives confidence in the conclusions drawn from these results.

An argument can also be made that while the compliant surface reduces turbulent skin friction, it may increase the pressure drag at the same time. This argument comes together with the third drag delta measurement, where a drag increase was observed. Further investigation is required to resolve the contributions of each drag component.

5.3. Quadrant analysis of zoomed-in PIV Data

Quadrant analysis is conducted on the velocity field of the PIV zoomed-in view FOVs. First, the vorticity field of the FOVs is verified to see if the data properly represents the flow. Then, quadrant analysis of the flowfield is conducted on the two zoomed-in FOVs, and the streamwise change of event occurrence probability is evaluated and discussed. The streamwise evolution of weach test plate's JPDF is also investigated.

5.3.1. Validation of zoomed-in PIV data: Vorticity field

The zoomed-in view of the PIV is used to conduct quadrant analysis of the turbulent boundary layer. Figure 5.10 shows the vorticity field of the leading and trailing edge FOVs of the PIV zoomed-in view for each test plate. The flow direction is from left to right of the figures. The x and y locations are based on the scaling settings within DaVis. The flow structure within the boundary layer is properly visualised by applying the curl to the 2D velocity field to acquire the vorticity field. 2D slices of the 3D coherent structures are seen to be properly visualised, with the head (spanwise-direction vortex) of the hairpin vortices clearly seen. This visualisation gives confidence in the PIV data acquired from the zoomed-in view.

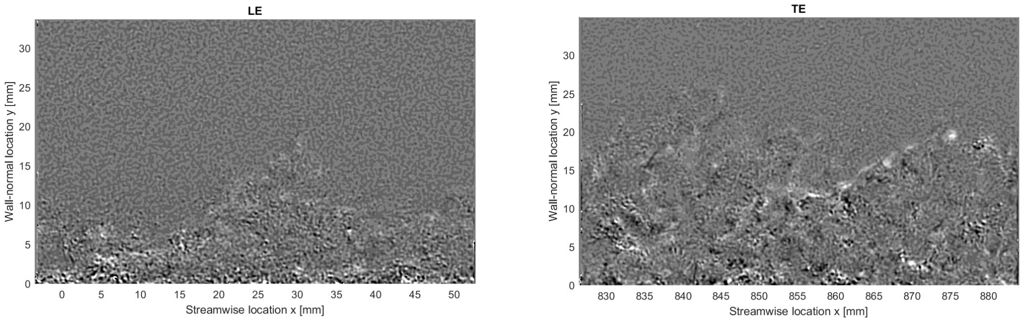

(a) TP0000

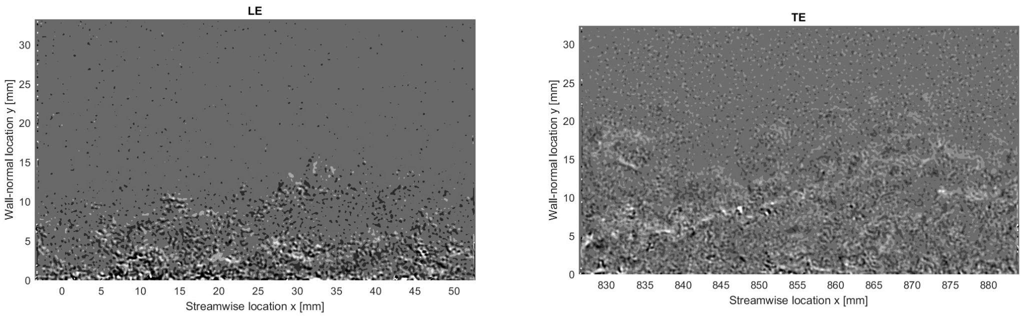

(b) CC207 Rev.

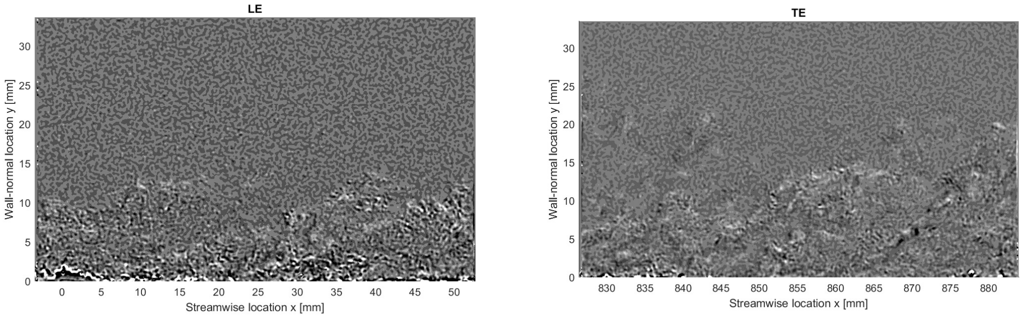

(c) CC204 Norm.

Figure 5.10. Vorticity field contour plot of the leading and trailing edge FOVs of the PIV zoomed-in view.

5.3.2. Quadrant event occurrence probability

Four streamwise locations for each test plate at each zoomed-in FOV were considered for the quadrant analysis. These locations sum up to 2,400 data points (image pairs) for each test plate-FOV pairing to conduct the quadrant analysis. One exception is the CC204 Norm.-trailing edge pairing, where only 300 image pairs were acquired, leading to 1,200 data points. All of the quadrant analysis was conducted at $y^+ = 100$, which is around the outer rim of the buffer layer. This evaluation height was the closest location to the wall where good quality data points were available for all three test plates. While for the reference test plate, the lowest resolved height averaged around $y^+ = 50$, this was not possible for the compliant surfaces due to the laser sheet reflections on the surface.

Figure 5.11 shows the scatter plot of quadrant events at wall-normal distances of $y^+ = 100$ and $y^+ = 30$ from DNS data of Lin (2021) for a turbulent flow above a flat plate. The quadrant events at $y^+ = 100$ still maintain the elliptical distribution typical of turbulent flows, which is also visible at $y^+ = 30$, albeit approaching the circular scatter distribution of isotropic turbulence in the mean flow. While $y^+ = 100$ is not as ideal for quadrant analysis, the artefacts of the quadrant events in turbulent boundary layers are still visible and therefore worthy of analysis.

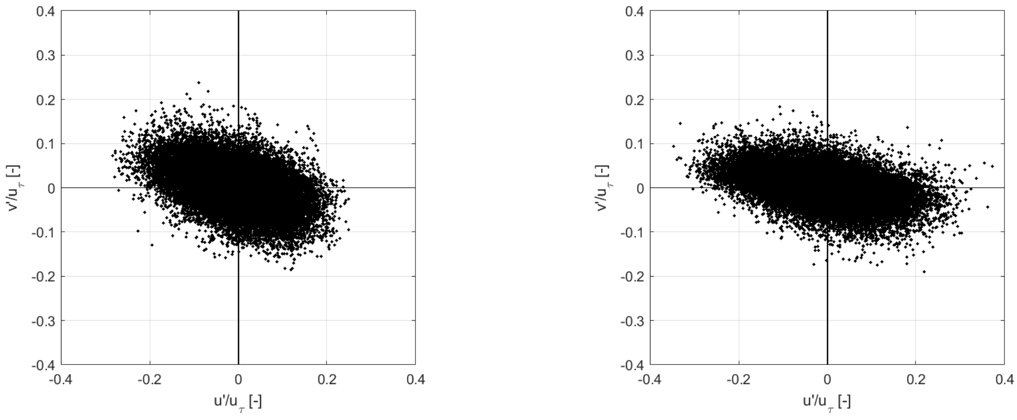

(a) $y^+ = 100$ **(b)** $y^+ = 30$

Figure 5.11. Quadrant event scatter plot for DNS data from Lin (2021) at $y^+ = 100$ and $y^+ = 30$

Figure 5.12 shows the scatter plot of the quadrant events for each test plate; the black and red dots signify the leading and trailing edge FOV, respectively. The velocity fluctuations are all normalised by u_τ. For all test plates, an elliptical distribution of the events is observed, with the ellipse's major axis aligned to the Q2 and Q4 quadrants. This distribution is an indication that the boundary layer measured is properly turbulent with ejection and sweep events present. For the trailing edge FOV, the distribution is more condensed near the origin than the leading edge FOV; this is consistently seen in all test plates. This effect is thought to be the mild steps at the leading edge of the test plate, leading to noise in the velocity fluctuations. Discernible differences were not observed in the raw images and velocity field. Also, the acquisitions for the leading edge FOV were directly followed by the trailing edge FOV, ruling out effects by environmental variables such as temperature and humidity.

Figure 5.13 shows the quadrant event occurrence probability delta between the leading edge and trailing edge FOVs for each test plate. The quadrant event occurrence probability is calculated by counting the number of points for each quadrant event and dividing the total number of data points considered. The delta is then calculated by subtracting the probability at the trailing edge FOV with the probability at the leading edge FOV. For the Q2 event, the drag-reducing compliant surface increases the event probability by a mere 0.04%, while the reference plate has a probability decrease of -0.29%. However, a significant change of Q2 event probability is observed for the drag-increasing compliant surface, with a 1.83% increase. Q2 events are associated with the bursting stage of the development of coherent structures in turbulent flows; corresponding with the hypothesis of Bushnell et al. (1977), a drag-reducing compliant surface should have a reduction of Q2 events, and vice versa. While the drag-increasing compliant surface satisfies this hypothesis, the drag-reducing compliant surface does not show a significant change. Furthermore, the drag-reducing compliant surface increases the Q2 event probability by 0.33% referenced to the reference test plate. A possible explanation may be the CC207 Rev. has become a drag-increasing surface, as was measured in the 3rd drag

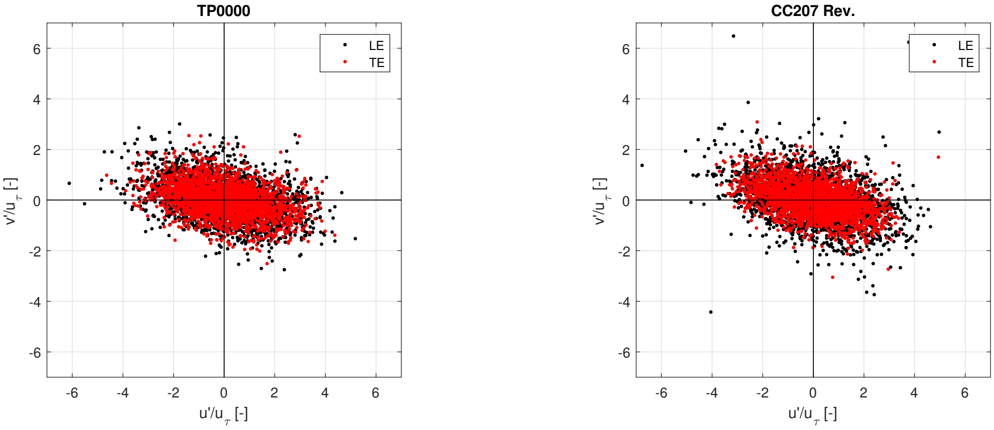

(a) TP0000 **(b)** CC207 Rev.

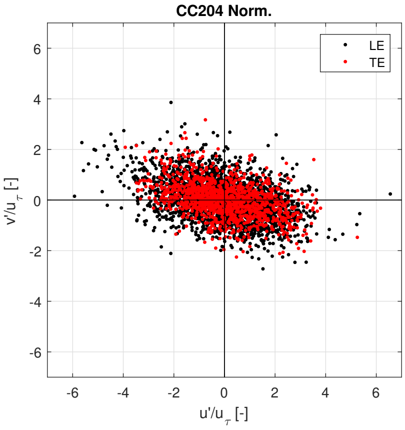

(c) CC204 Norm.

Figure 5.12. Quadrant event scatter plot for each test plate at the leading and trailing edge FOVs of the PIV zoomed-in view.

measurement of the surface.

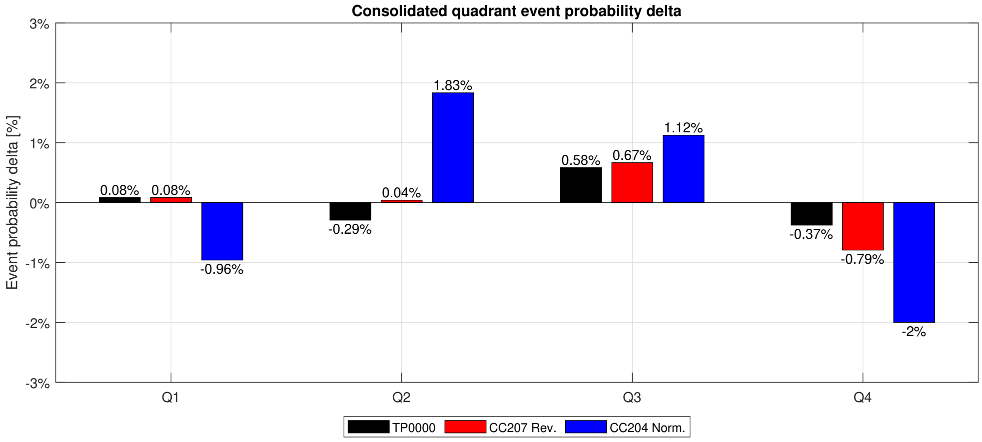

Figure 5.13. Quadrant event occurrence probability delta for each test plate

In addition to the Q2 event, which corresponds to the ejection events of the near-wall flow, the sweep event in Q4 equally contributes to the production of Reynolds stress. Figure 5.14 shows the sum of the Q2 and Q4 event occurrence probability delta for all test plates. The event occurrence probability at the trailing

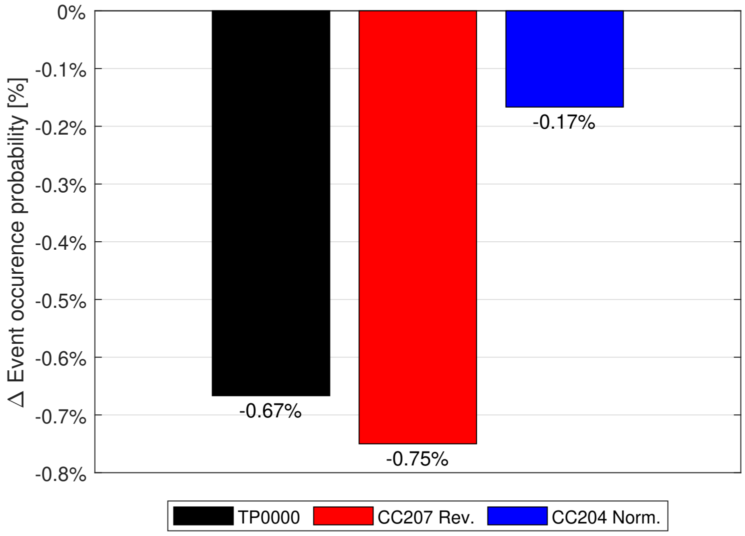

Figure 5.14. Sum of Q2 and Q4 event occurrence probability delta for each test plate

edge FOV is subtracted with the event occurrence probability at the leading edge FOV. The relative difference between the test plates coincides with the outcome of drag delta measurements, while all of the test plates reduce the overall Reynolds stress. The drag-reducing compliant surface has an overall higher decrease in Q2 and Q4 events, followed by the reference plate, and the drag-increasing compliant surface. However, the absolute difference between the drag-reducing compliant surface and the reference plate is only 0.08%, which is close to the uncertainty of the zoomed-in PIV data.

A significant difference in probability is observed for the drag-increasing compliant surface compared to the reference test plate (0.50%) and the drag-reducing compliant surface (0.58 %). Looking back at Figure 5.13, this is due to the significant increase and decrease of the Q2 and Q4 events. This result could be a clear indication of the drag-increasing capabilities of the compliant surface. However, the reduction of Q4 events is even larger than both the reference test plate and the drag-reducing compliant surface. This result might be an indication that a drag-increasing compliant surface would reduce the occurrence of sweep events. If assuming that CC207 Rev. is drag-increasing surface per the third drag delta measurement, the magnitude of Q2 and Q4 event probability sum corresponds to the drag increase for the two compliant surfaces. Further investigation is warranted to clear up the vagueness of these possible outcomes.

5.3.3. Joint probability density function (JPDF)

A further look into the scatter of quadrant events is done by evaluating the joint probability density function (JPDF) of the event scatter plot shown previously in Figure 5.12. Figure 5.15 shows the contour plot of JPDF delta for each test plate, with the JPDF at the trailing edge FOV subtracted by the leading edge FOV. The contour colour is white around zero, with green and red indicating an increase and decrease of the JPDF, respectively. The crosses and circles indicate the three largest and smallest JPDF delta, respectively. The domain is meshed into squares of 0.4 normalised velocity units. This discretisation level involved trial and error, where the highest level of discretisation with a complete JPDF contour plot was chosen (Wallace, 2016). The outcome of the chosen discretisation is shown in the JPDF contour plot of the leading edge FOV of CC204 Norm. in Figure 5.15a; contour plots for the other test plate-FOV location pairings had a comparable quality of contours, and therefore are not shown here.

The contraction of the event spread observed in Figure 5.12 is also present, indicated by the red region surrounding the perimeter of the elliptical distribution. The JPDF delta increase surrounding the origin is larger for the drag-reducing surface than the reference plate. No differences can be discerned between the reference test plate and the drag-reducing compliant surface, as the regions of positive JPDF delta range surrounding the origin and maximum JPDF deltas coincide with each other. However, an explicit peak in Q2 events can be observed for the drag-increasing compliant surface, which coincides with the event occurrence

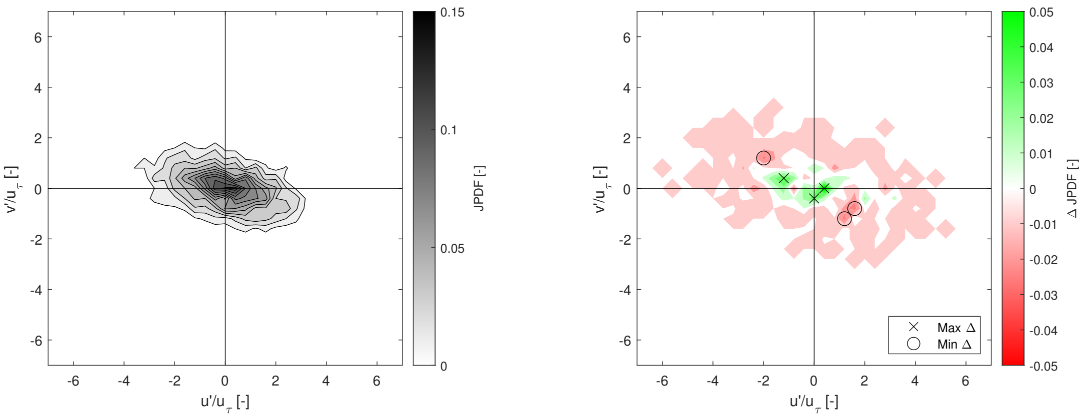

(a) JPDF of LE FOV of CC204 Norm.

(b) TP0000

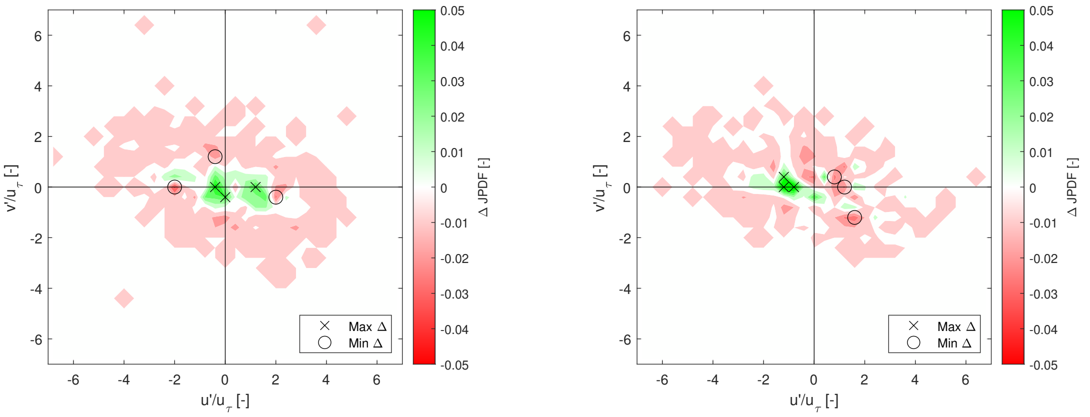

(c) CC207 Rev.

(d) CC204 Norm.

Figure 5.15. The JPDF of the leading edge FOV of CC204 Norm., and the delta JPDF of quadrant events for each test plate at the leading and trailing edge FOVs of the PIV zoomed-in view.

probability seen before. Due to the low number of samples, further discretisation of the domain was not possible, which led to statistically insignificant results. This warrants further quadrant analysis of compliant surface FSI with a larger sample size.

The weighted JPDF is evaluated to consider both the statistical occurrence and magnitude of each velocity fluctuation; the delta of the weighted JPDF is shown in Figure 5.16, which is a subtraction of the weighted-JPDF at the trailing edge FOV with the leading edge FOV. The cross and circles indicate the three largest and smallest delta of the weighted JPDF, with a green and red contour indicating a positive and negative weighted JPDF delta, respectively. The weighted JPDF is seen to suffer even more from insufficient data points, where the level of domain discretisation is observed throughout the domain. Also, the amount of considered data points leads to the low signal-to-noise ratio, amplifying the noise with larger velocity fluctuations. This is observed in Figure 5.16b, where the largest and smallest deltas are dominated by the outlying noise. While it was possible to change the level of discretisation, the results vary significantly and therefore is not considered and shown here. Therefore, no definite conclusions can be drawn from the weighted-JPDFs.

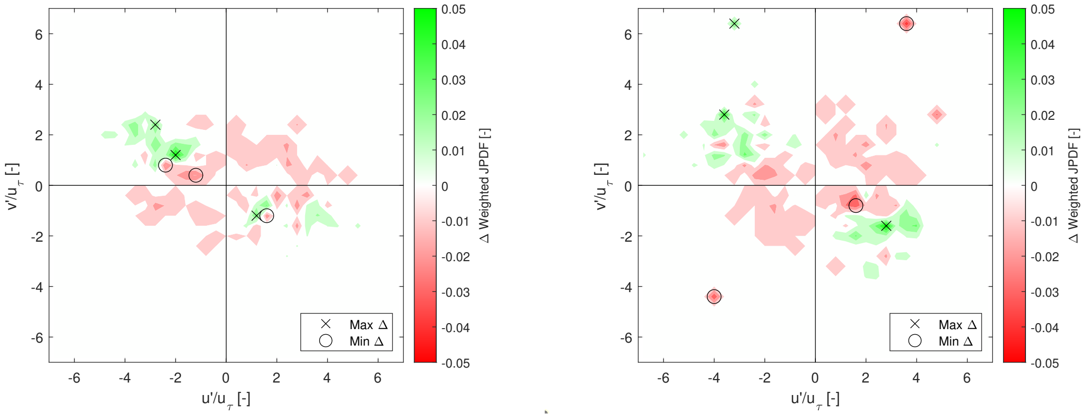

(a) TP0000 **(b)** CC207 Rev.

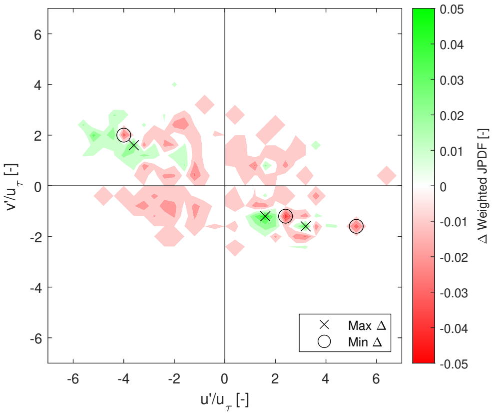

(c) CC204 Norm.

Figure 5.16. The delta weighted JPDF of quadrant events for each test plate at the leading and trailing edge FOVs of the PIV zoomed-in view.

6

Conclusion

Sparked by the observations by Gray (1936), and the first implementations by Kramer (1960), compliant surface research for turbulent viscous drag reduction has come a long way but remains a debated topic. While much of the focus has been put on water flows, air flows have long been unexplored due to its low density and assumed low inertial capability to deform a compliant surface. While taking this into account, the author believes with the proper scaling, the potential of compliant surfaces should not be diminished in air flows, as this research aims to shed some light on its unexplored potential. This research serves as an initial dive into the possibility of turbulent viscous drag reduction by compliant surfaces in air flows with a parameter sweep of the thickness and stiffness.

The initial plan to measure surface deformation was postponed to an ongoing follow-up research due to time limitations of the MSc thesis and complexity of the setup. Therefore, this research has been mainly focused on resolving the fluid part of the FSI. This change has led to some of the proposed research questions and hypothesis not being answered and verified. Below are the conclusions reached in the hope of answering the hypothesised research questions at the beginning of the research:

- **Drag reduction was measured in air flows with a compliant surface in comparison with a flat plate**

  Repeatable turbulent drag reduction in air with a compliant surface was measured. The measurements had a small RMSE spread, with minimal pressure drag correction. The drag reduction is further supported by:

  1. **Reduction of 1D turbulence intensity and uplift of mean streamwise velocity profile near the test plate trailing edge**
     This observation was measured by the Hill's hot-wire probe. Statistical tests of the hot-wire signal also indicate a statistical significance of such a result.
  2. **Smaller decay of the shape factor H**
     The drag-reducing compliant surface had a smaller decay of the shape factor than the reference flat plate and the drag-increasing compliant surface from the panorama PIV data. The results are further supported by observing a larger decay of the shape factor for the drag-increasing compliant surface than the reference flat plate. A higher shape factor indicates a leaner boundary layer velocity profile, which means a lower velocity gradient at the wall, hence the lower skin friction.
  3. **Reduction of combined Q2 and Q4 event occurrences**
     Quadrant analysis of the zoomed-in PIV data revealed the most reduction of combined Q2 and Q4 event occurrences, compared with a flat plate and a drag-increasing compliant surface.

  However, several observations also contradict the drag reduction measured:

  1. **Drag increase measured in one of the three repeatability measurements**
     While the drag reduction result for the second drag delta measurement was a near carbon copy of the 1st measurement, the third drag delta measurement resulted in a drag increase. The discrepancy may be explained by two reasons: the use of a different test section, and the slight shrinkage of the compliant surface. Further investigation is needed to clarify this discrepancy.

    2. **Downshift of the logarithmic layer**
       A downshift of the logarithmic layer was observed instead of the upshift observed by Choi et al. (1997), where drag reduction was similarly observed.
    3. **An increase in Q2 event occurrence in comparison with a flat plate**
       The drag-reducing compliant surface had an increase in Q2 events compared with a flat plate, which goes against the burst frequency-reduction hypothesis by Bushnell et al. (1977)

- **The drag-reducing compliant surface was the thickest and softest of all of the surfaces, with** $\delta_s \sim 4\,\text{mm}$ **and** $|G^*| \sim 2.18\,\text{kPa}$**. It also had a notably high loss tangent of** $\tan(\delta_p) = 0.37$

  The drag-reducing compliant surface had a stiffness closer to the inner scaling result than that of the outer scaling. This outcome makes sense since the near-wall boundary layer directly interacts with the surface, rather than the outer region. The inner scaling uses an alternative form of the inertia ratio, replacing the product of the fluid density and fluid velocity squared with the pressure fluctuations at the wall. The use of the inertia ratio in the inner scaling also gives confidence in this scaling parameter in determining the compliant surface parameter space for given flow conditions. The use of the inertia ratio for outer scaling is showed the convergence of drag-reduction cases within a certain range, for both the reference cases and this research. These cases are mostly lower than the instability onset threshold proposed by Duncan et al. (1985). This research also comes together with results of Choi et al. (1997) in disagreeing with the compliant surface drag reduction range proposed by Semenov (1991).

  The drag-reducing compliant surface also had a significantly higher loss tangent. In addition, a subtle correlation between the magnitude of the drag reduction and the loss tangent was observed. This observation raises the possibility that the loss tangent's influence may not be so minimal as was expected.

  While the stiffness sweep correlated with the amount of drag reduction, the thickness sweep did not generate a clear correlation. However, it is certain that the quality of the manufactured compliant surfaces certainly hindered the quality of the measurements. Therefore the drag-reducing capabilities of the thinner surfaces should not be disregarded. Thinner compliant surfaces have potential applications on aircraft, as it saves a lot more weight with the large fuselage area, and thus fuel costs.

- **The drag-reducing compliant surface had the most reduction in the combined occurrence of Q2 and Q4 events compared with the reference test plate and the drag-increasing compliant surface. Yet, the Q2 events for drag-reducing compliant surface increased compared with the reference test plate, coming against the burst frequency-reduction hypothesis by Bushnell et al. (1977)**

  Quadrant analysis of the PIV zoomed-in view at the leading and trailing edge of the test plates indicated that the drag-reducing compliant surface had a 0.75% decrease in the combined occurrence of Q2 and Q4 events. However, this decrease was only 0.08% larger than the 0.67% decrease caused by the reference test plate. In addition, the drag-reducing compliant surface had an increase in Q2 ejection events. This result comes against the drag-reduction hypothesis by Bushnell et al. (1977), where a reduction of bursting frequency was expected. This being said, the drag-increasing compliant surface had a significantly smaller 0.17% decrease in combined Q2 and Q4 events, with a significant 1.83% increase in Q2 events, agreeing with the hypothesis.

  This preliminary quadrant analysis was hampered by an insufficient number of data points and the lack of resolved boundary layer depth due to the laser sheet reflections on the compliant surface. Also, the lack of near-wall points in characterised boundary layer data from the PIV zoomed-in view is a source of error. Furthermore, this quadrant analysis was based on planar PIV, where the spanwise variations of the flow were not considered. These points warrant further investigation with quadrant analysis with more good quality data points to resolve the occurrence of these events.

- **While drag reduction was observed, the experiments need to be further refined for better understanding of the compliant surface parameter space and the resultant FSI**

  This research initially set out as mapping the compliant surface parameter space for drag delta trends. Indeed, drag reduction was observed for one of the compliant surfaces with distinguishable good quality and properties from the other ten compliant surfaces. However, an overall trend of the parameter space correlated with the drag delta could not be properly mapped out. A more refined experimental setup is warranted for further investigation in the parameter space, and also a correlation with the drag delta results of this research for further verification

7

Recommendations for future research

This research has opened up a pool of interesting topics for future research into compliant surfaces for turbulent viscous drag reduction in air. From both the practical and the theoretical angle, below are the recommendations for future research into this topic.

- **Improvements to the drag measurement setup**

    1. **Increase number of connector tray supports**
    The number of supports for the connector tray can be increased from the current four corners. A centre-heavy weight distribution did not allow the connector tray to properly move back and forth in the streamwise direction to force the force sensor. This was also due to the long streamwise length of the test plate and the connector tray leading to reduced stiffness in the centre, allowing for the connector tray's bending.
    2. **Better characterisation of the pressure distribution across the test plate**
    The current setup applies pressure corrections only at the test plate's leading edge and trailing edge. Better characterisation of the pressure above the compliant surface can lead to a better understanding of the pressure drag, the other component of the turbulent viscous drag.

- **Improvements to the compliant surface test plate manufacture and design**

    1. **Improved test plate design**
    The test plate design can be improved to mitigate the steps at the edge and avoid detachment from the base plate. A one-piece rimmed cavity design could be a potential solution. Also, the test plate's rigidity could be increased to prevent the flexing of the entire test plate.
    2. **Increase opacity of compliant surface to reduce reflections**
    The compliant surface can be mixed with a non-reflective black pigment to avoid laser sheet reflections when conducting PIV experiments.
    3. **A better controlled environment for manufacture**
    The compliant surface manufacture could be conducted in a climate-controlled clean room to avoid significantly higher ambient temperatures and dust. The controlled ambient temperature would avoid premature curing due to temperature gradients within the mixture. Also, the prevention of dust will increase the quality of the surface finish and hence the quality of the measurements.
    4. **Non-contact preservation method of the compliant surfaces**
    Non-contact conservation of the compliant surface should be considered. This method would avoid the oily patterns present in the current conservation method with plastic foils.
    5. **Materials capable of easier manipulation of individual viscoelastic properties**
    The magnitude of the complex shear modulus of the current PlatSil Gel OO mixture can be easily manipulated with the addition of the deadener and hardener. However, the addition of the hardener is also coupled with the increase of the loss tangent. Finding a material with the possibility of manipulating a single property, while keeping the other properties at a constant value might shed a more precise correlation between the viscoelastic properties and the drag delta.

- **Improvements to rheology measurements**
    1. **Use of time-temperature superposition to expand measurement range**
    The range of the rheometer's measurement frequency may be increased by heating the sample and applying the time-temperature superposition principle. This principle makes it possible to measure the viscoelastic properties at frequencies where it coincides with the frequency of the flow's pressure fluctuations. A possible clearer link between the flow and the surface could be found by applying this principle.
    2. **Consistent method to better keep rheometer sample in place**
    Local measurement errors occurred for samples that are less tacky, namely samples with the hardener additive. A consistent method of better fixing the sample in place should be used. The axial force may be increased, but this creates a bias in the results. Roughness elements may be added between the parallel plates and the sample, but the effect of this addition must also be investigated.
- **Use other wind tunnels for drag and flow visualisation measurements**
It is recommended to use another wind tunnel with better inflow conditions that may increase the confidence in the results. The current M-Tunnel has free-stream turbulence that may affect the resultant FSI. Also, pressure gradients might be present due to the uniform cross-section before the test section and after the wind tunnel's contraction zone.
- **Improvements to the PIV setup and data processing**
    1. **Experimental setup that avoids the contact of the laser sheet with the compliant surface to reduce reflections**
    In addition to adding opaque pigment on the manufacturing side, the PIV experimental setup can be improved to mitigate the reflection problems. A knife-edge may be used just downstream of the test plate to allow only the laser sheet just above the test plate to pass into the test section. This placement avoids the laser sheet coming in contact with the compliant surface that causes reflections.
    2. **More consistent PIV data-processing settings**
    The PIV data-processing settings could have been more consistent for all of the data points. Due to the reflections and the slight deformations of the compliant surface test plate, the masking settings were changed for every test plate and FOV location. These settings introduced an abundance of errors when stitching the FOVs, of which the results were not presented in this report.
- **Potential research topics**
    1. **Numerical modelling of FSI to correlate with experimental results**
    Numerical analysis of the compliant surface FSI has been fairly prevalent alongside the experimental approach. With continuing experimental studies underway here in Delft, a parallel numerical study can aid the experimental studies and vice-versa.
    2. **Scale to higher Reynolds number**
    The FSI of compliant surfaces at higher Reynolds numbers would be of interest to see how the scaling of the FSI evolves with velocity. A higher Reynolds number would also mean that the compliant surface does not have to be that soft to achieve two-way-coupling per the inertia ratio. This assmption would mean that aircraft applications could have a stiffer coating that would be less prone to surface damage and abrasion by foreign substances.
    3. **Surface deformation measurements**
    This research has been focused only on the fluid part of the FSI. The surface deformations were also too small to be resolved in this research's PIV experiments, as the reflections prevented the visualisation of the near-wall region. Therefore, resolving the structure in the FSI with surface deformation measurements will also be of great interest to shed some light on the great abyss of turbulent viscous drag reduction by compliant surfaces.
    4. **Time-resolved-PIV**
    Temporal analysis of the FSI could help gain insight into the bursting frequency reduction hypothesis by Bushnell et al. (1977). The time-resolved analysis may also help in better characterising the compliant surface other than the material properties.

5. **Tomographic PIV**
   Tomographic PIV may be conducted to visualise and resolve the spatial flow characteristics of the FSI. Deformations of the compliant surface have been seen to be highly 3D; resolving the FSI in a 3D manner might be a chance to gain insight into the two-way coupling of the compliant surface and the flow. The resolved spatial terms would also open up opportunities for 3D turbulence analysis, such as the spatial term in the Fukagata-Iwamoto-Kasagi (FIK) identity.

Appendix

A

Compliant surface logbook

In this appendix, the logbook of every compliant surface rheometer sample and test plate is presented in Table A.1 and A.2. Five different mixtures were tested in the initial material search, with the PlatSil Gel OO chosen for manufacturing the compliant surface test plates. In the following paragraphs, descriptions are made to provide context to the content in the tables.

For the **EcoFlex 0010** silicone, it is a room temperature cured (or room temperature vulcanised (RTV)) A and B-component silicone which cures with a weight ratio of 1:1. There were no additives mentioned in the technical bulletin allowing it to be softened or stiffened. One of the samples were tested to see if applying release agent (for better release from the mould when cured) would affect the material properties (CC002). The other sample, CC003, was heated after the mixture was cured to achieve maximum physical and performance properties, per the technical bulletin.

For the **PlatSil 25 and OO** gels, they are also 1A and 1B component silicones. Additives such as deadener and hardener are added to soften and stiffen the resultant mixture, respectively. The number that comes in front of additive (e.g. 2 Deadener), indicates the weight ratio of such additive with respect to the main mixture of A and B components. Therefore, if a total mixture weighs 1000 [g] with a weight ratio of A : B : Deadener = 1 : 1 : 2, this means that the A and B component consists of 250 [g] each, and the deadener 500 [g].

For the **Resion Shore 8** mixture, it is also a 1A and 1B component silicone. Silicone oil is added for some of the samples to soften the cured silicone. The amount being added is a weight percentage of the combined weight of the A and B components. The number mentioned in the remarks of samples with silicone oil added is the kinematic viscosity of the silicone oil in centistokes.

For **Sylgard 184**, it has a one-component elastomer base with curing agent added. Silicone oil is added to soften the cured silicone. The amount of silicone oil is calculated by the weight percentage of the total mixture of elastomer, curing agent, and silicone oil. Therefore, if the total mixture of a 95% silicone oil sample were to weigh 10 [g], the silicone oil within the mixture weighs 9.5 [g].

For the **gelatine** samples, they are supermarket-bought gelatine sheets mixed with water. The ratio mentioned in the Remarks column is the weight ratio of the gelatine to water. For a 101 [g] sample with a weight ratio of 1 : 100, the gelatine in the mixture would be 1 [g] with 100 [g] of water.

A.1. Rheometer samples

Table A.1. List of compliant surface rheometer samples manufactured

ID	Date	Mixture	Additive	Remarks
CC001	May 06 2020	EcoFlex 0010		
CC002	May 06 2020	EcoFlex 0010		Release agent applied
CC003	May 06 2020	EcoFlex 0010		Post-cure heating applied
CC004	May 06 2020	PlatSil Gel 25		
CC005	May 06 2020	PlatSil Gel 25	0.5 Deadener	
CC006	May 06 2020	PlatSil Gel 25	2 Deadener	
CC007	May 06 2020	Resion Shore 8		
CC008	May 06 2020	Resion Shore 8	7.5% Silicone oil	350 [cSt]
CC009	May 06 2020	Resion Shore 8	15% Silicone oil	350 [cSt]
CC010	May 06 2020	RubberMagazijn		
CC011	Jun 04 2020	PlatSil Gel OO		Range
CC012	Jun 04 2020	PlatSil Gel OO	0.5 Deadener	Range
CC013	Jun 04 2020	PlatSil Gel OO	1 Deadener	Range
CC014	Jun 04 2020	PlatSil Gel OO	2 Deadener	Range
CC015	Jun 05 2020	PlatSil Gel OO	0.25 Hardener	Range
CC016	Jun 05 2020	PlatSil Gel OO	0.5 Hardener	Range
CC017	Jun 04 2020	PlatSil Gel OO	1 Hardener	Range
CC018	Jun 05 2020	Gelatine (Dr.Oetker)	1:100	
CC019	Jun 05 2020	Gelatine (Dr.Oetker)	4:100	
CC020	Jun 05 2020	Gelatine (Dr.Oetker)	6:100	
CC021	Jun 05 2020	Gelatine (Dr.Oetker)	10:100	
CC022	Jul 02 2020	PlatSil Gel OO		Baseline
CC023	Jul 02 2020	PlatSil Gel OO		Thickness
CC024	Jul 02 2020	PlatSil Gel OO		Thickness
CC025	Jul 02 2020	PlatSil Gel OO		Manufacture repeatability
CC026	Jul 02 2020	PlatSil Gel OO		Manufacture repeatability
CC027	Jul 02 2020	PlatSil Gel OO	2 Deadener	Range
CC028	Jul 02 2020	PlatSil Gel OO	0.25 Deadener	Range
CC029	Jul 02 2020	PlatSil Gel OO	0.35 Hardener	Range
CC030	Jul 02 2020	PlatSil Gel OO	0.75 Hardener	Range
CC031	Jul 16 2020	Sylgard 184		
CC032	Jul 16 2020	Sylgard 184	91% Silicone oil	350 [cSt]
CC033	Jul 16 2020	Sylgard 184	95% Silicone oil	350 [cSt]
CC034	Aug 06 2020	Sylgard 184	90% Silicone oil	50 [cSt]
CC035	Aug 06 2020	Sylgard 184	95% Silicone oil	50 [cSt]
CC036	Aug 06 2020	Sylgard 184	99% Silicone oil	50 [cSt]
CC037	Sep 02 2020	Sylgard 184	87.5% Silicone oil	350 [cSt]
CC038	Sep 02 2020	Sylgard 184	90% Silicone oil	350 [cSt]
CC039	Sep 02 2020	Sylgard 184	92.5% Silicone oil	350 [cSt]
CC040	Sep 02 2020	Sylgard 184	95% Silicone oil	350 [cSt]
CC041	Sep 02 2020	Sylgard 184	97.5 % Silicone oil	350 [cSt]
CC042	Sep 02 2020	PVC		

A.2. Test plates

Table A.2. List of compliant surface test plates manufactured

ID	Date	Mixture	Additive	Mould version	Target δ_s [mm]	Target $\lvert G^*\rvert$ [kPa]
CC201	Jul 08 2020	PlatSil Gel OO		v1.0	4.5	40
CC202	Jul 10 2020	PlatSil Gel OO		v1.0	4	40
CC203	Jul 30 2020	PlatSil Gel OO		v2.0	4	40
CC204	Aug 04 2020	PlatSil Gel OO	0.25 Deadener	v2.1	4	20
CC205	Aug 05 2020	PlatSil Gel OO	0.35 Hardener	v2.2	4	60
CC206	Aug 06 2020	PlatSil Gel OO	0.75 Hardener	v2.2	4	100
CC207	Aug 07 2020	PlatSil Gel OO	2 Deadener	v2.2	4	5
CC208	Aug 10 2020	PlatSil Gel OO		v2.3	2	40
CC209	Aug 11 2020	PlatSil Gel OO		v2.3	1	40
CC210	Aug 11 2020	PlatSil Gel OO	2 Deadener	v2.3	2	5
CC211	Aug 12 2020	PlatSil Gel OO	2 Deadener	v2.3	1	5
CC212	Aug 13 2020	PlatSil Gel OO	0.75 Hardener	v2.3	1	100
CC213	Aug 14 2020	PlatSil Gel OO	0.75 Hardener	v2.3	2	100
CC214	Aug 14 2020	PlatSil Gel OO	0.75 Hardener	v2.3	4	100
CC215	Aug 17 2020	PlatSil Gel OO	2 Deadener	v2.3	4	5
CC216	Oct 07 2020	PlatSil Gel OO	2 Deadener	v2.3	4	5

Table A.3. Description of mould versions mentioned in Table A.2

Version	Description
v1.0	Original mould design with Scotch Weld adhesive applied between the rim and base
v2.0	New mould design with mould rim and base screwed together onto $40 * 40[mm^2]$ aluminium profiles, rectangular structure with 2 cross beams in the spanwise direction; rested on two large aluminium profiles with item double t-slots attached
v2.1	4 feet incorporated sitting on a long table; levelled with normal level
v2.2	Assembly levelled at perfectly level table at LSL; further levelled with accurate level; 3 feet support; placed on the floor
v2.3	v2.2 without the suction cups and weights

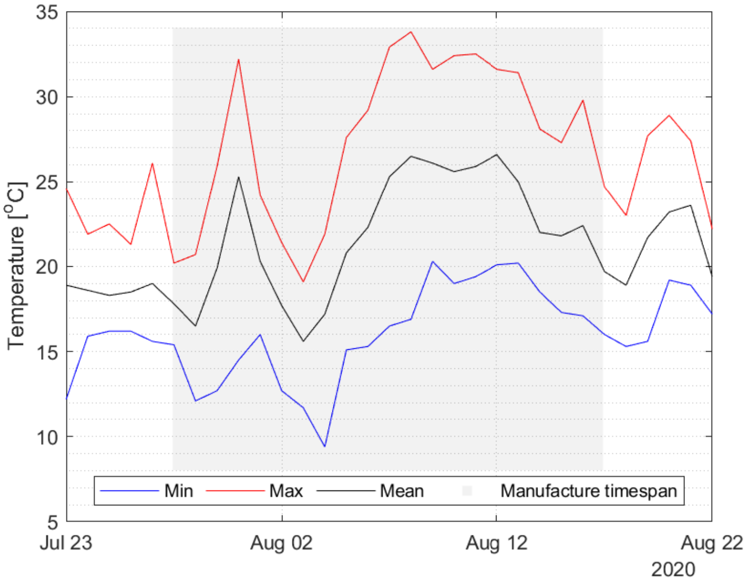

Figure A.1. Meteorological temperature at the time of compliant surface manufacture (from Rotterdam station of KNMI near Rotterdam The Hague Airport)

B

Technical data for PlatSil Gel OO

Table B.1. Physical properties of PlatSil Gel OO
(Adapted from Polytek Development Corp. (2017b))

Mix ratio, by weight or volume	1A:1B
Shore hardness	A10
Pour time [min]	6
Demould time [min]	30
Cured color	Milky white
Mixed viscosity [cP]	15,000
Specific volume [in^3/lb]	25
Specific gravity @ 25 °C	1.1
Shrinkage upon cure	Nil

Table B.2. Physical properties of PlatSil Gel OO with various ratios of deadener added
(Adapted from Polytek Development Corp. (2017a))

Mix ratio	**1A:1B**	**1A:1B:0.5D**	**1A:1B:1D**	**1A:1B:2D**
Pour time [min]	8	10	15	18.5
Demould time [min]	40	40	40	45
Shore hardness	OO30	OO11	OOO45	OOO15
Tack	No	No	Yes	Very

Table B.3. Physical properties of PlatSil Gel OO with various ratios of hardener added
(Adapted from Polytek Development Corp. (2017a))

Mix ratio	**1A:1B**	**1A:1B:1H**
Pour time [min]	6	8
Demould time [hr]	1	2.5
Shore hardness	A25	A40
Tack	No	No

C

Shore hardness and shear modulus

The Shore hardness is an industrial standard of measuring the stiffness of a material; this may include polymers, elastomers, or rubbers. The magnitude of the shore hardness can be measured by a Shore durometer; with values ranging from 0 to 100, it defines a material's resistance to indentation. The ASTM D2240 standard defines multiple scales (types) of Shore hardness suitable for materials in different stiffness ranges. For example, if a type-A shore durometer measures a material at 50 hardness, this material is said to have an A50 hardness.

The technical bulletin of the materials surveyed in Appendix A all gave stiffness in shore hardness. As the shear modulus is used in this research as a scaling parameter for the FSI, it was necessary to have a grasp in the shear modulus range of the materials at hand. Larson (2016) gives an overall review of the various methods presented in literature for the conversion of the Shore hardness to the elastic modulus E. Of which, Mix and Giacomin (2011) gives a parametric method of such a conversion. For a flat type durometer tip, the dimensionless elastic modulus can be calculated by

$$\mathscr{Y} = \frac{1 + \mathrm{Mi}\mathscr{H}}{1 - \mathscr{H}} \tag{C.1}$$

where Mi is the mechanical indentability, $\mathscr{H}$ the Shore hardness. The dimensionless elastic modulus can be further converted to the dimensional elastic modulus by:

$$E = \frac{3F_0\mathscr{Y}}{8rp_0} \tag{C.2}$$

where F_0 the spring preload, r the indentor radius, p_0 the initial indentor protrusion. While $\mathscr{H}$ is given by the durometer, Mi, F_0, r, and p_0 are constants given by the ASTM D2240 standard. These constants for the Shore hardness scale A, OO, and OOO, which fall within the target shear modulus range for this research, are listed here in Table C.1.

Table C.1. Constants for the Shore hardness to elastic modulus conversion method by Mix and Giacomin (2011)

Shore hardness scale	Mi	F_0	r	p_0
A	13.64	0.55	$2.5 * 10^{-3}$	$3.95 * 10^{-4}$
OO	4.47	0.203	$2.5 * 10^{-3}$	$1.19 * 10^{-3}$
OOO	4.47	0.203	$2.5 * 10^{-3}$	$6.35 * 10^{-3}$

The resultant conversion is shown in Figure C.1, with an assumption of constant Poisson's ratio, leading to a constant multiple conversion of the elastic modulus to the shear modulus by 3.

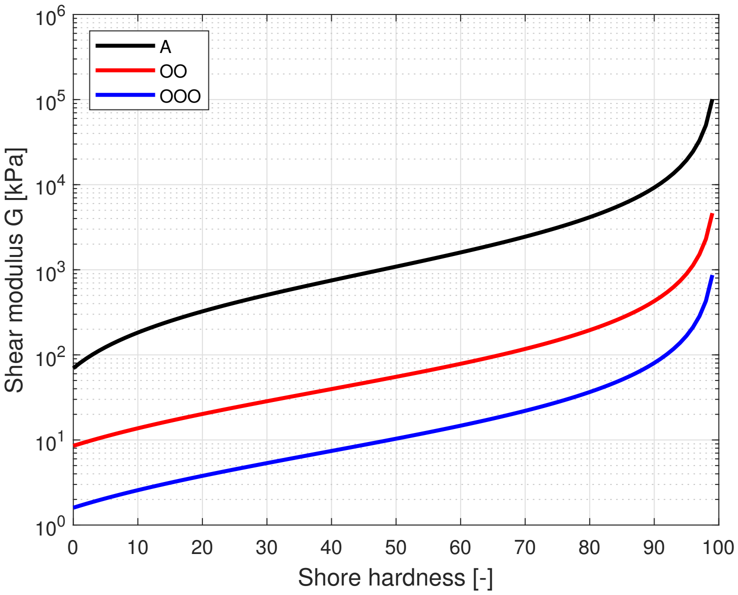

Figure C.1. Conversion of shore hardness to shear modulus (Adapted from Mix and Giacomin (2011))

D

Experimental routines

D.1. Manufacture of compliant surfaces

Table D.1. Experimental routine for manufacture of compliant surfaces (A): Mould setup

Mould setup	1. Check if base plate fits in the mould • File of base plate edges if necessary 2. Remove base plate • Mark on base plate alignment with respect to the mould 3. Wipe clean mould and base plate with alcohol • Be sure to apply cover at all times after wipe to prevent dust in the mould 4. Apply release agent to the mould • Mainly apply to rim • Apply to larger area with less viscous mixtures (i.e. mixtures with deadener) 5. Place base plate into the mould 6. Attach suction cups and weights to the bottom opening of the mould • Apply moisture to the suction cups 7. Check levelness of the mould 8. Put on wood cover 9. Label mould with current surface designation

Table D.2. Experimental routine for manufacture of compliant surfaces (B): Mixing

Mixing	1. Preparation (a) Clean mixing cup for main mixture • Or use new cup and clean afterwards during curing (b) Clean and label mixing cup for rheometre sample (c) Measure depth of cavity with the base plate and inlay placed in the mould • Measure across ten points and take the mean (d) Calculate mixture weight composition for each component • Overestimate for the rheometre sample and for security (Thickness +0.5 mm) (e) Write down calculation for reference 2. Check if all necessary silicone components are in place 3. Prepare pieces of tissue to wipe silicone residue and overflow 4. Pour component A and B from the barrel into the respective mixing cups 5. Thoroughly mix the old and new components within the mixing cup of component A and B 6. Pour component A into the main mixture cup 7. Pour additives • Retarder • Deadener • Hardener 8. Mix thoroughly 9. Degas in degassing chamber until the formation of bubbles reach a steady state 10. Pour component B and mix thoroughly

Table D.3. Experimental routine for manufacture of compliant surfaces (C): Pouring, surface release and post-curing

Pouring	1. Pour mixture into mixing cup for the rheometre sample 2. Pour into the mould 3. Weigh mixing cup to check amount of mixture being poured into the mould 4. Spread mixture in mould with spatula 5. Swipe overflow and pour mixture where necessary • Make sure to not swipe or pour when surface is visibly curing
Surface release and post-curing	1. Cut off overflow with scalpel along the edges if necessary 2. Remove weights and suction cups 3. Push gently upwards the base plate from the mould openings at the bottom • Be more vigilant with softer surfaces as adherence to the mould is more prominent 4. Cut off overflow on the bottom of the base plate with a scalpel 5. Apply plastic wrap and label surface 6. Clean main mixture mixing cup 7. Clean silicone residue in the mould and on the inlay

D.2. Direct drag measurements by the Hill

Table D.4. Experimental routine for direct drag measurements (A): Initialisation

Initialisation	1. Activate equipment (a) Turn on laptop and connect power adapter (b) Turn on control box and connect to laptop via USB cabel (c) Connect M-Tunnel ethernet cable to laptop (make sure properly connected) (d) Connect and turn on pneumatic air pressure for test plate release pistons (4 bars) 2. Start LabView control program (a) Main control program (b) M-Tunnel control program 3. Run LabView main control program (a) M-Tunnel status window should be automatically opened 4. Initialisation final checklist (a) No errors (b) M-Tunnel status window indicating "Ready to switch on" • If window indicates “Fault”, click “Reset” in global_variables.vi (c) Nominal sensor output • Temperature • Pressure • Force • Velocity (Pitot) (d) Nominal operation of test plate release piston

Table D.5. Experimental routine for direct drag measurements (B): Run

Run	1. Check in main LabView program if the force sensor is "not Active" before approaching the Hill 2. Slide open test section 3. Insert paper slips in the gap to avoid oscillating the tray 4. Actuate piston to release test plate 5. Retrieve test plate 6. Relieve pressure for piston 7. Place test plate into tray (a) Check test plate orientation (b) Check test plate fit 8. Remove paper slips Check if tray is properly oscillating; if not, troubleshoot weight distribution issue 9. Close test section 10. Modify output .csv file name • Time stamp YY/MM/DD will be automatically appended in the back) 11. Start run in main LabView program (a) "Autostart" starts run after the defined creep timer finishes (b) "Start" starts run after 20 seconds 12. Once tunnel starts humming (a) Start timer (on phone) for 8 minutes (b) Leave tunnel hall (c) If tunnel does not start properly, refer to section "If Tunnel Does Not Start" 13. Once phone timer has ended, repeat steps 1 to 10 within "Creep timer" • Creep timer preset: 5 minutes (Adjustable in "Setup" page of top box in main LabView program) • Approx. 4 minutes 30 seconds has elapsed if the tunnel motor fan stops running.

Table D.6. Experimental routine for direct drag measurements (C): Shutdown, in case of errors/problems, if tunnel does not start

Shutdown	1. Press "Quit", wait for LabView program to stop (a) Do not press the red stop button 2. Unplug control box USB cabel from laptop 3. Turn off control box 4. Turn off M-Tunnel 5. Turn off pneumatic air for test plate release piston (a) Turn off source only unless uninstalling the Hill 6. Release air from the tubes
In case of errors/problems	1. Quit main Labview program by pressing "Quit" (a) Press Enter key repeatedly to supress errors 2. Close all LabView windows 3. Power off M-Tunnel 4. Wait 10 seconds 5. Power on M-Tunnel 6. Follow steps 2 to 4 in the "Initialisation" section
If tunnel does not start	1. Press "Stop" 2. Delete failed measurement files 3. Press "Reset" 4. Restart run

D.3. Flow visualisation by PIV

[!]: Wear eye, respiratory and ear protection during experiments

Table D.7. Input parameters for M-Tunnel and PIV acquisition

Flow velocity [m/s]	10	20	33
WT set point [RPM]	925	1795	2900
Δt [μs] (for $f = 60$ lens)	55	27	16
Δt [μs] (for $f = 105$ lens)	26	14	8

Table D.8. Experimental routine for PIV (A): Initialisation

Determining Δt	**Optimum displacement of particle: 14 [pix]** 1. Take double-frame snapshots of flow at target flow velocities with different Δt 2. Post-process snapshots to determine maximum particle displacement and optimum Δt *See correlation map for visualisation of cross-correlation peaks

Table D.9. Experimental routine for PIV (A): Initialisation

Setup initialisation	
	1. Turn on equipment (a) Wind tunnel (b) Laser i. Change mode to external switch and trigger ii. Set both laser to full power; adjustments of the laser intensity should be made in DaVis (c) Smoke generator (d) Programmable timing unit (PTU) (e) PIV acquisition computer i. Open DaVis (f) M-tunnel control computer i. Open M-Tunnel control program ii. Open M-Tunnel data acquisition program • Choose proper calibration file 2. Validate laser sheet quality [!] (a) Align laser to mid-plane marker at the LE and TE (b) Visualise the laser sheet thickness and height across the streamwise direction with the spanwise calibration board (c) Adjust the laser optics (if necessary) to improve the laser sheet quality 3. Adjust camera lens to focus (a) Place streamwise calibration board and align with LE and TE markers (b) Set $f_{\#}$ to smallest value for smallest depth of field (c) Adjust lens to focus on the streamwise calibration board (d) Zoom-in on DaVis to further check focus 4. Take calibration photo 5. Check particle image size (a) Calculate magnification factor M and resultant $f_{\#}$ for optimal particle image size (2 ~ 3 [px]) (b) Change $f_{\#}$ on the camera lends to the calculated value (c) Smoke test section and turn on laser [!] i. Wait for the ready (green) light on the smoke generator to turn on before use (d) Take snapshot and check particle image size

Table D.10. Experimental routine for PIV (A): Initialisation

Changing camera location	1. Place streamwise calibration board and align with LE TE markers on the PHill 2. Adjust camera location and align accordingly to location indicated on the streamwise calibration board 3. Adjust camera lens to focus 4. Zoom-in on DaVis to further check focus 5. Take calibration photo

Table D.11. Experimental routine for PIV (A): Initialisation

Pre-run/acquisition	1. Zero pressure for M-Tunnel data acquisition program 2. Check correct inputs for DaVis and M-Tunnel control (a) Laser pulse intensity (50% for both Pulse A and B) (b) Double frame mode (c) Camera exposure time (15 [μs]) (d) Δt (Change according to flow speed (table D.7)) (e) Recording length (300 images) (f) Recording name (Date_Test Plate_Location_Flow velocity) (g) WT set point (table D.7) (h) M-Tunnel data acquisition time (Coincide with DaVis acquisition duration) 3. Create .txt file for M-Tunnel data acquisition

Table D.12. Experimental routine for PIV (A): Initialisation

Run/acquisition	1. Check correct inputs (a) Δt (table D.7) (b) Recording name (c) WT set point (table D.7) 2. Run wind tunnel [!] 3. Add smoke (up to feel; 100% for $2 \sim 5$ [sec]) [!] 4. Wait for flow to settle (20 [sec]) 5. Start acquisition [!] (a) Press record in DaVis i. Make sure light source is set to "On" or "Standby" (b) Log flow characteristics in M-Tunnel flow data acquisition

Table D.13. Experimental routine for PIV (A): Initialisation

Post-run/acquisition	1. Log zero flow conditions for M-Tunnel (Settling time 20 [sec]) 2. Test process images to "close the loop" 3. Backup data (when possible)

Table D.14. Experimental routine for PIV (A): Initialisation

Things to keep in mind	1. Remember to de-smoke the tunnel of if not doing run for a while (a) Turn on suction fan (b) Open windows 2. Open window slightly during runs to prevent smoke from entering the LSL (smoke detector) 3. Only put up Laser on sign when laser is on 4. Turn off power and Q-switches of the laser when not in use (to increase laser lifespan) 5. Prevent cables from hanging solely on the connector; place cables in a way that it is supported 6. Do not step on the orange fibre-optic cables

E

Recommended best practices for experiments

E.1. Rheometer

1. When making the rheometer samples, make sure the punch is level with the sample patty. Tap the punch with the hammer in multiple gentle taps to acquire a quasi-cylinder sample. Once the punch is nearly on top of the chopping board (by feeling the impact of the hammer), give one final normal tap to cut of the rheometer sample from the patty.

2. The stress response from the sample should be a proper sine wave. If the response is a high-frequency oscillation, the measurements have to be restarted. This might mean that the rheometer sample is not properly fixed between the parallel plates.

E.2. The Hill

1. When placing the test plate in the connector tray, check if the connector tray properly oscillates in the streamwise direction. If the tray does not oscillate, this does not allow the force sensor pin to properly measure the drag, as the connector tray can not properly apply force on the sensor.

2. Place the test plate into the connector tray with the inner streamwise edge first placed in, then releasing the test plate for it to rest into the connector tray.

3. Avoid oscillating the connector tray other than checking if the test plate is properly mounted in.

E.3. PIV

1. Make sure the cable connections to the camera, laser, and computer don't hang on the connector; this might loosen and break the connector. Place the cables somewhere that provides sufficient support.

2. Avoid bending or stepping on the orange optics table; treat with care.

3. Close physical shutter of the laser head to avoid unwanted direct eye contact due to laser misfire.

Bibliography

Airbus. Global Market Forcast: Cities, Airports & Aircraft. Technical report, Airbus SE, 2019. URL `https://www.airbus.com/content/dam/corporate-topics/strategy/global-market-forecast/GMF-2019-2038-Airbus-Commercial-Aircraft-book.pdf`.

Ash, R. L., Bushnell, D. M., Weinstein, L. M., and Balasubramanian, R. Compliant wall surface motion and its effect on the structure of a turbulent boundary layer. *Symposia on Turbulence in Liquids. 25*, 1975.

Bandyopadhyay, P. R., Henoch, C., Hrubes, J. D., Semenov, B. N., Amirov, A. I., Kulik, V. M., Malyuga, A. G., Choi, K. S., and Escudier, M. P. Experiments on the effects of aging on compliant coating drag reduction. *Physics of Fluids*, 17(8):85104, 2005. doi: 10.1063/1.2008997. URL `https://doi.org/10.1063/1.2008997`.

Barthlott, W., Mail, M., Bhushan, B., and Koch, K. Plant surfaces: Structures and functions for biomimetic innovations. *Nano-Micro Letters*, 9(2):1–40, 2017. ISSN 21505551. doi: 10.1007/s40820-016-0125-1.

Benedict, L. H. and Gould, R. D. Towards better uncertainty estimates for turbulence statistics. *Experiments in Fluids*, 22(2):129–136, 1996. ISSN 1432-1114. doi: 10.1007/s003480050030. URL `https://doi.org/10.1007/s003480050030`.

Benjamin, T. B. Effects of a flexible boundary on hydrodynamic stability. *Journal of Fluid Mechanics*, 9(4): 513–532, 1960. doi: 10.1017/S0022112060001286.

Benjamin, T. B. The threefold classification of unstable disturbances in flexible surfaces bounding inviscid flows. *Journal of Fluid Mechanics*, 16(3):436–450, 7 1963. ISSN 14697645. doi: 10.1017/S0022112063000884. URL `http://www.journals.cambridge.org/abstract_S0022112063000884`.

Benjamin, T. B. Fluid Flow with Flexible Boundaries. In *Gortler, H., Ed,. Proc. II-th Int. Congr. Appl. Math*, pages 109–128, Berlin, 1964. Springer Verlag.

Benschop, H. O. G. Private communication, 2019.

Benschop, H. O. G., Greidanus, A. J., Delfos, R., Westerweel, J., and Breugem, W. P. Deformation of a linear viscoelastic compliant coating in a turbulent flow. *Journal of Fluid Mechanics*, 859:613–658, 2019. ISSN 14697645. doi: 10.1017/jfm.2018.813.

Bhushan, B. and Jung, Y. C. Natural and biomimetic artificial surfaces for superhydrophobicity, self-cleaning, low adhesion, and drag reduction. *Progress in Materials Science*, 56(1):1–108, 2011. ISSN 00796425. doi: 10.1016/j.pmatsci.2010.04.003. URL `http://dx.doi.org/10.1016/j.pmatsci.2010.04.003`.

Bhushan, B., Israelachvili, J. N., and Landman, U. Nanotribology: Friction, wear and lubrication at the atomic scale. *Nature*, 374(6523):607–616, 1995. ISSN 00280836. doi: 10.1038/374607a0.

Blick, E. F. and Walters, R. R. Turbulent boundary-layer characteristics of compliant surfaces. *Journal of Aircraft*, 5(1):11–16, 1968. doi: 10.2514/3.43900. URL `https://doi.org/10.2514/3.43900`.

Blick, E. F., Walters, R. R., Smith, R., and Chu, H. H. Compliant coating skin friction experiments. In *AIAA 7th Aerospace Sciences Meeting*, New York City, NY, 1969. American Institute of Aeronautics and Astronautics (AIAA). doi: 10.2514/6.1969-165. URL `https://arc.aiaa.org/doi/abs/10.2514/6.1969-165`.

Breugem, W. P., Boersma, B. J., and Uittenbogaard, R. E. *The influence of wall permeability on turbulent channel flow*, volume 562. Cambridge University Press, 2006. ISBN 0022112006. doi: 10.1017/S0022112006000887.

Bruun, H. H. Hot-Wire Anemometry: Principles and Signal Analysis. *Measurement Science and Technology*, 7(10), 1996. ISSN 0957-0233. doi: 10.1088/0957-0233/7/10/024. URL `http://dx.doi.org/10.1088/0957-0233/7/10/024`.

Buckles, J., Hanratty, T. J., and Adrian, R. J. Turbulent flow over large-amplitude wavy surfaces. *Journal of Fluid Mechanics*, 140:27–44, 1984. ISSN 14697645. doi: 10.1017/S0022112084000495.

Bushnell, D. M. Aircraft drag reduction - A review. In *Proceedings of the Institution of Mechanical Engineers, Part G: Journal of Aerospace Engineering*, volume 217, pages 1–18, 2003. doi: 10.1243/095441003763031789.

Bushnell, D. M., Hefner, J. N., and Ash, R. L. Effect of compliant wall motion on turbulent boundary layers. *The Physics of Fluids*, 20(10):S31–S48, 1977. ISSN 00319171. doi: 10.1063/1.861756. URL `https://aip.scitation.org/doi/10.1063/1.861756`.

Carpenter, P. W. The Optimization of Compliant Surfaces for Transition Delay. In Liepmann, H. W. and Narasimha, R., editors, *Turbulence Management and Relaminarisation*, pages 305–313, Berlin, Heidelberg, 1988. Springer Berlin Heidelberg. ISBN 978-3-642-83281-9.

Carpenter, P. W. Status of Transition Delay Using Compliant Walls. *Viscous Drag Reduction in Boundary Layers*, pages 79–113, 1990. doi: 10.2514/5.9781600865978.0079.0113.

Carpenter, P. W. and Garrad, A. D. The hydrodynamic stability of flow over Kramer-type compliant surfaces. Part 1. Tollmien—Schlichting instabilities. *Journal of Fluid Mechanics*, 155:465–510, 1985. ISSN 14697645. doi: 10.1017/S0022112085001902.

Carpenter, P. W. and Garrad, A. D. *The hydrodynamic stability of flow over Kramer-type compliant surfaces. Part 2. Flow-induced surface instabilities*, volume 170. 1986. ISBN 0022112086000. doi: 10.1017/S002211208600085X.

Cherukat, P., Na, Y., Hanratty, T. J., and McLaughlin, J. B. Direct numerical simulation of a fully developed turbulent flow over a wavy wall. *Theoretical and Computational Fluid Dynamics*, 11(2):109–134, 1998. ISSN 09354964. doi: 10.1007/s001620050083.

Chin, C., Örlü, R., Monty, J., Hutchins, N., Ooi, A., and Schlatter, P. Simulation of a Large-Eddy-Break-up Device (LEBU) in a Moderate Reynolds Number Turbulent Boundary Layer. *Flow, Turbulence and Combustion*, 98(2):445–460, 2017a. ISSN 15731987. doi: 10.1007/s10494-016-9757-y.

Chin, C., Örlü, R., Schlatter, P., Monty, J., and Hutchins, N. Influence of a Large-Eddy-Breakup-Device on the Turbulent Interface of Boundary Layers. *Flow, Turbulence and Combustion*, 99(3):823–835, 12 2017b. ISSN 1573-1987. doi: 10.1007/s10494-017-9861-7. URL `https://doi.org/10.1007/s10494-017-9861-7`.

Choi, K. S. Near-wall structure of a turbulent boundary layer with riblets. *Journal of Fluid Mechanics*, 208: 417–458, 1989. ISSN 14697645. doi: 10.1017/S0022112089002892.

Choi, K. S. European drag-reduction research - recent developments and current status. *Fluid Dynamics Research*, 26(5):325–335, 2000. ISSN 01695983. doi: 10.1016/S0169-5983(99)00030-1. URL `http://www.iop.org/journals/FDR`.

Choi, K. S. Experimental Research on Turbulent Flow over Compliant Walls. *Flow Past Highly Compliant Boundaries and in Collapsible Tubes*, pages 275–292, 2003. doi: 10.1007/978-94-017-0415-1{_}12.

Choi, K. S., Yang, X., Clayton, B. R., Glover, E. J., Atlar, M., Semenov, B. N., and Kulik, V. M. Turbulent drag reduction using compliant surfaces. *Proceedings of the Royal Society A: Mathematical, Physical and Engineering Sciences*, 453(1965):2229–2240, 1997. ISSN 13645021. doi: 10.1098/rspa.1997.0119.

Choi, K. S., Le Huu Nho, E., Clayton, B. R., and Escudier, M. P. Turbulence structure over a compliant surface and a possible drag-reduction mechanism. In *APS Division of Fluid Dynamics Meeting Abstracts*, 1999.

Choi, K. S., Le Huu Nho, E., Clayton, B. R., and Escudier, M. P. Turbulent boundary-layer structure over a compliant surface. In *IUTAM Symposium on Flow in Collapsible Tubes and past other Compliant Boundaries, University of Warwick, 26–30 March*, 2001.

Chu, H. H. *Drag characteristics for a compliant surface airfoil*. PhD thesis, The University of Oklahoma, 1971.

Chu, H. H. and Blick, E. F. Compliant Surface Drag As a Function of Speed. *Journal of Spacecraft and Rockets*, 6(6):763–764, 1969. ISSN 00224650.

Clauser, F. H. Turbulent Boundary Layers in Adverse Pressure Gradients. *Journal of the Aeronautical Sciences*, 21(2):91–108, 1954. doi: 10.2514/8.2938. URL `https://doi.org/10.2514/8.2938`.

Daniello, R. J., Waterhouse, N. E., and Rothstein, J. P. Drag reduction in turbulent flows over superhydrophobic surfaces. *Physics of Fluids*, 21(8), 2009. ISSN 10706631. doi: 10.1063/1.3207885.

Darcy, H. Les fontaines publiques de la ville de Dijon. *Recherche*, 1856.

De Angelis, V., Lombardi, P., and Banerjee, S. Direct numerical simulation of turbulent flow over a wavy wall. *Physics of Fluids*, 9(8):2429–2442, 1997. ISSN 10706631. doi: 10.1063/1.869363.

Dean, B. and Bhushan, B. Shark-skin surfaces for fluid-drag reduction in turbulent flow: A review. *Philosophical Transactions of the Royal Society A: Mathematical, Physical and Engineering Sciences*, 368(1929): 4775–4806, 10 2010. ISSN 1364503X. doi: 10.1098/rsta.2010.0201.

Delfos, R., Greidanus, A. J., Charruault, F., and Westerweel, J. Wave characteristics of a compliant coating under a turbulent flow. In *AMT'17 Conference Proceedings. Hydro Testing Forum*, 2017.

Duncan, J. H. The response of an incompressible, viscoelastic coating to pressure fluctuations in a turbulent boundary layer. *Journal of Fluid Mechanics*, 171:339–363, 1986. ISSN 14697645. doi: 10.1017/S0022112086001477.

Duncan, J. H., Waxman, A. M., and Tulin, M. P. The dynamics of waves at the interface between a viscoelastic coating and a fluid flow. *Journal of Fluid Mechanics*, 158:177–197, 1985. doi: 10.1017/S0022112085002609.

Endo, T. and Himeno, R. Direct numerical simulation of turbulent flow over a compliant surface. *Journal of Turbulence*, 3(December 2014):37–41, 2002. ISSN 14685248. doi: 10.1088/1468-5248/3/1/007.

Enyutin, G. V., Lashkov, Y. A., Samoilova, N. V., Fadeev, I. V., and Shumilkina, E. A. Experimental investigation of the effect of longitudinal riblets on the friction drag of a flat plate. *Fluid Dynamics*, 22(2):284–289, 1987. ISSN 00154628. doi: 10.1007/BF01052264.

Ffowcs-Williams, J. E. Reynolds Stress near a Flexible Surface Responding to Unsteady Airflow. *The Journal of the Acoustical Society of America*, 35(11):1887, 11 1963. ISSN 0001-4966. doi: 10.1121/1.2142669. URL `https://doi.org/10.1121/1.2142669`.

Fischer, M. C. and Ash, R. L. A General Review of Concepts for Reducing Skin Friction, Including Recommendations for Future Studies. Technical Report March, National Aeronautics and Space Administration (NASA), 1974.

Fisher, D. H. and Blick, E. F. Turbulent damping by flabby skins. *Journal of Aircraft*, 3(2):163–164, 1966. ISSN 00218669. doi: 10.2514/3.43722.

Fukagata, K., Iwamoto, K., and Kasagi, N. Contribution of Reynolds stress distribution to the skin friction in wall-bounded flows. *Physics of Fluids*, 14(11):L73–L76, 2002. ISSN 10706631. doi: 10.1063/1.1516779.

Fukagata, K., Kasagi, N., and Sugiyama, K. Feedback control achieving sublaminar friction drag. In *Proceedings of the 6th Symposium on Smart Control of Turbulence*, pages 143–148. Center for Smart Control of Turbulence Tokyo, 2005.

Fukagata, K., Kasagi, N., and Koumoutsakos, P. A theoretical prediction of friction drag reduction in turbulent flow by superhydrophobic surfaces. *Physics of Fluids*, 18(5):16–20, 2006. ISSN 10706631. doi: 10.1063/1.2205307.

Fukagata, K., Kern, S., Chatelain, P., Koumoutsakos, P., and Kasagi, N. Evolutionary optimization of an anisotropic compliant surface for turbulent friction drag reduction. *Journal of Turbulence*, 9(35):1–17, 2008. doi: 10.1080/14685240802441126.

Gad-el Hak, M. Boundary Layer Interactions With Compliant Coatings: An Overview. *Applied Mechanics Reviews*, 39(4):511–524, 4 1986a. ISSN 0003-6900. doi: 10.1115/1.3143723. URL `https://doi.org/10.1115/1.3143723`.

Gad-el Hak, M. The Response of Elastic and Viscoelastic Surfaces to a Turbulent Boundary Layer. *Journal of Applied Mechanics*, 53(1):206–212, 3 1986b. ISSN 0021-8936. doi: 10.1115/1.3171714. URL `https://doi.org/10.1115/1.3171714`.

Gad-el Hak, M. *Flow Control: Passive, Active, and Reactive Flow Management*. Cambridge University Press, 2000. doi: 10.1017/CBO9780511529535.

Gad-El-Hak, M. Compliant coatings for drag reduction, 2002. ISSN 03760421.

Gad-El-Hak, M., Blackwelder, R. F., and Riley, J. J. On the interaction of compliant coatings with boundary-layer flows. *Journal of Fluid Mechanics*, 140:257–280, 1984. ISSN 14697645. doi: 10.1017/S0022112084000598.

Garcia, S. J. Private comunication, 2019.

García-Mayoral, R. and Jiménez, J. Drag reduction by riblets. *Philosophical Transactions of the Royal Society A: Mathematical, Physical and Engineering Sciences*, 369(1940):1412–1427, 4 2011. ISSN 1364503X. doi: 10.1098/rsta.2010.0359.

Gómez-De-Segura, G., Fairhall, C. T., MacDonald, M., Chung, D., and García-Mayoral, R. Manipulation of near-wall turbulence by surface slip and permeability. *Journal of Physics: Conference Series*, 1001(1), 2018. ISSN 17426596. doi: 10.1088/1742-6596/1001/1/012011.

Goody, M. Empirical Spectral Model of Surface Pressure Fluctuations. *AIAA Journal*, 42(9):1788–1794, 9 2004. ISSN 0001-1452. doi: 10.2514/1.9433. URL `https://doi.org/10.2514/1.9433`.

Gose, J. W., Golovin, K., Boban, M., Mabry, J. M., Tuteja, A., Perlin, M., and Ceccio, S. L. Characterization of superhydrophobic surfaces for drag reduction in turbulent flow. *Journal of Fluid Mechanics*, 845:560–580, 2018. ISSN 14697645. doi: 10.1017/jfm.2018.210.

Gray, J. Studies in Animal Locomotion. *Journal of Experimental Biology*, 13(2):192 LP – 199, 4 1936. URL `http://jeb.biologists.org/content/13/2/192.abstract`.

Greidanus, A. J. Private communication, 2019.

Greidanus, A. J. *Turbulent shear flow over complex surfaces: An experimental study*. PhD thesis, Delft University of Technology, 2020. URL `https://doi.org/10.4233/uuid:5d46cffe-032b-4084-8c09-88ab7f0f767d`.

Greidanus, A. J., Delfos, R., and Westerweel, J. Fluid-structure interaction of compliant coatings under turbulent flow conditions: force and PIV analysis. In *AMT'17 Conference Proceedings. Hydro Testing Forum*, 2017.

Hahn, S., Je, J., and Choi, H. Direct numerical simulation of turbulent channel flow with permeable walls. *Journal of Fluid Mechanics*, 450:259–285, 2002. ISSN 0022-1120. doi: 10.1017/s0022112001006437.

Hansen, R. J. and Hunston, D. L. An experimental study of turbulent flows over compliant surfaces. *Journal of Sound and Vibration*, 34(3):297 – IN2, 1974. ISSN 0022-460X. doi: https://doi.org/10.1016/S0022-460X(74)80314-7. URL `http://www.sciencedirect.com/science/article/pii/S0022460X74803147`.

Hansen, R. J. and Hunston, D. L. Fluid-property effects on flow-generated waves on a compliant surface. *Journal of Fluid Mechanics*, 133:161–177, 1983. ISSN 0022-1120. doi: DOI:10.1017/S0022112083001846. URL `https://www.cambridge.org/core/article/fluidproperty-effects-on-flowgenerated-waves-on-a-compliant-surface/9591BEE4A5F3F504DC6FE0F86EBB29CE`.

Hansen, R. J., Hunston, D. L., Ni, C. C., Reischman, M. M., and Hoyt, J. W. Hydrodynamic Drag and Surface Deformations Generated by Liquid Flows Over Flexible Surfaces. In *Viscous Flow Drag Reduction*, Progress in Astronautics and Aeronautics, pages 439–452. American Institute of Aeronautics and Astronautics, 1 1980. ISBN 978-0-915928-44-6. doi: doi:10.2514/5.9781600865466.0439.0452. URL `https://doi.org/10.2514/5.9781600865466.0439.0452`.

Hudson, J. D., Dykhno, L., and Hanratty, T. J. Turbulence production in flow near a wavy wall. *Experiments in Fluids*, 20:257–265, 1996.

Huynh, D. and McKeon, B. Measurements of a turbulent boundary layer-compliant surface system in response to targeted, dynamic roughness forcing. *Experiments in Fluids*, 61(4):94, 2020. ISSN 1432-1114. doi: 10.1007/s00348-020-2933-9. URL `https://doi.org/10.1007/s00348-020-2933-9`.

Ivanov, O. O., Vedeneev, V. V., Kulik, V. M., and Boiko, A. V. The influence of compliant coatings on skin friction in the turbulent boundary layer. *Journal of Physics: Conference Series*, 894:12036, 10 2017. doi: 10.1088/1742-6596/894/1/012036. URL `https://doi.org/10.1088%2F1742-6596%2F894%2F1%2F012036`.

Johnson, R. P. Review of Compliant Coating Research of MO Kramer. Technical report, 1980.

Józsa, T. I., Balaras, E., Kashtalyan, M., Borthwick, A. G. L., and Viola, I. M. Active and passive in-plane wall fluctuations in turbulent channel flows. *Journal of Fluid Mechanics*, 866:689–720, 2019. ISSN 14697645. doi: 10.1017/jfm.2019.145.

Kármán, T. V. Über laminare und turbulente Reibung. *ZAMM - Journal of Applied Mathematics and Mechanics / Zeitschrift für Angewandte Mathematik und Mechanik*, 1(4):233–252, 1 1921. ISSN 0044-2267. doi: https://doi.org/10.1002/zamm.19210010401. URL `https://doi.org/10.1002/zamm.19210010401`.

Kiknadze, G. I., Krasnov, Y. K., and Chushkin, Y. V. Investigation of the enhancement of heat transfer due to self-organization of ordered dynamic twisted heat-carrier structures on a heat-transfer surface. *Report IV Kurchatov Institute of Atomic Energy*, 1984.

Kim, E. and Choi, H. Space-time characteristics of a compliant wall in a turbulent channel flow. *Journal of Fluid Mechanics*, 756:30–53, 2014. ISSN 14697645. doi: 10.1017/jfm.2014.444.

Kramer, M. O. Boundary Layer Stabilization By Distributed Damping. *Journal of the American Society for Naval Engineers*, 72(1):25–34, 1960. ISSN 15593584. doi: 10.1111/j.1559-3584.1960.tb02356.x.

Kramer, M. O. The dolphin's secret. *Journal of the American Society for Naval Engineers*, 73(1):103–108, 1961. doi: 10.1111/j.1559-3584.1961.tb02422.x. URL `https://onlinelibrary.wiley.com/doi/abs/10.1111/j.1559-3584.1961.tb02422.x`.

Kramer, M. O. Boundary Layer Stabilization By Distributed Damping. *Naval Engineers Journal*, pages 341–348, 1962.

Kulik, V. M. Action of a turbulent flow on a hard compliant coating. *International Journal of Heat and Fluid Flow*, 33(1):232–241, 2012. ISSN 0142727X. doi: https://doi.org/10.1016/j.ijheatfluidflow.2011.10.003. URL `http://www.sciencedirect.com/science/article/pii/S0142727X11001342http://dx.doi.org/10.1016/j.ijheatfluidflow.2011.10.003`.

Kulik, V. M., Poguda, I. S., and Semenov, B. N. Experimental investigation of one-layer viscoelastic coatings action on turbulent friction and wall pressure pulsations. In Choi, K.-S., editor, *Recent Developments in Turbulence Management*, pages 263–289. Springer Netherlands, Dordrecht, 1991. ISBN 978-94-011-3526-9. doi: 10.1007/978-94-011-3526-9{_}14. URL `https://doi.org/10.1007/978-94-011-3526-9_14`.

Kulik, V. M., Boiko, A. V., and Lee, I. Influence of the thickness of monolithic compliant coatings on the skin friction drag. *MATEC Web of Conferences*, 115, 2017. ISSN 2261236X. doi: 10.1051/matecconf/201711502024.

Kuwata, Y. and Suga, K. Lattice Boltzmann direct numerical simulation of interface turbulence over porous and rough walls. *International Journal of Heat and Fluid Flow*, 61:145–157, 2016. ISSN 0142727X. doi: 10.1016/j.ijheatfluidflow.2016.03.006. URL `http://dx.doi.org/10.1016/j.ijheatfluidflow.2016.03.006`.

Lai, Y.-J. C. Turbulent viscous drag reduction by means of passive flow control - Focus on compliant surfaces. Technical report, Delft University of Technology, Delft, the Netherlands, 2020.

Landahl, M. T. On the stability of a laminar incompressible boundary layer over a flexible surface. *Journal of Fluid Mechanics*, 13(4):609–632, 1962. doi: 10.1017/S002211206200097X.

Larson, K. Can you estimate modulus from durometer hardness for silicones. *Dow Corning Corporation*, pages 1–6, 2016.

Lee, I., Kulik, V. M., Boiko, A. V., and Chun, H. H. Experimental investigation of drag reducing mechanism of compliant coating with optimal viscoelastic properties. *6th International Symposium on Turbulence and Shear Flow Phenomena, TSFP 2009*, 2009-June(June):891–895, 2009.

Lee, T., Fisher, M., and Schwarz, W. H. The measurement of flow-induced surface displacement on a compliant surface by optical holographic interferometry. *Experiments in Fluids*, 14(3):159–168, 1993. ISSN 1432-1114. doi: 10.1007/BF00189506. URL `https://doi.org/10.1007/BF00189506`.

Lin, J. C., Walsh, M. J., and Balasubramanian, R. Drag of Two-Dimensional Small-Amplitude Symmetric and Asymmetric Wavy Walls in Turbulent Boundary Layers. *NASA Technical Paper*, 1984. ISSN 01488341.

Lin, Y.-Y. *Numerical investigation of the turbulent boundary layer over dimpled surfaces.* PhD thesis, Delft University of Technology, 2021.

Lindgren, E. R. Experimental study on turbulent pipe flows of distilled water. Technical report, 1965.

Lissaman, P. B. S. and Harris, G. L. Turbulent skin friction on compliant surfaces. *AIAA Journal*, 7(8):1625–1627, 8 1969. ISSN 0001-1452. doi: 10.2514/3.5452. URL `https://doi.org/10.2514/3.5452`.

Looney, W. R. and Blick, E. F. Skin-friction coefficients of complaint surfaces in turbulent flow. *Journal of Spacecraft and Rockets*, 3(10):1562–1564, 1966. ISSN 00224650. doi: 10.2514/3.28706.

Lucey, A. D. and Carpenter, P. W. Boundary layer instability over compliant walls: Comparison between theory and experiment. *Physics of Fluids*, 7(10):2355–2363, 1995. ISSN 10706631. doi: 10.1063/1.868748.

Luchini, P., Manzo, F., and Pozzi, A. Resistance of a grooved surface to parallel flow and cross-flow. *Journal of Fluid Mechanics*, 228:87–109, 1991. ISSN 14697645. doi: 10.1017/S0022112091002641.

Lumley, J. L. Drag reduction in turbulent flow by polymer additives. *Journal of Polymer Science: Macromolecular Reviews*, 7(1):263–290, 1973. doi: 10.1002/pol.1973.230070104. URL `https://onlinelibrary.wiley.com/doi/abs/10.1002/pol.1973.230070104`.

Lynn, T. B., Bechert, D. W., and Gerich, D. A. Direct drag measurements in a turbulent flat-plate boundary layer with turbulence manipulators. *Experiments in Fluids*, 19(6):405–416, 1995. ISSN 07234864. doi: 10.1007/BF00190258.

Maaß, C. and Schumann, U. Direct Numerical Simulation of Separated Turbulent Flow over a Wavy Boundary. In Hirschel, E. H., editor, *Flow Simulation with High-Performance Computers II: DFG Priority Research Programme Results 1993–1995*, pages 227–241. Vieweg+Teubner Verlag, Wiesbaden, 1996. ISBN 978-3-322-89849-4. doi: 10.1007/978-3-322-89849-4{_}17. URL `https://doi.org/10.1007/978-3-322-89849-4_17`.

Mamori, H., Fujimura, M., Udagawa, S., Iwamoto, K., Murata, A., Kawaguchi, Y., Ando, H., Kawashima, H., and Mieno, H. Effect of wavelength of sinusoidal wavy wall surface on drag and heat transfer at turbulent thermal boundary layer flow. *Journal of Thermal Science and Technology*, 13(2):1–11, 2018. ISSN 18805566. doi: 10.1299/jtst.2018jtst0023.

McAlister, K. W. and Wynn, T. M. Experimental evaluation of compliant surfaces at low speeds. Technical report, National Aeronautics and Space Administration (NASA), 1974.

McLean, J. D., George-Falvy, D. N., and Sullivan, P. P. Flight-test of turbulent skin-friction reduction by riblets. *Turbulent drag reduction by passive means*, pages 408–424, 1987. URL `http://scholar.google.com/scholar?hl=en&btnG=Search&q=intitle:Flight-test+of+turbulent+skin-friction+reduction+by+riblets#0`.

McMichael, J. M., Klebanoff, P. S., and Mease, N. E. Experimental Investigation of Drag on a Compliant Surface. *Viscous Flow Drag Reduction*, pages 410–438, 1980. doi: 10.2514/5.9781600865466.0410.0438. URL `https://arc.aiaa.org/doi/abs/10.2514/5.9781600865466.0410.0438`.

Min, T. and Kim, J. Effects of hydrophobic surface on skin-friction drag. *Physics of Fluids*, 16(7):1–5, 2004. ISSN 10706631. doi: 10.1063/1.1755723.

Mix, A. and Giacomin, A. Standardized Polymer Durometry. *Journal of Testing and Evaluation*, 39(4):696–705, 7 2011. ISSN 0090-3973. doi: 10.1520/JTE103205. URL `https://compass.astm.org/DIGITAL_LIBRARY/JOURNALS/TESTEVAL/PAGES/JTE103205.htm`.

Nieuwstadt, F. T. M., Westerweel, J., and Boersma, B. J. *Turbulence: introduction to theory and applications of turbulent flows*. Springer, 2016. ISBN 3319315994.

Nijemeisland, M. Private communication, 2020.

Nisewanger, C. R. Flow noise and drag measurements of vehicle with compliant coating. Technical report, NAVAL ORDNANCE TEST STATION CHINA LAKE CA, 1964.

Orszag, S. A. Prediction of compliant wall drag reduction - Part 1. Technical report, National Aeronautics and Space Administration (NASA), 1977.

Polytek Development Corp. Deadener & Hardener for Platsil Gels - Technical Bulletin, 2017a. URL `https://www.polytek.com/sites/default/files/Deadener_Hardener_TechnicalBulletin_Polytek.pdf`.

Polytek Development Corp. Platsil Silicone Gels - Technical Bulletin, 2017b. URL `https://www.polytek.com/sites/default/files/PlatSilGels_TechnicalBulletin_Polytek_0.pdf`.

Puryear, F. W. Boundary layer control drag reduction by compliant surfaces. *US Dept. of Navy, David Taylor Model Basin. Report*, 1668, 1962.

Riley, J. J., Gad-el Hak, M., and Metcalfe, R. W. Compliant coatings. *Annual Review of Fluid Mechanics*, pages 393–420, 1988.

Ritter, H. and Messum, L. T. Water tunnel measurements of turbulent skin friction on six different compliant surfaces of one foot length. *Admiralty Research Laboratory Report ARL/G N*, 9:1964, 1964.

Ritter, H. and Porteous, J. S. Water tunnel measurements of skin friction on a compliant coating. *Admiralty Research Laboratory Report ARL/N3/G/HY/9/7*, 1965.

Robert, J. P. Drag reduction: an industrial challenge. Technical report, Airbus Industrie Blagnac (France), 1992.

Rodríguez-López, E., Bruce, P. J. K., and Buxton, O. R. H. A robust post-processing method to determine skin friction in turbulent boundary layers from the velocity profile. *Experiments in Fluids*, 56(4):68, 2015. ISSN 1432-1114. doi: 10.1007/s00348-015-1935-5. URL `https://doi.org/10.1007/s00348-015-1935-5`.

Rossing, T. D. and Fletcher, N. H. Coupled Vibrating Systems BT - Principles of Vibration and Sound. pages 95–124. Springer New York, New York, NY, 1995. ISBN 978-1-4612-2502-7. doi: 10.1007/978-1-4612-2502-7{_}4. URL `https://doi.org/10.1007/978-1-4612-2502-7_4`.

Rosti, M. E. and Brandt, L. Numerical simulation of turbulent channel flow over a viscous hyper-elastic wall. *Journal of Fluid Mechanics*, 830:708–735, 2017. ISSN 14697645. doi: 10.1017/jfm.2017.617.

Rosti, M. E., Brandt, L., and Pinelli, A. Turbulent channel flow over an anisotropic porous wall - Drag increase and reduction. *Journal of Fluid Mechanics*, 842:381–394, 2018. ISSN 14697645. doi: 10.1017/jfm.2018.152.

Savill, A. M. and Mumford, J. C. Manipulation of turbulent boundary layers by outer-layer devices: Skin-friction and flow-visualization results. *Journal of Fluid Mechanics*, 191:389–418, 1988. ISSN 14697645. doi: 10.1017/S0022112088001624.

Semenov, B. N. On conditions of modelling and choice of viscoelastic coatings for drag reduction BT - Recent Developments in Turbulence Management. pages 241–262. Springer Netherlands, Dordrecht, 1991. ISBN 978-94-011-3526-9. doi: 10.1007/978-94-011-3526-9{_}13. URL `https://doi.org/10.1007/978-94-011-3526-9_13`.

Semenov, B. N., Amirov, A. I., Kulik, V. M., and Malyuga, A. G. Experimental studies of compliant coatings for reduction of turbulent friction. *Thermophysics and Aeromechanics*, 14(1):133–142, 2007. ISSN 08698643. doi: 10.1134/S0869864307010155.

Shen, L., Zhang, X., Yue, D. K. P., and Triantafyllou, M. S. Turbulent flow over a flexible wall undergoing a streamwise travelling wave motion. *Journal of Fluid Mechanics*, 484(484):197–221, 2003. ISSN 00221120. doi: 10.1017/S0022112003004294.

Spalart, P. R. and McLean, J. D. Drag reduction: Enticing turbulence, and then an industry. *Philosophical Transactions of the Royal Society A: Mathematical, Physical and Engineering Sciences*, 369(1940):1556–1569, 2011. ISSN 1364503X. doi: 10.1098/rsta.2010.0369.

Spalding, D. B. A Single Formula for the “Law of the Wall”. *Journal of Applied Mechanics*, 28(3):455–458, 9 1961. ISSN 0021-8936. doi: 10.1115/1.3641728. URL https://doi.org/10.1115/1.3641728.

Suga, K., Matsumura, Y., Ashitaka, Y., Tominaga, S., and Kaneda, M. Effects of wall permeability on turbulence. *International Journal of Heat and Fluid Flow*, 31(6):974–984, 2010. ISSN 0142727X. doi: 10.1016/j.ijheatfluidflow.2010.02.023. URL http://dx.doi.org/10.1016/j.ijheatfluidflow.2010.02.023.

Suga, K., Nakagawa, Y., and Kaneda, M. Spanwise turbulence structure over permeable walls. *Journal of Fluid Mechanics*, 822:186–201, 2017. ISSN 14697645. doi: 10.1017/jfm.2017.278.

Szodruch, J. Viscous drag reduction on transport aircraft. In *29th Aerospace Sciences Meeting*, Reno, Nevada, 1 1991. American Institute of Aeronautics and Astronautics (AIAA). doi: 10.2514/6.1991-685. URL http://arc.aiaa.org/doi/10.2514/6.1991-685.

Takahashi, H., Kurita, M., Koga, S., and Endo, S. Evaluation of skin friction drag reduction in turbulent boundary layer using riblets. In *AIAA Aerospace Sciences Meeting, 2018*, Kissimmee, Florida, 2018. ISBN 9781624105241. doi: 10.2514/6.2018-0839.

United Nations General Assembly. Transforming Our World: The 2030 Agenda for Sustainable Development, 2015. URL https://undocs.org/en/A/RES/70/1.

van Campenhout, O. W. G., van Nesselrooij, M., Veldhuis, L. L. M., van Oudheusden, B. W., and Schrijer, F. F. J. An experimental investigation into the flow mechanics of dimpled surfaces in turbulent boundary layers. In *AIAA Aerospace Sciences Meeting, 2018*. American Institute of Aeronautics and Astronautics Inc, AIAA, 2018. ISBN 9781624105241. doi: 10.2514/6.2018-2062.

van Nesselrooij, M., Veldhuis, L. L. M., van Oudheusden, B. W., and Schrijer, F. F. J. Drag reduction by means of dimpled surfaces in turbulent boundary layers. *Experiments in Fluids*, 57(9), 9 2016. ISSN 07234864. doi: 10.1007/s00348-016-2230-9.

Vedeneev, V. V. Propagation of waves in a layer of a viscoelastic material underlying a layer of a moving fluid. *Journal of Applied Mathematics and Mechanics*, 80(3):225–243, 2016. ISSN 00218928. doi: 10.1016/j.jappmathmech.2016.07.004.

Virk, P. S. Drag reduction fundamentals. *AIChE Journal*, 21(4):625–656, 1975. doi: 10.1002/aic.690210402. URL https://aiche.onlinelibrary.wiley.com/doi/abs/10.1002/aic.690210402.

Viswanath, P. R. Aircraft viscous drag reduction using riblets. *Progress in Aerospace Sciences*, 38(6-7):571–600, 2002. ISSN 03760421. doi: 10.1016/S0376-0421(02)00048-9.

Wallace, J. M. Quadrant Analysis in Turbulence Research: History and Evolution. *Annual Review of Fluid Mechanics*, 48(1):131–158, 1 2016. ISSN 0066-4189. doi: 10.1146/annurev-fluid-122414-034550. URL https://doi.org/10.1146/annurev-fluid-122414-034550.

Wallace, J. M., Eckelmann, H., and Brodkey, R. S. The wall region in turbulent shear flow. *Journal of Fluid Mechanics*, 54(1):39–48, 1972. ISSN 0022-1120. doi: DOI:10.1017/S0022112072000515. URL https://www.cambridge.org/core/article/wall-region-in-turbulent-shear-flow/F38FABEC434430051BE92BAEDAE3EC14.

Walsh, M. J. Effect of detailed surface geometry on riblet drag reduction performance. *Journal of Aircraft*, 27 (6):572–573, 1990. ISSN 00218669. doi: 10.2514/3.25323.

Walsh, M. J. and Weinstein, L. M. Drag and heat transfer on surfaces with small longitudinal fins. In *AIAA 11th Fluid and Plasma Dynamics Conference*, Seattle, Washington, 1978. American Institute of Aeronautics and Astronautics (AIAA). doi: 10.2514/6.1978-1161.

Walters, R. R. *Turbulent boundary layer characteristics of flow over a compliant surface*. PhD thesis, University of Oklahoma, 1969.

Welch, B. L. The significance of the difference between two means when the population variances are unequal. *Biometrika*, 29(3-4):350–362, 2 1938. ISSN 0006-3444. doi: 10.1093/biomet/29.3-4.350. URL `https://doi.org/10.1093/biomet/29.3-4.350`.

White, F. M. and Corfield, I. *Viscous fluid flow*, volume 3. McGraw-Hill New York, 2006.

Wilkinson, S. P., Anders, J. B., Lazos, B. S., and Bushnell, D. M. Turbulent drag reduction research at NASA langley: progress and plans. *International Journal of Heat and Fluid Flow*, 9(3):266–277, 1988. ISSN 0142727X. doi: 10.1016/0142-727X(88)90037-9.

Xu, S., Rempfer, D., and Lumley, J. Turbulence over a compliant surface: Numerical simulation and analysis. *Journal of Fluid Mechanics*, 478(478):11–34, 2003. ISSN 00221120. doi: 10.1017/S0022112002003324.

Zhang, C., Miorini, R., and Katz, J. Integrating Mach–Zehnder interferometry with TPIV to measure the time-resolved deformation of a compliant wall along with the 3D velocity field in a turbulent channel flow. *Experiments in Fluids*, 56(11):203, 11 2015. ISSN 1432-1114. doi: 10.1007/s00348-015-2072-x. URL `https://doi.org/10.1007/s00348-015-2072-x`.

Zhang, C., Wang, J., Blake, W., and Katz, J. Deformation of a compliant wall in a turbulent channel flow. *Journal of Fluid Mechanics*, 823:345–390, 7 2017. ISSN 14697645. doi: 10.1017/jfm.2017.299.